



**HAL**  
open science

# The effects of electric field, illumination and their interplay on the transport properties of cuprate superconductor thin films and heterostructures

Ralph El Hage

► **To cite this version:**

Ralph El Hage. The effects of electric field, illumination and their interplay on the transport properties of cuprate superconductor thin films and heterostructures. Superconductivity [cond-mat.supr-con]. Université Paris-Saclay, 2021. English. NNT : 2021UPASP030 . tel-03616843

**HAL Id: tel-03616843**

**<https://theses.hal.science/tel-03616843v1>**

Submitted on 23 Mar 2022

**HAL** is a multi-disciplinary open access archive for the deposit and dissemination of scientific research documents, whether they are published or not. The documents may come from teaching and research institutions in France or abroad, or from public or private research centers.

L'archive ouverte pluridisciplinaire **HAL**, est destinée au dépôt et à la diffusion de documents scientifiques de niveau recherche, publiés ou non, émanant des établissements d'enseignement et de recherche français ou étrangers, des laboratoires publics ou privés.

The effects of electric field, illumination  
and their interplay on the transport  
properties of cuprate superconductor thin  
films and heterostructures

Les effets de champ électrique, de lumière et leurs  
interactions sur les propriétés de transport des films minces  
et d'hétérostructures à base de cuprates supraconducteurs

**Thèse de doctorat de l'université Paris-Saclay**

École doctorale n°564 : physique de l'Ile-de-France (PIF)

Spécialité de doctorat : Physique

Unité de recherche : Université Paris-Saclay, CNRS, Thales, Unité mixte de physique  
CNRS/Thales, 91767, Palaiseau, France.

Référent : Faculté des sciences d'Orsay

**Thèse présentée et soutenue à Paris-Saclay, le 23 Mars  
2021, par**

**RALPH EL HAGE**

**Composition du Jury**

**Dafiné RAVELOSONA**

Directeur de recherche, Université Paris-Saclay

Président

**Fabio MILETTO GRANOZIO**

Professeur, University of Naples  
Frederico II

Rapporteur & Examineur

**Xavier OBRADORS**

Professeur, Universitat Autònoma de  
Barcelona

Rapporteur & Examineur

**Beatriz NOHEDA**

Professeure, University of Groningen

Examinatrice

**Laurence MECHIN**

Directrice de recherche, ENSICAEN

Examinatrice

**Direction de la thèse**

**Javier VILLEGAS**

Directeur de recherche, Université Paris-Saclay / Unité Mixte de Physique CNRS-Thales

Directeur de thèse

**Anke SANDER**

Ingénieure de recherche, Université  
Paris-Saclay / Unité Mixte de Physique  
CNRS-Thales

Co-Encadrante & Examinatrice

**Titre :** Les effets de champ électrique, de lumière et leurs interactions sur les propriétés de transport des films minces et d'hétérostructures à base de cuprates supraconducteurs

**Mots clés :** Champ électrique, Lumière, Interactions, transport, hétérostructures, cuprate

**Résumé :** Les cuprates sont un exemple d'oxydes de métaux de transition caractérisé par une phase de supraconductivité à haute température critique. Il est possible de modifier leur état fondamental grâce à l'application de stimulus externe. L'objectif de cette thèse est d'étudier les interactions entre les effets de champ et de lumière sur des hétérostructures de cuprates. Premièrement nous avons étudié les effets de photo-dopage sur des films minces d'YBCO sous-dopé. Après l'illumination par de la lumière nous observons une augmentation persistante de la température critique du film et une diminution de sa résistivité. Ces changements sont corrélés à un changement de la mobilité des porteurs de charge. Nous avons ensuite étudié le phénomène de « resistive switching » qui relate un changement de la résistance d'une jonction composée d'YBCO et d'un métal MoSi après l'application d'un champ électrique. Cet effet est expliqué grâce à une réaction d'oxydoréduction qui a lieu à l'interface entre les deux électrodes.

Enfin, nous décrivons l'interaction entre les effets d'un champ électrique et les effets de lumière sur des jonctions composées de YBCO et d'un métal transparent, l'ITO. Sous l'action d'un champ électrique nous notons un effet de « resistive switching ». De plus, et après illumination, nous avons mesuré un effet photovoltaïque et un changement persistant de la résistance de la jonction, qui dépend de son historique. Le photo-voltage observé est dû à un effet photovoltaïque observé dans des jonctions pn. En revanche, les effets persistants sont interprétés grâce à une réaction d'oxydoréduction causée par lumière. Nous concluons cette thèse par des travaux de « resistive switching » sur des jonctions de nickélates qui sont similaires à celles des jonctions à base de cuprate. Ceci est particulièrement intéressant pour des applications en tant que memristors dans le domaine du neuromorphisme.

**Title :** The effects of electric field, illumination and their interplay on the transport properties of cuprate superconductor thin films and heterostructures

**Keywords :** Electric field, illumination, interplay, transport, heterostructures, thin films

**Abstract :** Transition metal oxides (TMO) are a class of materials characterized by a dense phase diagram which arises from their interlinked degrees of freedom leading to various competing ground states. The main ingredient of this work is a cuprate  $YBa_2Cu_3O_{7-\delta}$  (YBCO) widely studied for its dome-like superconducting phase. Various studies have shown that the properties of cuprates can be altered by applying an electric field or light. We have thus investigated the interplay between the effects of electric field and light on TMOs based heterostructures. We first studied the effects of light on underdoped YBCO thin films. We have observed a persistent increase in its superconducting transition temperature as well as a decrease of its resistivity. A correlation between these changes and the changes in the carrier mobility has been established. Second, we covered the effects of electric field induced resistive switching observed in vertical junctions composed of YBCO and the alloy MoSi. By applying a voltage

pulse, we have observed a persistent, fast and reversible switch in resistance. This effect has been attributed to a reversible electrochemical reaction occurring at the interface. Finally, by switching the opaque MoSi with a transparent electrode ITO, we have managed to investigate the interplay between electric field and light on the transport properties of these junctions. We have observed a photovoltaic effect (PVE) under visible light as well as a history-dependent persistent change of the resistive state of the junction. The PVE has been linked to standard photovoltaic effect observed in a pn junctions and the persistent changes to a light-induced electrochemical reaction. As an outlook, we covered the investigation of electric field induced resistive switching in nickelate based heterostructures. A similar effect to the one described previously has been observed. These effects might be exploited for neuromorphic applications as potential memristive devices.

# Table of contents

Table of contents .....	3
Acknowledgments.....	8
Résumé en français.....	10
1) Introduction .....	17
1.1) Transport theories .....	19
1.1.1) Drude Model .....	19
1.1.1.1) Matthiessen's rule: .....	19
1.1.1.2) Hall effect .....	20
1.1.2) Free electron gas.....	21
1.1.3) Nearly free electron gas.....	22
1.1.4) Fermi liquid .....	22
1.2) Conventional superconductivity .....	24
1.2.1) The London Equation .....	25
1.2.2) The Ginzburg-Landau theory .....	25
1.2.3) BCS theory.....	26
1.3) Transition metal oxides.....	27
1.4) YBCO general description .....	28
1.4.1) Crystal field splitting.....	30
1.4.2) Jahn-Teller distortion .....	30
1.4.3) Mott-Hubbard model.....	31
1.4.4) Parent compound of cuprates as a Mott insulator.....	32
1.4.5) Charge transfer insulator .....	34
1.4.6) Zhang Rice Singlet .....	35
1.5) Cuprate phase diagram.....	35
1.5.1) High T <sub>c</sub> superconductivity.....	35
1.5.2) Pseudogap.....	37
1.5.3) Quantum critical point and Strange Metal .....	39
1.5.4) Stripe order .....	40
1.5.5) Anomalous transport behaviour in cuprates.....	40
1.5.6) Electron doped cuprates.....	42
1.6) Electric field effects in correlated oxides.....	43
1.6.1) Field effect transistors (FET) .....	44
1.6.2) High permittivity gates.....	44
1.6.3) Ferroelectric gates .....	44

1.6.4)	Screening length .....	45
1.6.5)	Tunnelling Junctions.....	46
1.6.5.1)	Blonder-Tinkham-Klapwijk model.....	48
1.6.5.2)	Ferroelectric Tunnel Junctions (FTJ) and Tunnel Electro Resistance (TER).....	49
1.6.5.3)	Resistive switching by redox reaction.....	51
1.7)	Light-induced effects in correlated oxides.....	52
1.7.1)	2D electron gas at LAO/STO interface .....	53
1.7.2)	Manganites .....	55
1.7.3)	Cuprates.....	57
2)	Experimental Techniques.....	61
2.1)	Pulsed Laser Deposition.....	62
2.2)	Sputtering.....	64
2.3)	Oxygen stoichiometry control.....	65
2.4)	Ion irradiation .....	66
2.5)	X-ray diffraction .....	68
2.6)	Atomic Force Microscopy .....	69
2.6.1)	Piezoresponse Force Microscopy.....	70
2.6.2)	Conductive Tip AFM .....	70
2.7)	Scanning Transmission Electron Microscopy.....	71
2.8)	Resonant Inelastic X-ray Scattering .....	72
2.9)	Nanofabrication .....	73
2.9.1)	Vertical junctions: .....	74
2.9.2)	YBCO Thin Films: .....	76
2.10)	Transport.....	77
2.10.1)	Cryostation and sample preparation .....	77
2.10.2)	Temperature Calibration.....	78
2.10.3)	Transport measurements.....	78
2.10.4)	Superconducting Critical Temperature .....	78
2.10.5)	Hall effect.....	79
2.10.6)	Mobility and Hall angle .....	80
2.10.7)	Vertical junctions .....	81
2.11)	Illumination .....	81
2.11.1)	Sources.....	81
2.11.2)	Heating.....	83
3)	Photo-induced effects on $YBa_2Cu_3O_{7-\delta}$ films.....	87
3.1)	Motivation & key findings.....	88

3.2)	Sample description .....	90
3.2.1)	Oxygen deficient YBCO films.....	90
3.2.1.1)	Oxygen content determination.....	91
3.2.2)	Ion Irradiated YBCO films.....	91
3.2.3)	Comparison between the two sets of samples.....	92
3.3)	Correlation between carrier density, carrier mobility and superconducting critical temperature.....	92
3.4)	Temperature behaviour .....	94
3.5)	Visible/UV light illumination .....	96
3.5.1)	Basic effect.....	96
3.5.2)	Dependence on irradiance.....	97
3.5.3)	Doping dependence .....	97
3.5.4)	Spectral dependence .....	99
3.6)	Illumination of oxygen deficient vs ion irradiated samples .....	100
3.7)	Summary .....	102
3.8)	Relaxation .....	102
3.9)	Resonant Inelastic Xray Scattering.....	105
3.10)	Concluding remarks .....	107
4)	Tunnel electroresistance in $YBa_2Cu_3O_{7-\delta}/BiFeO_3 - Mn/Mo_80Si_{20}$ vertical tunnel junctions.....	109
4.1)	Motivation & key findings.....	110
4.2)	Fabrication and structural characterization of the junctions .....	111
4.2.1)	AFM & XRD characterization of YBCO/BFO heterostructures .....	112
4.2.2)	PFM & CT-AFM characterization of YBCO/BFO heterostructures .....	112
4.2.3)	Characterisation of superconducting properties of YBCO and MoSi.....	114
4.2.4)	HAADF-EELS of YBCO/BFO/MoSi heterostructures .....	115
4.3)	Electrical measurements on the junctions.....	116
4.3.1)	Wiring.....	116
4.3.2)	As-grown state .....	116
4.3.2.1)	BDR fit .....	116
4.3.3)	Poling.....	118
4.4)	Thickness dependence of BFO layer .....	120
4.4.1)	Conductance curves.....	121
4.4.2)	Hysteresis loop.....	121
4.4.3)	Temperature behaviour .....	122
4.4.4)	Size effects .....	123

4.4.5)	Effect of the duration of the $V_{pol}$ pulses.....	124
4.4.6)	Changing the interlayer and the top electrode .....	125
4.4.7)	Retention.....	126
4.4.8)	Asymmetry in the poling voltages .....	127
4.5)	Temperature and bias analysis of YBCO gap .....	128
4.5.1)	BTK modelling of the conductance .....	130
4.6)	Model.....	132
4.7)	Conclusion.....	133
5)	Interplay between field effect and light induced effects in $YBa_2Cu_3O_7 - \delta/ITO$ vertical tunnel junctions.....	134
5.1)	Motivation & main results .....	136
5.2)	Growth and characterization .....	136
5.3)	Optical properties of top electrodes.....	137
5.4)	Electric poling and transport measurements .....	138
5.5)	Temperature dependence of the conductance .....	139
5.6)	Thermally activated relaxation .....	140
5.7)	Illumination effects: general portrait.....	141
5.8)	Volatile illumination effects: photovoltage .....	143
5.8.1)	Dependence of $V_{oc}$ on temperature.....	143
5.8.2)	Dependence of $V_{oc}$ on optical power .....	145
5.8.3)	Dependence of $V_{oc}$ on the junction conductance .....	145
5.9)	Persistent illumination effects in the ON state.....	146
5.9.1)	Temperature vs photon induced effects.....	148
5.9.2)	Spectral Response .....	149
5.9.3)	Time dependence.....	150
5.9.4)	Temperature dependence .....	151
5.10)	Persistent illumination effects in the OFF state.....	152
5.10.1)	Time dependence.....	153
5.10.2)	Temperature dependence .....	154
5.11)	Illumination effects in intermediate junction states .....	155
5.11.1)	Characteristic behaviour across the OFF to ON branch of the hysteresis loop .....	155
5.11.2)	Characteristic behaviour across the ON to OFF branch of the hysteresis loop .....	156
5.11.3)	Similarity between Persistent changes in conductance and photovoltage $V_{oc}$ .....	157
5.12)	Model .....	161
5.12.1)	Photovoltaic effect.....	161
5.12.2)	Illumination effects in the ON state.....	162

5.12.3)	Illumination effects in the OFF state.....	164
5.12.4)	Illumination effect in intermediate conductance states.....	165
5.13)	Conclusion.....	168
5.14)	Supplementary measurements.....	169
5.14.1)	Thermal vs photo-induced effects .....	169
5.14.2)	Absence of effects under infrared illumination .....	169
5.14.3)	Light induced fatigue.....	170
5.14.4)	Aluminium vs Gold wires .....	171
6)	Tunnel electroresistance observed in <i>NdNiO3</i> /MoSi vertical tunnel junctions.....	173
6.1)	Motivation & main results .....	174
6.2)	Nickelate structure.....	174
6.3)	Film Growth and Device Fabrication.....	175
6.3.1)	Film Characterization .....	176
6.3.2)	Device Fabrication.....	177
6.4)	Transport Measurement.....	178
6.4.1)	Differential conductance in the ON (low resistance) and OFF (high resistance) states 178	
6.4.2)	Influence of poling on MIT .....	180
6.5)	Poling Efficiency as a function of Poling temperature .....	181
6.6)	Relaxation dynamic.....	182
6.7)	Model .....	184
6.8)	Conclusion.....	185
7)	Conclusions and perspectives.....	187
	Bibliography .....	187

# Acknowledgments

I would first like to thank the two referees, Professor Fabio Miletto and Professor Xavier Obradors for agreeing to review this doctoral thesis as well as the rest of the jury for their comments on the content of this work.

These past four years have been a journey that I will remember for the remainder of my days, and I would like to express my sincere gratitude to my Ph.D. advisor Javier Villegas for his dedication and mentorship throughout. Javier, you have always been supportive of me across the various challenges and inherent setbacks of experimental research. But it was not all hardship, as we also experienced the thrill of new discoveries and exciting results – accompanied by some pretty good laughs! I am especially grateful for your help through the countless discussions we've had, which would often start with "five minutes of your time" - only to take up more than an hour. I am still processing how much I've learned from you, and am positive I'll end up telling a student someday: "My thesis director used to say..."

I am also grateful to my co-supervisor Anke Sander for her precious input on all the structural and deposition issues I've encountered. Anke, I cannot thank you enough for taking the time to review the first draft of this manuscript – and for your invaluable help in structuring and channelling my thoughts and ideas.

I owe a lot of this work to the supra group: you have all managed to combine cheerfulness and professionalism perfectly. The innumerable discussions with Javier B., Juan, Denis, Yves et al. have contributed enormously to this manuscript. A big thanks to my office mates (current and past) Santiago, Aurélien, Isa, Xavier, Philippe, Victor, and Vincent, among others, for punctuating our scientific talks with odd comments leading to vibrant discussions! This made the office a lovely space to work in. A special mention to Victor for his patience while teaching me the ropes of experimental physics during my first couple of years; and to Vincent for his blend of work ethic and humour (not to mention every earworm you caused, Vincent). I've learned so much from you guys!

This work could not have been completed without the help of our many collaborators, namely the LPICM researcher J. Charliac for his expertise in metallic depositions, as well as A. Nicolaou and N. Jaouen, for both their expertise in XAS and RIXS techniques and their time for the actual experiments. I owe a big part of the work to the researchers at the Universidad Complutense de Madrid for the steady flow of samples they have sent us and the numerous discussions that allowed us to refine our understanding of transition metal oxides. Special thanks to professor Jacobo Santamaria for our talks, scientific or otherwise. I feel fortunate to have had the chance to witness the work of a great researcher for several months. Gracias por todo profe!

I am certainly not the first one to say that the "UMR" is a haven full of brilliant researchers who have taught me a great deal, both professionally and personally. I want to thank both Sophie and Florian for their immeasurable help in all the "clean room" and metal deposition issues we've had to deal with; and Nicolas for the uncountable hours spent on the bonding machine. I've had the chance to meet incredible people in this lab, and to name them all would be too long. But a special mention is addressed to the Badminton and "Foot en salle" crews, who have beared with my below-average cardio every week. Finally, I would like to thank the two directing teams of Fred<sup>2</sup> as well as Paolo and Vincent for their help and guidance across this journey.

I would surely not have been able to get to the end of this thesis without the unwavering support of my friends. The old ones, who have been there since the beginning, and who seldom needed more

than a couple of words to show up with a (or several) bottle(s). And the new ones I've met along the road and shared many gatherings with.

Last but not least, my family has been the steady rock behind everything I've undertaken – and this is no exception. I dedicate this thesis to you.

## Résumé en français

# Les effets de champ électrique, de lumière et leurs interactions sur les propriétés de transport des films minces et d'hétérostructures à base de cuprate supraconducteurs

### I. Illumination de couches minces d'YBCO :

Le premier volet de cette thèse consiste à étudier les effets de la lumière sur des couches minces d' $\text{YBa}_2\text{Cu}_3\text{O}_{6+x}$  (YBCO). Des couches minces d'YBCO ont été fabriquées à Madrid par le groupe de Jacobo Santamaria et sont encore étudiées au laboratoire. Pour moduler le dopage du supraconducteur, en particulier sa température critique, une étape de recuit est nécessaire après la croissance par pulvérisation cathodique des couches d'YBCO : la pression partielle d'oxygène et la température contrôlent la teneur en oxygène des échantillons. Ce jeu d'échantillons est appelé « *échantillon désoxygéné* ». Un processus lithographique est utilisé pour permettre de définir un barreau d'YBCO et de déposer un barreau d'Au qui servirait de thermomètre local nécessaire pour correctement estimer la température de l'YBCO sous irradiation. Dans le reste de ce document, la température indiquée est toujours celle estimée à l'aide de ce thermomètre. Les propriétés électriques de l'YBCO sont mesurées avant et après illumination par différentes sources de lumière : lumière ultraviolette (largeur de bande 260-310nm) et LED monochromatiques dans le visible à haute puissance. Un deuxième groupe d'échantillons irradiés est étudié sous les mêmes conditions. L'irradiation par des atomes d'oxygène induit du désordre dans la structure de l'YBCO. Ainsi les propriétés obtenues -résistance dans l'état normal,  $T_c$ , densité de porteur etc. - sont semblables à celles obtenus en désoxygénant les couches d'YBCO. Ce jeu d'échantillons est appelé « *échantillon irradié* ».

Après illuminations par de la lumière UV et visible, on observe d'une part une augmentation de 5% de la température critique des échantillons, ainsi qu'une augmentation de leur densité de porteurs de 12% (mesure d'effet Hall) et d'autre part, une diminution de leur résistivité dans l'état normal et une diminution de leur mobilité – mobilité qui est le ratio entre le coefficient de Hall et la résistivité longitudinale (c.f. fig. 1). Cet état dû à la lumière est permanent lorsque la température de l'échantillon est maintenue en dessous d'environ 250K.

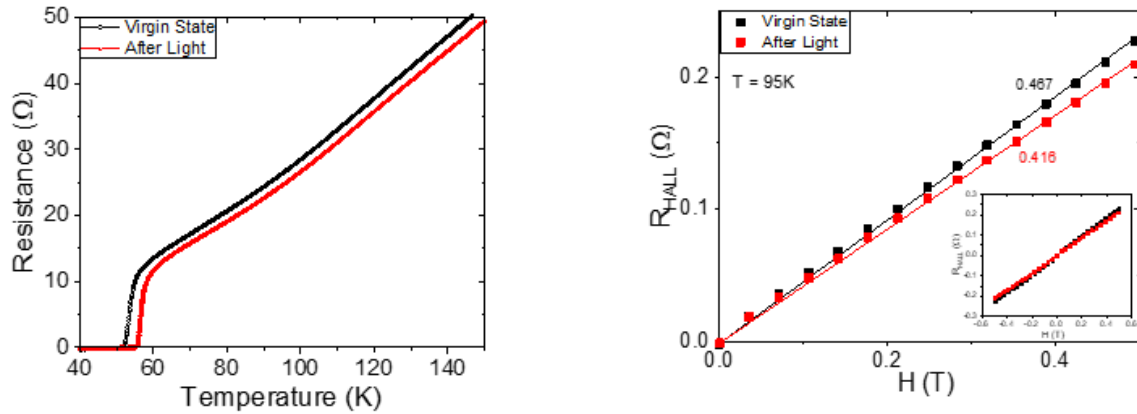


Figure 1 : Evolution de la résistance d'un film d'YBCO désoxygéné avant et après illumination (Gauche). Mesure d'effet de Hall effectué à 95K avant et après illumination ((Droite). L'encart représente la mesure en fonction de champs positifs et négatifs. (Illumination : fluence = 100mW/cm<sup>2</sup>, λ=560nm et T = 95K)

En comparant les changements observés après illumination, on s'aperçoit qu'il existe une forte corrélation entre l'augmentation de la température critique des échantillons et l'augmentation de leur mobilité ; plutôt que leur densité de porteur (à T=95K). En effet, nous observons une augmentation de la température critique dans les échantillons lorsque leur densité de porteurs ET leur mobilité augmentée après illumination. Les changements de densité de porteur induits par la lumière sont similaires pour les deux jeux d'échantillons et les deux longueurs d'onde utilisées. (c.f. fig. 2)

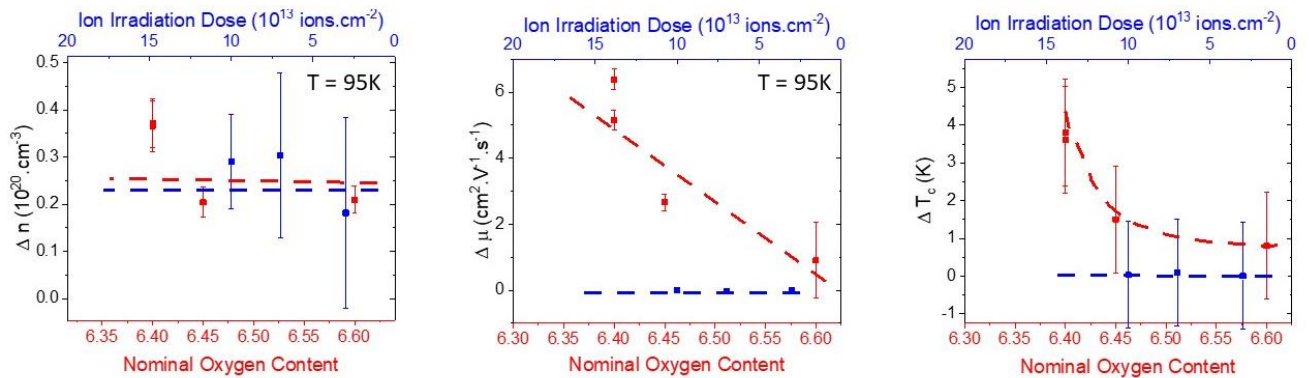


Figure 2 : Variation de la densité de porteur (Gauche), de la mobilité (Milieu) et de la température critique (Droite) en fonction de le contenu d'oxygène pour le jeu d'échantillons désoxygénés (rouge) et de la dose d'irradiation pour le jeu d'échantillons irradiés (bleu).

Nous nous sommes aussi intéressés au comportement de relaxation du phénomène. Une étude systématique de la relaxation de l'effet de la lumière a été réalisée sur un film mince désoxygéné. On étudie la dynamique de deux paramètres : la densité de porteur et la mobilité des porteurs à différentes températures après avoir illuminé l'échantillon à une température de 95 K pendant 3 heures. La figure (3) indique l'évolution de la densité de porteur (Gauche) et de la mobilité (Droite) en fonction du temps à des températures différentes. Les valeurs dans l'état initial (*virgin state*) sont aussi indiquées. On observe une dynamique différente dans le comportement des deux paramètres : les temps caractéristiques associés à la relaxation sont clairement différents à haute température.

Leur comportement en fonction du temps de la densité de porteur est une « *stretched exponential* » contrairement à la mobilité qui est plus complexe.

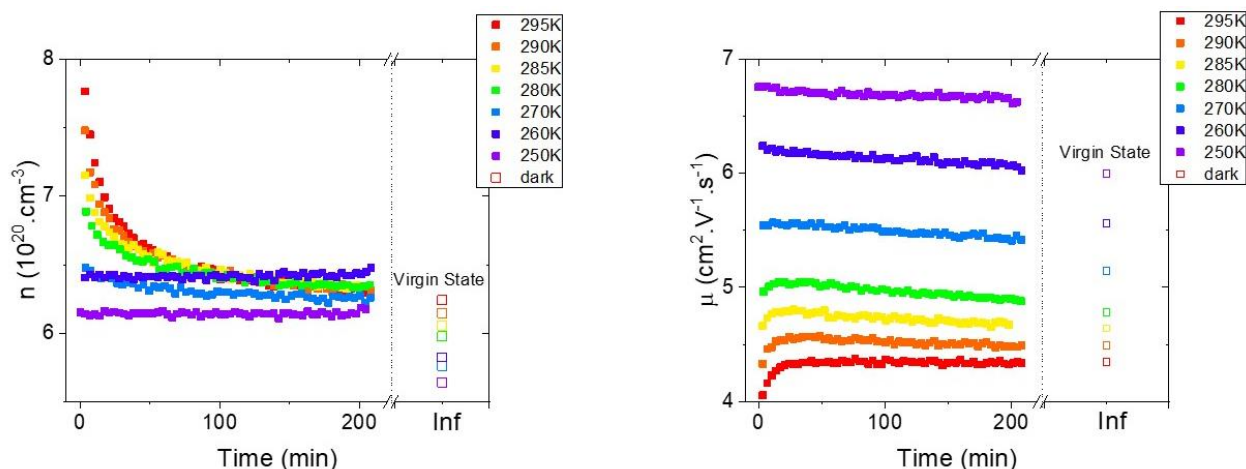


Figure 3 : Evolution de la densité de porteurs (Gauche) et de la mobilité (Droite) en fonction du temps à différentes températures après une illumination à 95K. Les points libellés « virgin state » représentent les valeurs avant le début de l'expérience.

Pour approfondir notre investigation, des mesures préliminaires de RIXS ont été effectuées sur des échantillons d'YBCO désoxygénés sur la ligne SEXTANT du synchrotron SOLEIL. Nous avons commencé par acquérir un spectre d'absorption au seuil du cuivre ( $L_3 \sim 930$  eV) à basse température. Des spectres de RIXS sont effectués à certaines énergies avant l'illumination de l'échantillon et après. Les changements observés dans les spectres peuvent être dus à un changement de la structure locale des atomes de cuivre après l'illumination de l'échantillon (c.f. fig. 4). Des mesures complémentaires sont prévues pour continuer l'étude de cet effet.

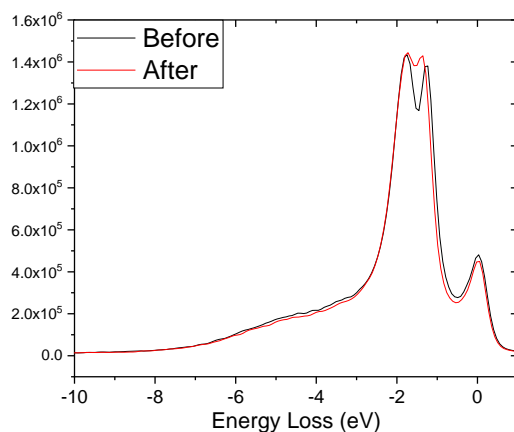


Figure 4 : Spectre RIXS obtenu sur un échantillon d'YBCO désoxygéné avant et après illumination.

## II. Etude d'effet de champs sur des jonctions verticales de cuprates YBCO/MoSi :

La deuxième partie de cette thèse traite des effets de champs sur des jonctions tunnels verticales composées d'un cuprate supraconducteur YBCO et d'un supraconducteur métallique MoSi. Des couches d'YBCO de 30nm d'épaisseur ont été fabriquées au laboratoire par PLD. Une étape de lithographie nous permet de définir des jonctions de quelques dizaines de microns carrés. Puis un

alliage de molybdène et silicium  $Mo_{80}Si_{20}$  est déposée par *sputtering*. Des mesures de transport à basse température sont effectuées sur ces jonctions pour les caractériser. Un changement important et permanent de la résistance de la jonction suite à l'application d'un pulse électrique - *Tunnel ElectroResistance* (TER) - est observé sur ces jonctions. Suite à l'application d'une tension de quelques Volts en DC, nous notons un changement de plusieurs ordres de grandeur de la conductance d'une jonction (c.f. fig. 5). La conductance différentielle est définie comme la dérivée du courant mesuré en fonction de la tension de *bias* appliquée. Nous définissons deux états particuliers : un état de haute conductance nommé « ON » et un état de basse conductance nommé « OFF ».

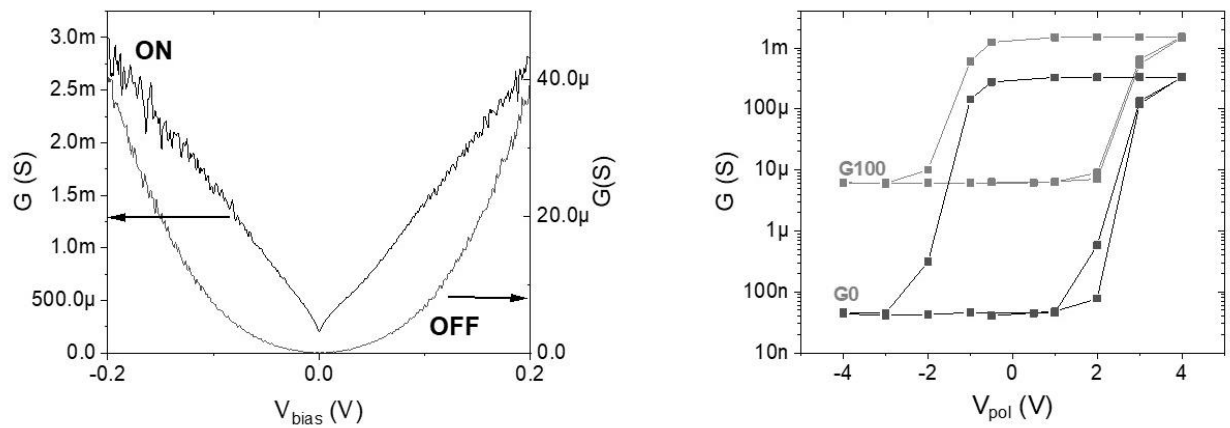


Figure 5: (Gauche) Conductance différentielle en fonction de la tension bias dans les deux états de conductance d'intérêt ON et OFF. (Droite) Conductance différentielle calculée à une tension bias de 100mV (gris) et de 0mV (noir) en fonction de la tension de pol.

Nous notons aussi un effet hystérétique de la conductance différentielle en fonction de la tension de polarisation ( $V_{pol}$ ) (cf fig. 5). L'application d'un  $V_{pol}$  positif permet de passer de l'état OFF vers l'état ON. Une inversion de la polarité de  $V_{pol}$  permet ainsi de retourner vers l'état OFF de manière entièrement réversible.

De plus nous notons une modulation des propriétés supraconductrices du film d'YBCO par l'application de  $V_{pol}$ . Une étude détaillée de la conductance différentielle à bas *bias* permet d'identifier un *dip* de conductance, plus prononcé dans l'état ON que dans l'état OFF. Son étude en fonction de la

température indique une corrélation à la température critique supraconductrice de la couche mince d'YBCO.

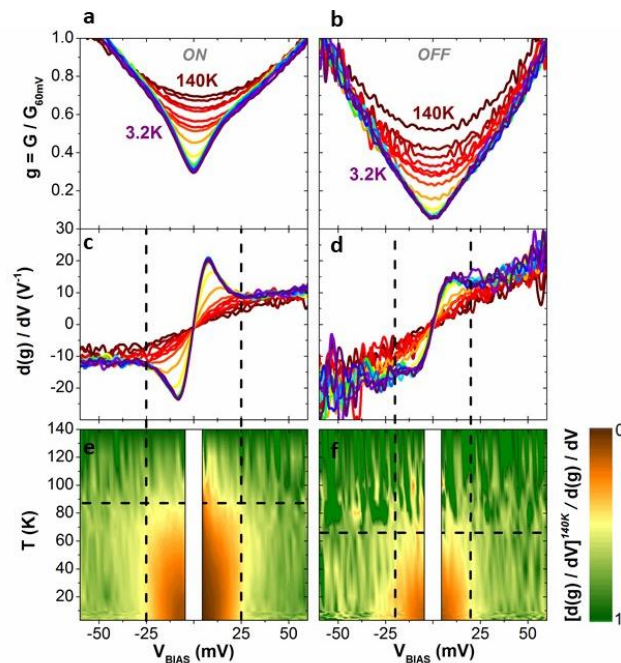


Figure 6: Conductance différentielle normalisée par la conductance calculée à un bias de 60mV en fonction de la tension de bias à des températures différentes dans l'état ON (a) et dans l'état OFF (b). Dérivée de la conductance différentielle en fonction de la tension bias pour ces mêmes températures dans l'état ON (c) et OFF (d). "Color plot" des courbes de la dérivée de la conductance différentielle en fonction de la température et de la tension de bias dans l'état ON (e) et OFF (f).

Cette différence est due à un changement des propriétés supraconductrices de la couche d'YBCO entre un état supraconducteur optimal dans l'état ON ayant une température critique de  $\sim 90K$ , et un état supraconducteur amoindri ayant une température critique de  $\sim 70K$  (c.f. fig. 6).

Le mécanisme microscopique à l'origine de cet effet est une réaction d'oxydoréduction entre les deux électrodes de la jonction. Dans l'état OFF la couche d'YBCO est réduite au dépend de la couche de MoSi : cela augmente la taille de la barrière tunnel diminuant ainsi la conductance de la jonction. Dans l'état ON, à la suite de l'application d'un  $V_{pol}$  positif, la couche d'YBCO s'oxyde au dépend de la couche de MoSi, la taille de la barrière tunnel diminue et la conductance de la jonction augmente.

### III. Etude d'effet de champs et de lumière sur des jonctions verticales de cuprates YBCO/ITO :

Dans un troisième temps, nous nous sommes intéressés à l'effet de la lumière sur des jonctions verticales YBCO/ITO. Le processus de fabrication des jonctions a été préalablement développé par l'équipe et est basé sur les jonctions YBCO/MoSi préalablement étudiée. L'électrode supérieure métallique et transparente est un oxyde d'un alliage indium-étain (ITO), et est déposée au LPCIM. L'échantillon est d'abord mesuré ( $I$  vs  $V$ ) à  $T=3.2K$  avant illumination pour s'assurer de la possibilité de polariser correctement la jonction entre deux états à conductance différente -un état OFF à basse conductance et un état ON à haute conductance. La jonction créée est constituée de l'interface isolante séparant la couche d'YBCO et celle d'ITO (c.f. fig. 7). Dans un second temps, l'échantillon est illuminé

par une LED à longueur d'onde  $\sim 560$  nm. L'illumination est ensuite interrompue et l'échantillon relaxe dans le noir pendant environ une heure avant d'effectuer une nouvelle mesure  $I$  vs  $V$ .

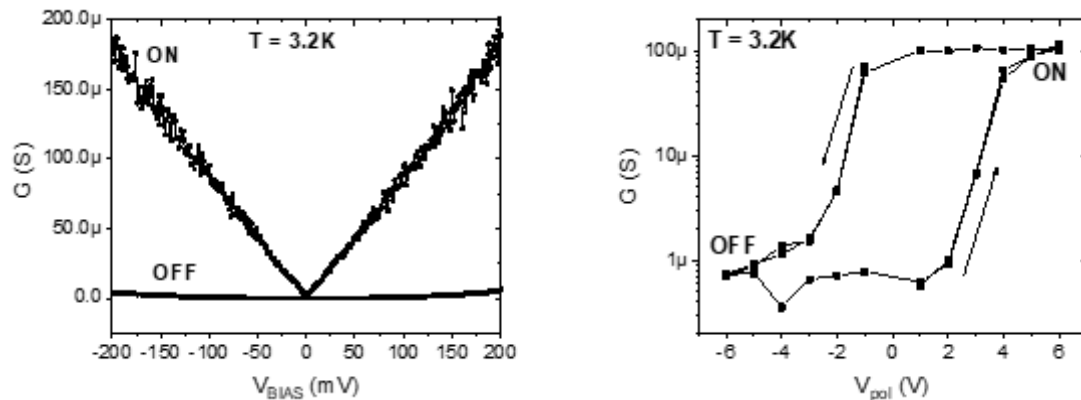


Figure 7 : (Gauche) Conductance différentielle en fonction de  $V_{bias}$  obtenue à  $T = 3.2K$ . (Droite) Conductance différentielle à  $V_{bias} = 100mV$  en fonction de la tension de polarisation  $V_{pol}$ .

Après illumination, on observe que la conductance de la jonction baisse drastiquement lorsque la jonction est préalablement dans l'état ON, et augmente lorsque celle-ci est dans l'état OFF (c.f. fig. 8). Cet effet est non-volatile - la mesure est effectuée une fois la lampe éteinte- et réversible à basse température après quelques itérations. Une fois l'illumination terminée, il est possible de rétablir les états ON et OFF d'origines en polarisant la jonction.

Un effet photovoltaïque classique est aussi mesuré aux bornes des jonctions sous illumination par une lumière UV. On note l'apparition d'une tension « open-circuit » ( $V_{oc} \sim 0.7V$ ) et d'un courant « short-circuit » ( $J_{sc} \sim 0.2A \cdot cm^{-2}$ ) de manière instantanée lorsque la jonction est illuminée, et leur disparition instantanée lorsque la lumière est éteinte (Cf fig. 8). L'amplitude de  $V_{oc}$  est corrélée à la conductance de la jonction: plus celle-ci diminue plus la photo-tension mesurée augmente.

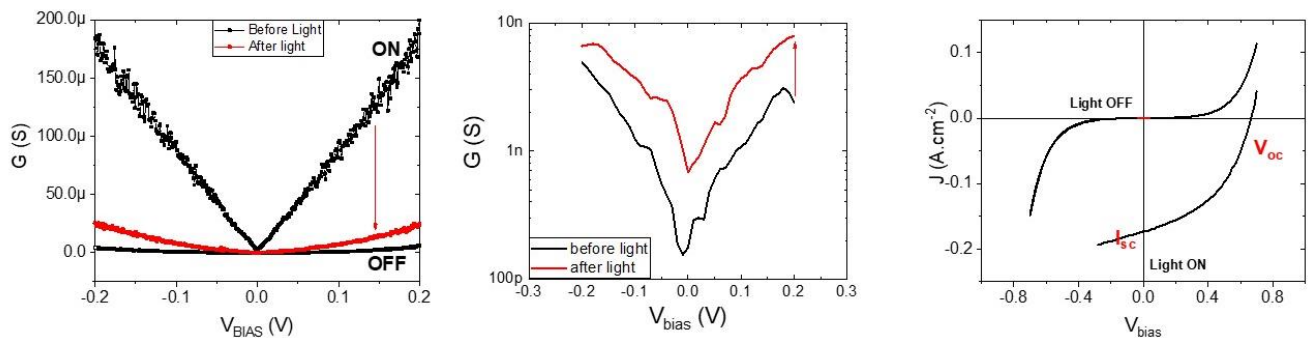


Figure 8 : (Gauche) Conductance différentielle en fonction de  $V_{bias}$  pour différents états de la jonction lorsque celle-ci est initialement dans l'état ON. La courbe rouge représente la conductance après illumination. (Milieu) Conductance différentielle en fonction de  $V_{bias}$  pour différents états de la jonction lorsque celle-ci est initialement dans l'état OFF. La courbe rouge représente la conductance après illumination. (Droite) Courant mesuré aux bornes d'une jonction YBCO/ITO en fonction de la tension appliquée dans le noir et sous illumination par une lumière UV.

Nous interprétons ces effets dus à la lumière grâce à un scénario de réaction d'oxydoréduction entre les deux électrodes de la jonction. Dans l'état OFF, les photons absorbés participent à une réaction d'oxydation de la couche d'YBCO à l'interface. Ceci diminue ainsi la taille de la barrière tunnel et augmente la conductance de la jonction. A l'inverse, lorsque la jonction est dans l'état ON, la lumière accélère une réaction de relaxation naturelle qui tendrait à ramener le système vers son état fondamental. Ceci conduit à la réduction de la couche d'YBCO au niveau de l'interface, a

l'augmentation de la taille de la barrière tunnel et ainsi à la diminution de la conductance de la jonction.

#### IV. Etude d'effet de champs et de lumière sur des jonctions verticales de nickelites :

Dans un quatrième temps, et dans le but d'étudier les conséquences des effets de champs et de lumière sur des d'autres oxides de métaux de transition, des jonctions verticales de nickelites NdNiO<sub>3</sub>/MoSi sont créées puis étudiées. Une couche mince d'un nickelite est déposée sur des substrats différents permettant ainsi de modifier ses propriétés électroniques au DCMI Strasbourg. Cette nickelite présente une transition métal-isolant (MIT) à 100 K, métallique (paramagnétique) au-dessus et isolante (antiferromagnétique) au-dessous. Le processus de fabrication des jonctions est le même que celui décrit ci-dessus. Une électrode supérieure de MoSi est déposée par *sputtering* au laboratoire. Nous avons suivi le même protocole pour caractériser les jonctions obtenues : Une tension «  $V_{pol}$  » de plusieurs volts est appliquée aux bornes de la jonction dans un premier temps permettant de changer son état, puis une basse tension «  $V_{bias}$  » inférieur a 200mV est appliquée aux bornes de la jonction pour lire son état et calculer sa conductance. Nous observons l'existence de deux états stables : un état ON de haute conductance et un état OFF de basse conductance ( $G_{ON}/G_{OFF}=10^2$ ).

Une étude systématique de la polarisation des jonctions en fonction de la température a été effectuée. Nous notons que la polarisation des jonctions est d'une efficacité maximale à la température de transition métal isolant de la couche mince de NNO. Polariser la jonction à une température supérieure à la MIT engendre une dégradation non réversible des propriétés de la jonction. Cependant, polariser la jonction à une température inférieure à la MIT est de moins en moins efficace en diminuant la température. De plus grâce à une étude de l'évolution de l'état d'une jonction en fonction de la température, nous notons que l'état ON relaxe vers l'état initial à haute température contrairement à l'état OFF qui lui reste stable indépendamment de la température de l'échantillon. Des études complémentaires sur ces jonctions en fonction de la lumière seront effectuées.

# 1)Introduction

## Contents

1) Introduction .....	17
1.1) Transport theories .....	19
1.1.1) Drude Model .....	19
1.1.2) Free electron gas.....	21
1.1.3) Nearly free electron gas.....	22
1.1.4) Fermi liquid .....	22
1.2) Conventional superconductivity .....	24
1.2.1) The London Equation .....	25
1.2.2) The Ginzburg-Landau theory .....	25
1.2.3) BCS theory.....	26
1.3) Transition metal oxides.....	27
1.4) YBCO general description .....	28
1.4.1) Crystal field splitting.....	30
1.4.2) Jahn-Teller distortion .....	30
1.4.3) Mott-Hubbard model.....	31
1.4.4) Parent compound of cuprates as a Mott insulator.....	32
1.4.5) Charge transfer insulator .....	34
1.4.6) Zhang Rice Singlet .....	35
1.5) Cuprate phase diagram.....	35
1.5.1) High Tc superconductivity.....	35
1.5.2) Pseudogap.....	37
1.5.3) Quantum critical point and Strange Metal .....	39
1.5.4) Stripe order .....	40
1.5.5) Electron doped cuprates.....	42
1.5.6) Anomalous transport behaviour in cuprates.....	40
1.6) Electric field in correlated oxides.....	43
1.6.1) Field effect transistors (FET) .....	44
1.6.2) High permittivity gates.....	44
1.6.3) Ferroelectric gates .....	44
1.6.4) Screening length .....	45
1.6.5) Tunnelling Junctions.....	46
1.7) Light-induced effects in correlated oxides.....	52
1.7.1) 2DEG electron gas at LAO/STO interface .....	53

1.7.2)	Manganites .....	55
1.7.3)	Cuprates .....	57

In this chapter we will describe the different transport theories used in literature to describe several materials followed by a quick introduction of the superconducting state as observed in conventional superconductors.

The next section will present a general discussion of the theoretical models used to characterise cuprate oxides. We will then describe the high  $T_c$  superconductor state per se as well as the various “normal” states from which it appears. The subsequent sections will cover the context surrounding the response of these materials to external stimuli such as electric field or light.

## 1.1) Transport theories

### 1.1.1) Drude Model

Not long after the discovery of the electron in 1897 by Thompson, Drude formulated his theory of electrical and thermal conduction inspired by the successful kinetic theory of gases. He considered the electrons as negatively charged particles that do not interact with one another (independent electron approximation). On the other hand, he considered the atomic ions as large and heavy immobile particles (free electron approximation). He also considered that collisions are the only scattering mechanism and introduced the scattering time  $\tau$  (probability per unit time for an electron to experience a collision is  $\tau^{-1}$ ).

This allowed him to describe the electron motion in a solid by the following equation of motion:

$$m \frac{d\vec{v}}{dt} = e\vec{E} - \frac{m\vec{v}}{\tau}$$

Where  $m$  is the electron mass,  $\vec{v}$  is its average velocity and  $e$  is the electrical charge.

In the stationary regime where  $\frac{d\vec{v}}{dt} = 0$ , the average velocity can be written as:

$$\vec{v} = \frac{e\tau\vec{E}}{m}$$

By defining the current density as the number of electrons crossing an area perpendicular to the average velocity vector per unit of time, we can write:

$$\vec{j} = ne\vec{v} = \frac{ne^2\tau}{m}\vec{E} = \sigma\vec{E}$$

With  $\sigma$  as the conductivity (coefficient linking the current density to the applied electric field). It is given by:

$$\sigma = \frac{ne^2\tau}{m}$$

This model is a good starting point for the description of most metals but not for other materials. This is mostly due to the fact that the primary scattering process of electrons is not lattice collisions.

#### 1.1.1.1) Matthiessen's rule:

As a matter of fact, the primary contributions to the scattering probability of charge carriers in metals arise from lattice vibrations (phonons), defects, boundaries etc... According to Augustus Matthiessen (Matthiessen, 1863) the resistivity of a metal is the sum of the individual resistivity contributions emanating from different sources namely:

$$\rho_{Metal} = \rho_{Phonons} + \rho_{Defects} + \rho_{Boundaries} + \dots$$

Which leads to  $\frac{1}{\tau_{Metal}} = \frac{1}{\tau_{Phonons}} + \frac{1}{\tau_{Defects}} + \frac{1}{\tau_{Boundaries}} + \dots$

These different contributions are usually characterized by different temperature behaviour. For example, in most metals the resistivity decreases linearly as a function of temperature because of the linear contribution of  $\rho_{Phonons}(T)$ . At low temperature electron-electron interactions become important in the material, before reaching a plateau ( $\rho_{Residual}$  which is a measure of the scattering of charge carriers on defects and impurities) at low enough temperature.

### 1.1.1.2) Hall effect

The Hall effect is used in a standard Hall effect transport measurement which allows to access various parameters such as a material's carrier density and carrier mobility. The basic principle behind this technique consists in measuring a transverse voltage while applying a driving current to the electrons and a perpendicular magnetic field. A schematic of the measurement is shown in Figure 1-1. This effect makes use of the fact that charges in motion because of an applied electric field  $E_x$  (in the x direction) will experience a Lorentz force due to an applied magnetic field  $H_z$  (in the z direction) in a direction transverse to both (in the y direction). As the charge carriers are deflected in the y direction an electric field  $E_y$  will build up to oppose their motion until the system reaches equilibrium.

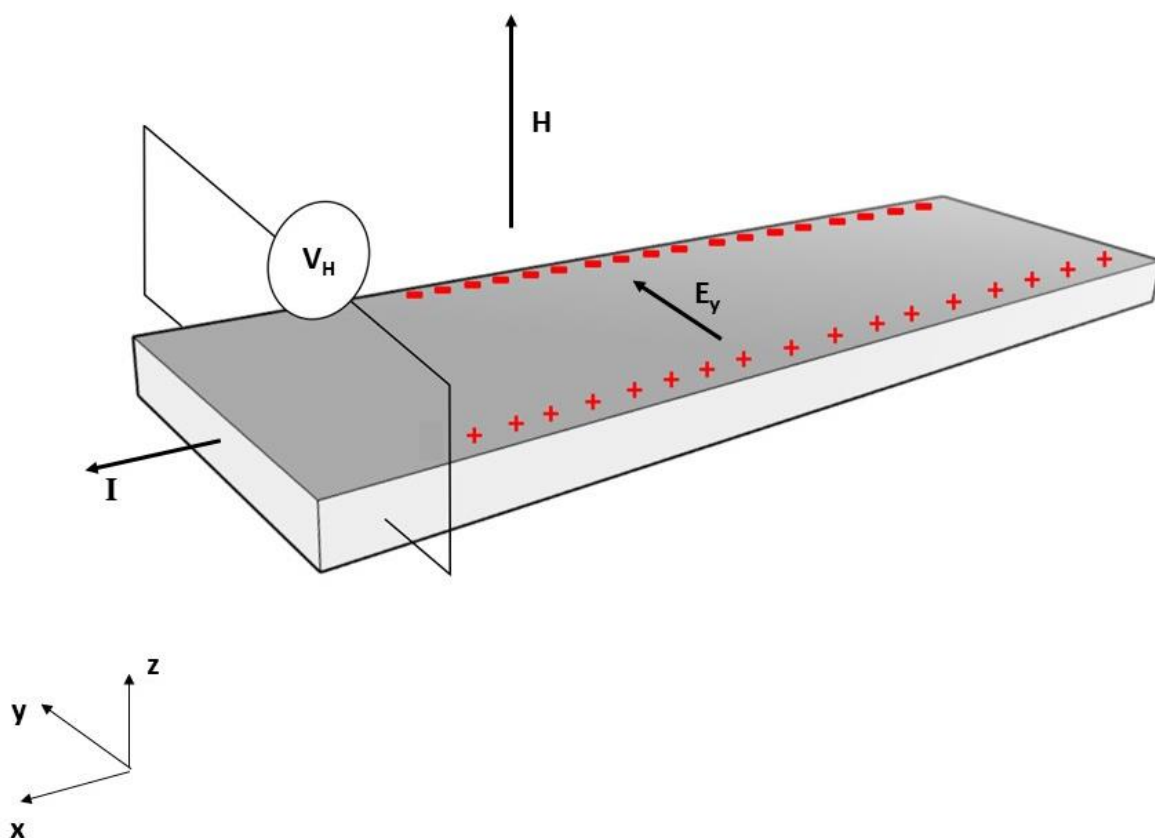


Figure 1-1: Schematic representation of a Hall effect. The red "+" and "-" represent an accumulation of charges due to the Lorentz Force.

One can define the Hall coefficient  $R_H$  as:

$$R_H = \frac{E_y}{j_x H}$$

Starting from the equation of motion of a charged particle in the presence of an electric field in the x and y directions and a magnetic field in the z direction we get:

$$m \frac{d\vec{v}}{dt} = e(\vec{E} - \vec{v} \times \vec{H}) - \frac{m\vec{v}}{\tau}$$

By considering the steady state where  $\frac{d\vec{v}}{dt} = 0$  we get:

$$0 = eE_x - v_y H - \frac{m\vec{v}_x}{\tau}$$

$$0 = eE_y + v_x H - \frac{m\vec{v}_y}{\tau}$$

By rearranging the following equations and noting that in the steady state no current flows in the y direction we get to the equation

$$E_y = -\frac{H}{ne} J_x$$

This allows us to calculate the Hall coefficient as:

$$R_H = -\frac{1}{ne} \quad 1$$

The Hall coefficient is expressed in  $\text{m}^3/\text{C}$ . This equation states that the Hall coefficient depends solely on the carrier density and on no other material parameter. The Hall coefficient sign indicates the nature of the majority charge carriers in the material. Since the polarity of the Hall voltage depends on the nature of the charges deflected by the Lorentz force, the Hall effect can be a useful tool to investigate the nature of charge carriers in a material.

### 1.1.2) Free electron gas

The next step in our description of the transport properties in materials is through a theory called the free electron gas. This theory was developed by Sommerfeld a couple of years after the formulation of Pauli's exclusion principle. The success of this theory lies in the use of Fermi-Dirac statistics rather than Maxwell-Boltzmann to describe electronic distributions. The independent electron approximation and the free electron approximation are maintained (meaning the electron-electron interactions and the electron lattice interactions are neglected). The goal is to find the ground state properties of N electrons confined in a cube of volume V.

The starting point is Schrodinger's equation:

$$-\frac{\hbar^2}{2m} \nabla^2 \psi(r) = \epsilon \psi(r)$$

The electrons are confined to the volume V which allows us to write boundary conditions in the form:  $\psi(x) = \psi(x + L)$  where L is the cube length ( $V = L^3$ ).

By solving the previous equation, we obtain wavefunctions of the form:

$$\psi(k) = \frac{1}{\sqrt{V}} e^{ik \cdot r} \text{ with energy } \epsilon(k) = \frac{\hbar^2 k^2}{2m}. \text{ k is a wavevector given by } k = \frac{2\pi n}{L} \text{ where n is an integer.}$$

The Pauli exclusion principle and the spin degeneracy allows us to place up to two electrons in each of the calculated energy levels starting by the lowest lying ones. This allows us to define a wavevector  $k_F$  (Fermi wavevector) such that  $E_F = \frac{\hbar^2 k_F^2}{2m}$  (Fermi energy) defined as the energy of the highest occupied electronic state. The surface in k space separating the unoccupied from the occupied levels is called the Fermi surface which holds an important signification in the transport properties of materials.

### 1.1.3) Nearly free electron gas

In the nearly free electron gas theory, we allow the charge carriers to be weakly affected by the lattice. We introduce the lattice interaction into the theory by adding a crystalline periodic potential  $U(r)$  to the Schrodinger equation. It thus becomes:

$$\left( -\frac{\hbar^2}{2m}\nabla^2 + U(r) \right) \psi(r) = \epsilon \psi(r)$$

We will then apply boundary conditions specific to transport in a crystal (Born Von Karman boundary conditions):  $\psi(r) = \psi(r + N_i a_i)$  with  $i = x, y, z$ . "a" is a primitive vector of the material's unit cell and N is an integer such that  $N = N_1 N_2 N_3$  is the total number of primitive cells in the crystal. These boundary conditions assure a continuity of the wavefunctions over the crystal volume. Wavefunctions solution to this equation are defined as Bloch waves:  $\psi(r) = e^{i(\vec{k} \cdot \vec{r})} u(r)$  where  $u(r)$  has the periodicity of the crystal lattice.

Due to Bragg reflections of electron waves in the crystal lattice, an energy gap made out of forbidden levels between two different bands appears. The material will behave as a metal or as an insulator depending on the position of the Fermi energy with respect to this energy gap. If an energy band crosses the Fermi energy the material will act as a metal, if it does not and the Fermi energy lies in an energy gap it will behave as an insulator. Note that some materials have an energy gap comparable to the thermal energy at room temperature are therefore classified as semiconductors.

### 1.1.4) Fermi liquid

The previous models have been made following the assumption of the independent electron approximation. However, the reality is different as the electron-electron interaction can play an important role in the properties of a material. The present theory is a refinement of the nearly free electron published by Landau in 1957 (Landau, 1957) called the Fermi liquid theory. The starting point of the theory is a set of non-interacting electrons where the interactions are gradually turned on until their maximal value at time  $t$ . The system then slowly evolves from the ground state of non-interacting particles to the ground state of interacting particles.

The validity of the approach lies in the fact that the scattering time due to electronic interactions is much larger than the one associated with other scattering mechanisms. This basically allows the conservation of a free electron model with the use of renormalized transport coefficients such as the effective mass. This assumption can be justified if one considers an N electron state whose Fermi surface is a sphere and an additional (the N+1) particle whose energy  $\epsilon_1$  must be higher than  $\epsilon_F$ . If this additional particle were to scatter off an electron with energy  $\epsilon_2$  within the Fermi sphere ( $\epsilon_2 < \epsilon_F$ ) the Pauli exclusion principle would force their new energies  $\epsilon_3$  and  $\epsilon_4$  to lie outside the Fermi sphere ( $\epsilon_3 > \epsilon_F$ ,  $\epsilon_4 > \epsilon_F$ ). Energy conservation would also require  $\epsilon_1 + \epsilon_2 = \epsilon_3 + \epsilon_4$ . When  $\epsilon_1$  is close to  $\epsilon_F$ , the phase space corresponding to the scattering event would be a shell around the Fermi surface of radius  $|\epsilon_1 - \epsilon_F|$ , meaning the scattering time would evolve as  $(\epsilon_1 - \epsilon_F)^{-2}$ . If we allow for a finite temperature the scattering rate will be:  $\frac{1}{\tau} \sim a(\epsilon_1 - \epsilon_F)^2 + b(k_B T)^2$  This means that the scattering time associated to electron-electron interactions will increase significantly as the temperature decreases and the energy of the considered electrons is close to the Fermi energy. The temperature dependence of the scattering time is consistent with the observed

temperature dependence of a Fermi liquid resistivity at low temperature. As a matter of fact, the electrical resistivity in a Fermi liquid has a typical  $T^2$  dependency at low temperature.

A practical way to look at a quasiparticle is the following: Starting from a bath of  $N$  non-interacting particles we add an additional particle with momentum  $\mathbf{P}$  to the system at  $t = 0$ . We then slowly turn on interactions and start perturbing the particles in proximity to the additional particle. At time  $t$  when the interactions reach their actual value the additional particle is surrounded by a cloud that represents the interactions it has with the bath. (c.f. Figure 1-2) This does not affect the momentum of the particle per se but its effective mass. The additional particle and its cloud are called a quasiparticle.

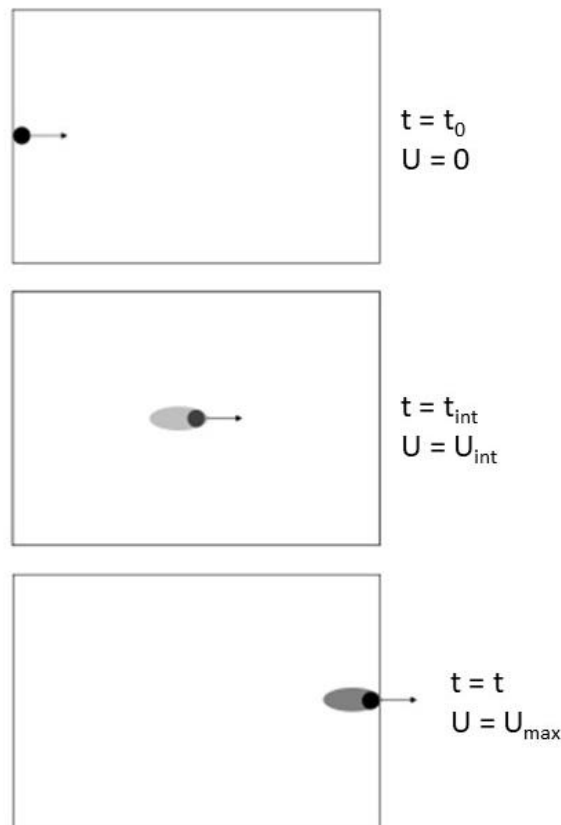


Figure 1-2: Particle starts at  $t = t_0$  in a bath of non-interacting particles. The arrow represents its momentum. The interactions are slowly turned on until  $t = t$ . The shaded area represents the interaction of the added particle with the bath.

In this quasiparticle picture the primary effect of turning on the electron-electron interactions will be to change the one-electron levels  $\varepsilon(k_i)$  describing the system. The difference in electronic distribution functions is given by  $\delta n_k(k) = n_k - n_k^0$  where  $n_k^0$  is the ground state electronic distribution function. The free energy of the system is given by:

$$F = F_0 + \sum_k (\varepsilon_k - \mu) \delta n_k + \frac{1}{2} \sum_{k,k'} f_{k,k'} \delta n_k \delta n_{k'}$$

Where  $F_0$  is the ground state energy,  $\varepsilon_k$  is the quasiparticle kinetic energy and  $f_{k,k'}$  is the Landau interaction function defined as the 2<sup>nd</sup> functional derivative of the energy. The last term in the previous equation relates the interaction between 2 quasiparticles.

This theory predicts the behaviour of several measurable thermodynamic and electronic properties. The specific heat follows the same law as in the free electron gas but with a renormalized effective mass. It is found to be:

$$c_V = \left(\frac{\partial F}{\partial T}\right)_\mu = \frac{m^* k_F}{3\hbar^2} k_B^2 T$$

## 1.2) Conventional superconductivity

In 1911 H. Kammerleng Onnes discovered that the resistance of Mercury completely disappeared when its temperature reached a few kelvins, he coined this phenomenon superconductivity. Two decades later Meissner and Ochsenfeld discovered that the transition into a perfect conductor state was always accompanied by a transition into a perfect diamagnet state i.e. all magnetic field lines are expelled from the material. This property is now called the Meissner effect and it constitutes, together with the perfect conductor property and a diverging specific heat at the critical temperature, the chief properties characterising a superconducting state. Figure 1-3(a-b) depicts the transition of mercury to a state with 0 electrical resistance and a schematic of the Meissner effect respectively.

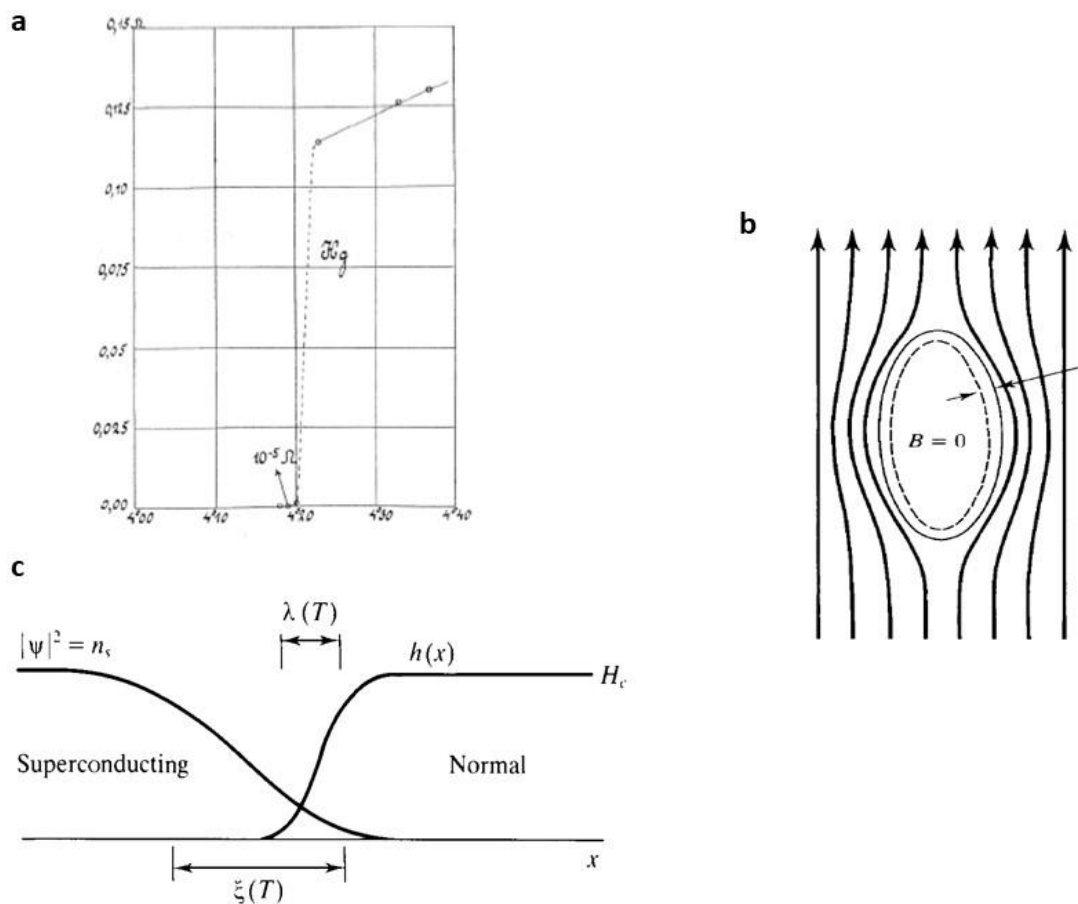


Figure 1-3: (a) Temperature dependence of the resistivity of Hg as measured by Kammerleng Onnes (b) Schematic representation of the Meissner effect in a superconductor (c) Representation of the coherence length and penetration depth of a superconductor. Adapted from (M.Tinkham, 1973)

In 1935 the London brothers proposed an electrodynamic theory that could explain the Meissner effect and in 1950 Ginzburg and Landau came up with a phenomenological theory describing the superconducting state. However, it wasn't until the 1957 that a satisfactory microscopic theory was proposed by Bardeen, Cooper and Schrieffer (BCS theory). They postulated that electrons exchange a virtual phonon to form a bound state (Bardeen, Cooper and Schrieffer, 1957). This theory became

popular because it paved the way for the prediction of other phenomena such as the Josephson effect which was subsequently predicted by Josephson in 1962 (Josephson, 1962). A major revolution occurred in 1986 in the superconductivity field when two IBM researchers Muller and Bednorz discovered that a lanthanum copper oxide underwent a transition into a superconducting state at a temperature of  $T_c = 34\text{K}$  (Bednorz and Müller, 1986). This discovery rocked the superconducting world because the critical temperature of this material was higher than the maximal theoretical value of  $T_c$  predicted by the BCS theory (which was close to 28K). It also belongs to a class of materials where superconductivity was not expected. The hype around this discovery was such that it led to a memorable American Physics Society meeting in 1987 now referred to as the “Woodstock of physics” where presentations lasted until 3am. This opened the road to the discovery of a series of copper oxide materials exhibiting superconducting transitions at temperature as high as 135K at ambient pressure (Iqbal *et al.*, 1994).

In this section we will state the principal properties of superconducting materials according to the different theories stated above then we will detail the superconducting state observed in cuprates.

### 1.2.1) The London Equation

The London brothers have developed a quantitative theory behind the Meissner effect observed in superconductors. The major assumption used is that at temperatures  $T < T_c$  only a fraction of the electron density  $n_s/n$  participate in a supercurrent. In the presence of an electric field and according to the equation of motion the velocity of superconducting electrons is given by:

$$m \frac{dv_s}{dt} = eE$$

Using Maxwell's equations:  $\nabla \times E = -\frac{\partial B}{\partial t}$ ,  $\nabla \times B = \mu_0 j$  and the current density  $j = n_s e v_s$  we get:

$$\nabla^2 B = \frac{n_s e^2}{m} B = \frac{1}{\lambda_L^2} B$$

Where

$$\lambda_L = \left( \frac{n_s e^2}{m} \right)^{1/2}$$

is the London penetration depth. It implies that screening surface currents are responsible for expelling the magnetic field from the material, these surface currents occur over a thickness  $\lambda_L$  over which the magnetic field decreases exponentially to 0.

### 1.2.2) The Ginzburg-Landau theory

This theory is based on Landau's approach of the theory of 2<sup>nd</sup> order phase transitions. The free energy is expressed in terms of a complex order parameter that is 0 above  $T_c$  and non-zero below. This order parameter can be thought of as the one particle wave function of the Cooper pair centre of mass. Note that in 1959 Gor'kov unifies the Ginzburg-Landau (GL) theory with the BCS theory (presented in the next section) close to the superconducting transition temperature (Gor'kov, 1959). The free energy is given by:

$$F_s = F_n + \alpha |\psi|^2 + \frac{\beta}{2} |\psi|^4 + \frac{1}{2m^*} \left| \left( \frac{\hbar}{i} \nabla - \frac{e^*}{c} \vec{A} \right) \psi \right|^2 + \frac{H^2}{8\pi}$$

By minimizing this equation and without any external field a characteristic length appears from the equations given by:

$$\zeta(T) = \sqrt{\frac{\hbar^2}{2m^*|\alpha|}} = \sqrt{\frac{\hbar^2}{2m^*\alpha_0(T - T_c)}}$$

This characteristic length describes the distance over which the superconducting properties disappear when in contact with a non-superconducting material. Figure 1-3c illustrates both the coherence length and the London penetration depth.

### 1.2.3) BCS theory

It wasn't until 1957 that a comprehensive microscopic theory of superconductivity emerged, it was developed by Bardeen Cooper and Schrieffer (the BCS theory) and earned them a Nobel prize in 1972. The basis of the theory revolved around the pairing of electrons (widely called Cooper pairs) through the interaction with collective lattice vibrations (phonons). Frohlich pointed in 1950 that the screening of electrons by ionic motion would lead to an effective attractive interaction between electrons. The BCS theory leads to a Hamiltonian of the form:

$$H_{BCS} = \sum_{k\sigma} \xi_k c_{k\sigma}^\dagger c_{k\sigma} + \frac{1}{N} \sum_{kk'} V_{kk'} c_{k\uparrow}^\dagger c_{-k\downarrow}^\dagger c_{k'\uparrow} c_{-k'\downarrow}$$

Where  $c_{k\sigma}^\dagger$ ,  $c_{k\sigma}$  are the creation and annihilation operators for electron with momentum  $k$  and spin  $\sigma$  and  $\xi_k = \epsilon_k - \mu$ . We shall not delve into the subsequent calculations to derive the parameters of interest but an understanding of the mechanisms can be obtained using the so called Jellium model in a "hands on approach".

The argument can be illustrated as follows: When an electron moves inside a conductor it will attract the positive ions creating a region with increased positive charge density. Due to the inertia of the ion, the lattice distortion will perdure in time and tend to attract another electron. In order to form a Cooper pair however this situation has to fulfil some requirements: Due to the Pauli exclusion principle the final state has to be available, the two electrons have to be of opposite spin and momentum and the energy and the difference between the two electrons has to be smaller than  $\hbar\theta_D$  (the typical energy of a phonon) restricting the electronic energies to a region close to  $E_F$ .

It was shown by Cooper that the attractive interaction could lead to the formation of a pair no matter how weak it may be due to the Pauli exclusion principle. This theory predicted a number of properties (that are now associated with the field of superconductivity) that have been observed experimentally. For example, the electronic excitation spectrum of a superconductor is characterized by the existence of a gap

$$\Delta = \frac{\hbar\omega}{\sinh(\frac{1}{N(0)V})}$$

The energy gap at  $T=0$  is given by  $\Delta(0) = 2\hbar\omega e^{-1/N(0)V}$ . This gap represents the binding energy of the Cooper pair, i.e. the energy gained by the system through the paring of electrons. In the absence of a magnetic field and in the limit of weak coupling, the theory predicts the appearance of a superconducting state at a temperature given by:

$$k_B T_c = 1.13\hbar\omega e^{-1/N(0)V}$$

Which leads to the weak coupling limit of the BCS theory giving the ratio between the superconducting critical temperature and the gap at 0 temperature of

$$\frac{\Delta(0)}{k_B T_c} = 1.76$$

This theory also predicts a discontinuity in the electronic specific heat of the superconductor at the critical temperature. At low temperature and in the absence of a magnetic field it is given by:

$$\frac{c_s}{T_c} = 1.34\gamma \left(\frac{\Delta(0)}{T}\right)^{3/2} e^{-\frac{\Delta(0)}{T}}$$

However, the BCS theory is unable to predict the properties of exotic superconductors such as the main subject of this thesis: cuprates. We first briefly describe the transition metal oxide family of materials to which the cuprates belong because of their shared properties.

### 1.3) Transition metal oxides

The main subjects of this thesis are a class of materials called transition metal oxides (TMO) which are characterized by the chemical formula  $ABO_3$  where A is a rare earth element, B is a transition metal oxide (elements with partially filled 3d electronic bands are the main interest of this thesis) and O is an oxygen ion. The research around this class of materials has started in the 1950's when manganites were first investigated and has intensified at the end of the 1980's with the discovery of high  $T_c$  superconductivity in cuprates by Bednorz and Müller (Bednorz and Müller, 1986) which was awarded with a Nobel prize in 1987.

Due to the combination of complex crystal structures and peculiar electronics properties of the elements involved, the intertwined degrees of freedom of these materials offer a significant playground for researchers. The subtle interplay of charge, lattice, spin and orbital degrees of freedom grant these materials complicated phase diagrams where a multitude of phases compete and coexist. Figure 1-4a depicts a schematic representation of the main degrees of freedom at play in a transition metal oxide. Figure 1-4b shows a schematic phase diagram of a nickelate of the form  $RNiO_3$  where R is a rare earth element adapted from (Freeland, Van Veenendaal and Chakhalian, 2016). This graph indicates the various electronic, structural and magnetic phases observed in this material. By substituting the rare earth element in the structure (rare earth doping), the electrical and magnetic properties of the material are critically affected. In this example the chemical substitution is the lever used to tune the properties of a nickelate material.

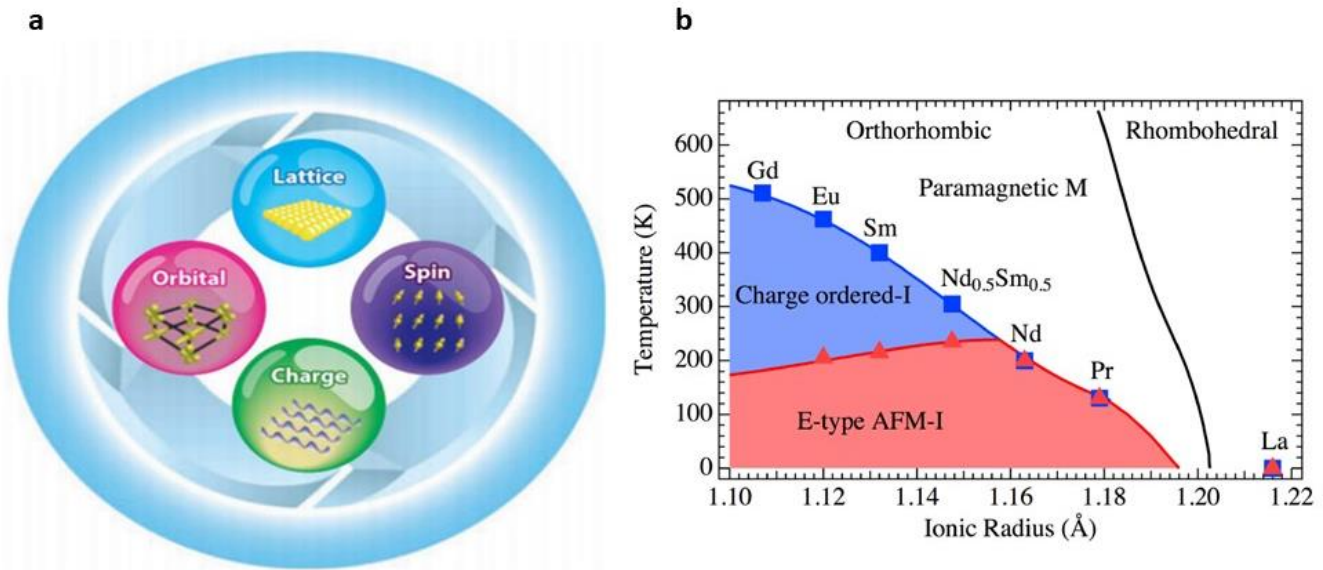


Figure 1-4: (a) Schematic representation of the main degrees of freedom in a typical transition metal oxide (b) Nickelate phase diagram showing the different electronic, magnetic and structural phases as a function of the ionic radius of the rare earth element. Adapted from (Freeland, Van Veenendaal and Chakhalian, 2016)

The fact that a significant number of phases are present in a single phase diagram points to the small energy differences required to pass from one to another. This makes TMOs very interesting candidates for technological applications (by making use of their large functionalities such as their electronic conduction or ferroic properties). Their sensitivity to external stimuli such as electric fields, magnetic fields, light or pressure grants the researchers a panel of external knobs to study and control the different phases. In addition, technological advances in deposition techniques have also allowed the combination of these materials into heterostructures. Nowadays we can find TMOs in a number of different applications such as piezoelectric actuators (Chiang, Farrey and Soukhojak, 1998), intelligent coatings (Taha *et al.*, 2017) or even superconducting magnets.

The main subject of this thesis is a cuprate (a family of TMOs) superconductor, the next sections will be dedicated to a general description of the theoretical tools required to describe some of its exotic phases as well as a detailed description of its rich phase diagram. The subsequent sections will be devoted to a description of the various effects observed in TMOs under the influence of external stimuli such as electric field or light.

#### 1.4) YBCO general description

We have focused on the cuprate high  $T_c$  superconductor  $Y_1Ba_2Cu_3O_{7-\delta}$  (YBCO), where  $\delta$  represents the amount of missing oxygen in the crystal structure. It has a perovskite structure of type "ABO" characterized by an orthorhombic structure with lattice parameters  $a = 3.82 \text{ \AA}$ ,  $b = 3.89 \text{ \AA}$  and  $c = 11.68 \text{ \AA}$  at optimal doping.

The usual YBCO cell with a "123" structure (the 123 represents the proportion of yttrium, barium and copper in a unit cell) is characterized by the presence of oxygen vacancies in its unit cell. By adjusting the growth parameters one can control the average oxygen content such as  $0 < \delta < 1$  in the structure. In our work, the oxygen content effectively represented by the value  $7 - \delta$  plays the role of doping parameter allowing to control the material's superconducting properties such as its transition temperature (Tallon *et al.*, 1995; Mundet *et al.*, 2020).

Figure 1-5a shows a schematic representation of the YBCO unit cell. We can distinguish two highlighted areas in the structure:

- 1) The  $\text{CuO}_2$  planes that extend in the (ab) direction. They are believed to play a crucial role in the superconducting properties of the material. These planes are common to all superconducting cuprates.
- 2) The CuO chains that extend in b direction. Changing the oxygen stoichiometry of YBCO boils down to changing the number of oxygen vacancies in the CuO chains. They are believed to play the role of a charge reservoir by injecting extra charge carriers into the  $\text{CuO}_2$  planes (Uimin, 1994). In a  $\text{YBCO}_{6.5}$  sample for example, the CuO chains alternate between empty and full chains throughout the structure.

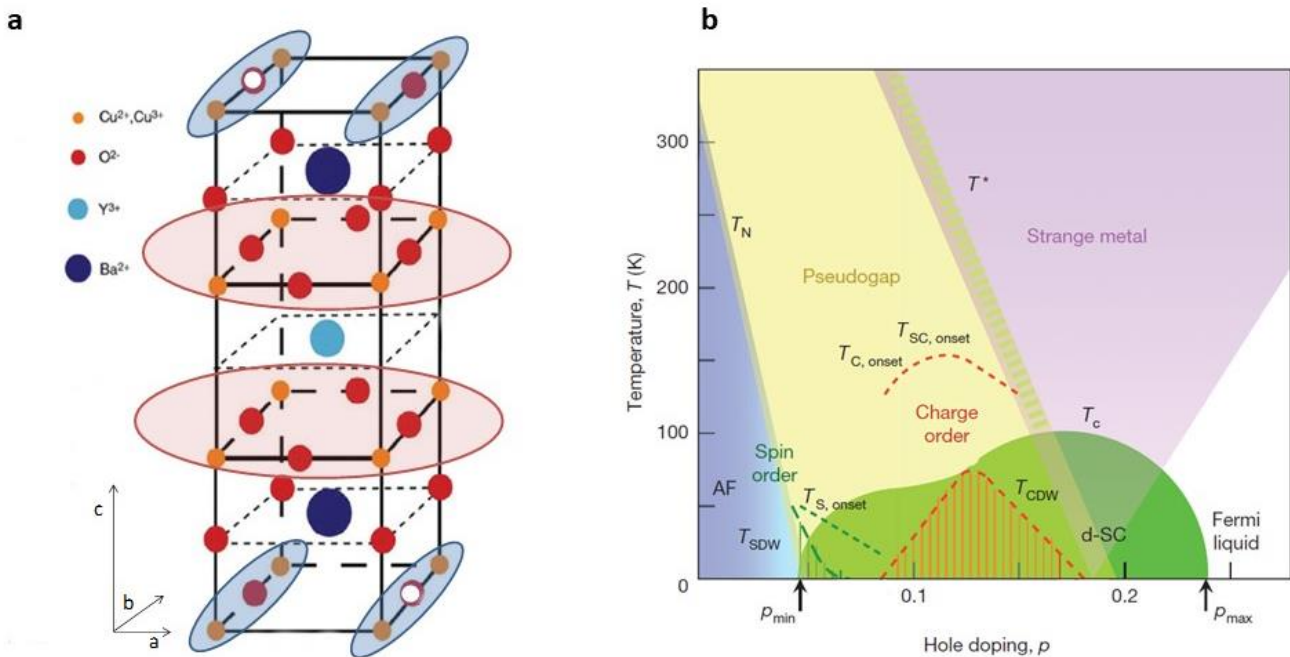


Figure 1-5: (a) Schematic representation of the YBCO structure. The red circles highlight the  $\text{CuO}_2$  planes and the blue the CuO chains (b) Cuprate phase diagram: Temperature vs hole doping showing different competing phases. Superconducting dome for doping ranges between  $p_{min}$  (0.048) and  $p_{max}$  (0.23),  $p_{opt}$  (0.18) is the doping level corresponding to the highest superconducting critical temperature ( $T_c = 92\text{K}$ ). Parent compound of YBCO is an antiferromagnetic insulator for doping ranges smaller than  $p_{min}$ . Crossover for to a pseudogap regime occurs at a temperature  $T_N$  for an intermediate range of doping. Strange metal and Fermi liquid phases appear at higher doping above temperatures  $T^*$  and  $T_F$ . Adapted from (Keimer *et al.*, 2015)

Figure 1-5b shows the typical temperature doping phase diagram of a cuprate. The doping ( $p$ ) represents the charge carrier density within the structure. The parent compound (undoped) of these materials is an antiferromagnetic insulator with a Neel temperature higher than 500K (Tranquada *et al.*, 1988). As the doping is increased the antiferromagnetic order collapses rapidly and the material becomes poorly conducting. High  $T_c$  superconductivity kicks in close to  $p = 0.05$  and extends in a dome-shape like manner until  $p \approx 0.25$ . The highest superconducting critical temperature in YBCO  $T_c = 92\text{K}$  is obtained at an optimal doping of  $p \approx 0.18$ . The underdoped region of the phase diagram designates the region with a doping  $p < 0.18$ . It is characterized by the crossover region below a temperature  $T^*$ , labelled pseudogap, that represents the opening of a partial gap in the spectroscopic data of the material. Charge and spin density wave regimes can be found in this region at lower temperature. Above the superconducting dome at optimal doping the material enters a strange metal phase (labelled this way for its non-adherence to a Fermi liquid model) characterized by a peculiar linear resistivity that extends to the highest temperature. Finally, as the doping becomes large the material enters the overdoped regime where it more or less fits a Fermi liquid model.

In order to better understand the exotic electronic phases present in cuprates, we will start by introducing a couple of concepts more or less common to all TMOs.

#### 1.4.1) Crystal field splitting

An important correlation between orbital and lattice degrees of freedom in a TMO is the crystal field splitting. It describes the lifting of the energetic degeneracy of the metal 3d electronic orbitals. These orbitals are the outermost electronic shell and as such are subject to electric fields originating from the oxygen octahedra. Thus, the fivefold degenerate 3d orbitals will split into two groups: the lower triplet  $t_{2g}$  consisting of the  $d_{xy}$ ,  $d_{yz}$  and  $d_{xz}$  orbitals and the upper  $e_g$  doublet consisting of the  $d_z^2$  and  $d_{x^2-y^2}$  orbitals. The degeneracy lifting is caused by the electrostatic Coulomb interaction between the 3d metal electrons and the 2p oxygen electrons. As one can see from Figure 1-6, the orbitals corresponding to the triplet  $t_{2g}$  have their lobes pointing at  $45^\circ$  with respect to the oxygen orbitals. On the other hand, the doublet  $e_g$  orbitals have their lobes pointing directly at the oxygen orbitals and as such are subject to higher Coulomb repulsion. One can thus easily imagine that any distortion in the crystal structure will affect the energy splitting which will influence the orbital degree of freedom through the crystal field splitting.

#### 1.4.2) Jahn-Teller distortion

Jahn-Teller distortion (Jahn and Teller, 1936) is a geometrical distortion leading to a lowering of its overall energy by lifting of the energetic orbital degeneracy. It takes the form of a tetragonal elongation in cuprates. The distances between the metal ion and the neighbouring oxygen ions in the z direction increase while those in the x and y directions decrease leading to a tetragonal like distortion in the structure c.f. Figure 1-6. This lifts the degeneracy of the  $e_g$  doublet since it lowers the  $d_z^2$  orbital in energy with respect to the  $d_{x^2-y^2}$  because of the reduced electrostatic interaction in the z direction compared to the x and y directions.

Because of this interlink between the structural and electronic/orbital degrees of freedom it is widely accepted that the highest lying orbital in cuprates has a  $d_{x^2-y^2}$  character.

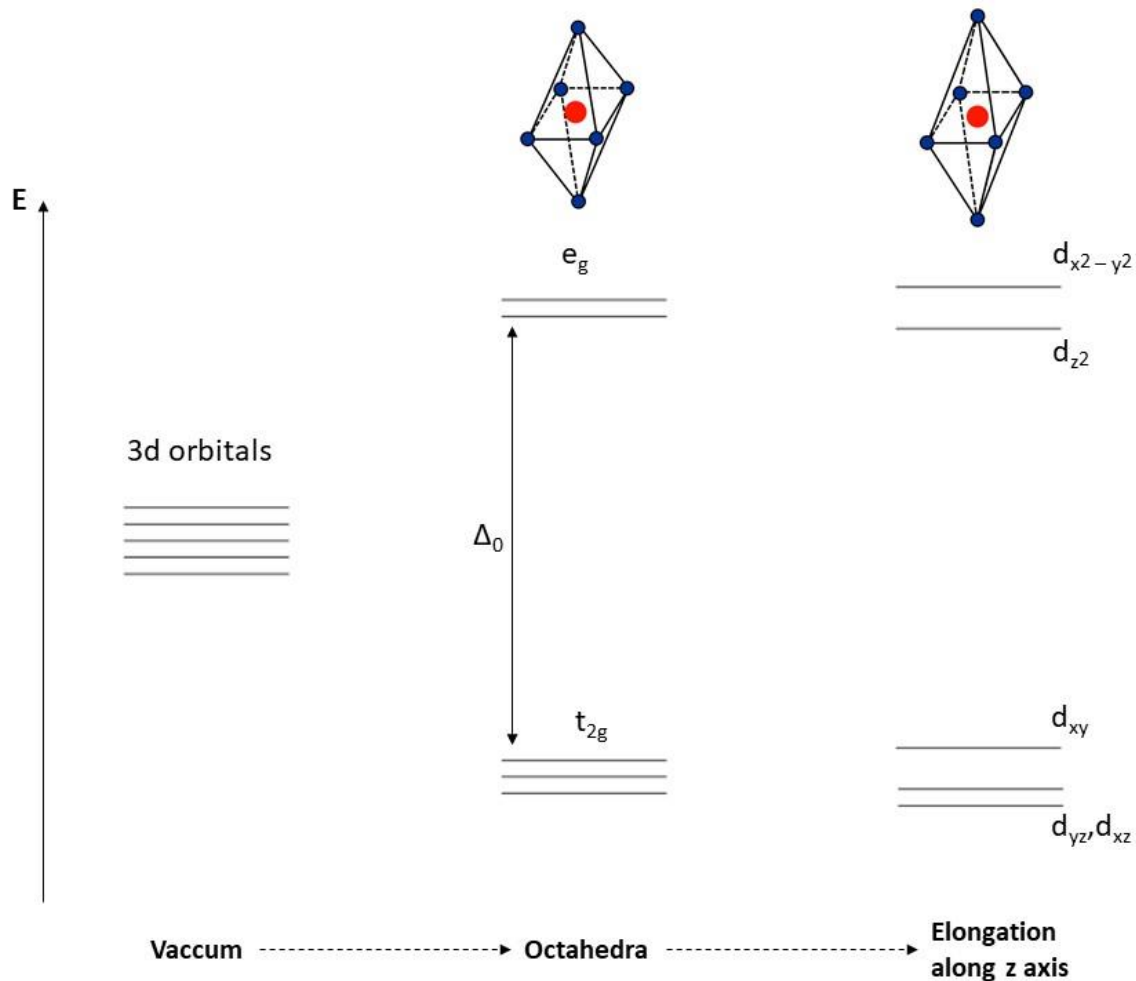


Figure 1-6: Schematic representation of the energy of 3d orbitals in different environment. The fivefold degeneracy of the 3d orbitals in vacuum is lifted when the metallic atom is inserted in an octahedral environment.  $\Delta_0$  is the crystal field energy. An additional degeneracy is lifted by considering the Jahn Teller distortion (an elongation along the z axis).

### 1.4.3) Mott-Hubbard model

Transition metal oxides are characterized by strong electronic correlations meaning the free electron assumption used in tight binding models to describe the electronic properties of materials fails. Historically the first material that could be described by such a theory was NiO discovered in 1937 by DeBoer and Verwey (De Boer and Verwey, 1937). The electronic configuration of the nickel atom is  $3d^8$  leading to an expected metallic behaviour predicted by standard band theory (because of a half filled band). However, this material and many others belonging to this group of materials behave as insulators contrary to tight binding predictions. It is in this context that Mott took electron-electron interactions in a model now referred to as the Mott-Hubbard model. The insight lies in the introduction of a repulsive on site coulomb interaction in the standard tight binding Hamiltonian which can now be written (Imada, Fujimori and Tokura, 1990) as:

$$H = \sum_{i,j,\sigma} t_{ij}(c_{i,\sigma}^\dagger c_{j,\sigma} + h.c.) + U \sum_i n_{i,\uparrow} n_{i,\downarrow}$$

Where  $t_{ij}$  is the hopping integral between sites  $i$  and  $j$  and  $U$  is the coulomb interaction taken to be positive. It is interesting to consider the limits of this Hamiltonian as a function of the ratio  $U/t$ :

When  $U/t \ll 1$  the correlations do not play an important role in the behaviour of the material and it is accurately described by the tight binding Hamiltonian.

Figure 1-7 illustrates from a density of electronic states perspective the difference between the two limits. When  $U/t \geq 1$  however, the electronic correlations play an important role in the conduction properties of electrons essentially splitting the metallic d band into the so called upper Hubbard band (UHB) and the lower Hubbard band (LHB). The system thus behaves as an insulator with an energy gap of the order of  $U$ .

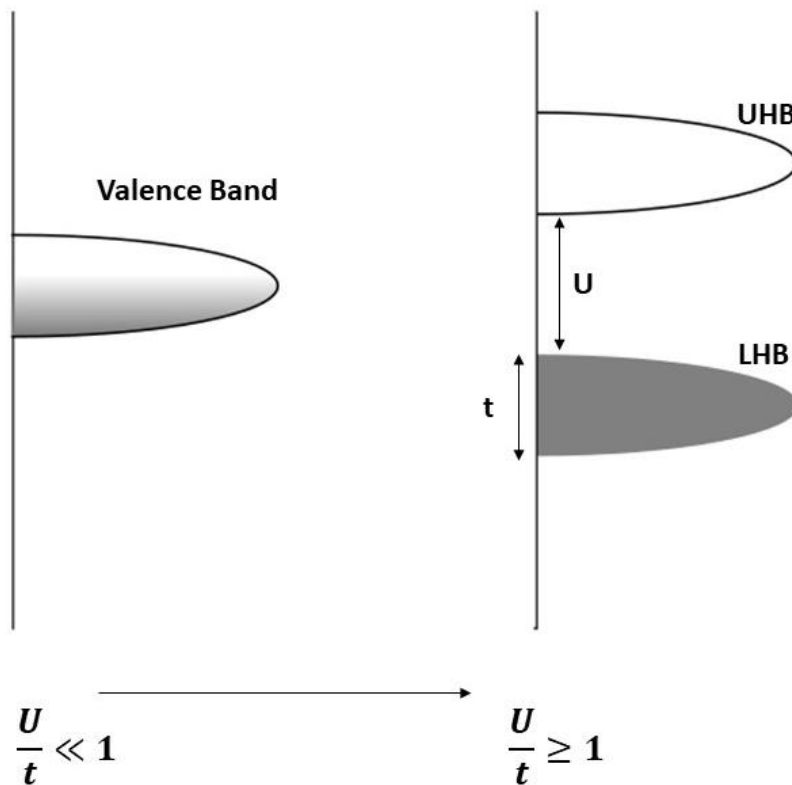


Figure 1-7: Schematic representation of the opening of a band gap in Mott Hubbard scenario. As the ratio  $U/t$  increases a gap of the order of  $U$  appears between the Upper Hubbard Band (UHB) and Lower Hubbard Band (LHB)

The 3d metal bands being rather localized lead to small hopping intervals between nearest neighbours and the Coulomb interaction associated with electron occupying the same atomic site is rather important and typically of the order of 5eV for nickelates and 8eV for cuprates. Thus, those two classes of materials are better described by a Hubbard band model.

In the next section we will detail the electronic properties of cuprates starting with the description of the undoped parent compound  $Y_1Ba_2Cu_3O_6$ .

#### 1.4.4) Parent compound of cuprates as a Mott insulator

The parent compound of most cuprates is an antiferromagnetic Mott insulator. As was stated earlier, the basic unit found in all cuprates is a copper oxygen plane  $CuO_2$  that extends in the (ab) direction. The structure is composed of a stacking of those planes separated by charge neutral entities. Different materials are characterized by different structural entities, but the copper oxygen planes are common to all cuprates.

It is believed that its transport and magnetic properties are coupled due to the interplay between electronic interactions and magnetic superexchange. Superexchange is the magnetic coupling

between two next nearest cations mediated by an anion. It can favour parallel or anti-parallel spin dispositions depending on the bond angles and band fillings (Imada, Fujimori and Tokura, 1990)(Anderson, 1959)(Goodenough, 1955). The superexchange mechanism can be thought of as a virtual electronic hopping process between the different elements that depends on the spin direction of the ions with an energy gain that can be estimated using second order perturbation theory(Lee, Nagaosa and Wen, 2006). The system would choose the configuration that satisfies its constraints and minimizes its total energy. Copper atoms in the YBCO structure are mostly in the  $\text{Cu}^{2+}$  configuration in the  $3d^9$  thus because of crystal field splitting and the Jahn Teller distortion, the  $3d_{x^2+y^2}$  orbital ends up half filled with all other 3d orbitals filled. On the other hand, the oxygen atoms are mostly in the  $\text{O}^{2-}$  configuration which means that their in-plane p orbitals are completely filled. The 3d lobes of copper atoms point directly towards the oxygen in plane p orbitals leading to a large hopping integral  $t_{pd}$ . Due to the Pauli exclusion principle the virtual hopping process is only possible when the spins of the magnetic ions are anti-parallel on adjacent sites, leading to an anti-ferromagnetic coupling that will lower the total energy of the system. Following these arguments, one can understand that the YBCO parent compound shows an antiferromagnetic coupling. Figure 1-8 depicts a schematic representation of the antiferromagnetic order present in the undoped copper oxygen planes.

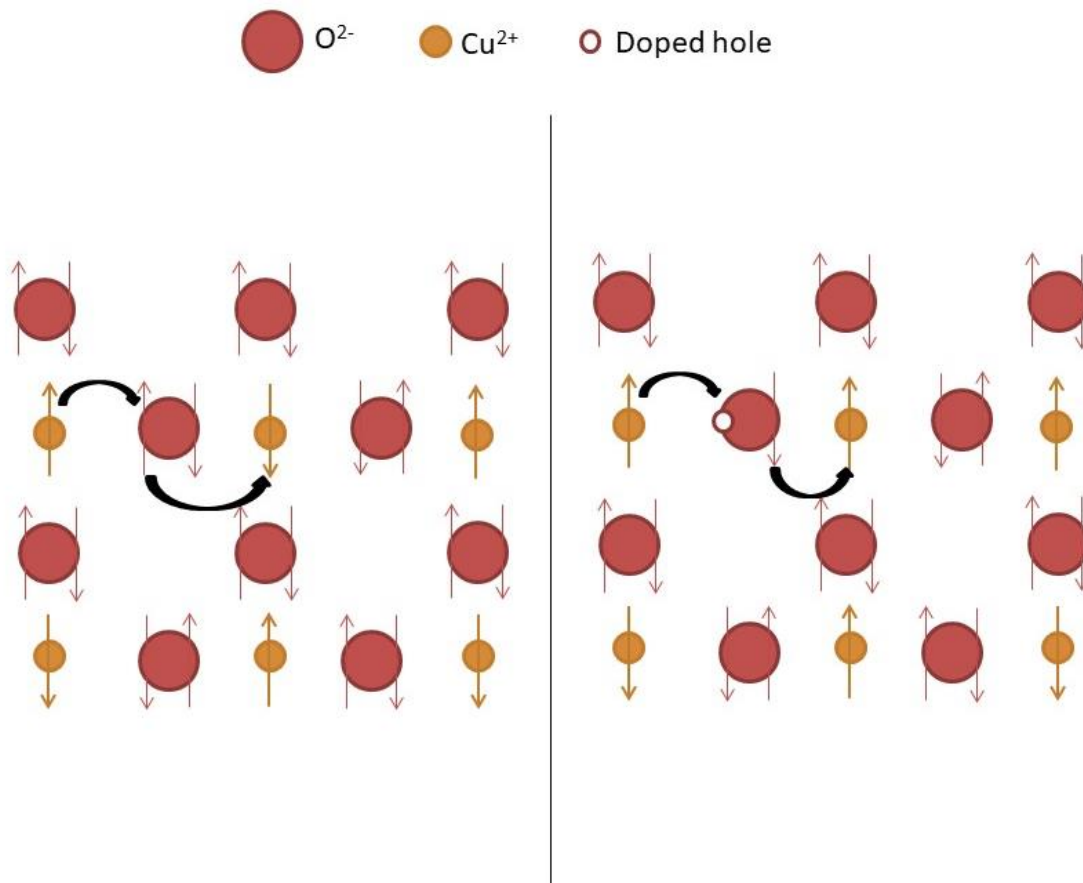


Figure 1-8: Schematic representation of the spin ordering on the  $\text{CuO}_2$  planes. On the left the undoped case where there are no holes on the oxygen bands. On the right the doped case where the white circle represents a possible hole on an oxygen atom. The black arrows represent the virtual hopping processes.

On the other hand, when one dopes cuprate, the hole carrier density in its  $\text{CuO}_2$  planes increases. This doping process happens mostly on the oxygen p bands because of their relative position with respect to the metallic bands (c.f. section 1.4.5)). Thus, the previous image changes as parallel spin configurations are not prohibited by the Pauli exclusion principle anymore as is shown in Figure 1-8.

So, the number of parallel spins on neighbouring metal atoms will start to increase with an increasing doping level. One can thus understand both the disappearance of the antiferromagnetic order and the insulating behaviour with an increase in the hole concentration.

#### 1.4.5) Charge transfer insulator

The crystal field splitting and the overlap between 3d Cu orbitals and 2p O orbitals render the so called 3 band model an accurate model for the electronic properties of cuprates. The Hamiltonian describing such a system is the following:

$$H_{3B} = \varepsilon_p \sum_i p_i^\dagger p_i + \varepsilon_d \sum_i d_i^\dagger d_i + t_{pd} \sum_i (d_i^\dagger p_j + h.c.) + U_{dd} \sum_i n_{d_i,\uparrow} n_{d_i,\downarrow} + U_{pp} \sum_i n_{p_i,\uparrow} n_{p_i,\downarrow} + U_{pd} \sum_i n_{p_i,\uparrow} n_{d_i,\downarrow}$$

With  $\varepsilon_p$  and  $\varepsilon_d$  the energy of p and d orbitals respectively.  $\Delta = \varepsilon_p - \varepsilon_d$  as the charge transfer energy,  $t$  the hopping integral between p and d orbitals and  $U_{dd}$  is the onsite Coulomb interaction on a d orbital,  $U_{pp}$  on a p orbital and  $U_{pd}$  between electrons on p and on a d orbital.

Two different energies are of interest in this approach: the onsite Coulomb repulsion on copper atoms  $U_{dd}$  and the charge transfer energy  $\Delta$  describing the difference in energy between the copper 3d band and the oxygen 2p bands. These energies represent the excitations corresponding to localized d electrons on the metal 3d sites and the excitation of an electron from the ligand 2p orbital to the metal 3d orbital. The correct energy scale to understand the low energy excitations of these materials will depend on the ratio between these two energies. In nickelates and cuprates it has been observed that  $\Delta$  is much smaller than  $U_{dd}$  making it the correct energy scale in these systems. Figure 1-9 represents the electronic band diagrams of a charge transfer insulator compared to the one of a classical Mott insulator. One can see that the low energy physics are governed by  $\Delta$  rather than  $U$ .

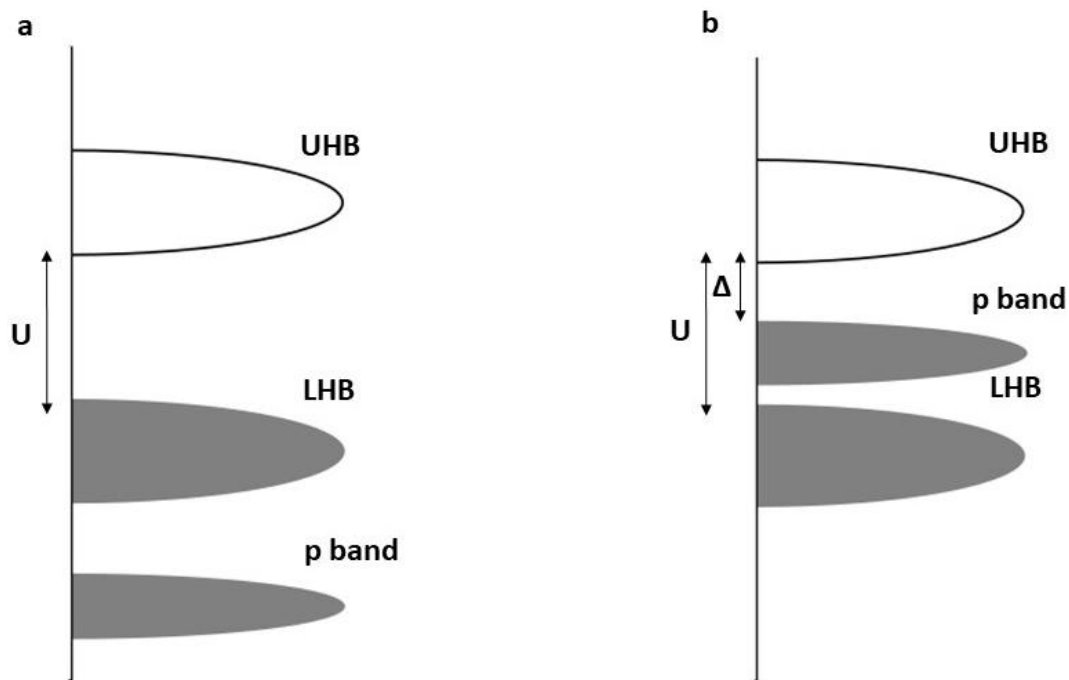


Figure 1-9: Schematic illustration of energy levels for (a) a Mott-Hubbard insulator and (b) a charge-transfer insulator generated by the d-site interaction effect.

#### 1.4.6) Zhang Rice Singlet

The complicated three band diagram explained earlier has been simplified by Zhang and Rice in 1988 (Zhang and Rice, 1988) where they used a single band model to describe the doping of a cuprate. This allows to simplify the electronic structure from a three band to a one band model - since the low energy physics of these systems can be mostly described by one- where the upper Hubbard band is separated from the Zhang Rice band by a gap of the order of  $\varepsilon_p - \varepsilon_d$ . By introducing a hole into the cuprate, and thus doping it, the system changes from a  $d^9$  state to a  $d^9L$  state where L denotes the hole on the oxygen site. The insight lies in the delocalization of the hole on the 4 neighbouring oxygen and on the combination of the doped spin with the copper spin in a singlet formation. This splits the state into two separated by  $t_{pd}^2 / \Delta$ .

In the next section we will describe the cuprate phase diagram with an emphasis on the dome-like superconducting state as well as the various normal states in close proximity to it.

### 1.5) Cuprate phase diagram

#### 1.5.1) High Tc superconductivity

An unresolved question behind high Tc superconductivity remains the mechanism responsible for its appearance in a doped Mott insulator. While sharing some of its properties with standard BCS superconductivity it also exhibits properties that differ from it significantly. The main unanswered questions lie in the role of collective excitations that mediate pairing and the role the pseudogap plays in the mechanism responsible for superconductivity. Physicist have tried solving this particular problem since the appearance of high Tc superconductivity in the 1990's and while a definitive answer is still lacking, some progress has been made on both the theoretical and experimental aspects.

At first glance the macroscopic superconducting properties of this new class of materials are not different from the standard BCS superconductors. When the temperature is lowered under a critical temperature  $T_c$  these materials transition into a state with a null electrical resistance and expel all magnetic field lines from their bulk. Early investigations have also shown that electrons condensate in Cooper pairs as a quantization of magnetic flux leads to a flux quantum given by  $h/2e$  (Gough *et al.*, 1987). However, differences start to arise when one looks more carefully. The coherence length of this superconducting state is small compared to standard BCS superconductors ( $\sim 10 \text{ \AA}$  vs a couple hundred angstroms). The layered structural nature of the material also grants its superconducting properties high anisotropy between in plane and out of plane directions. As a matter of fact, the Josephson effect is also observed in these materials where planes of  $\text{CuO}_2$  are coupled with one another in a Josephson junction like manner (Kleiner and Muller, 1994). But perhaps most importantly the symmetry of the superconducting order parameter is different in both classes of materials. BCS theory lies on the appearance of a superconducting gap characterized by a "s-wave" symmetry and a minimal momentum dependence however common consensus has been reached over the "d-wave" nature of the superconducting gap in cuprates(c.f. Figure 1-10). This has been confirmed by several measurements: band structure measurements (Shen *et al.*, 1993), penetration length (Hardy *et al.*, 1993), phase sensitive measurements (Van Harlingen, 1995) and critical current density measurements (Lombardi *et al.*, 2002).

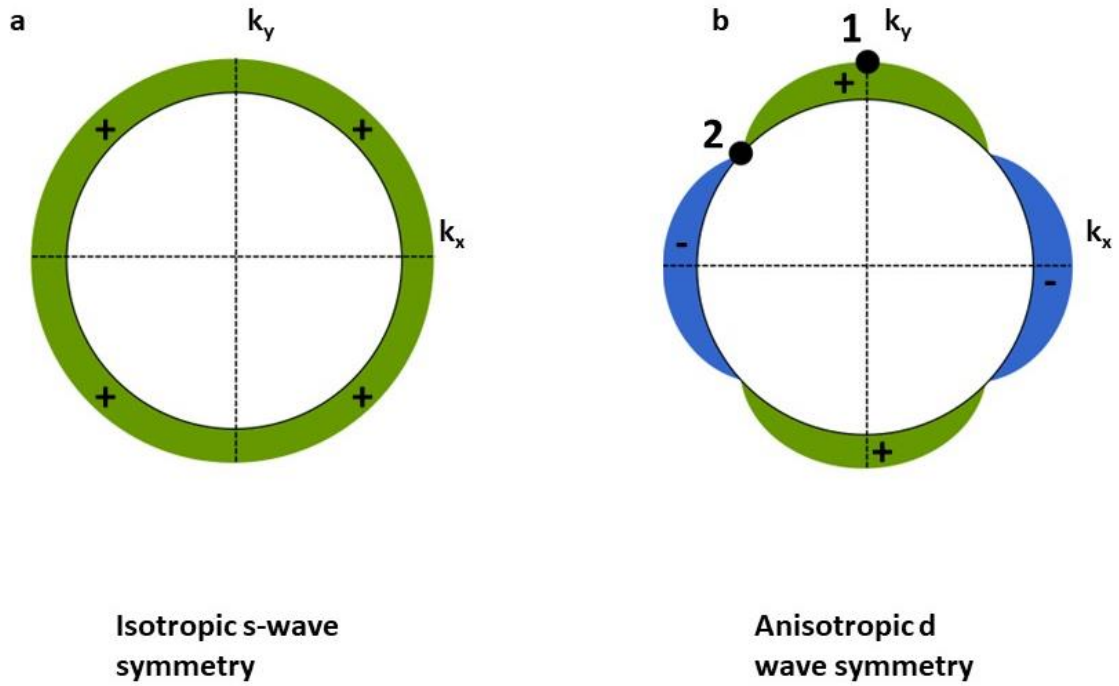


Figure 1-10: Schematic representation of the order parameter symmetry in the case of an (a) isotropic s wave symmetry and (b) anisotropic d wave symmetry. The highlighted points indicate the high symmetry regions at the antinode (1) where the gap is the largest and the node (2) where the gap is null

The d-wave character of the superconducting gap is given by the following formula in momentum space:

$$\Delta_k = \Delta_0(\cos k_x a + \cos k_y a) \quad 2$$

Where  $k_x$ ,  $k_y$  are wavevectors in the x and y direction respectively and  $a$  is the in-plane lattice constant. On Figure 1-10b the  $d_{x^2-y^2}$  character of the superconducting gap is displayed. On the Fermi surface, two zones of high symmetry are defined: the antinode which lies at edge of the BZ near the point  $(\pi, 0)$  where the gap is the largest and the node where the gap disappears. The gap gradually decreases between the antinode and the node then changes sign.

Electron phonon interactions are at the heart of conventional BCS superconductors, but it is very probable that the physics behind high  $T_c$  superconductivity is very different. As a matter of fact, the doping dependence of the gap in cuprates differs from the one expected in a BCS superconductor. It has been shown that in the underdoped region of the phase diagram the gap decreases as the doping increases towards the optimally doped region (Hashimoto *et al.*, 2014). Additionally, the anisotropy of the electronic properties of cuprate superconductors constitutes another important difference to the standard BCS superconductors.

As was stated previously, the parent compound of these cuprate superconductors are Mott insulators where antiferromagnetic fluctuations are the underlying interactions. A good description of the different ground states a cuprate exhibits can be obtained by the use of a doped Hubbard Model. This model describes the electronic and magnetic properties as a function of the bandwidth  $W$  describing the charge delocalization ( $W \sim 8t$  where  $t$  is the hopping energy) and the onsite Coulomb repulsion  $U$ . Theoretical treatments of this model generally lead to a superconducting gap with a “d wave” character (Proust and Taillefer, 2019) (Keimer *et al.*, 2015). As a matter of fact, in the strong correlation limit the opening of a pseudogap was predicted (Gull *et al.*, 2010). However, the main issue in the

theoretical treatments of this problem is that in cuprates  $U$  and  $W$  are comparable and there exists no complete analytical solution.

### 1.5.2) Pseudogap

In this section we will detail the properties of the pseudogap. As stated previously, a superconducting gap with a “d wave” character is observed in cuprate superconductors at  $T < T_c$ . One could expect that the superconducting gap closes at  $T > T_c$ . However, the opening of a partial spectroscopic gap has been observed at temperatures  $T$  such that  $T_c < T < T^*$ . Where  $T^*$  denotes the temperature regime above which the spectroscopic features disappear. This transition is not a proper phase transition but resembles a crossover between two regimes. The first glimpses of this phenomenon have been inferred from nuclear magnetic resonance showing a reduction in the low frequency spin excitations (Warren *et al.*, 1989). It has now been observed by different techniques ranging from ARPES (Marshall *et al.*, 1996), STS (Vishik *et al.*, 2009), NMR (Warren *et al.*, 1989), low and high frequency transport (Homes *et al.*, 1993) (Puchkov, Basov and Timusk, 1996) (Ito, Takenaka and Uchida, 1993). The opening of this partial gap is usually accompanied by a loss in the density of states DOS below a critical doping  $p^*$  (Proust and Taillefer, 2019). Its relationship with the superconducting phase however is still under debate. Two of its possible interpretations are the following:

1. The pseudogap phase is a precursor to superconductivity and is an indicator of Cooper pair preforming at a temperature higher than  $T_c$ .
2. The pseudogap phase is unrelated to superconductivity and the plethora of order phases observed within the phase diagram are competing with superconductivity.

This unusual phase is best to described through the lens of electronic spectroscopies. As can be seen from Figure 1-11(a-b), the symmetrized energy dispersive ARPES spectra taken in the antinodal section of the BZ highlight a conservation of the gap features at temperatures higher than  $T_c$ . By contrast, the spectra observed at the near nodal section of the BZ show a distinct quasiparticle peak at  $T \sim T_c$  which indicates the closing of a gap. The gap feature in the antinodal region leads to a formation of a partial portion of the Fermi surface at  $T > T_c$ . This feature shown in Figure 1-11c is called the “Fermi arc”. Subsequently as the doping increases this feature grows until it encompasses the whole “Fermi liquid like” Fermi surface characteristic of overdoped cuprates (Proust and Taillefer, 2019) c.f. Figure 1-11d. The discrepancy between the behaviour of the gap features in different sections of the BZ is called the nodal-antinodal dichotomy (Hashimoto *et al.*, 2014). The fact that the structure of the pseudogap mimics crudely the superconducting gap leads naturally to the precursor pairing scenario: where charge carrier pair up but no long range phase coherence exists at a temperature higher than  $T_c$ . However the mechanism that could be at the root of this pairing effect with no long range coherence has not yet been discovered (Keimer *et al.*, 2015).

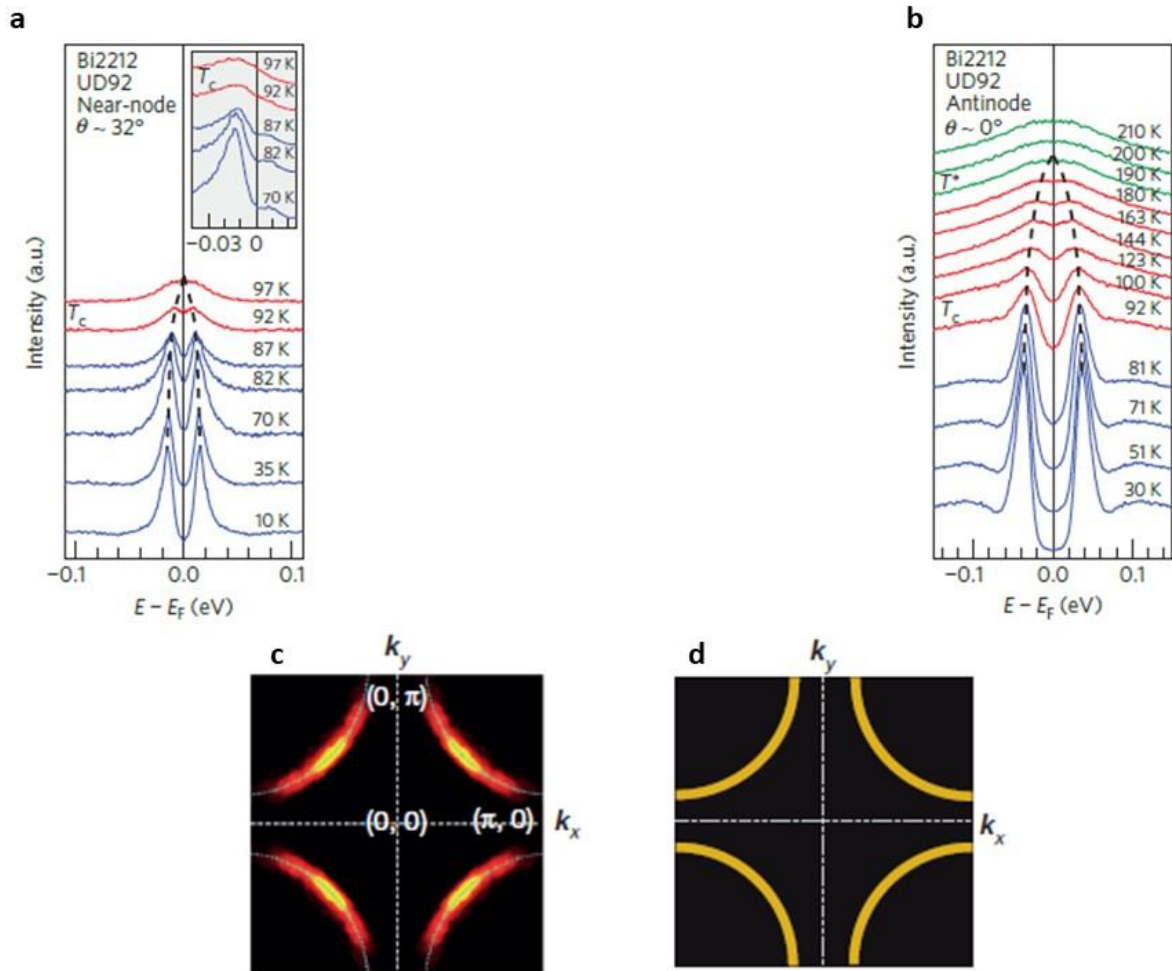


Figure 1-11: (a-b) ARPES measurement in the nodal and antinodal regions of the Brillouin zone showing the temperature behaviour of a quasiparticle peak. Adapted from (Hashimoto *et al.*, 2014) (c) Fermi surface of an underdoped cuprate: Fermi arcs characterized by the absence of signal in the nodal areas (d) "Closed" Fermi surface characteristic of overdoped cuprates. Adapted from (Keimer *et al.*, 2015).

The Knight Shift ( $K_s$ ) in nuclear magnetic resonance measurements, represents the shift in nuclear magnetic resonance frequency observed in paramagnetic materials. In metals this quantity allows to quantify the interaction between electronic and nuclear spins. It has been shown that this shift is proportional to the density of states at the Fermi level. Thus, in a Fermi liquid the shift is independent of temperature. However, in the superconducting state  $K_s$  is expected to suddenly drop because of the formation of spin singlets. The Knight Shift measured on an optimally doped YBCO crystals is independent of temperature for  $T > T_c$  until it suddenly drops when the temperature reaches the superconducting critical temperature  $T_c$ . However, the Knight Shift measured on underdoped YBCO crystals starts decreasing as the temperature drops below a characteristic temperature  $T^*$  while no particular feature is observed at  $T = T_c$ . This has been interpreted as the opening of spin gap in the underdoped region of the cuprate phase diagram (Warren *et al.*, 1989).

In addition, prior to entering the pseudogap phase the resistivity evolves as a linear function of temperature (which is an indicator of the strange metal phase). But as the sample enters the pseudogap phase the resistivity deviates from linearity by displaying a downturn below a characteristic temperature  $T^*$ . This decrease in the resistivity has been interpreted as a decrease in the scattering rate caused by a decrease in the electronic spectral weight (opening of a partial gap).

The temperature at which the deviation from linear behaviour is observed has been associated with the appearance of a gap in the spin excitations observed by NMR. (Ito, Takenaka and Uchida, 1993)

An additional measurement allowing to shed some light on the physics behind the appearance of this phase is the behaviour as a function of temperature and doping of the electronic specific heat. Early on, it has been shown that the normal state electronic specific heat has a peculiar temperature behaviour across the doping phase diagram. This measurement allows to investigate the possible opening of a gap since the electronic specific heat is known to be proportional to the electronic density of states at the Fermi level in a metal. The specific heat remains constant for overdoped YBCO crystals above  $T_c$ . A peak then appears at  $T_c$  before a subsequent decrease is observed below  $T_c$  in the superconducting state as would be expected from a superconducting sample. However, the situation is different in the case of underdoped crystals where at temperatures  $T > T_c$ , a decrease in the specific heat is observed pointing towards a decrease in the electronic density of states. (Loram *et al.*, 1997)

It has been shown that the specific heat exhibits a peculiar behaviour as a function of doping where a peak is observed at a critical doping  $p^*$  (Proust and Taillefer, 2019) in the limit  $T=0K$ . This feature is reminiscent of the existence of a quantum critical point in the phase diagram.

### 1.5.3) Quantum critical point and Strange Metal

A quantum critical point (QCP) is a continuous phase transition at  $T = 0K$  as a function of tuning an external order parameter. In the case of cuprates this parameter is the doping per Cu atom normally used to represent phase diagrams. This would point to the existence of a critical doping above which a disordered quantum state would exist (Fermi liquid like phase) and below which an ordered state would appear (pseudogap phase). The existence of such a transition is associated with a diverging length scale describing the order at its source. In such a scenario, the quasiparticle peak vanishes logarithmically at the Fermi surface and the imaginary part of the corresponding self-energy function is a function of the temperature solely (Varma *et al.*, 1989). The presence of a quantum critical point leads to the energy scale at which the scale invariance remains to increase gradually as the temperature is increased leading to a “wedge” appearing in the phase diagram above the QCP.

In hole doped cuprates, a number of signatures associated with the existence of a quantum critical point have been observed. The peak in the specific heat vs doping representation (Proust and Taillefer, 2019) is one of the thermodynamic classic signatures. A second signature resides in the  $T$  linear behaviour of the resistivity above the (QCP) in the so called strange metal regime (Martin *et al.*, 1990). However, no direct measurement of a diverging length scale has been made to ascertain the existence of the quantum critical point in the hole doped cuprate phase diagram.

The strange metal regime is the denomination given to the normal state region above the superconducting dome at the optimal doping. It is the least investigated phase in the cuprate phase diagram. The peculiar nature of this phase lies in the absence of quasiparticles in the description of its transport properties. As a matter of fact, in conventional metals, the resistivity saturates at high enough temperatures. This coincides with the temperature at which the carrier mean free path becomes greater than the electron Fermi wavelength. This however does not occur in cuprates as reports have showed that the normal state resistivity maintains its linearity in temperature for as high as can be measured. (Martin *et al.*, 1990)

Furthermore, cuprates in the strange metal phase are characterized by a peculiar temperature dependence of the Hall coefficient. In a standard metal one expects the Hall coefficient to have a weak temperature dependence since the carrier density (proportional to the inverse Hall coefficient) would

have to remain approximately constant as a function of temperature. In the strange metal phase on the other hand, the Hall coefficient exhibits a non-monotonic temperature dependence and even changes sign (Proust and Taillefer, 2019).

#### 1.5.4) Stripe order

An important feature in the investigation of cuprates is the presence of charge order phases in the underdoped region of the phase diagram. A multitude of such orders have been investigated in the literature ranging from “crystallization of electrons in the form of stripes” (Keimer *et al.*, 2015) to more novel quantum liquids.

Intertwined spin and charge ordering (in the form of stripes) has been investigated first through neutron diffraction experiments in LSCO back in the 1990’s (Tranquada *et al.*, 1995). More recently types of order have been observed using a multitude of techniques such as STM (Hoffman *et al.*, 2002), transport measurements (quantum oscillations and Hall effect) (LeBoeuf *et al.*, 2007) etc. These stripes are most easily described by an inhomogeneous separation of charge and spin degrees of freedom into 1D regions rich in charges and regions rich in spin as can be seen from Figure 1-12.

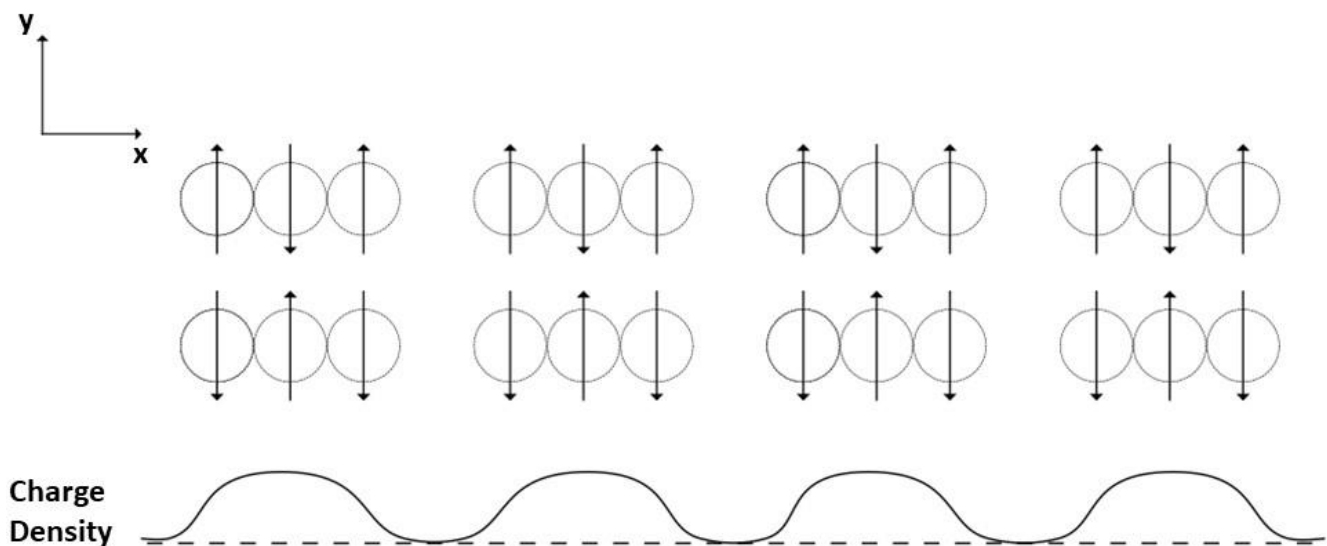


Figure 1-12: Schematic representation of a charge density wave (CDW) in the x direction.

The presence of density wave that breaks translation symmetry could lead to the formation of small closed electron pockets in the Fermi surface (LeBoeuf *et al.*, 2007). However, the exact mechanism behind the Fermi surface reconstruction is still under debate.

For example, in YBCO two distinct types of charge order exist. First, an incommensurate 2D charge density wave with an in plane correlation length of at most 20 lattice constants is observed in the underdoped region above  $T_c$  (Blanco-Canosa *et al.*, 2014). Then a field dependent 3D density wave that extends along the CuO chains that persists below  $T_c$ . (Chang *et al.*, 2016) These different orders exist at the same temperatures and dopings (Laliberté *et al.*, 2018)

#### 1.5.5) Anomalous transport behaviour in cuprates

Cuprates are characterized by anomalous temperature and doping dependence of the resistivity and Hall coefficient as will be discussed in section 3.3).

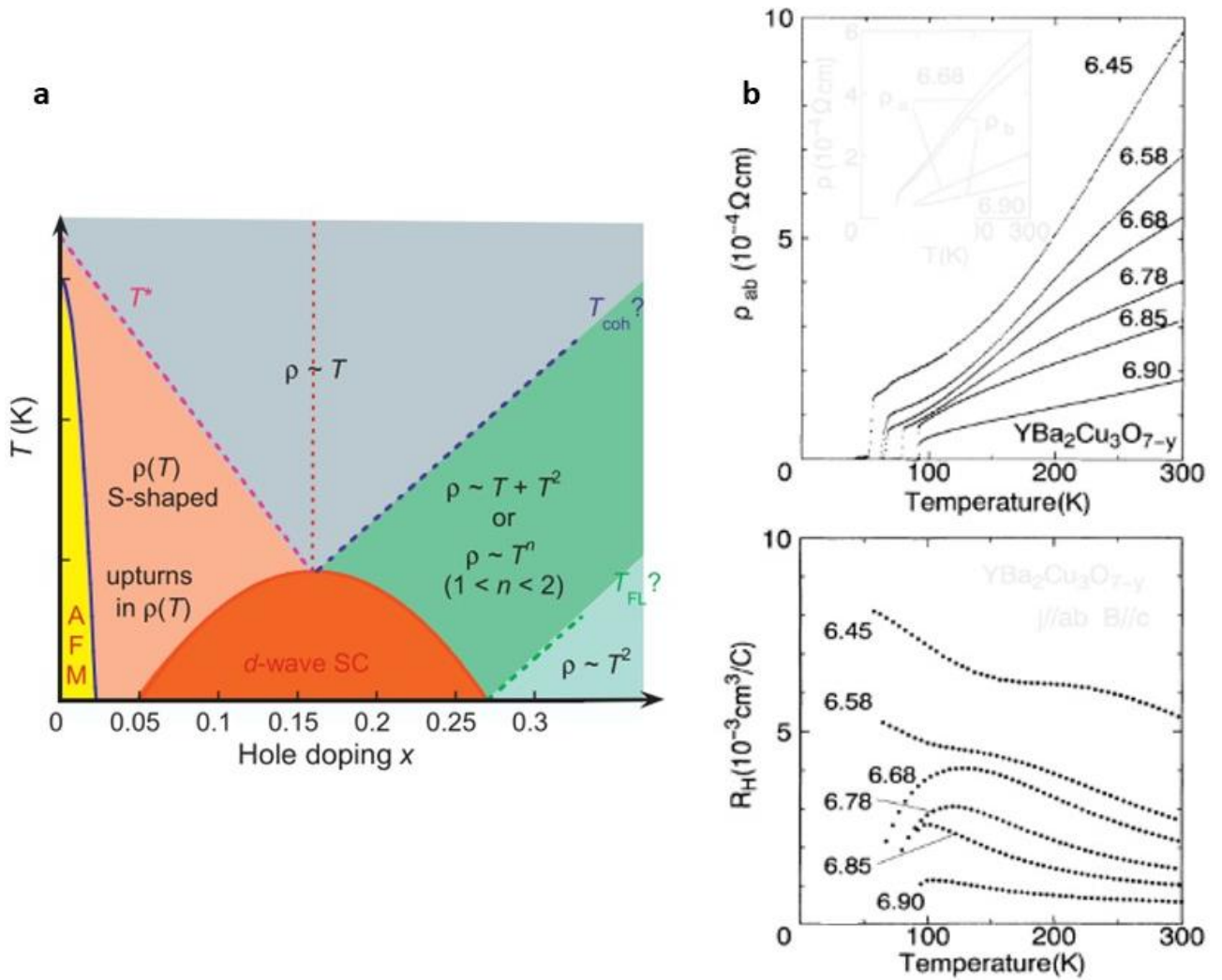


Figure 1-13: (a) Schematic temperature vs doping phase diagram of a cuprate highlighting the temperature dependence of the resistivity in different phases. Adapted from (Hussey, 2008) (b) Temperature dependence of the resistivity (up) and Hall coefficient (down) of an oxygen deficient set of YBCO samples. adapted from (Ito, Takenaka and Uchida, 1993).

Figure 1-13a shows a schematic temperature vs doping phase diagram of the resistivity behaviour in cuprates. In the optimally doped regime, the resistivity is characterized by linear dependence on temperature for all  $T > T_c$ . This feature has been linked to the presence of a QCP in the cuprate phase diagram (c.f. section 1.5.3)). For lower doping, i.e. in the underdoped region of the phase diagram, the resistivity is linear at high enough temperature but deviates downward at a temperature labelled  $T^*$  that has been linked to the pseudogap phase (Ito, Takenaka and Uchida, 1993). As the temperature decreases an upturn in the resistivity of underdoped cuprates is observed suggesting the onset of electronic localization (Hussey, 2008). These different phases can be seen in Figure 1-13b.

In the optimally doped regime, the in plane Hall coefficient has a  $1/T$  dependence which is in contradiction to standard Fermi Liquid theory predictions. In conventional metals one should expect a near temperature independent Hall coefficient. As the doping decreases and at low temperature however, the Hall number approaches the true hole density as predicted by the standard Drude model:  $R_H = 1/ne$  (Ando, Kurita, *et al.*, 2004). In addition, reports have shown that at a fixed low temperature, variations of the Hall number are proportional to variations of the true carrier density (Jones, Christen, Thompson, Feenstra, Zu, *et al.*, 1993; Stockinger *et al.*, 1998).

The description of these properties within a standard Fermi Liquid scenario has been difficult. In the remainder of this section we will detail the different scenarios that were developed in the literature to explain them.

Scenarios within a Fermi liquid (FL) picture considering an anisotropy in k space of a single scattering length  $l(k)$  have been proposed to explain the anomalous behaviour of  $R_H(T, p)$  and  $\rho(T, p)$ . This scenario can be traced back to (Ong, 1991) where the non-monotonous behaviour of the transport properties is attributed to the local curvature of the Fermi surface (FS) and the strong anisotropy in the in-plane scattering length. It is the temperature behaviour of the anisotropy that dictates the anomalous temperature and doping behaviour of the Hall coefficient. Within this scenario however, the behaviour of  $\cot \theta_H(T)$  will be dominated by regions of the FS where the scattering is the weakest and the FS curvature is the strongest (Hussey, 2007). The in-plane scattering length has been attributed to Umklapp scattering (Hussey, 2003) coupled to single bosonic modes including spin fluctuations (Monthoux and Pines, 1994) and charge fluctuations (Castellani, Di Castro and Grilli, 1995).

The inability to explain the whole body of evidence within a FL picture has fuelled the emergence of non-FL theories. The main two are the “separation of lifetimes” scenario by Anderson and the Marginal Fermi Liquid (MFL) by Varma. The former is based on (Anderson, 1991) and revolves around the assumption that there exists two independent scattering rates with different temperature behaviours. It introduces a scattering time associated with process perpendicular to the Fermi surface ( $1/\tau_H$ ) and another one for processes parallel to it ( $1/\tau_{tr}$ ). The longitudinal resistivity and the Hall effect are dependent on both these scattering rates and end up with a complex temperature behaviour. The Hall angle on the other hand depends only on  $\tau_H$  and thus evolves with temperature according to:  $\cot \theta_H = \alpha T^2 + C$  where  $C$  is the impurity contribution and  $\alpha$  is related to the excitation bandwidth. This physical quantity has been shown to robustly represent  $1/\tau_H$  within this scenario (Harris *et al.*, 1995) (Chien, Wang and Ong, 1991).

Finally, in the MFL scenario presented by Varma *et al.* (Varma *et al.*, 1989), the anomalous transport behaviour near optimal doping in the normal state of a cuprate superconductor emanate from a quantum critical point in the phase diagram. A single scattering anisotropic scattering lifetime explains the quadratic temperature behaviour of the Hall angle. The anisotropy is introduced into the model via the impurity scattering rate by assuming small angle scattering off impurities in the Cu-O plane (Varma and Abrahams, 2001). This scenario offers a good explanation for the anomalous temperature behaviour of the Hall coefficient, resistivity and cotangent of the Hall angle near optimal doping.

The next sections will describe some of the examples of the various effects observed in cuprates, and more generally in TMOs, under the influence of external stimuli that are reported in literature.

#### 1.5.6) Electron doped cuprates

Most of the results and theories in this thesis concern the hole doped region of the cuprate phase diagram. However, it might be of interest to highlight the properties of the electron doped region as well. Starting from the insulating antiferromagnetic parent compound it is possible to dope the material with electrons by chemical substitution for example. The most investigated compound is the cuprate (NCCO)  $\text{Nd}_{2-x}\text{Ce}_x\text{CuO}_4$  and the general formula of these compounds is  $\text{R}_{2-x}\text{M}_x\text{CuO}_4$  where R can be Pr, Nd, Sn or Eu and M is Ce or Th. Figure 1-14 shows a phase diagram showing both the hole doped region and the electron doped region. The electron doped section is rather similar to the hole doped one except for a couple of characteristics. The AF region disappears at much higher doping than in the hole doped region, the maximal superconducting critical temperature at  $\sim 30\text{K}$  is lower in the electron doped region, the steepness of the superconducting dome is bigger in electron doped cuprates (difficult to define underdoped and overdoped regions).

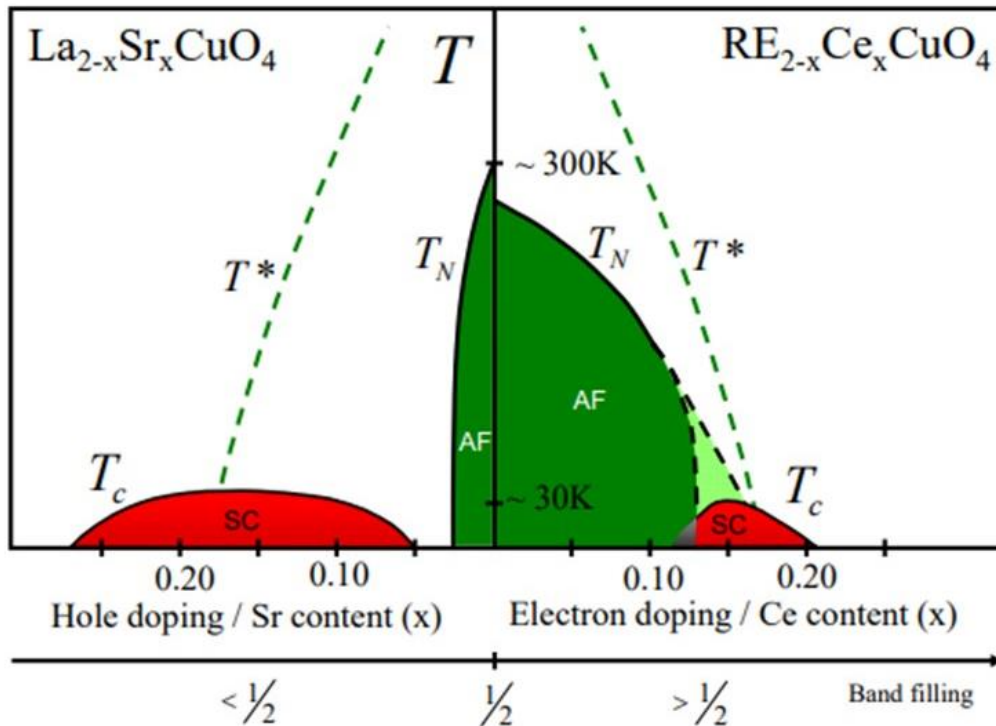


Figure 1-14: Phase diagram of electron and hole doped cuprates as a function of charge carrier doping. Adapted from (Armitage, Fournier and Greene, 2010)

The phenomenology of electron doped cuprates has been more or less established around the existence of a Quantum critical point existing in the phase diagram at a doping  $n^*$  with antiferromagnetic order. The AF correlation length seems to diverge below  $n^*$  (Motoyama *et al.*, 2007). A Fermi surface reconstruction occurs at this doping where it transitions from a cylinder to small closed pockets of electrons (Armitage *et al.*, 2002)(Helm *et al.*, 2009). T-linear resistivity is observed at the critical doping  $n^*$ , at low doping a characteristic upturn appears in the resistivity and at doping  $n \gg n^*$  it has a typical  $T^2$  dependence (Proust and Taillefer, 2019).

An additional section describing the anomalous transport behaviour of cuprates is required in order to obtain a comprehensive description of its normal state properties.

### 1.6) Electric field effects in correlated oxides

Since most of the phases present in a TMO phase diagram are separated by rather small energy differences one can imagine inducing a phase transition through the application of an external stimuli. This section will be dedicated to the effects of electric fields on correlated oxides. The effects of light on these materials will be detailed in the next section.

In most cases when an electric field is applied on a TMO it alters its carrier density and thus changes its properties as in the standard field effect transistors (Bibes, Villegas and Barthélémy, 2011)(Ahn, Triscone and Mannhart, 2003). However, the use of electric fields has also been associated with more dramatic changes in the properties of TMOs, notably a change in the oxygen stoichiometry of the material (Sawa, 2008). The notorious experiments of field-effect on transition metal oxides were performed on high  $T_c$  superconductors (Ahn, Triscone and Mannhart, 2003), colossal magnetoresistance compounds (Tanaka, Zhang and Kawai, 2002) etc...

It is interesting to note the link between the emerging field effect on transition metal oxide and the mature technology of semi-conductor field effect transistors (FET) that constitutes the backbone of

our technology. Due to the ever-increasing demand of computational power, the semiconductor technology has decelerated recently because of practical issues. This allowed the burgeoning field of field effect in TMOs to present itself as a potential successor.

### 1.6.1) Field effect transistors (FET)

A field effect transistor is constituted in its simplest form of a thin semi conducting channel separated from a metallic electrode by an insulating barrier. The semiconducting channel is enclosed between two metallic electrodes (the source and the drain) and an insulating barrier separates the channel from a gate electrode. By applying a gate voltage across the insulator, one can modify through carrier accumulation or depletion the channel's carrier density. Its resistance is then measured by applying a voltage between the source and the drain.

### 1.6.2) High permittivity gates

The areal charge density  $\sigma_s$  depends on  $\epsilon_r$  (dielectric permittivity) and  $V_G$  (the gate voltage). In order to maximize the change in areal charge density the use of high permittivity dielectrics is paramount. As a matter of fact, in order to achieve charge accumulation or depletion in TMOs the usual gate dielectric  $\text{SiO}_2$  is not sufficient since its breakdown field and its dielectric constant do not allow to exceed  $10^{13}$  carriers/cm<sup>2</sup> which is not enough to create the desired changes in the films (Ahn, Triscone and Mannhart, 2003). This is why high permittivity dielectrics (such as  $\text{SrTiO}_3$ ) that belong to the TMO family have been used to circumvent this problem.

### 1.6.3) Ferroelectric gates

A ferroelectric material is a material characterized by a spontaneous polarization that can be reversibly switched through the application of an electric field. Since most of them are insulators with high permittivity one can understand why they would be interesting candidates as insulating barriers. The advantages of ferroelectric over standard dielectrics are twofold: Because of the spontaneous polarization the magnitude of the effect is strongly enhanced and the remnant character of the polarization allows for non-volatile effects. A typical example of such a ferroelectric is the bismuth ferrite  $\text{BiFeO}_3$  (BFO) with a spontaneous polarization of  $\sim 90 \mu\text{C}/\text{cm}^2$ , it would theoretically allow for charge transfers reaching  $10^{14}$  carriers/cm<sup>2</sup>. By depositing BFO on top of a cuprate superconductor YBCO, A. Crassous et al. were able to modulate the superconducting properties of the cuprate thin film through field effect (Crassous *et al.*, 2011). Figure 1-15 shows the resistance across the YBCO film for two directions of the BFO polarization. One can see that as the polarization of the BFO film changes from towards to away from the YBCO layer the resistance of the film decreases, and its superconducting critical temperature increases by up to  $\sim 15\text{K}$ . The changes observed in the cuprate film are consistent with an accumulation/depletion of carriers in the film as is depicted in the two schematics in Figure 1-15 by the decrease/increase of the white line in the YBCO layer under the BFO layer in the case of depletion and accumulation. The authors also show that this effect is reversible by subsequent measurements where they were able to recover both states. It is interesting to note that in this experiment the electric field used to reverse the BFO polarization was applied through a conductive nanometric tip rather than a standard transistor like gate. This highlights the versatility of field effect on TMOs and allows a nanometric control of the direction of polarization.

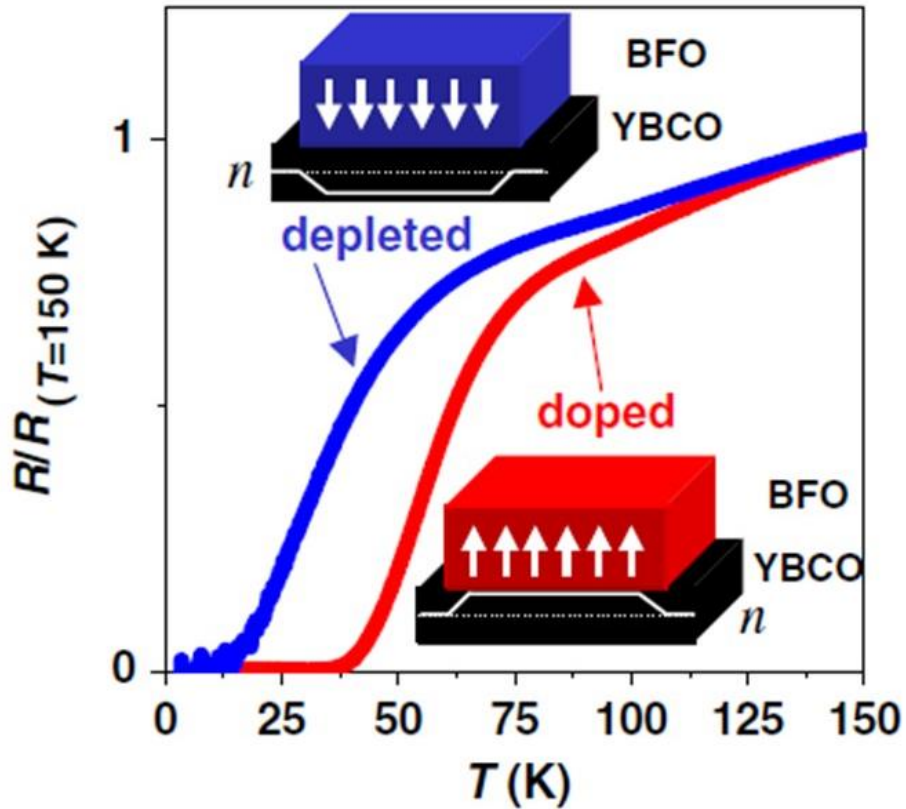


Figure 1-15: Temperature dependence of the normalized resistance measured on the YBCO film. The polarization across the BFO is reversed by applying an electric field across the heterostructure at the nanoscale. Figure adapted from (Crassous et al., 2011)

#### 1.6.4) Screening length

An important aspect that comes into play in these devices is the distance over which the charge accumulation/depletion occur in these devices. The charge accumulation in the dielectric in close proximity to the metal will be screened over a certain distance c.f. Figure 1-16. The screening of interfacial charges will decay exponentially over the metal thickness with a characteristic length given by

$$\lambda_{TF} = \left( \frac{\epsilon_s \epsilon_0}{n_{eff} e^2} \right)^{1/2} \quad 3$$

according to the Thomas-Fermi approach with  $\epsilon_s$  the metal permittivity,  $\epsilon_0$  the vacuum permittivity,  $n_{eff}$  the effective charge density in the metal and  $e$  the electric charge.

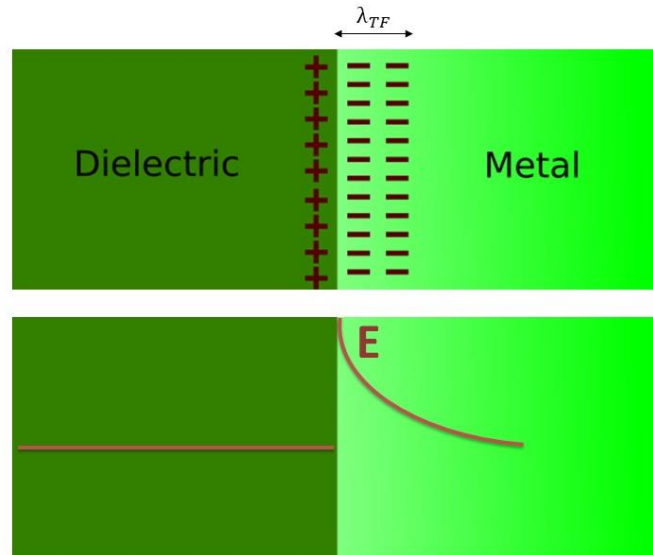


Figure 1-16: Schematic representation of the charge accumulation occurring at the interface between a dielectric and a metal. The accumulation of charges in the metal is high at the interface but decays exponentially over a characteristic distance: The Thomas Fermi-Length  $\lambda_{TF}$ . The electric field profile across the interface associated with the charge accumulation is also shown.

The next section will cover some of the properties of tunnelling junctions since they constitute one of the main approaches used to investigate the effects of external stimuli in this work.

#### 1.6.5) Tunnelling Junctions

Tunnelling is a quantum mechanical phenomenon where a particle is able to penetrate a potential barrier when its kinetic energy is smaller than the barrier height. In solid state physics this phenomenon occurs often when electrons tunnel through an insulating barrier separating two metallic electrodes as can be seen from Figure 1-17. When an electron reaches the barrier most of its intensity is reflected at the interface but a portion decays exponentially through the barrier. Thus, if the barrier is thin enough (usually in the nanometre scale) there is a non-negligible probability – proportional to the square of the electron wavefunction- to find the electron on the other side of the barrier as is represented by the smaller intensity wavelike pattern in Figure 1-17.

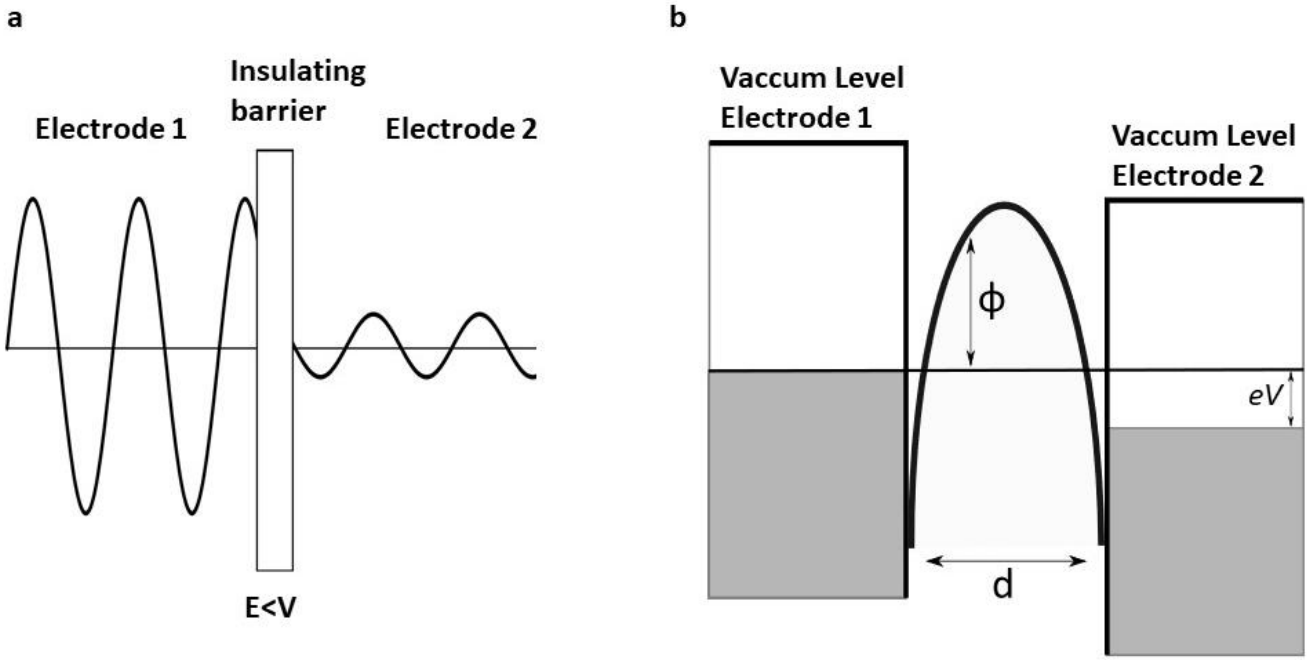


Figure 1-17: (a) Schematic representation of the quantum tunnelling effect. (b) Schematic representation of the tunnelling effect occurring between two metallic electrodes separated by an insulating barrier of height  $\phi$  and thickness  $d$ .

Significant insight into this phenomenon can be obtained by considering a simple case of Metal/Insulator/Metal junction characterized by a step potential barrier. When a voltage  $V$  is applied across the junction the Fermi levels of one electrode will be shifted by " $eV$ " with respect to the other electrode where " $e$ " is the electronic charge. The current flowing through the junction will be proportional to the product of the density of states in the two electrodes at the same energy multiplied by the matrix element  $|M|^2$  representing the probability of transmission across the barrier. One has to also consider the probability that the states in the 1<sup>st</sup> electrode are occupied and those in the 2<sup>nd</sup> electrode are empty by using Fermi-Dirac statistics. Thus, the current flowing between the two electrodes through the insulating barrier is given by

$$I_{M1 \rightarrow M2}(V) = \int_{-\infty}^{+\infty} \eta_1(E) \eta_2(E + eV) |M|^2 f(E) [1 - f(E + eV)] dE \quad 4$$

Where  $\eta_{M1}$  is the 1<sup>st</sup> electrode DOS,  $\eta_{M2}$  is the 2<sup>nd</sup> electrode DOS and  $f(E)$  is the Fermi-Dirac function. Note that the total current flowing across the junction will be the difference between  $I_{M1 \rightarrow M2}$  and  $I_{M2 \rightarrow M1}$ .

It has been shown that for a free electron approximation, at 0 temperature and according to the Simmons formula (Simmons, 1963) the current density can be written as:

$$J(V) = \frac{J_0}{d^2} \left( \phi - \frac{eV}{2} \right) \exp \left( -Ad \sqrt{\phi - \frac{eV}{2}} \right) - \frac{J_0}{d^2} \left( \phi + \frac{eV}{2} \right) \exp \left( -Ad \sqrt{\phi + \frac{eV}{2}} \right) \quad 5$$

Where  $J_0 = e/2\pi\hbar$ ,  $A = 4\pi\sqrt{2m^*\hbar}$ ,  $m^*$  is the electron effective mass,  $\phi$  is the average barrier height and  $d$  is the barrier thickness. A schematic representation of this tunnelling model can be seen in Figure 1-17b. Applying a bias  $V$  shifts the Fermi level of one electrode by an amount  $eV$  with respect to the other.

This shows that the tunnelling current depends on a multitude of factors, the most important being an exponential dependence on the electrostatic barrier profile through its height  $\phi$  and width  $d$  and the electrodes electronic density of states. One can thus understand that small changes in either of these parameters can lead to important changes in the current density and thus in the characteristics of the junction.

For moderate values of voltage, it was shown that the current density is a function of the voltage cube which means that the differential conductance (the derivative of the current flowing through the junction over the voltage applied across it) is a square function of the voltage.

$$G \propto \beta V^2$$

#### 1.6.5.1) Blonder-Tinkham-Klapwijk model

It is of interest to note here that most of the work presented in this thesis revolves around the tunnelling junctions composed of a normal metal and a superconductor. In order to introduce this aspect of the work we shall briefly introduce a theory developed by Blonder, Tinkham and Klapwijk in 1982 (Blonder, Tinkham and Klapwijk, 1982) (BTK theory) to describe the limit between two regimes: quasiparticle tunnelling in Normal Metal (N)/Insulator(I)/Superconductor(S) like junctions and Andreev reflexion in N/S junctions using a single dimensionless parameter the barrier transparency “Z”. This parameter describes the barrier strength between the metal and the superconductor.

In this model, the interface between the metal (N) and the superconductor (S) is modelled as a repulsive delta function potential. By considering solely elastic tunnelling processes the theory leads to four possible scenarios when an electron is incident on the N/S interface: Andreev reflected hole, reflected electron, transmitted electronlike quasiparticle and transmitted hole like quasiparticle. The tunnelling regime at the interface will depend on the balance between Andreev reflections and normal reflections. Typically, the tunnelling current increases because of Andreev reflections and decreases because of normal reflections. The dimensionless parameter Z conveys that balance in the model. The theory in its original formulation describes the tunnelling regimes at the interface between a metal and an s-wave superconductor.

Figure 1-18a shows the differential conductance as a function of the applied voltage for several barrier transparencies. In the case of  $Z = 0$  note that the conductance for  $V < \Delta$  is doubled because most of the incident electrons are Andreev reflected and the transmitted electron pairs carry double the electric charge. As Z increases note that the conductance within the YBCO gap decreases (c.f. cases  $Z = 1.5$  and  $Z = 5$  in Figure 1-18a). In the high Z limit on the other hand, the behaviour of the junction resembles one of a classical tunnel junction. For intermediate values, the behaviour continuously varies between the two limits. A generalized BTK formalism developed by Tanaka (Kashiwaya *et al.*, 1995)(Wei *et al.*, 1998) allows to treat the unconventional d-wave characteristics of the superconducting state observed in cuprates by adding an anisotropic component to the model. This can be seen in Figure 1-18b that shows the normalized conductance as a function of the applied voltage expressed in terms of normalized energy for the tunnelling along different directions into a superconducting cuprate. The ab axis tunnelling with  $\alpha = 0$  resembles the standard U shape feature observed in BCS. On the other hand, a V-shape feature is observed in the tunnelling conductance along the c-axis of the cuprate.

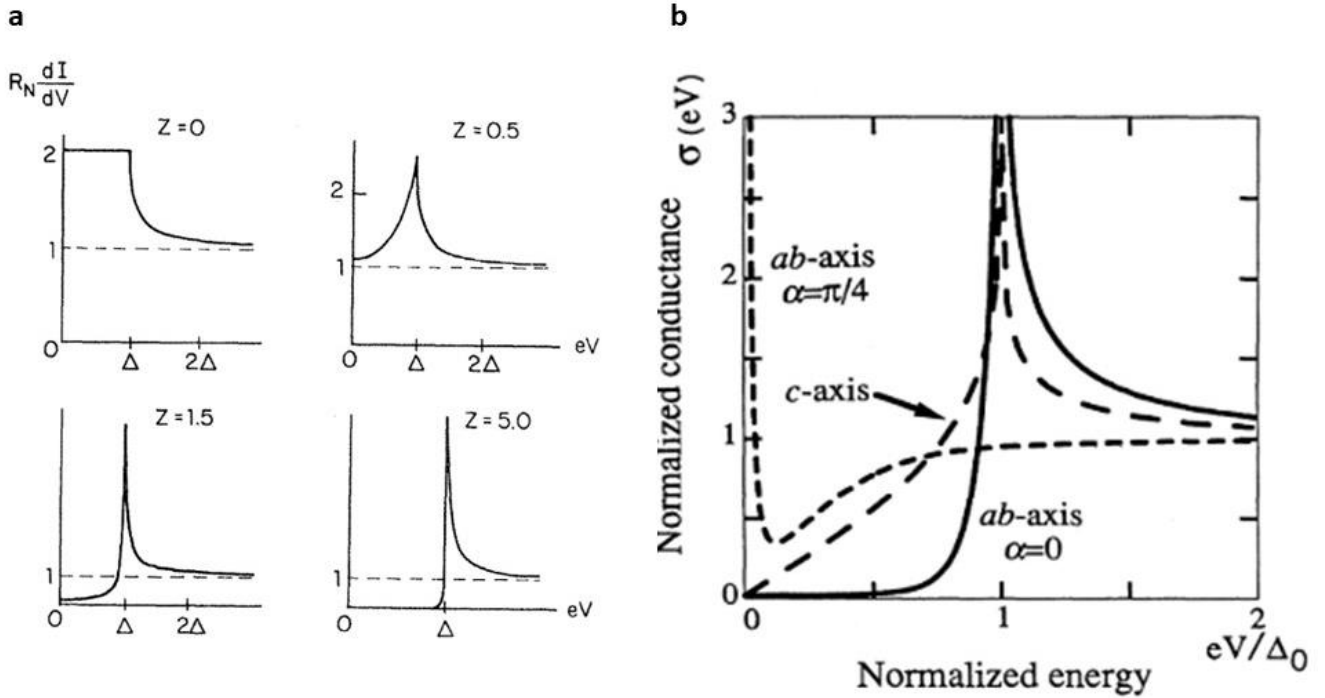


Figure 1-18: (a) Differential conductance ( $dI/dV$ ) vs applied voltage for various barrier transparencies  $Z$ . adapted from (Blonder, Tinkham and Klapwijk, 1982) (b) Normalized conductance as a function of the normalized energy  $eV/\Delta_0$  where  $\Delta_0$  is the energy gap of the superconductor when allowing for the  $d$  wave symmetry of the superconducting gap in the case of  $ab$ -axis ( $\alpha = 0 / \alpha = \frac{\pi}{4}$  and  $Z = 10$ ) tunnelling where  $\alpha$  is the angle of the incident electrons with respect to the interface and  $c$  axis tunnelling. Adapted from (Kashiwaya et al., 1995)

### 1.6.5.2) Ferroelectric Tunnel Junctions (FTJ) and Tunnel Electro Resistance (TER)

The device geometry adopted for the devices investigated in this thesis (in chapters 4), 5) and 6)) is the one of a vertical tunnel junction where two electrodes are separated by an insulating barrier. This section is dedicated to a description of this particular geometry as encountered in the literature.

Ferroelectric tunnel junctions are composed of an ultra-thin ferroelectric tunnel barrier sandwiched between two different metallic electrodes. By applying an electric field on the junction (reversing the polarization) it is possible to alter the junction conductance. This phenomenon is labelled Tunnel Electro Resistance (TER). It was first predicted by Esaki in 1971 (Esaki, Laibowitz and Stiles, 1971) but for a long time it was deemed unfeasible because the critical thickness below which ferroelectricity would disappear was higher than the tunnelling barrier required range (a few nm). The advances in deposition technology and the discovery of ferroelectricity in the nm range allowed the field to prosper. The ongoing development of FeRAM (Ferroelectric random access memories) (Garcia and Bibes, 2014) -a memristor based on the ferroelectric TER effect- is one of the many applications in the field.

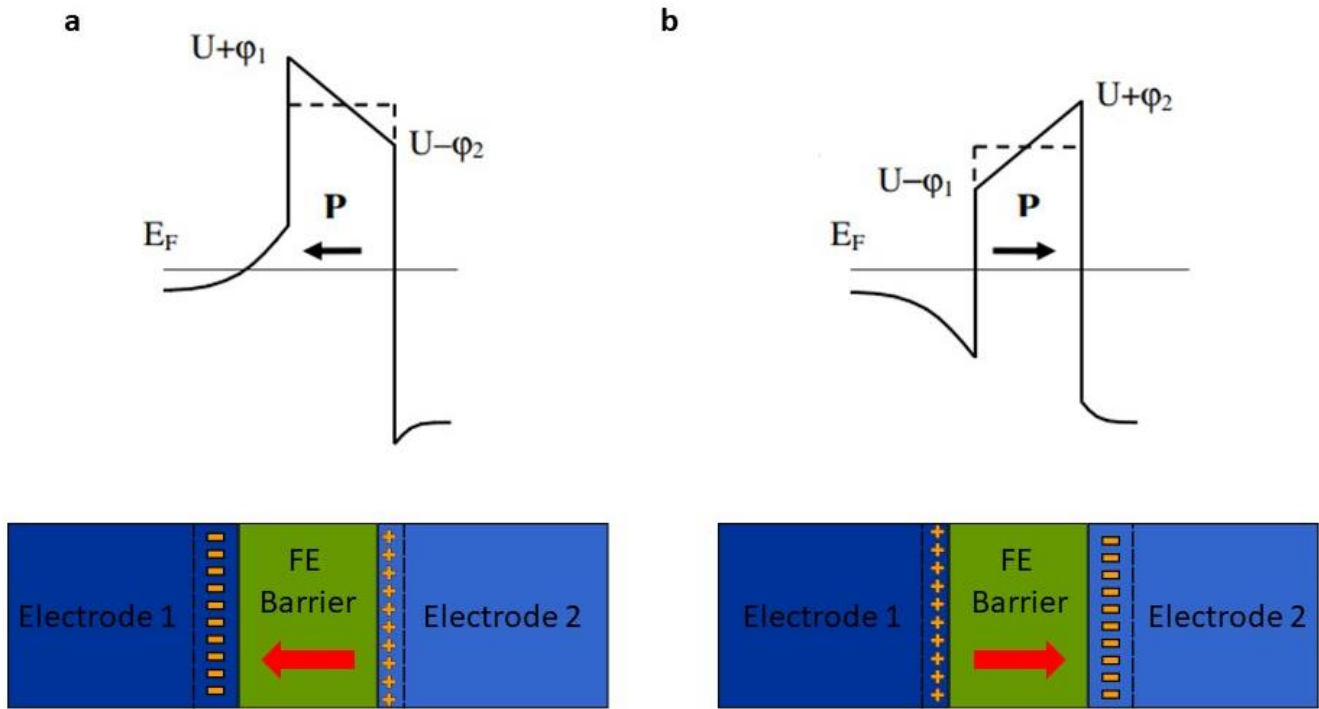


Figure 1-19: Schematic representation of the potential profile across a ferroelectric tunnel junction.  $\varphi_1$  and  $\varphi_2$  are the screening potentials at the interface between the ferroelectric and electrode 1 and 2 respectively (a). Adapted from (Zhuravlev *et al.*, 2005) Schematic representation of a ferroelectric tunnel junction. A ferroelectric barrier separates two different metallic electrodes. (b) By reversing the ferroelectric polarization, the potential profile across the barrier is changed which affects the tunnelling conductance.

The first experimental observations of the TER effect in tunnel junction containing a ferroelectric barrier have appeared approximately a decade ago. (Tsymbal and Kohlsted, 2006; Garcia *et al.*, 2009; Maksymovych *et al.*, 2009)(Gruverman *et al.*, 2009; Crassous *et al.*, 2010) By sandwiching an ultrathin ferroelectric layer ( $\sim$ nm) between two dissimilar electrodes, the authors have observed a non-volatile switch between very different resistive state following the application of a few-volts electric pulse. Figure 1-19 depicts a schematic representation of an FTJ.

It is believed that the conductance in an FTJ is affected by the polarization through 3 different processes. First, the partial screening of charges at the interface between the ferroelectric barrier and the two electrodes creates finite size charge depletion regions at the interfaces. This leads to an asymmetric potential profile of the barrier across the junction. The reasons behind this are twofold: The Thomas-Fermi screening length  $\lambda_{TF}$  occurring at the interface differs in two different metals (Zhuravlev *et al.*, 2005)(This leads to different effective barrier heights depending on the direction of the polarization) and the accumulation of screening charges at the interface can alter the electrode ground state. Second, a change in the barrier profile is also caused by the inverse piezoelectric effect when the strain is applied along the direction of the junction (Tsymbal and Kohlsted, 2006) . The inverse piezoelectric effect is the apparition of a strain field caused by an accumulation of charge in a material (by the appearance of a spontaneous polarization). Finally, orbital hybridization at the interface can alter the probability of electron transmission across the barrier (Tsymbal and Kohlsted, 2006).

Bruno *et al.* (Bruno *et al.*, 2016) have observed a millionfold tunnel electro resistance effect (TER) in ferroelectric tunnel junctions (FTJ) composed of the multiferroic BiFeO<sub>3</sub>(BFO)/LaNiO<sub>3</sub>(LNO)/LaAlO<sub>3</sub>(LAO) heterostructure. A first set of junctions was studied under piezoelectric force microscopy (PFM). In order to reverse the BFO polarization nanosecond voltage

pulses were applied on the junctions. Figure 1-20(a-h) shows amplitude and phase images taken by PFM of BFO/LNO heterostructures showing different states of the junction. The light colours in the phase images indicate a polarization pointing towards the nickelate electrode and the dark colours indicate a polarization pointing outwards. In the as grown virgin state the BFO polarization points towards the nickelate electrode but after the application of voltage pulses the polarization can be reversed. The second set of identical junctions was used to perform transport measurements as a function of temperature in a cryostat. By applying voltage pulses on the devices, the authors managed to reversibly switch between several resistive states of the junction. A negative voltage leads to a decrease of the junction resistance labelled the ON state while a positive one leads to an increase of the junction resistance labelled the OFF state. Figure 1-20i shows the resistance measured across the junctions as a function of the writing. The resistance of the BFO layer, the constant area-resistance product and the temperature of the resistance indicate that the major electron transport mechanism is through direct tunnelling.

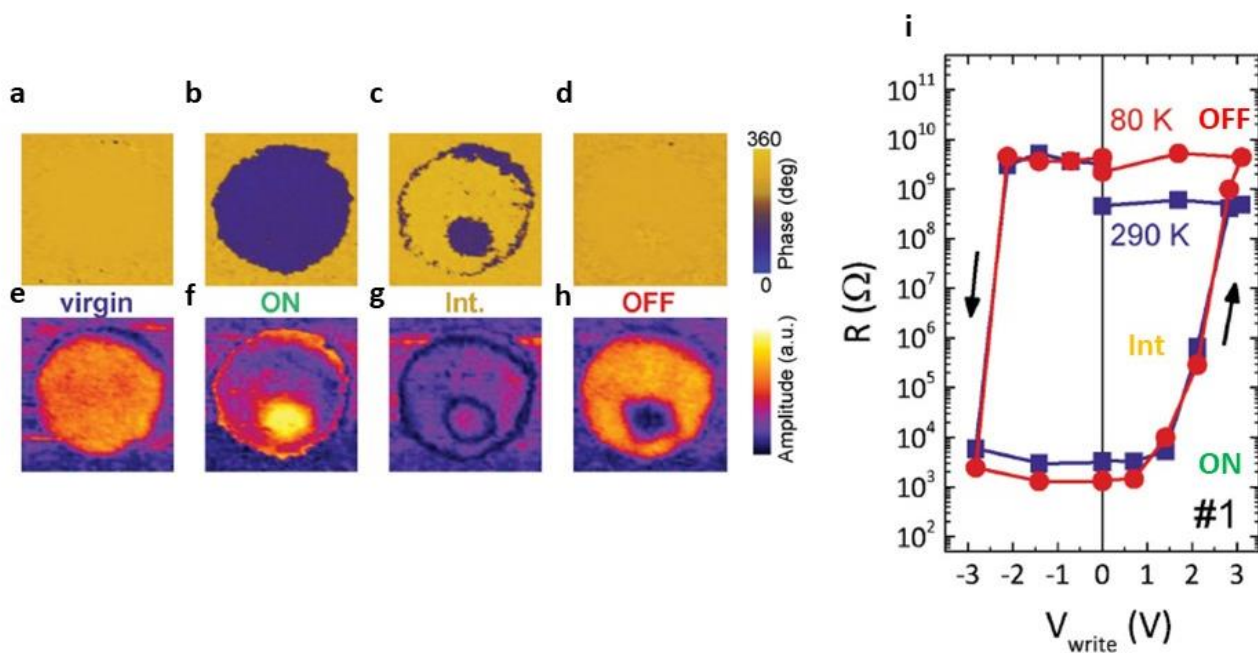


Figure 1-20: Tunnel electroresistance in a ferroelectric tunnel junction. Piezoelectric force microscopy (PFM) phase and amplitude images of a 300 nm junction in the virgin state (a-e), the ON state (b-f), an intermediate state (c-g) and the OFF state (d-h). The polarization of the BFO is reversed using nanosecond pulses applied using the PFM tip (i) Resistance as a function of writing voltage displaying a millionfold tunnel electroresistance of sub micrometer Pt/Co/BFO/LNO heterostructures. Adapted from (Bruno *et al.*, 2016)

### 1.6.5.3 Resistive switching by redox reaction

A more general definition of the TER is the fast, non-volatile and reversible change in the conductance state of a tunnel junction through the application of an electric field. The effects of the electric field include polarization reversal in the presence of a ferroelectric (as presented in the previous section), but TER effects have also been observed in junctions without a ferroelectric barrier. In these cases, the main phenomenon explaining the TER is an electric field mediated redox reaction occurring between the metallic electrodes (Moreno *et al.*, 2010; Gonzalez-Rosillo *et al.*, 2019). This redox reaction concerns mostly oxygen ions but can also include other halogens (Yang, Strukov and Stewart, 2013).

Two main mechanisms have been used to explain the resistive switching effects in TMOs. The creation of conducting filaments in an insulating matrix through the tunnel barrier following the application of

an electric field and an interface related switching mechanism where an electric field changes in the electrochemical properties of the interface. The two scenarios are schematized in Figure 1-21.

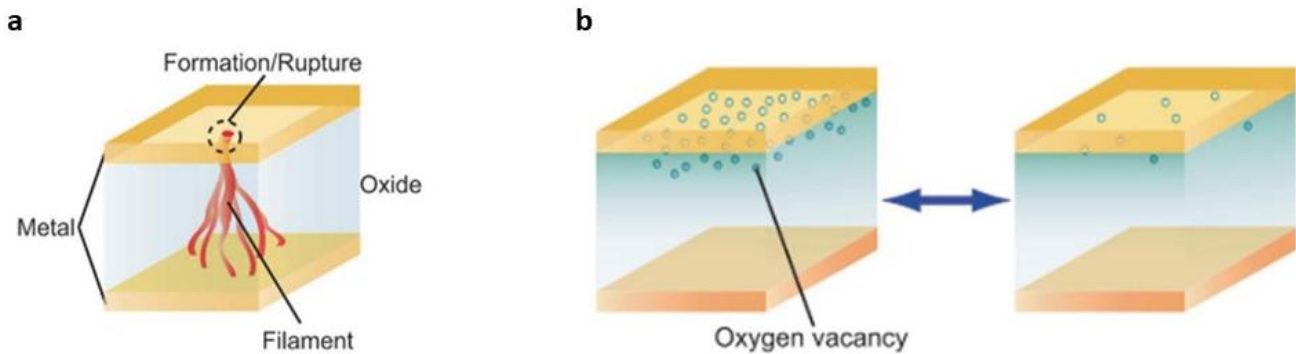


Figure 1-21: Schematic representation of the microscopic scenarios responsible for resistive switching by redox reactions in the case of (a) formation of conducting filaments tracks and (b) interface type resistive switching. Adapted from (Sawa, 2008)

Concerning the conducting filament track, a possible mechanism behind filament creation would go as follows: a filament like structure is believed to form through the dielectric in a soft breakdown manner once an electric field is applied on the junction and thus reducing its effective resistance. The junction would then go through a reset procedure where a redox reaction would sever the link between the filament and one of the metallic electrodes and thus increase its resistance. This link would then be restored through the application of a reversed electric field which would lower the junction resistance again (Kinoshita *et al.*, 2006).

On the other hand, the interface type resistive switching would point towards a change in the contact resistance at the interface between the metal electrode and the dielectric. By changing the contact resistance from an Ohmic to a Schottky barrier for example the behaviour of the junction would change from a standard junction with no resistive switching to a rectifying diode behaviour accompanied by a large resistive switching. Different models were developed to explain these changes including trapping of charge carriers at the interface (Fujii *et al.*, 2005) and electromigration of oxygen ions across the barrier (Nian *et al.*, 2007).

These devices are usually composed of a thick insulating oxide separating two metal electrodes. The application of an electric field across the junction changes the properties of the insulating oxide and thus its transport properties. While the junctions studied in this thesis, detailed in chapters 4), 5) and 6), display a similar qualitative behaviour than the ones described in this section, an important difference has to be noted. Our devices are composed of two metallic oxides deposited on top of one another, with no external insulating barrier separating them. The interface between these two materials is the one affected by the external stimuli and acts as a tunnelling barrier. Because the external stimuli affect the ground state of the electrodes, the effects presented in this thesis are different from the one described in this section.

### 1.7) Light-induced effects in correlated oxides

One main objective of this thesis is to investigate the effects of light on TMOs. This external stimulus offers both persistent and transient, reversible and non-destructive effects that can be investigated in order to explore the different phase diagrams. The microscopic mechanisms behind these effects are various and depend on the materials and the particular phases they are in: it has been shown that the absorption of light in TMOs can enhance the carrier density by promoting charge carriers to the conduction band in a classical semiconducting picture or lead to changes related to the oxygen vacancy motion in the material for example.

In this section we will detail the effects of light on three different types of materials: high mobility 2D electron gas at the interface between two band insulators, manganite thin films and cuprate high  $T_c$  superconductors.

### 1.7.1) 2D electron gas at LAO/STO interface

When one combines two band insulators such as  $\text{LaAlO}_3$  and  $\text{SrTiO}_3$  a high mobility 2D electron gas (2DEG) appears at the interface (Ohtomo and Hwang, 2004). A critical thickness is associated with this phenomenon since the high mobility 2D gas appears above a critical thickness of LAO of 4 unit cells (Di Gennaro *et al.*, 2013). Reports have shown that it is possible to tune its resistive properties by visible or UV light illumination. Various light induced effects have been observed on the 2DEG ranging from persistent photoconductivity to photovoltaic effects (Liang *et al.*, 2013; Di Gennaro *et al.*, 2015) or even negative photoconductance effects (Liu *et al.*, 2019). The 2DEG also exhibits a superconducting critical temperature around 250mK (Reyren *et al.*, 2007). Light illumination also allows a tuning of these superconducting properties.

Tebano *et al.* have investigated the effects of illumination on a LAO/STO heterostructure (Tebano *et al.*, 2012). They have observed a persistent photo-induced decrease of the resistivity of a quasi 2D electron gas (q2DEG) in a LAO/STO heterostructures. They report a decrease of the gas sheet resistance by 5 orders of magnitude at room temperature under illumination by UV and visible light. The persistent characteristic of this effect emanates from the very long characteristic decay time observed at room temperature. To recover the intrinsic properties of the films they annealed the samples at high temperature. Figure 1-22 shows the inverse temperature behaviour of the conductivity of a LAO/STO heterostructure in dark and under illumination by UV and visible light.

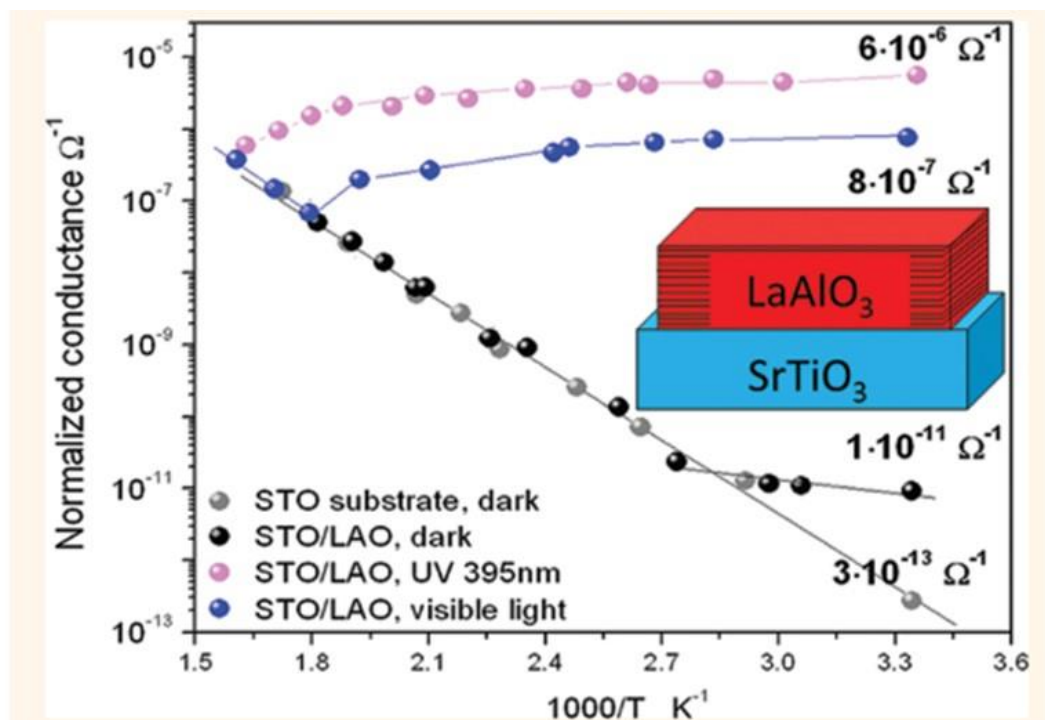


Figure 1-22: Inverse temperature behaviour of the normalized conductance of a 2DEG at the interface between LAO and STO in dark and under illumination with visible light and UV light. Adapted from (Tebano *et al.*, 2012)

On the other hand, Lei *et al.* showed that light illumination combined with field effect can lead to unusual behaviour in a 2D electron gas. They studied the effects of visible light illumination on standard field effect gating on LAO/STO heterostructures (Lei *et al.*, 2014). They have found that by combining these two stimuli the field effect gating efficiency is enhanced significantly. Figure 1-23b

shows the time evolution of the sheet resistance in dark and under illumination as well as under different gate biases. The 2DEG sheet resistance seems to increase significantly under the negative gate bias and visible light illumination, on the other hand when under positive gate bias it does not seem to change significantly. These changes in the sheet resistance have been attributed to changes in the sheet carrier density. The proposed mechanism by the authors is a light induced acceleration of interface polarization caused by migration of oxygen vacancies.

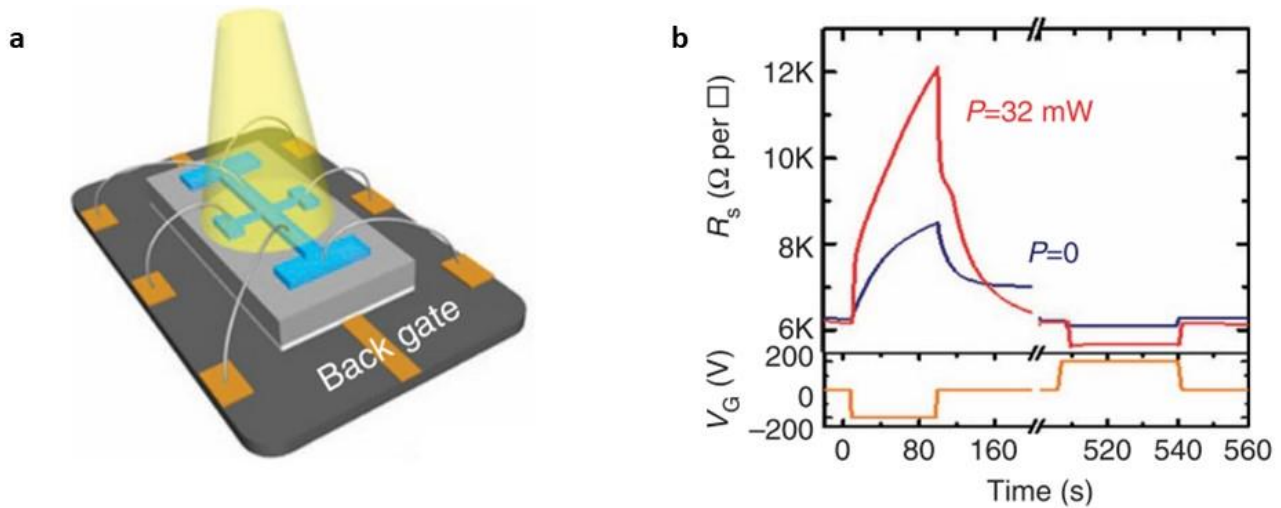


Figure 1-23: (a) Schematic representation of the measurement setup (b) Time dependence of the sheet resistance and gate voltage of a 2DEG at the interface between LAO and STO in dark (blue) and under illumination (red) for different gate voltages

In a more recent study Arnold et al. have shown that the superconducting properties of a 2DEG at the interface between LAO and STO can be tuned through visible light illumination (Arnold *et al.*, 2019). They have shown that under illumination the 2DEG sheet resistance decreases as a function of illumination time and that this decrease is a persistent effect at low temperature (below 1K). They have also observed changes in the superconducting critical temperature of the gas under illumination that scaled with the light irradiance. Figure 1-24 shows the temperature dependence of the sheet resistance after illumination with different radiant exposure  $D$ . The superconducting critical temperature decreases as a function of decreasing resistance.

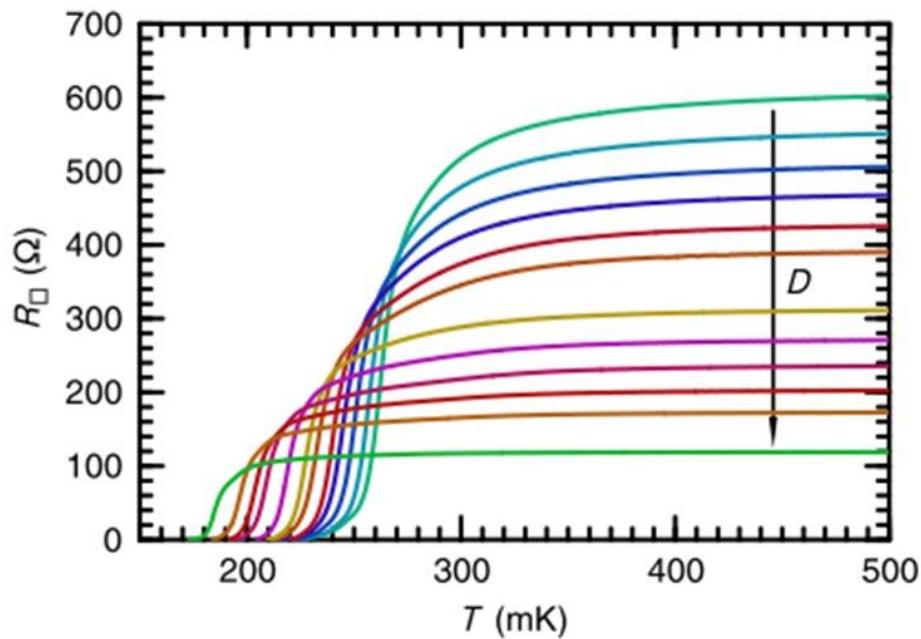


Figure 1-24: Temperature dependence of the sheet resistance of a 2DEG at the interface between LAO and STO under illumination for different illumination doses. The arrow indicates increasing illumination dose. Adapted from (Arnold *et al.*, 2019).

### 1.7.2) Manganites

Manganites are widely investigated because of their various electrical and magnetic properties for fundamental physics and technological application purposes. Because of the interplay between charge, lattice and orbital degrees of freedom, these materials exhibit a wide variety of ground states that can be accessed through the tuning of an order parameter. Manganites are associated with a transition separating a ferromagnetic metallic state from an antiferromagnetic charge ordered insulator state. The existence of these different phases can be understood through the prism of a double exchange theory (Goodenough, 1955) where electrons are exchanged between  $Mn^{3+}$  and  $Mn^{4+}$  ions through the ligand atoms. By changing the ratio between  $Mn^{3+}$  and  $Mn^{4+}$  one can tune the transition temperature separating the two phases. Several reports in the literature investigate the changes in the electrical properties of manganite thin films (Miyano *et al.*, 1997; Cauro *et al.*, 2001; Beyreuther *et al.*, 2009) and heterostructures (Beyreuther *et al.*, 2010) under the illumination with visible and UV light.

Miyano *et al.* have studied the metal-to-insulator transition (MIT) of  $Pr_{0.7}Ca_{0.3}MnO_3$  under visible light illumination (Miyano *et al.*, 1997). By monitoring the MIT through the photo-induced conductivity, they show a transient metal-to-insulator transition ( $\sim ns$ ) occurring under visible/IR (infrared) light illumination. Figure 1-25 shows the photocurrent measured after the illumination with increasing optical power. The authors claim the appearance of the MIT is triggered by the generation of photocarriers by the light creating metallic sections that conduct current under an applied electric field in an insulating matrix.

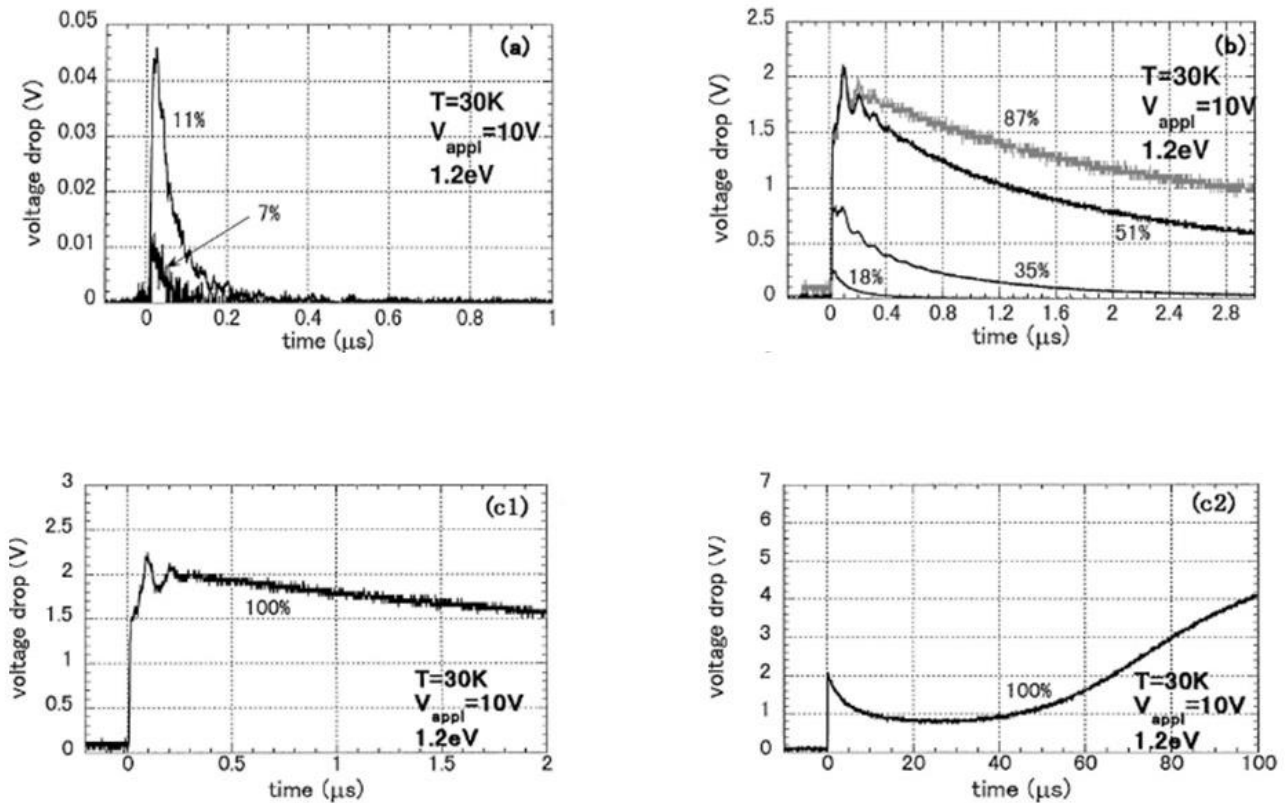


Figure 1-25: Measure of the photocurrent under illumination with different optical power of a PCMO thin film. The voltage drop is measured across a load resistance. The first microseconds under maximal power are shown in figure c1. Adapted from (Miyano *et al.*, 1997)

On the other hand, Cauro *et al.* have observed transient and persistent photoconductivity in oxygen deficient  $\text{La}_{1-x}\text{Sr}_x\text{MnO}_{3-\delta}$  (LSMO) films under white light illumination ( $250\text{nm} < \lambda < 900\text{nm}$ ) (Cauro *et al.*, 2001). They showed that slightly oxygen deficient films exhibit a persistent photoconductive effect (PPC) where the resistivity of the film is lowered after illumination and the effect persists after the light is turned off. The sample recovers its virgin properties after an annealing at temperatures  $T > 100\text{K}$ . The authors explain this effect by a photo-induced increase of the carrier density. A photon is absorbed by the material creating an electron hole pair, the electron is then trapped in an oxygen vacancy thus allowing the hole to contribute to conduction. Figure 1-26a shows the temperature evolution of the resistance before and after illumination. However, in highly oxygen deficient samples transient photoconductivity is observed at low temperature. Figure 1-26b shows the time evolution of the resistance in a highly oxygen deficient LSMO film before, during and after illumination. The authors favour a photo-induced increase of the carrier density in an electronic localization scenario where photodoping shifts the Fermi level beyond the energy corresponding to the mobility edge of the material.

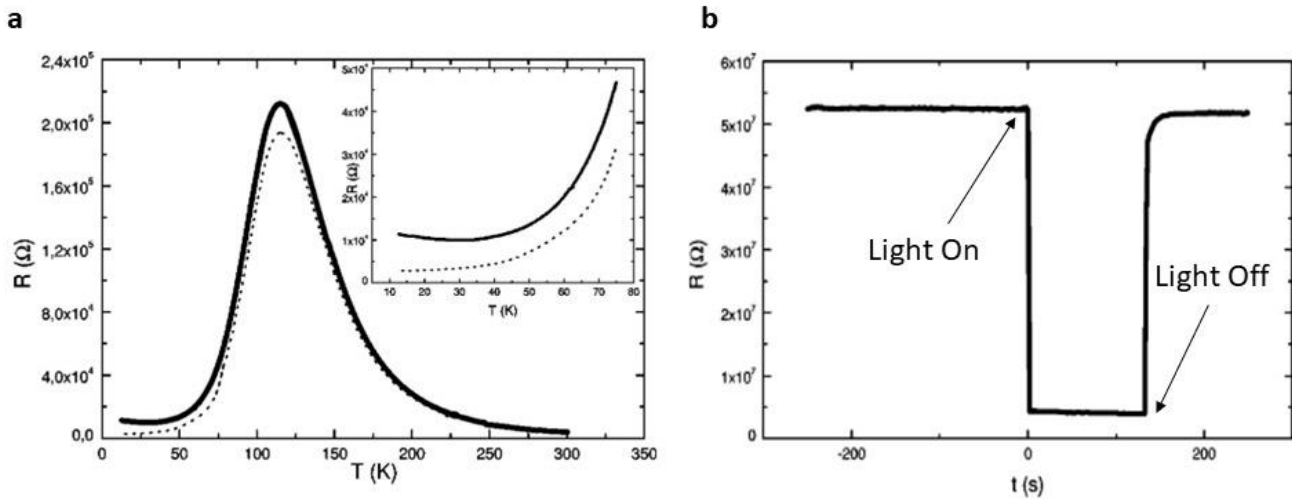


Figure 1-26: (a) Temperature dependence of the resistance measured in a slightly oxygen deficient LSMO film in dark (solid line) and under illumination (dashed line). The inset is a zoom of the resistance behaviour at low temperature. (b) Time dependence of the resistance in a highly oxygen deficient LSMO film in dark and under illumination. Light is on at  $t = 0$ s and is turned back off at  $t = 130$ s. Adapted from (Cauro *et al.*, 2001)

### 1.7.3) Cuprates

Cuprates have been widely investigated since their discovery because of their high  $T_c$  superconductivity phase amongst other exotic phases. It was discovered quickly that the superconducting properties of a cuprate crystal or thin film can be tuned by adjusting the doping of the material i.e. its carrier density. Multiple techniques have been used to alter the doping of a cuprate including chemical substitution, oxygen depletion or through the use of external stimuli. In this section we will focus on the changes observed in oxygen deficient cuprate thin films after illumination by visible and UV light. These effects were significantly different from what was observed in standard BCS superconductors where the absorption of photons with energy higher than the superconducting gap breaks the Cooper pair and weakens the superconducting state.

In 1990 a persistent photoconductive (PPC) phenomena was discovered in YBCO thin films after their illumination with visible light (Kirilyuk, Kreines and Kudinov, 1990)(Kudinov *et al.*, 1990). This decrease of the resistivity in the normal state was accompanied by an increase in the superconducting critical temperature of the sample (Nieva *et al.*, 1992). This effect was labelled persistent because the photo-induced changes persist in dark after the light is turned off and the virgin state properties are recovered through a thermal annealing treatment. Figure 1-27 shows the temperature dependence of the resistance measured on an oxygen deficient cuprate before and after illumination by visible light.

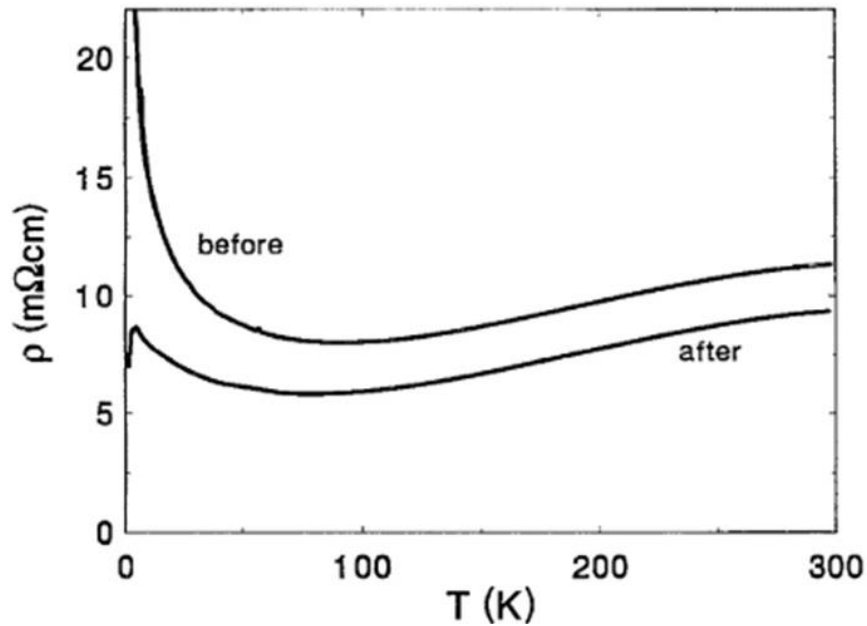


Figure 1-27: Temperature dependence of the resistivity across a GdBaCuO film before and after illumination by visible light. Adapted from (Nieva *et al.*, 1992)

The dynamics of the PPC were extensively studied (Kudinov, Kirilyuk and Kreines, 1992)(Markowitsch *et al.*, 2009)(Kudinov *et al.*, 1993) during the relaxation in dark at high temperature after illumination at low temperature. Figure 1-28 adapted from (Nieva *et al.*, 1992) shows the time dependence of several transport coefficients across a cuprate thin film during the relaxation. The relaxation dynamics was found to follow a stretched exponential behaviour (sharp increase in the resistivity first followed by a long tail) and the characteristic time was found to be of the order of hours at room temperature and close to 1200 hours at 250K (Kudinov *et al.*, 1993). In order to better understand the changes observed in the resistivity and superconducting critical temperature Hall measurements were performed to obtain information about the carrier density evolution during illumination. Note however that Hall measurements do not provide an exact determination of the carrier density because the Drude model used to extract the carrier density from a Hall measurement fail to describe cuprates (refer to section (I.5.1.5.5)) for further discussion of this issue). However, the Hall number as obtained from the Hall measurements is proportional to the carrier concentration, and variations of the (inverse) of the Hall coefficient upon light illumination are proportional to variation in the carrier concentrations (Jones, Christen, Thompson, Feenstra, Zu, *et al.*, 1993; Stockinger *et al.*, 1998). In particular, the Hall coefficient was found to decrease during illumination thus suggesting an increase in the carrier density. Figure 1-28(b-c) shows the time dependence of the carrier mobility and the Hall coefficient during and after illumination at room temperature. The carrier mobility gives a measure of the carrier scattering length (the length a charge carrier travels before it is scattered) according to standard transport theories. It is calculated from the Hall coefficient and the longitudinal resistivity and found to increase under illumination at low temperature but to behave in a non-monotonic manner at high enough temperature(Stockinger *et al.*, 1998).

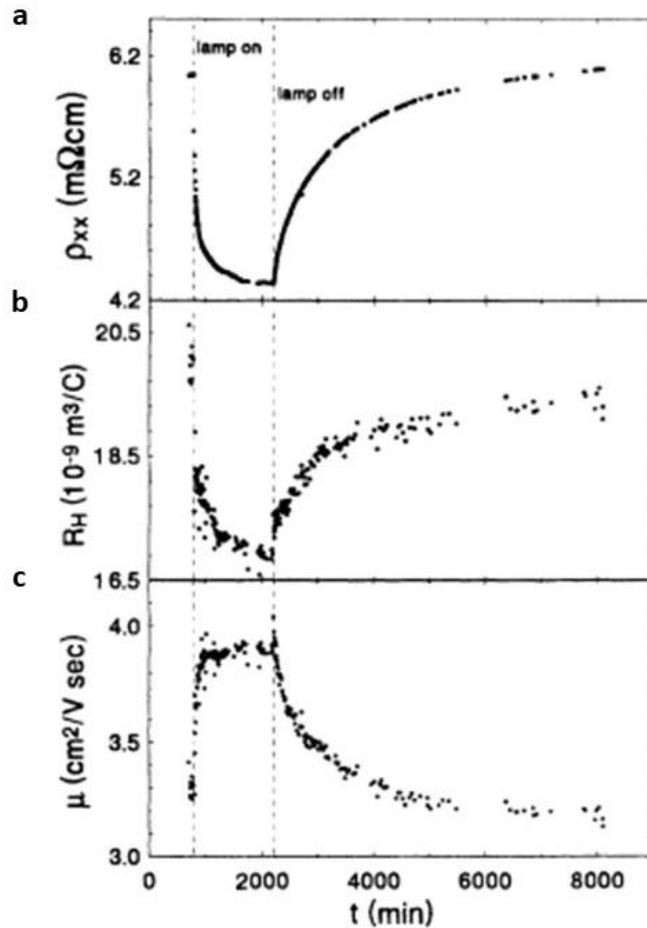


Figure 1-28: (a) Time dependence of the resistivity, (b) the Hall coefficient and (c) the carrier mobility in dark and under illumination (white light) in an oxygen deficient YBCO film at room temperature. Adapted from (Nieva *et al.*, 1992)

The illumination by visible or UV light also leads to structural changes as observed by Lederman *et al.* (Lederman *et al.*, 1994) where careful XRD spectra of an oxygen deficient YBCO thin film were taken under illumination. The c axis parameter is shown to contract under visible light illumination as can be seen from Figure 1-29a showing the time dependence of the normalized c axis parameter and resistivity under illumination. This contraction has been attributed by the authors to a contraction of the Ba Cu1 distance in the Cu O chains in the YBCO structure. The magnitude of the photo-induced changes have been found to increase with decreasing oxygen content (Hasen *et al.*, 1995). This means that the persistent photo-induced effects are only present in underdoped or overdoped regions of the phase diagram provided there are oxygen vacancies present in the sample (Gilbert *et al.*, 2000). The spectral dependence of the PPC was also widely investigated and it was shown that the photo-induced decrease of the resistance has pronounced spectral dependence as can be seen from Figure 1-29b. It was demonstrated that a PPC can be obtained by visible light illumination (Bud'ko *et al.*, 1993) but its efficiency is increased significantly when illuminated with UV light (Endo *et al.*, 1996). The peak shown in the previously mentioned plot was attributed to a 3d to 4p transition of a Cu atom in an O-Cu-O dumbbell (Kelly *et al.*, 1988). Note that the PPC can be partially quenched when the sample is irradiated with infrared light typically  $980\text{nm} < \lambda < 1040\text{nm}$ . (Chew *et al.*, 1996) This suggests that the energy barrier separating the virgin ground state from the metastable excited state is of the order of 1eV.

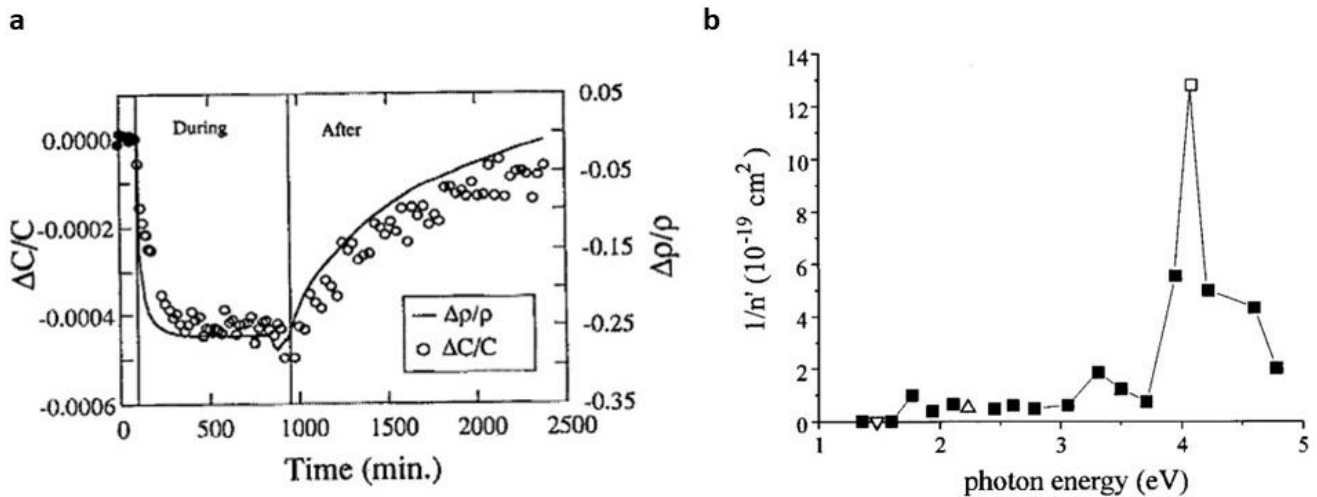


Figure 1-29: (a) Time dependence of the normalized c axis parameter and resistivity of an oxygen deficient YBCO film before, during and after illumination. adapted from (Lederman *et al.*, 1994) (b) Photon energy dependence of the PPC efficiency in oxygen deficient YBCO thin films.  $n'$  is the number of photons per unit area necessary to create a 2% change in the resistance. Adapted from (Endo *et al.*, 1996)

The microscopic mechanism behind the photo-induced effects on cuprates is still debated. Two main scenarios have emerged:

1. When a photon is absorbed by the material an electron hole pair is created. In the presence of oxygen vacancies, the electron is trapped and the hole can participate to the conduction in the material. At high enough temperature the electron is released from the trap and the pair can recombine thus allowing the system to relax to its ground state. The hole density increase thus explains the increase in the critical temperature (Kudinov *et al.*, 1993).
2. A photo-induced oxygen ordering occurs in the YBCO structure. A photon mediated diffusion of oxygen ions in the chains occurs thanks to local electric field created in the chains (Osquiguil *et al.*, 1994) (Kudinov *et al.*, 1993). This ordering of oxygen atoms in the chains will affect the effective hole density in the  $\text{CuO}_2$  planes and as such the superconducting critical temperature (Gauquelin *et al.*, 2014) (Ceder *et al.*, 1990).

A transient photo-induced effect was observed in highly oxygen deficient YBCO films (Yu *et al.*, 1992) where an increase of the conductivity was observed in the nanosecond range. Note that the photon range is smaller than  $10^{16}$  photons whereas the persistent effect occurred after illumination time ranging from the ms to the multiple hours which correspond to an incident photon dose of  $10^{29}$ - $10^{23}$  photons. $\text{cm}^2$ .

## 2) Experimental Techniques

### Contents

2) Experimental Techniques.....	61
2.1) Pulsed Laser Deposition.....	62
2.2) Sputtering.....	64
2.3) Oxygen stoichiometry control.....	65
2.4) Ion irradiation .....	66
2.5) X ray diffraction.....	68
2.6) Atomic Force Microscopy .....	69
2.6.1) Piezoresponse Force Microscopy.....	70
2.6.2) Conductive Tip AFM .....	70
2.7) Scanning Transmission Electron Microscopy.....	71
2.8) Resonant Inelastic X-ray Scattering .....	72
2.9) Nanofabrication .....	73
2.9.1) Vertical junctions: .....	74
2.9.2) YBCO Thin Films: .....	76
2.10) Transport.....	77
2.10.1) Cryostation and sample preparation .....	77
2.10.2) Temperature Calibration.....	78
2.10.3) Transport measurements.....	78
2.10.4) Superconducting Critical Temperature.....	78
2.10.5) Hall effect.....	79
2.10.6) Mobility and Hall angle .....	80
2.10.7) Vertical junctions .....	81
2.11) Illumination .....	81
2.11.1) Sources.....	81
2.11.2) Heating.....	83

*In this chapter we will describe the different methods and techniques used to prepare then measure our samples. The first section will cover the growth techniques such as pulsed laser deposition and magnetron sputtering used to deposit epitaxial thin films and metallic layers. We will then describe the ion irradiation process used to alter the properties of our high  $T_c$  superconducting films and typical characterization techniques as X-ray Diffraction (XRD), Atomic Force Microscopy (AFM), Scanning Transmission Electron Microscopy (STEM) combined with Electron Energy Loss Microscopy (EELS) and Resonant Inelastic X-ray Scattering (RIXS). Furthermore, we describe in this chapter the different nanofabrication processes necessary to measure transport properties. Finally, we detail the different illuminations performed during this thesis.*

## 2.1) Pulsed Laser Deposition

Pulsed laser deposition (PLD) is a thin film deposition technique where a high energy pulsed laser is focused onto a target and the ablated material is deposited on a substrate. This technique has been used to deposit a high number of different materials such as metals, compound semiconductors and perhaps most notably oxides with a plethora of different properties (Eason, 2007). Compared to other oxide film growth techniques, PLD holds an advantage because of its ability to easily translate the target stoichiometry to the deposited film. (Eason, 2007). In addition, this technique offers the possibility of reactive deposition in  $O_2$  filled chambers. This renders the technique especially well-suited to deal with oxide thin films combining several elements and requiring careful control of stoichiometry as in high  $T_c$  superconductors for example. The high deposition rate and versatility of this technique grant us an easy and accurate way to grow single oxide thin films or heterostructures (by piling different materials on top of each other).

Figure 2-1 depicts a typical representation of the PLD process where a high power short pulsed laser ( $\sim 10$ ns) is focused on a sintered target (usually a chemical compound of the desired material) ablating it and forming a plasma plume. To deposit the ablated material on the substrate, it is placed on a substrate holder facing the plume. The substrate can be heated (typically around  $700^\circ C$  for oxides) to facilitate diffusion of the ablated material on the substrate surface. The oxygen partial pressure in the chamber is controlled during the growth to ensure the correct stoichiometry is achieved.

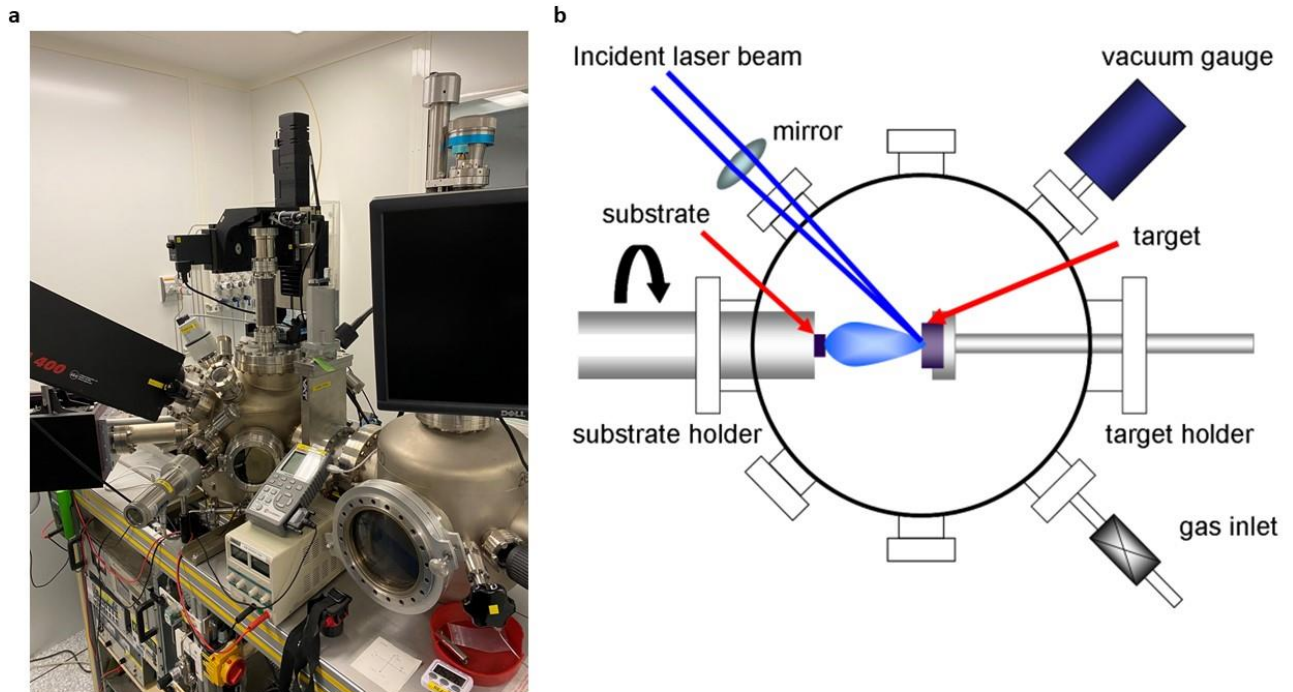


Figure 2-1: Picture (a) and scheme (b) of a Pulsed Laser Deposition (PLD) chamber. Adapted from (pngwing, no date)

However, it must be noted that finding the growth parameters to optimize the deposition of any particular material is quite complex. The plume composition depends on a multitude of factors such as temperature, oxygen partial pressure, composition of target, shape and density. It is rarely homogeneous since some species will react with oxygen or with others present in the plume before they can reach the substrate. Moreover, the composition of the target may vary in ablated areas, it might age or get oxidized, the laser power may vary, and the laser optics may blacken and thus change the beam profile. In order to optimize the growth of a material and maximize the reproducibility of samples a set of steps were taken:

- The targets are regularly polished.
- An area of the target is sufficiently pre-ablated before each deposition
- The substrate and substrate holder temperature are continuously measured using a pyrometer.
- The laser energy is measured using a calorimeter and is controlled using an attenuator until it reaches the adequate value.
- The growth parameters are noted in a notebook to ensure maximum reproducibility.
- Pictures of the plume are taken before each growth to check its shape, size and colour.

In the next section we will detail the growth parameters used to grow the various oxide thin films studied during this thesis.

Both the YBCO thin films and the various heterostructures studied in this thesis were grown by PLD on STO (001) substrates using a KrF 248 nm excimer laser with an energy density of  $\sim 1 \text{ J.cm}^{-2}$  and a repetition rate of 5Hz. To ensure the homogeneity of the deposited films the substrate rotated along its perpendicular axis. The YBCO growth temperature was 700°C in an oxygen partial pressure of 0.36 mbar. Unless stated otherwise a post growth annealing process was performed in an oxygen partial pressure of 800 mbar to reach optimal oxygen stoichiometry.

## 2.2) Sputtering

Sputtering is a physical vapor deposition technique used to deposit thin layers of a target material on a substrate. A discharge plasma is created by a high DC voltage or a RF source generating energetic ions that bombard the target material. Surface atoms of the target are sputtered and eventually condense on a substrate placed in front of it.

In this thesis, we have used magnetron sputtering to deposit metallic thin films on our samples. The deposition chamber is filled with Argon (Ar) gas at low pressure. A high DC voltage is then applied between the target material (constituting the negative pole) and the chamber wall (constituting the positive pole). The electric field created at the target ionizes the Ar gas creating  $\text{Ar}^+$  ions which will eventually collide with the target surface. If the energy of the incident ions is greater than the binding energy of the target atoms, they are ejected from the target creating a plasma in the chamber. This plasma condensates on the sample surface depositing a thin layer of the target material on its surface.

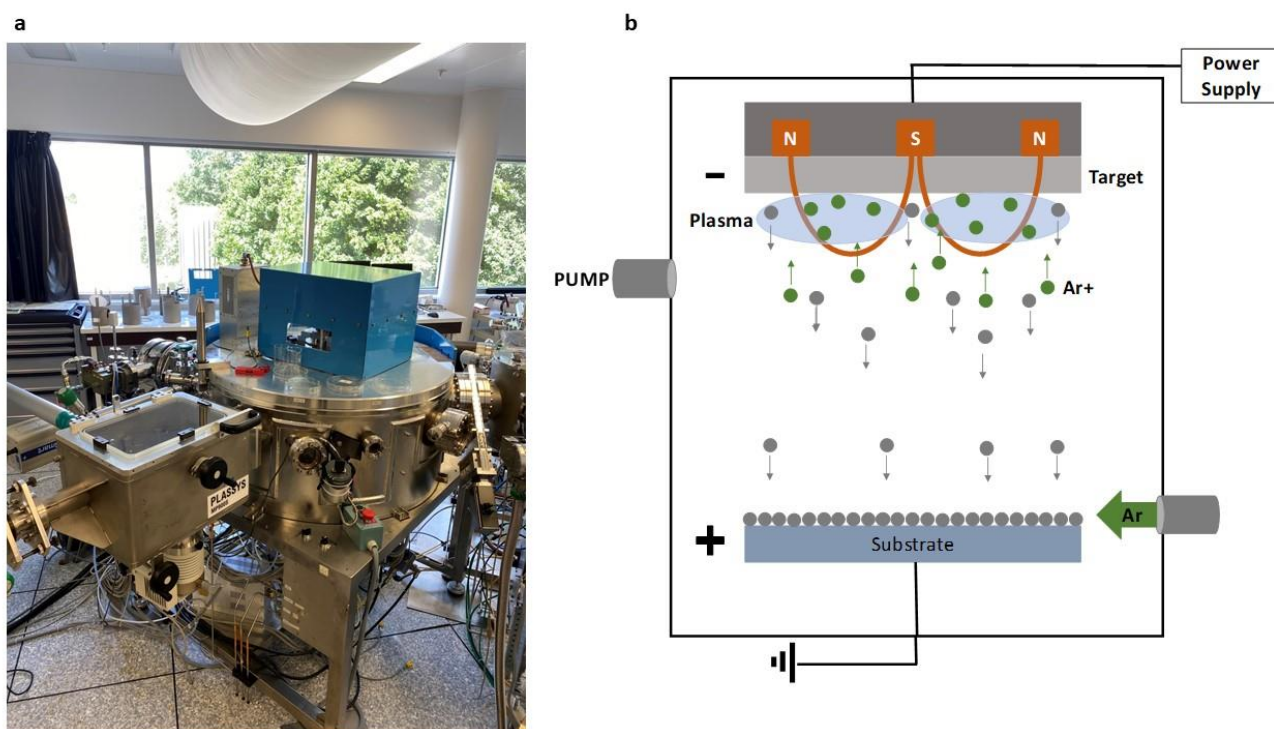


Figure 2-2:(a) Picture and (b) schematic representation of a magnetron sputtering deposition chamber. The orange lines represent the magnetic field.

To deposit our films, we have used a standard magnetron sputtering technique where a strong magnetic field is placed behind the target in order to confine the plasma in the region next to it. This increases the plasma density in the target proximity and allows for higher deposition rates while protecting the substrate and the remainder of the chamber from unwanted contact with the plasma. A picture of the deposition chamber as well as the schematic representation of the process are shown in Figure 2-2(a-b)

Note that some of the YBCO films studied in this thesis are grown by sputtering in the Universidad Complutense de Madrid in Jacobo Santamaria's group. There, the chamber is filled with oxygen instead of Ar gas allowing for a reactive sputter deposition and thus an increased control on the oxygen stoichiometry. This high pressure of oxygen also allows the plasma to be confined near the target without the use of magnetic fields.

### 2.3) Oxygen stoichiometry control

Part of this thesis revolved around the effects of illumination on YBCO thin films. The superconducting properties of this material are dependent on its oxygen stoichiometry and it is widely believed it has a maximal critical temperature of ( $T_c \sim 92\text{K}$ ) at an “optimal oxygen stoichiometry” ( $\text{YBa}_2\text{Cu}_3\text{O}_7$ ). However, the effects of illumination have been shown to be more important when the films are oxygen deficient (Gilabert *et al.*, 2000). In order to control the oxygen content in our samples we followed a **post-growth annealing step** consisting in following lines in an oxygen partial pressure vs substrate temperature (P-T) plot as is shown in Figure 2-3a. We start the process at the growth temperature of approximately  $700^\circ\text{C}$  and slowly decrease the temperature while adjusting the oxygen partial pressure in the chamber.

Note that determining the exact oxygen stoichiometry of a YBCO thin film is a difficult process. However, previous publications have established direct relationships between the measured c axis parameter and the oxygen content in YBCO films (Jorgensen *et al.*, 1990; Ye and Nakamura, 1993). The nominal oxygen contents shown in Figure 2-3 are deduced from the superconducting critical temperature and the c-axis parameter of the grown films and their comparison to the values found in literature.

This controlled annealing procedure is a post growth step hence it is applicable in various deposition techniques. As a matter of fact, Figure 2-3b shows the PT lines followed during the post growth annealing of YBCO samples grown by sputtering at the “Universidad Complutense de Madrid” (UCM) (refer to section 2.2). Decreasing the nominal oxygen content or in an equivalent manner increasing the number of oxygen vacancies in the structure reduces the superconducting properties of the YBCO thin films (Tallon *et al.*, 1995).

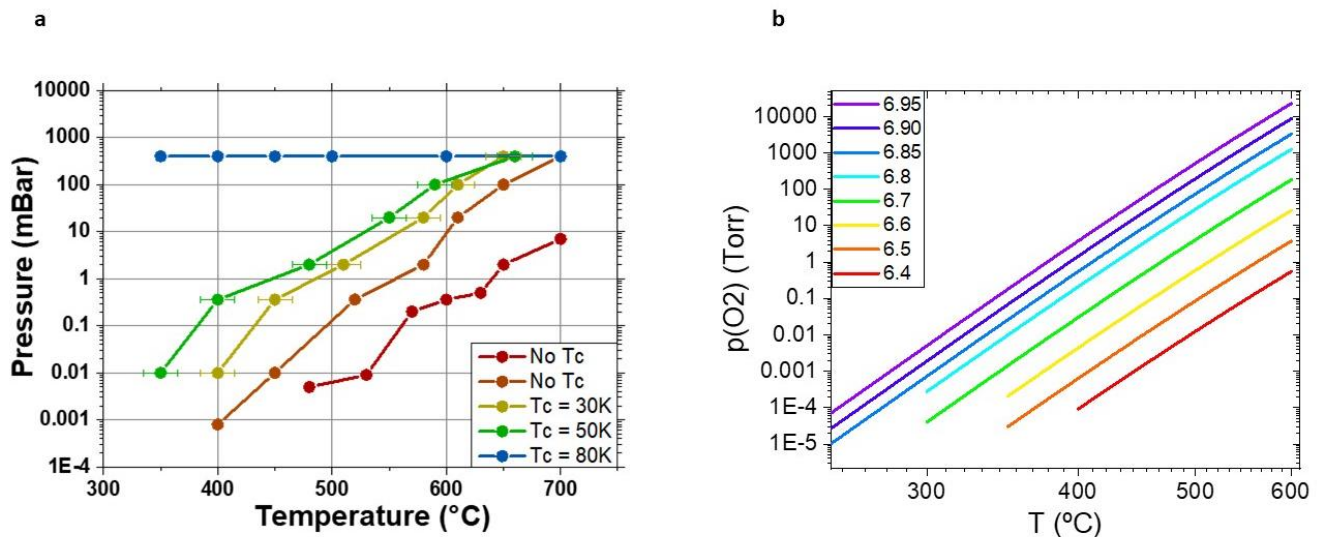


Figure 2-3: Oxygen partial pressure vs substrate temperature in the (a) PLD chamber at the “Unite Mixte de Physique CNRS-THALES (UMR)” and the (b) sputtering chamber at Universidad Complutense de Madrid (UCM) during the post-growth annealing process. The different lines in shown in these plots lead to samples with different oxygen stoichiometry and superconducting critical temperature.

Note that the samples were kept at a fixed pressure and temperature for an important amount of time at each point shown in the graph to ensure a minimal amount of oxygen disorder in the samples. A higher amount of disorder would be characterized by a high residual resistivity in the normal state. (Arias, 2001).

## 2.4) Ion irradiation

The films were grown by PLD following the recipes described in the previous section with an optimal oxygen stoichiometry. The samples were then sent to the ICUBE/D-ESSP laboratory in Strasbourg where they were irradiated by accelerated  $O^+$  ions.

The sample is glued to a holder and inserted into a chamber at a pressure of  $6.10^{-6}$  mbar. The oxygen ions are accelerated using an Eaton NV200 ion accelerator which is fed with  $O_2$  gas. This gas is ionized by an electric field whence a mass spectrometer selects the correct ions for the irradiation. These ions are then accelerated at an energy of 110 keV and the beam gets directed onto the sample. The irradiation dose is estimated by measuring the current flowing through the substrate. Our samples have been irradiated with doses ranging from  $10^{13}$  to  $10^{14}$  ions.cm<sup>-2</sup>.

The irradiation does not affect the YBCO surface morphology per se but creates point defects that will affect its properties. It does so by creating pairs of interstitial/vacancy by knocking some atoms off their usual position in the structure.

It has been shown that the critical temperature of irradiated YBCO ( $T_c$ ) depends on the elastic energy procured by the ion collisions (Lesueur *et al.*, 1990). Thus, it is of interest to compute the displacement per atom (dpa) generated by the irradiation as it is the relevant quantity to describe the disorder induced in the structure. The dpa represents the number of displaced atoms within the structure. It is related to the irradiation dose according to the following equation:

$$dpa = \phi * \frac{c}{d} * 10^8 \quad 6$$

Where  $c$  is the number of collision events per incident ion per Ångström and  $d \sim 7.53 \times 10^{22}$  atoms/cm<sup>3</sup> (Bergeal, 2006) is the atom density in YBCO and  $\phi$  is the ion irradiation dose. The number of collision events per irradiated ion per Ångström can be calculated using a Monte-Carlo simulation software TRIM. It has been shown that  $T_c$  follows the following equation: (Lesueur *et al.*, 1990)

$$\ln \frac{T_c}{T_0} = \psi \left( \frac{1}{2} \right) - \psi \left( \frac{1}{2} - \frac{0.14 * dpa * T_0}{0.07 * T_c} \right) \quad 7$$

Where  $\psi$  is the digamma function and  $T_0$  is the superconducting critical temperature of the sample before irradiation.

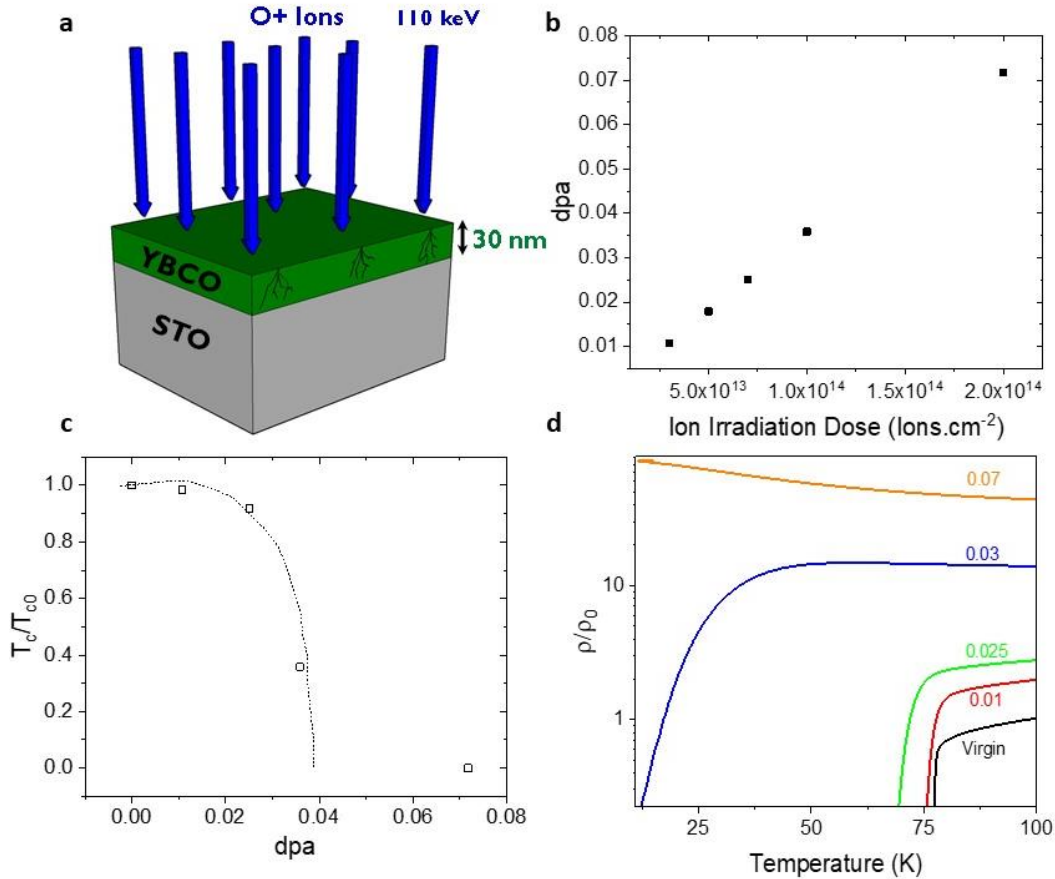


Figure 2-4: (a) Schematic representation of the ion irradiation process (b) Ion Irradiation dose dependence of the displacement per atom calculated according to Eq. 6 for a set of optimally doped YBCO thin films. (c) Evolution of the critical temperature of an irradiated YBCO film as a function of the displacement per atom (dpa) (d) Temperature dependence of the normalized resistivity of ion irradiated films at different dpa. The resistivity is normalized to the resistivity of the virgin sample at  $T=100\text{K}$  where  $\rho = 82.03 \mu\text{Ohms.cm}$

Figure 2-4b displays the ion irradiation dependence of the dpa calculated using the TRIM simulation performed by our group. The value attributed to c is 0.28 collision event per irradiated ion per Ångström. We note with an arrow the value corresponding to the critical dpa extracted from our set of samples. Note that this value actually falls in semi open interval between  $]1 \times 10^{14}, 2 \times 10^{14}]$  ions per cm<sup>2</sup>. Figure 2-4c shows the evolution of  $T_c$  with the dpa. We note that as the dpa increases the superconducting critical temperature decreases, in line with literature reports. Lesueur *et al.*, (1990) have found a critical dpa of close to 0.04. This is consistent with our measurements given that the true value of the dpa in our samples lies between 0.04 and 0.06. Figure 2-4d shows the temperature dependence of the normalized resistivity for samples with different dpa. As the dpa is increased the critical temperature of the samples decreases and their normal state resistivity increases.

Note that although the energy procured by the collisions between the oxygen ions and the material is enough to displace all the species present in YBCO, the changes observed in the irradiated films have been mostly attributed to oxygen displacement in the CuO chains (structural entity along the b direction in YBCO) (Arias *et al.*, 2003). Note that the dpa corresponding to the sample with a  $T_c = 0\text{K}$  (critical dpa) is close to 0.06. It is comparable to the oxygen vacancy proportion necessary to obtain a non-superconducting sample in an oxygen deficient YBCO film which is closer to 0.1 since an oxygen deficient YBCO sample with an oxygen content of 6.4 is insulating.

## 2.5) X-ray diffraction

X-ray diffraction measurements were performed on both our thin films and our heterostructures to ensure their structural quality. X-rays ( $\lambda \sim 0.1$  nm) are an effective tool to study crystalline materials because their wavelength is comparable to the interatomic distance and as such resolve structural features dependent on the atomic structure. This technique grants access to structural information of crystalline materials such as crystalline structure, thickness, existence of different phases etc...

When an X-ray is incident on a sample it will interact with the atoms on its path and more precisely with the electronic cloud of those atoms through a displacement with respect to the nucleus. As a result, the atoms will reemit secondary electromagnetic waves with a similar wavelength in all directions. If the sample is a crystal, constructive interference will lead to an addition of these secondary electromagnetic waves in certain directions. These directions are dictated by the following Bragg law:

$$2d_{hkl} \sin\theta = n\lambda \quad 8$$

Where  $\lambda$  is the wavelength of the X-ray,  $n$  is an integer,  $d_{hkl}$  is the interplanar distance and  $\theta$  is the incident angle. This law accounts for the fact that the distance travelled by rays coming from different planes (in the  $(hkl)$  family of planes) must be equal to an integer number of  $\lambda$  for it to interfere constructively. One can deduce the different lattice constants from the interplanar distance for a given structural symmetry. Figure 2-5a illustrates the conditions under which the Bragg law is satisfied.

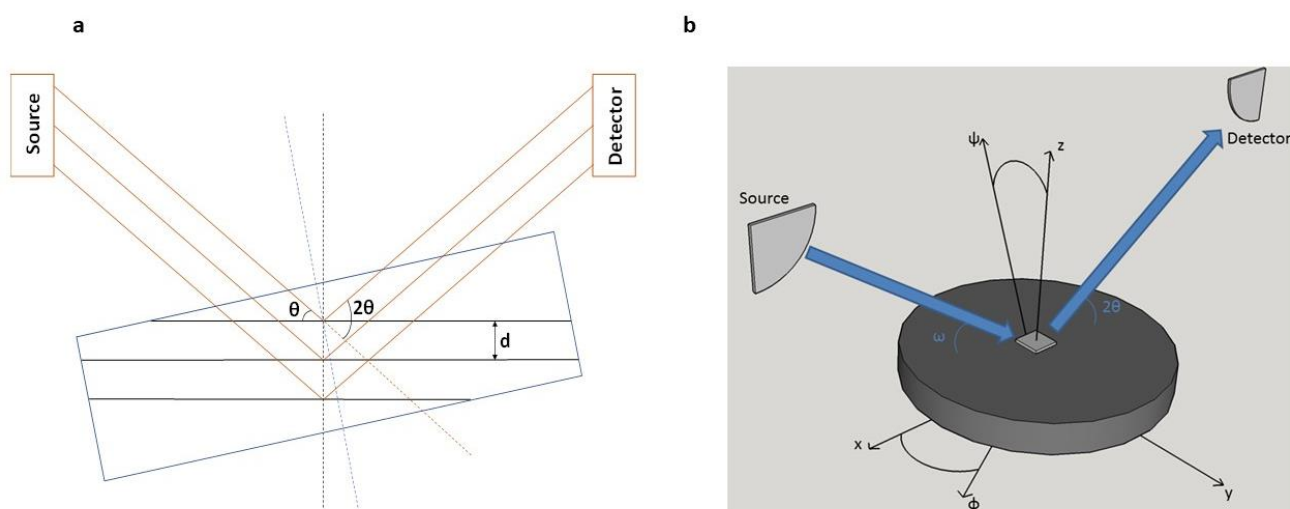


Figure 2-5: (a) Schematic representation of the Bragg law. The black lines represent the family of atomic planes satisfying the constructive interference conditions (b) Schematic of an X-ray 2theta-Omega scan.

We performed “ $\theta$ - $2\theta$ ” scans on several samples studied in this thesis. These measurements took place in a PANALYTICAL Empyrean diffractometer which uses a Cu source emitting at two wavelengths of  $\lambda_1 = 0.154056$  nm and  $\lambda_2 = 0.15439$  nm. A filter is used to filter out the  $\lambda_2$ . A schematic representation of the experiment is shown in Figure 2-5b which consists in varying the positions of the source and the detector simultaneously.

Figure 2-6a shows the XRD spectra of an oxygen deficient YBCO thin film on an STO substrate. The peaks appearing in the spectra belong to the YBCO(00l) and STO (00l) family of planes, indicating that the film maintains the crystallographic orientation of the substrate, proving its epitaxial growth.

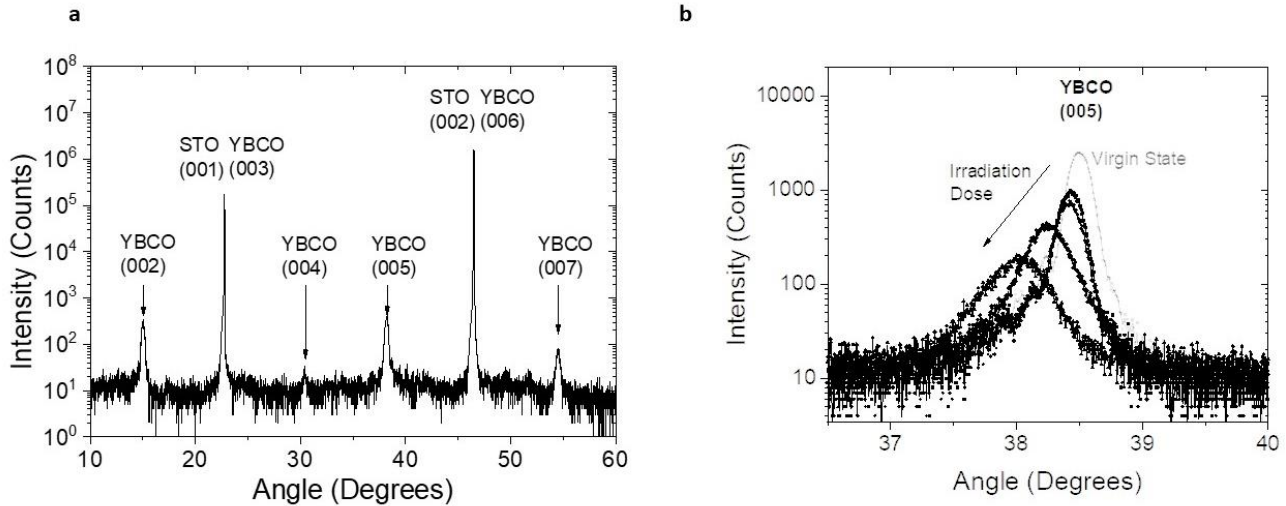


Figure 2-6: (a) Typical XRD spectra obtained on a YBCO thin film grown on an STO substrate (b) Evolution of the YBCO (005) peak as a function of the ion irradiation dose.

YBCO crystals are characterized by a tetragonal or an orthorhombic structure depending on their doping level (Tallon *et al.*, 1995). However, given that our thin films are grown epitaxially in the 001 direction, we have been mostly interested in the “c” axis parameter evolution **with both the oxygen content and ion irradiation dose**. In order to calculate this parameter, we have used the following formula that applies in the case of an orthorhombic structure:

$$\frac{1}{d^2} = \frac{h^2}{a^2} + \frac{k^2}{b^2} + \frac{l^2}{c^2} \quad 9$$

Figure 2-6b shows the evolution of a YBCO peak from the (00l) family with the ion irradiation dose. A shift to the left in the position of the peak indicates an increase in the c axis parameter of the YBCO structure.

## 2.6) Atomic Force Microscopy

Atomic force microscopy (AFM) is a surface probe microscopy technique that allows to image the surface morphology of a sample with a nanometric resolution.

A cantilever with a sharp tip is used to scan the surface of a sample. A laser diode points at the top of a cantilever and any deflection sensed by the cantilever while scanning the surface of the sample causes the light signal to be deflected on a photodetector. The changes observed on the photodetector describe the surface morphology sensed by the cantilever.

In our case, AFM has been used to characterize the thin film quality by measuring in tapping mode. The cantilever is oscillating at its natural resonant frequency before reaching the surface. The amplitude of oscillation, that reaches  $\sim 50 \text{ nm}$ , is referred to as the “free” amplitude. The cantilever is then lowered until the tip reaches the surface. While scanning the surface the changes in the oscillation amplitude caused by depressions or bumps on the surface are adjusted by an electrical feedback loop such that the amplitude remains constant. Bumps on the surface would cause the amplitude to decrease slightly and depressions would cause it to increase approaching its “free” amplitude. These changes are recorded and translated into vertical contrast to image the surface morphology. A scheme of the operating principle is showed in Figure 2-7a.

Figure 2-7b-c show AFM images of an optimally doped YBCO film and an oxygen deficient YBCO film grown on STO substrates. The colour contrast indicates the growth of 3D islands on atomically flat terraces showing that YBCO grows in Volmer Weber or Stranski-Krastanov mode.

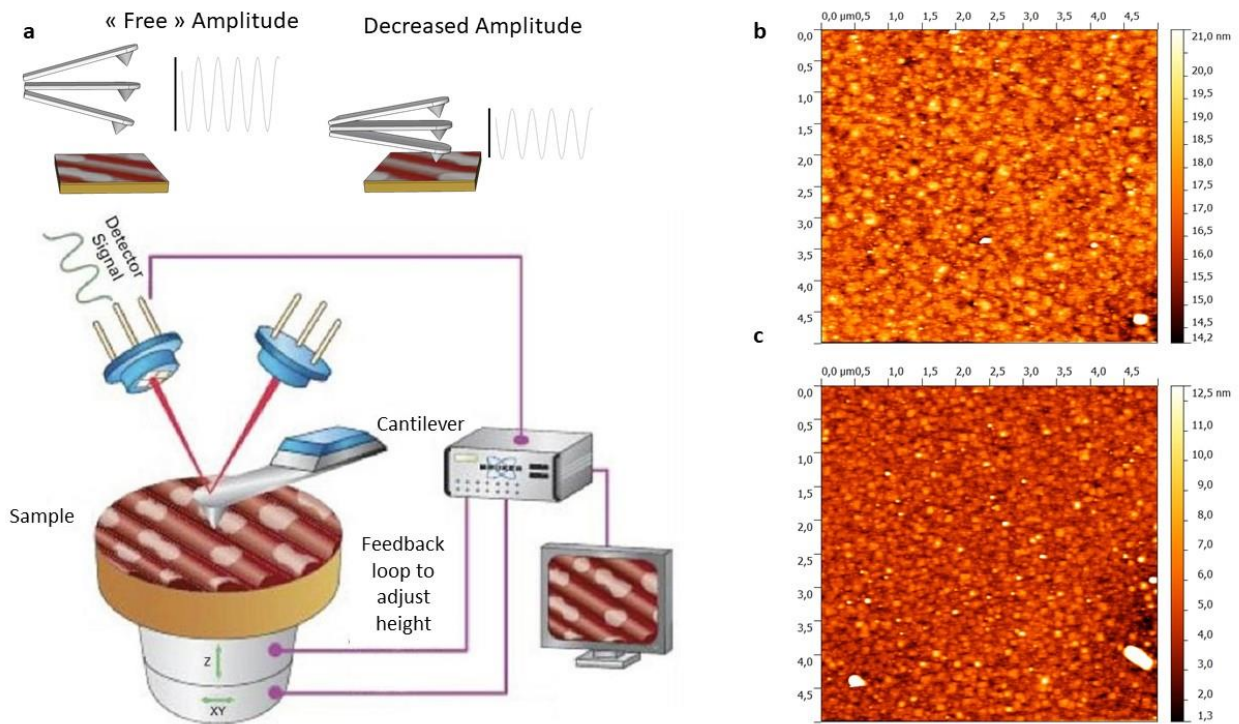


Figure 2-7: (a) Schematic representation of the AFM operating principle adapted from (Bruker.com, no date) (b) AFM image of an optimally doped YBCO film grown on an STO(001) substrate (c) AFM image of an oxygen deficient YBCO film grown on STO (001).

We note the similitude between the images taken on YBCO films with different oxygen contents. The differences in oxygen stoichiometry do not seem to affect the surface morphology.

### 2.6.1) Piezoresponse Force Microscopy

Piezoresponse force microscopy (PFM) is amongst the most popular techniques used to investigate the ferroelectric properties of thin films. It is based on the converse piezoelectric effect where mechanical strain is generated in the material in response to an applied electric field. The presence of a conductive tip - operated in contact mode - and a metallic bottom electrode are required. An AC excitation (usually  $V_{pp} \sim 1V$ ) is applied between the tip and the bottom electrode. In a grounded tip configuration (voltage is applied to the bottom electrode) the domains pointing up/down react in-phase/out-of-phase with the applied voltage. As the tip is scanned over the surface of the film, a lock-in is used to demodulate the low frequency topography induced signal from the piezoelectric signal. One thus obtains the phase (direction of polarization) and amplitude (strength of the signal) of the ferroelectric signals.

### 2.6.2) Conductive Tip AFM

Conductive tip AFM (CT-AFM) is a technique that allows to measure the local resistivity of a thin film in addition to its topography using an electrically conducting tip. It is a useful tool that allows to monitor the resistivity of insulating thin films for tunnelling junction applications. It is operated in contact mode and the presence of a bottom metallic electrode placed under the insulating layer is needed. One can obtain a resistive cartography of the sample surface by applying a DC voltage  $V_{read}$  between the electrode and the tip and measuring the current flowing through with an ammeter. As the measured current is usually small, a current amplifier has to be added to the circuit.

This technique suffers from some setbacks that depend on the nature of the sample. The accuracy of the measurement is affected by the resistance of the tip if the insulating layer (sample) is not insulating

enough. When applying  $V_{read}$  one has to take into account possible damage to the film as well as the dielectric breakdown of the insulating layer.

## 2.7) Scanning Transmission Electron Microscopy

In order to characterize the atomic structure of some of the samples studied during this thesis a combination of scanning transmission electron microscopy (STEM) and electron energy loss spectroscopy (EELS) was performed on different heterostructures.

STEM is a technique consisting in focusing a beam of electrons using a set of electromagnetic lenses to a narrow point (typically less than a nm) and scanning it over an ultrathin sample. The electrons are detected on the other side of the sample (transmission geometry) and its image is reconstituted. The focusing of the electron beam allows the user to obtain z-contrast images with atomic resolution as well as specific spectroscopic information on the sample. This grants the STEM a greater space resolution than other electron microscopy techniques. A schematic representation of the technique is shown in Figure 2-8a. Standard preparation techniques consist in thinning samples by mechanical polishing and ion milling until they become electron transparent.

In order to increase the gathered signal, the experiments were performed using a high angle dark-field imaging (HAADF) technique where electrons that are scattered by the sample are collected by an annular detector. This detector allows to significantly increase the number of scattered electrons collected compared to the ones collected by a conventional objective aperture (usually used in conventional STEM). This also allows the main beam to be analysed using electron energy loss spectroscopy (EELS) at the same time.

EELS on the other hand, can be used to determine the chemical and electronic properties of the sample. By using an electron spectrometer, one can analyse the inelastic scattering occurring between the sample and the beam of electrons. This offers valuable information about nature of the sample such as its chemical composition, its electronic valence and conduction band information. One can also study the surface termination of thin films and element specific pair distance distribution functions. A typical STEM image obtained on a YBCO/PBCO/BFO heterostructure is shown in Figure 2-8b-c along with the corresponding EELS map obtained at different element absorption edges. The STEM image shows a high quality heterostructure growth where the interface between the different materials is clearly defined. The EELS line shapes allow us to track the different elemental compositions of the different layers as a function of depth.

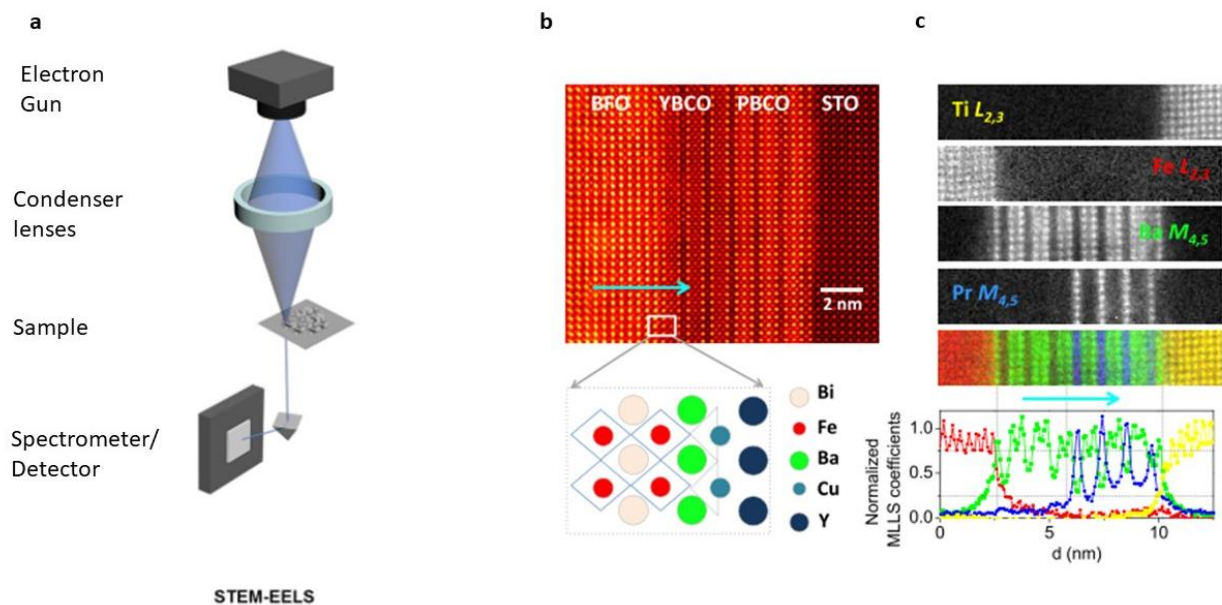


Figure 2-8: (a) Schematic representation of a STEM-EELS measurement. (b) High Resolution HAADF image of a BFO/YBCO/PBCO/STO sample and a sketch of the atomic stacking sequence at the interface. (c) EELS atomic resolution image across the stacking. From top to bottom: Ti  $L_{2,3}$ , Fe  $L_{2,3}$ , Ba  $M_{4,5}$ , and Pr  $M_{4,5}$  maps, along with an overlay of the Ti (yellow), Fe (red), Ba (green), and Pr (blue) signals taken from (Bégon-Lours et al., 2018).

## 2.8) Resonant Inelastic X-ray Scattering

X-ray absorption spectroscopy (XAS) is a technique used to probe in a non-destructive manner the electronic degrees of freedom of a material. If the energy of a photon incident on the sample corresponds to the binding energy of a core electron, this electron will get excited into an empty state above the Fermi level and subsequently detected. In this thesis we were interested in the Cu L3-edge corresponding to the promotion of a 2p core electron in the copper atom.

In contrast to XAS, resonant inelastic X-ray scattering (RIXS) is a photon in photon out technique that can be used to probe the occupied electronic states of a material. The term resonant holds for the fact that the energy of the incoming photon is chosen such that it corresponds with the absorption edge of a specific element thus allowing element specific analysis of various excitations. A photon is absorbed by the material, promotes a core electron to the valence band and creates a core hole. For the system to decay, an electron fills the empty core level and emits a photon at the same time. The energy and momentum of the outgoing photon are measured and used to gather information on the elementary excitations of the material. A scheme of the process is shown in Figure 2-9a. Figure 2-9b on the other hand shows the range of phenomena probed by RIXS. This technique allows to carefully probe a variety of different excitations. Electronic phenomena such as d-d excitations and charge transfer were of particular interest for this thesis.

The measurements were performed at the synchrotron SOLEIL on the SEXTANT beamline using soft X-rays typically in the range of 930eV (close to Cu L-edge). The maximum resolution reached was of the order of 350meV after optimization. The beam size was  $80 \times 2 \mu\text{m}^2$  on the sample surface. No explicit ageing due to the X-ray beam was observed. RIXS measurements were performed at a temperature of 100K before and after illumination with a UV/blue light.

Figure 2-9c shows a typical RIXS spectra obtained on an oxygen deficient YBCO thin film at an incident photon energy of 933.8eV. The peak features in the graph are attributed to d-d excitations and fluorescent phenomena.

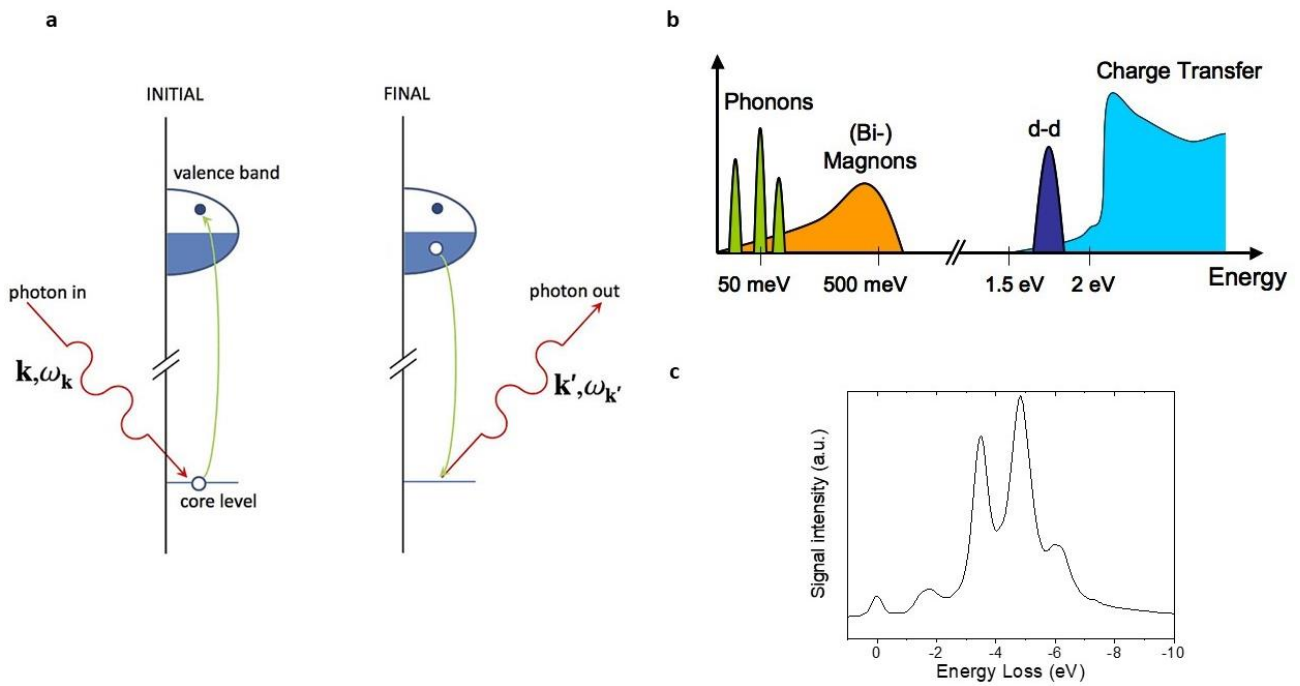


Figure 2-9: (a) Schematic of the processes involved in a RIXS measurement. Adapted from (Ament et al., 2011). (b) Energy scales probed by a RIXS measurement(right). The range around 1.5-2eV is of significant interest in this thesis. Adapted from (Ament et al., 2011). (c) Typical RIXS spectra obtained on oxygen deficient YBCO thin film at an incident energy of 933.8eV.

## 2.9) Nanofabrication

To allow for a well-defined measurement geometry, thin films have been patterned by standard photolithography processes. The samples studied in this work can be separated into two categories: thin films and vertical junctions. In this section we will present generalities concerning the patterning processes then detail the recipes we followed for both categories of samples.

- Illumination:

A mask displaying the target design is deposited on top of the sample in a mask aligner. Note that this step requires careful alignment of the mask on the sample to guarantee the design integrity. The resist that is not covered by the mask will then be exposed to UV light. This process will polymerize the resist rendering it soluble in a developer. By introducing the sample in a developer, the sections of the resist not covered by the mask will dissolve revealing the film underneath it.

- Etching:

In this thesis the YBCO thin films were etched in a Hall bridge pattern in order to accurately measure their properties. Because of the sensitive nature of the oxygen deficient YBCO a wet etching process was chosen to design the bridge. Resist is deposited on top of the film and designed in the shape of the Hall bridge by standard illumination and development. The sample is then introduced in diluted phosphoric acid  $\text{H}_3\text{PO}_4$  which will etch the sections of the film not covered by the resist. The process is stopped when the desired thickness of the film is reached. The process is shown in Figure 2-10a. Note however that the etching process is isotropic meaning the acid will etch the film in all directions once it comes in contact with it. In order to ensure the integrity of the design the adequate acid dilution which will effectively define the etching speed has to be sought. This process depends on the thickness of the film and on the chosen acid.

- Lift off:

A lift off process can be used in order to deposit a metal in a specific shape or area on a sample. A layer of resist is deposited on the sample and the design of the metal part is inscribed into the resist layer effectively opening a hole in it. The metal is then deposited over the whole surface of the sample. The next step consists in introducing the sample in a bath of acetone that will dissolve the resist still present on the sample. The metallic film that was on top of the resist will then be lifted leaving only the parts that were deposited directly on the film. The process is shown in Figure 2-10b.

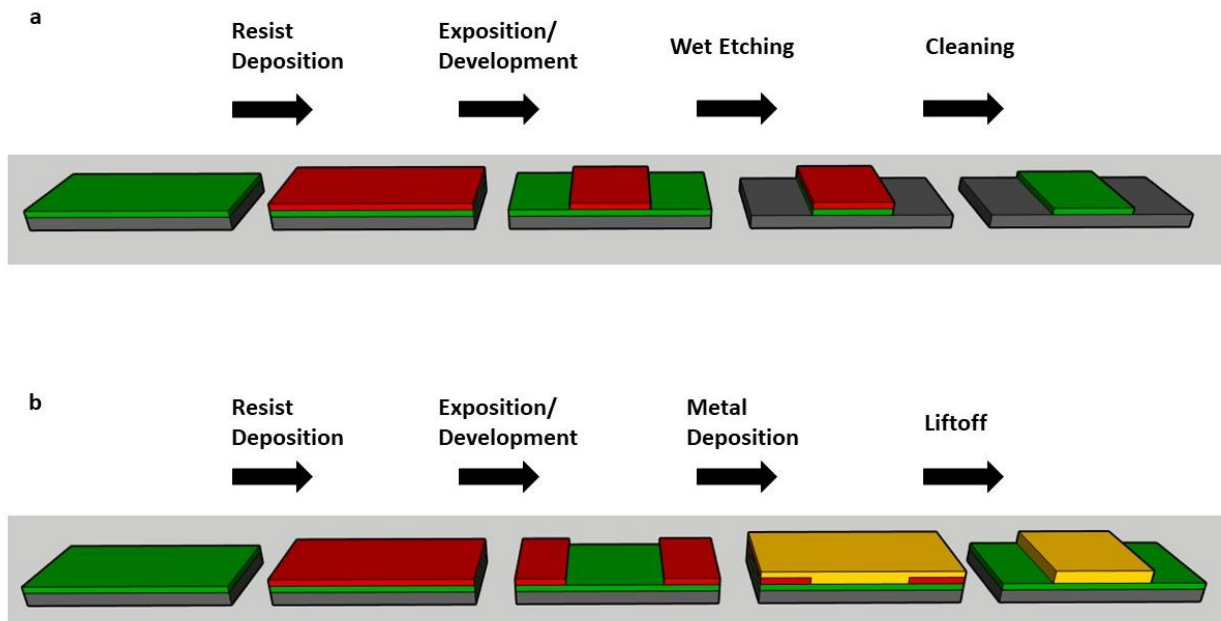


Figure 2-10: Schematic representation of two lithography processes: (a) Film Etching, (b) Liftoff

In the next section we will detail the recipes for the different samples we studied in this thesis.

### 2.9.1) Vertical junctions:

Vertical junctions have been designed to study electrical transport at the interface in oxide heterostructures. The bottom electrode is deposited prior to the lithography step by PLD on a substrate. A hard-baked layer of resist with small square openings ( $10\text{-}200\ \mu\text{m}^2$ ) defines the various junctions. The top electrode is deposited by sputtering on top of the opening thus filling it and assuring continuity in the device. Figure 2-11a displays a schematic representation of the vertical junction's architecture studied in this thesis. Throughout the thesis the design of these junctions remained unchanged. The pictures shown in Figure 2-11b-c illustrate MoSi/BFO/YBCO vertical junctions shown from the top under a microscope.

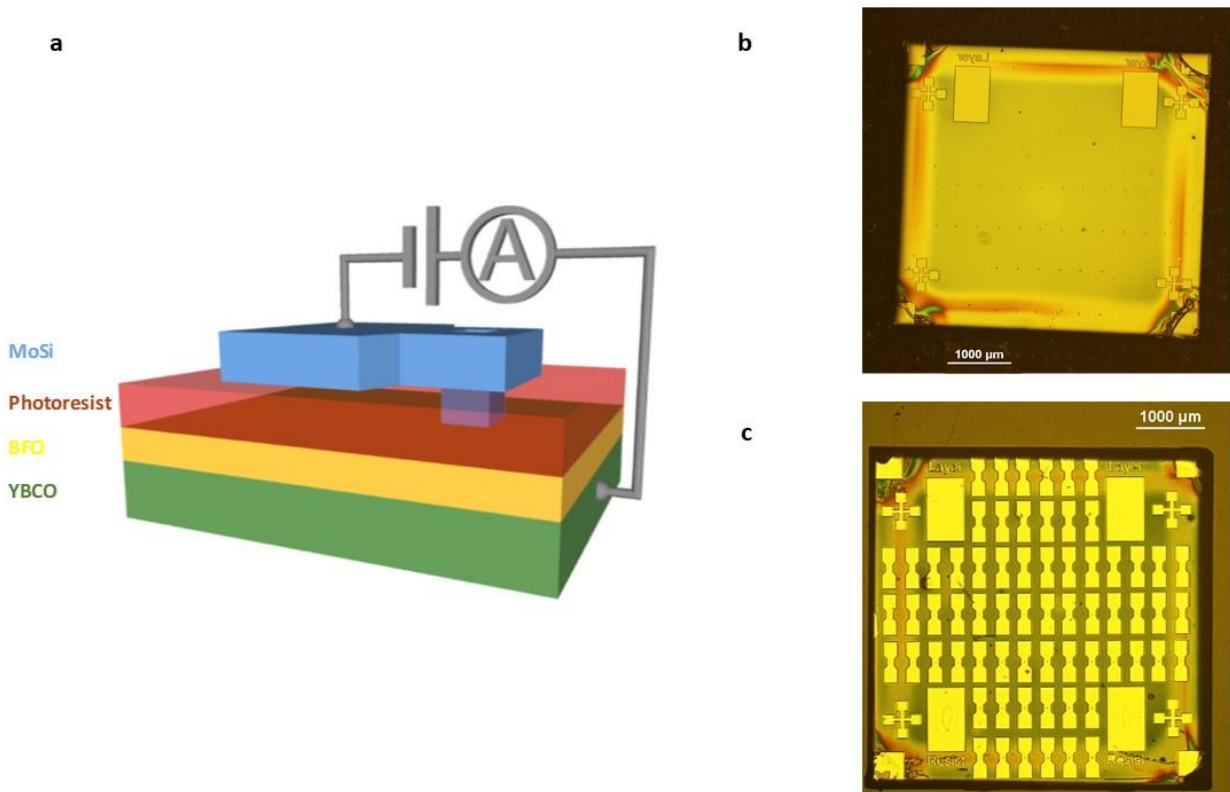


Figure 2-11: (a) Scheme of the vertical junctions used for transport measurements. Note in some samples labelled YBCO/ITO the BFO layer is removed and the top MoSi layer is replaced by a layer of ITO. Pictures showing a 5x5 mm sample (b) after step 1 and (c) after step 2 showing multiple vertical junctions.

The detailed recipe goes as follows:

#### Step 1

- The samples surface is first cleaned by rinsing them with standard solvents such as acetone and isopropanol. If the cleaning process requires it, one can use a pressurised flow of solvent or lightly brush the surface with an imbibed piece of fabric. To desorb any residual material on the surface the sample is dried at a temperature of 90°C for about 1 minute.
- A primer is deposited on the surface and then spin coated at 4000rpm for 60 seconds. This primer will allow a better wetting of the surface by the first resist.
- A first resist – SU1850 diluted at 50% in a solvent – is deposited on the surface and then spin coated at 4000rpm for 60 seconds.
- The resist is soft baked by drying it at a temperature of 90°C for 60 seconds.
- The sample is then illuminated with 60mJ of UV light to define a matrix of holes with multiple areas.
- The resist is developed by introducing the sample in a developer (MF310) for 20 seconds before rinsing it with deionized water and drying it with N<sub>2</sub> gas.
- The resist is rendered permanent by heating up the sample to a temperature of 180°C for 60 seconds (hard bake). The first layer of resist is now immune to illumination, developing and lift off processes.

## Step 2

- A second layer of resist (SPR 700 1.2) is deposited and then spin coated at 6000 rpm for 60 seconds.
- The resist is soft baked by drying it at a temperature of 90°C for 60 seconds.
- The resist is hardened by introducing the sample in chlorobenzene for 10 minutes before rinsing it with deionized water and drying it with N<sub>2</sub> gas. This step allows for a cleaner and simpler lift off process.
- The sample is illuminated with 100mJ of UV light to define the electrical pads.
- The resist is developed by introducing the sample in a developer (MF310) for 20 seconds before rinsing it with deionized water and drying it with N<sub>2</sub> gas.
- A soft O<sub>2</sub> plasma is used to eliminate any resist residue on the film surface (in the hole created by the first layer of resist).
- The metal is deposited by sputtering at room temperature.
- A lift off step is performed by introducing the sample in a beaker of acetone, waiting for 20 minutes and submitting the sample to a pressurized flow of acetone until the metal has lifted. Clean the sample in propanol and then dry it with N<sub>2</sub> gas.

### 2.9.2) YBCO Thin Films:

In order to accurately characterize the electrical transport of YBCO thin films we chose to pattern them into a standard Hall bridge. A 4x0.3mm rectangular slab defines the YBCO bridge where multiple voltage pads have been added on both sides. Note that the smallest length on these voltage pads is 15μm wide to minimize misalignment induced errors and maximize the accuracy of our measurements. A Gold (Au) thermometer is deposited by sputtering next to the YBCO bridge to serve as a makeshift thermometer. The reasons behind the necessity of this step are detailed in the section 2.11). Figure 2-12a illustrates the design of an oxygen deficient YBCO thin film under a microscope. Figure 2-12b shows a schematic representation of the geometry necessary to conduct the transport measurements on oxygen deficient YBCO films.

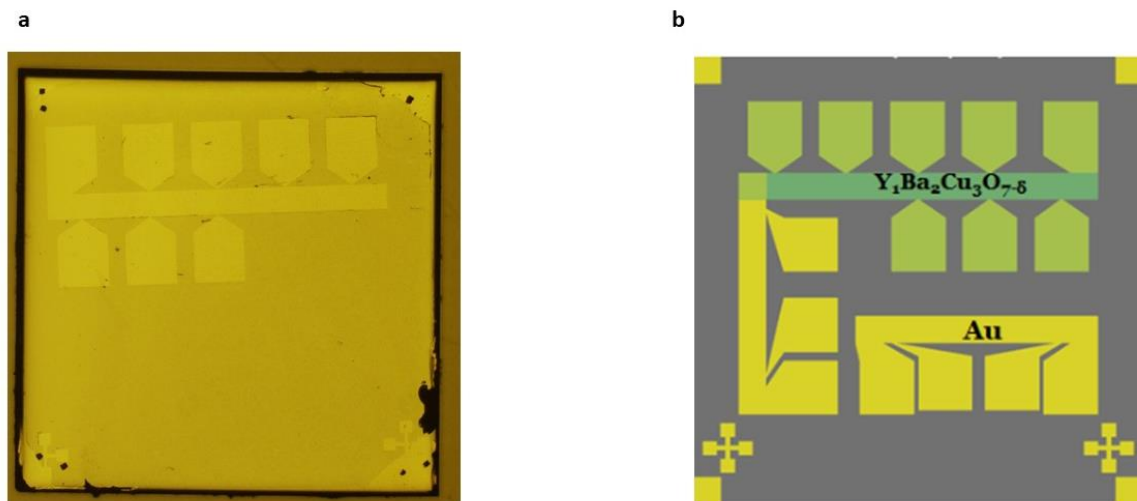


Figure 2-12: (a) YBCO bridge picture taken before the step 2 (b) Scheme of the final design used for transport film measurements.

The detailed recipe goes as follows:

## Step 1

- The samples surface is first cleaned by rinsing them with standard solvents such as acetone and isopropanol. If the cleaning process requires it, one can use a pressurised flow of solvent or lightly brush the surface with an imbibed piece of fabric. To desorb any residual material on the surface the sample is dried at a temperature of 60°C for about 1 minute. Note that throughout the process the temperature of the sample should not exceed 60°C.
- A layer of resist (SPR 700 1.2) is deposited and then spin coated at 6000 rpm for 60 seconds.
- The resist is soft baked by drying it at a temperature of 60°C for 60 seconds.
- The sample is illuminated with 100mJ of UV light to define the Hall bridge.
- The resist is developed by introducing the sample in a developer (MF310) for 20 seconds before rinsing it with deionized water and drying it with N<sub>2</sub> gas.
- The film is etched by introducing the sample in diluted phosphoric acid H<sub>3</sub>PO<sub>4</sub> (1/100 dilution) for 2-3 seconds then rinsing it in deionized water and drying it with N<sub>2</sub> gas.
- The remaining resist is cleaned by rinsing it in acetone and isopropanol before drying with N<sub>2</sub> gas.

## Step 2

- A layer of resist (SPR 700 1.2) is deposited and then spin coated at 6000 rpm for 60 seconds.
- The resist is soft baked by drying it at a temperature of 60°C for 60 seconds.
- The sample is illuminated with 100mJ of UV light to define the electrical pads and the thermometer.
- The resist is developed by introducing the sample in a developer (MF310) for 20 seconds before rinsing it with deionized water and drying it with N<sub>2</sub> gas.
- A soft O<sub>2</sub> plasma is used to eliminate any resist residue on the film and substrate surfaces.
- The Gold layer is deposited by sputtering at room temperature.

A lift off step is performed by introducing the sample in a beaker of acetone, waiting for 20 minutes and submitting the sample to a pressurized flow of acetone until the metal has lifted. Clean the sample in propanol and then dry it with N<sub>2</sub> gas.

## 2.10) Transport

### 2.10.1) Cryostation and sample preparation

The transport measurements performed during this thesis took place in a Montana cryostation. It is an optical closed cycle Gifford-McMahon 2-stage-cryocooler accompanied by its compressor that controls the flow of Helium gas. The sample chamber is equipped with a radiation shield allowing the base temperature of the chamber to reach 3.2K and optical windows facing multiple directions effectively allowing illumination measurements in multiple configurations. An electromagnet can be mounted in the chamber to apply magnetic fields reaching up to 0.7 T. It also achieves good mechanical and thermal stability.

The samples were mounted on a sample holder specifically designed for the Montana cryostation. The substrate was glued on the holder using silver paste and drops of Apiezon thermal grease were added on the edges of the sample to ensure maximum thermal contact between the holder and the sample. The sample was contacted using a K&S4523AD wedge bonding equipment with Aluminium or Gold wires.

Due to physical constraints and in order to measure Hall effect under illumination, the sample was placed at a defined angle of 45° between the applied magnetic field and the illumination (see Figure 2-13). This allowed us to apply an out of plane magnetic field on the YBCO bridge while allowing a significant number of photons to reach it. Solely the perpendicular component of the magnetic field was considered in the analysis of the Hall effect data.

It might be of interest to the reader to note that the use of Aluminium wires to bond YBCO films is discouraged. We have observed a gradual increase of the contact resistance at the Al/YBCO interface. We suspect the Al wire to react with the YBCO creating an insulating shell at the interface thus reducing the quality of the electrical contact.

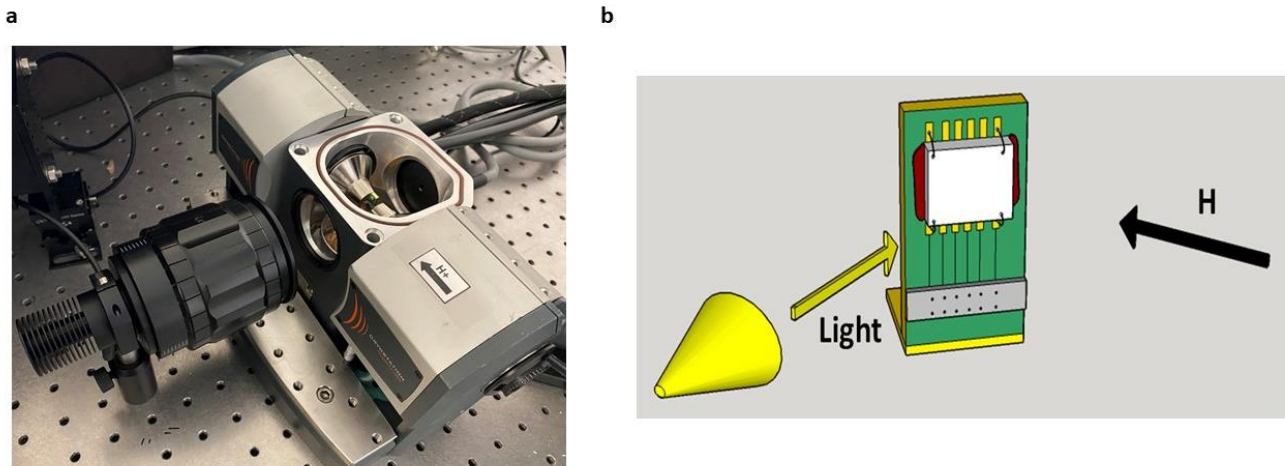


Figure 2-13: (a) Picture of the MONTANA cryostat (b) Schematic representation of geometrical setting of the illumination experiments on YBCO films.

### 2.10.2) Temperature Calibration

As will be explained in section 2.11), we used a gold bar deposited on the substrate next to the YBCO bridge to accurately follow changes in sample temperature. We calibrated the resistance measured across the gold bar  $R_{Au}$  to the temperature measured by the cryostat thermometer during the first cool down (corresponding to the sample's first temperature cycle). We then continuously measured the  $R_{Au}$  and used it as a measure of the actual sample temperature c.f. Figure 2-14.

### 2.10.3) Transport measurements

Standard 4-point measurements were performed to calculate the longitudinal resistivity. A fixed value of current is applied by a Keithley 6221 current source and the accompanied voltage drop is measured between successive voltage pads with a Keithley 2182 nanovoltmeter as is shown in Figure 2-14a. A current inversion technique was used to subtract the thermoelectric contribution from the calculated resistance. It naively consists in reversing the direction of the applied current and subtracting the measured voltages from one another. The thermoelectric offset is pair with respect to current inversion. The resistance of the film is then given by:

$$R = \frac{V_{I+} - V_{I-}}{2|I|} \quad 10$$

### 2.10.4) Superconducting Critical Temperature

One of the parameters of interest in this thesis is the evolution of the superconducting critical temperature in different sets of superconducting samples. To ensure the validity of the comparison

between the measured critical temperatures we established the peak in the first temperature derivative of the resistance as the criterion to define  $T_c$  (see Figure 2-14d).

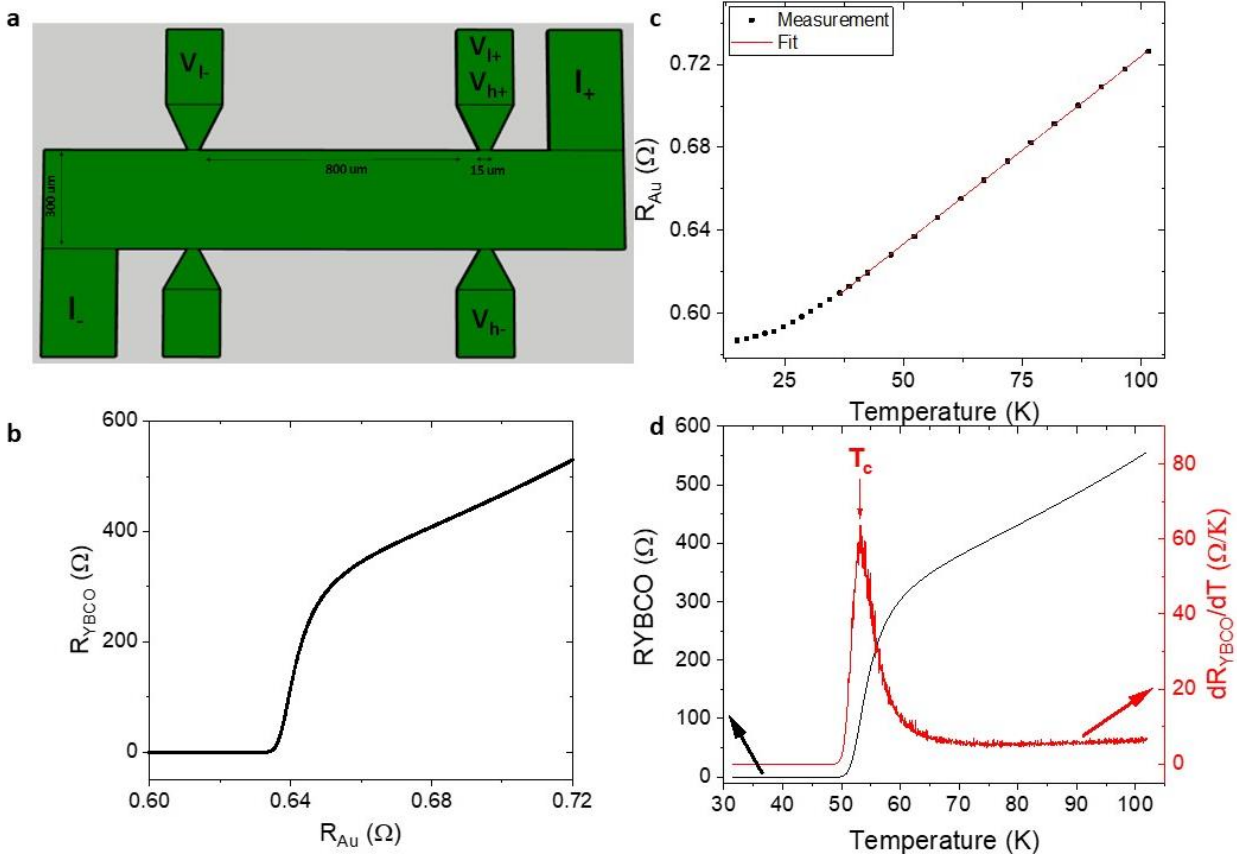


Figure 2-14: (a) Schematic of a YBCO bridge used for transport measurements.  $V_{l\pm}$  are the longitudinal voltage pads,  $V_{h\pm}$  are the transverse voltage pads and  $I_{\pm}$  are the current pads. Both the longitudinal and the transverse voltages are recorded at the same time. (b) Resistance measured across an oxygen deficient YBCO bridge as a function of the resistance measured across an Au bar during a heat up process (c) Temperature dependence of the resistance measured across the Au bar during a heat up process (d) Temperature dependence of the resistance measured across the oxygen deficient YBCO bridge. The right axis shows the first derivative of the resistance with respect to the temperature, used to define the superconducting critical temperature of the film.

### 2.10.5) Hall effect

The ordinary Hall effect is measured by applying a fixed current and measuring the transverse voltage drop across two voltage pads on two different sides of the bridge as is shown in Figure 2-14a. The main issue with this measurement is that the measured transverse voltage is the sum of the Hall voltage and of other several offset voltages. Two main techniques were employed to subtract these offset voltages from the measurement: The current inversion technique and the field inversion technique. By reversing the direction of the magnetic field, we can subtract the misalignment contributions to the measured voltages.

The measured Hall resistance is thus given by:

$$R_{Hall} = \frac{(V_{I+}(H) - V_{I-}(H)) - (V_{I+}(-H) - V_{I-}(-H))}{4|I|} = \frac{R(H) - R(-H)}{2}$$

Where  $R_{Hall}$  denotes the measured Hall resistance in  $[\Omega]$ . Figure 2-15b represents the magnetic field dependence of the transverse resistance. By applying a field inversion technique we obtain the graph shown in Figure 2-15c. Note that an ordinary Hall effect analysis is enough to analyse YBCO thin films since the measured Hall resistance is linear in both  $I$  and  $B$  as is shown in Figure 2-15a-c-d.

In order to extract the Hall coefficient  $R_H$  in  $[\text{m}^3 \cdot \text{C}^{-1}]$  and the carrier density  $n$  in  $[\text{m}^{-3}]$  from a Hall effect measurement, the measured resistance is plotted as a function of the applied magnetic field. The data points are fitted to a linear function whose slope is extracted.

We then obtain:

$$n = \frac{1}{R_H * e} = \frac{1}{\text{slope} * t * e}$$

Where  $R_H$  is the Hall coefficient,  $t$  is the sample thickness and  $e$  is the electric charge. The measurement is performed multiple times and the extracted parameters are averaged over the whole set of measurements.

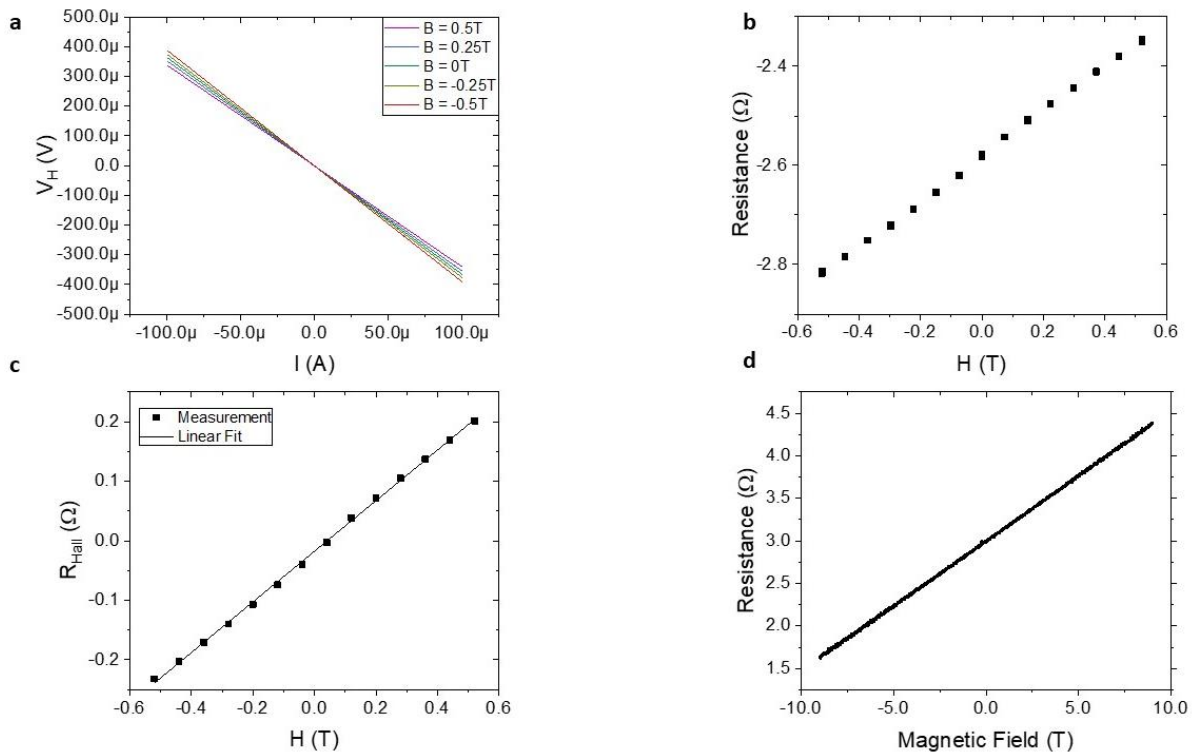


Figure 2-15: (a) Transverse voltage as a function of current in a YBCO bridge for different *magnetic fields* (b) *Magnetic field dependence of the transverse resistance measured across an oxygen deficient YBCO film* (c) *Magnetic field dependence of the Hall resistance measured across an oxygen deficient YBCO film* (d) *Hall effect measurement of a YBCO film under a magnetic field reaching up to 9T.*

### 2.10.6) Mobility and Hall angle

In a simple Drude model, the mobility expressed in  $[\text{m} \cdot (\text{V} \cdot \text{s})^{-1}]$  can be deduced from resistivity and Hall effect measurements following the formula:

$$\mu = \frac{R_H}{\rho_{xx}}$$

where  $R_H$  is the Hall coefficient and  $\rho_{xx}$  is the longitudinal resistivity.

The Hall angle can be expressed as:

$$\cot \theta_H = \frac{\rho_{xx}}{R_H * B}$$

It represents the ratio between the longitudinal and the transverse voltages under the action of a magnetic field.

### 2.10.7) Vertical junctions

Most of the transport measurements on the vertical junctions were performed using a Keithley Sourcemeter 2450. First of all, a poling voltage  $V_{pol}$  is applied on the junction (typically a few volts) to polarize it while measuring the current going through it.  $I$  vs  $V$  characteristics are measured by applying a bias voltage  $V_{bias}$  (typically reaching 200mV) and measuring the current flowing through the junction. The measured current is then differentiated with respect to the applied voltage to obtain the differential conductance spectra (c.f. Figure 2-16).

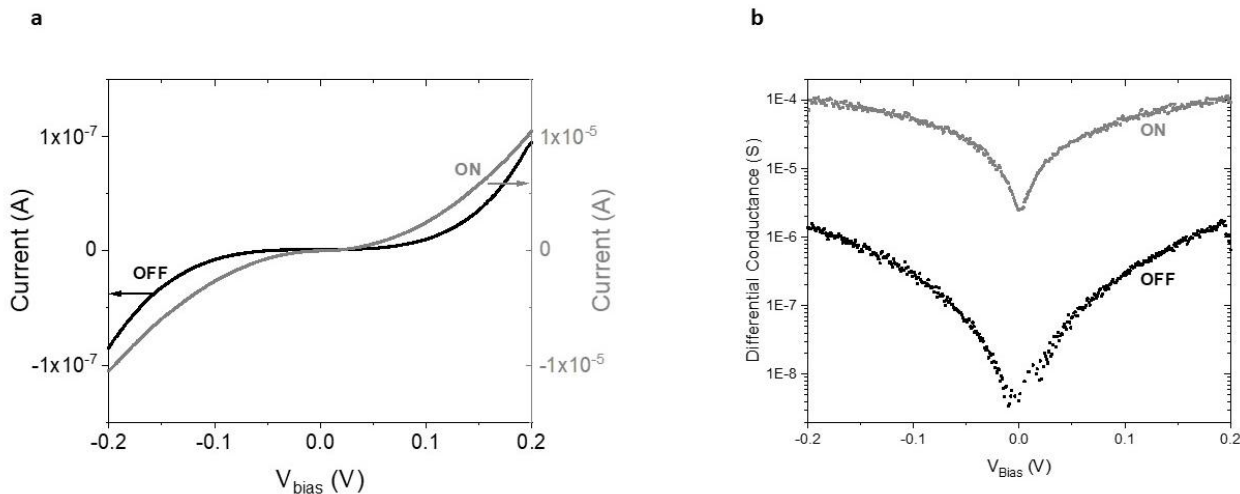


Figure 2-16: (a) Bias voltage dependence of the current measured across an YBCO/ITO junction (b) Bias voltage dependence of the differential obtained by differentiating the curves in (a). The two curves indicate the existence of an ON and OFF state.

The poling voltages were applied in ramps from 0V to  $V_{pol}$  and back to 0V. Unless otherwise stated the top electrode is grounded and the poling and bias voltages are applied on the bottom electrode.

Most of our junctions are characterized by high resistances compared to the “Contact Resistance” allowing us to mostly perform 2-point measurements on them.

## 2.11) Illumination

During this thesis we study the effects of various light sources on our samples. These sources differed in the maximum irradiance it could reach and in their wavelength distributions. Solely non-coherent light sources were used to limit the amount of losses due to misalignment and the tedious alignment procedures needed to reach maximum power.

### 2.11.1) Sources

The different sources are the following:

- 1) Several high-power LEDs emitting at various wavelength from the near UV region (300 nm) to the near IR region (800nm). These LEDs were connected to LED driver allowing to control the current applied to it. The irradiance of these light sources varied from  $10 \text{ mW} \cdot \text{cm}^{-2}$  to  $1 \text{ W} \cdot \text{cm}^{-2}$ . A set of collimating optics was connected to the LED output to collimate the beam towards the sample and thus reduce the losses due to a finite viewing angle. These LEDs were mounted on heat sinks to dissipate heat generated during operation thus granting the LED good thermal stability. Figure 2-17a.

- 2) The MSH-300F monochromator system connected to a Xe arc lamp source from LOT QD. A condenser optic and a set of adjusting lenses were added between the monochromator entrance slit and the arc light source output to align the beam light between the two fixed points and thus decrease misalignment losses. An optical fibre was mounted on the exit slit of the monochromator to allow the light to travel unimpeded until it reaches its target. This system allows for a wavelength average accuracy of 5 nm. The irradiance at the output of the optical fibre is of the order of a couple  $mW.cm^{-2}$ . A trade-off between the accuracy of the wavelength used and the irradiance could be achieved by changing the monochromator exit slit opening. Refer to Figure 2-17b.
- 3) A Halogen lamp with an adjustable output irradiance between two fixed values of  $50mW/cm^2$  or  $100mW/cm^2$ . This halogen light emitted over a wide range of wavelength going from the near ultraviolet (UV) to the near infrared (IR) thus creating a beam of white light. An accessory optical fibre was connected to the output of the lamp allowing the light to travel unimpeded until it reaches its target. Refer Figure 2-17c.
- 4) A Xe arc light source connected to beam turning assembly with dichroic mirror allowing us to select by reflecting all the photons whose wavelength fall within a wide band (260 - 320 nm) and discard the others. A set of adjusting optics allows to control the output irradiance by changing the amount of losses due to misalignment between the different parts of the system. Typical irradiance of  $100 mW.cm^{-2}$  was reached on this system. An optical fibre was mounted on the next to the beam turning assembly to allow the light to travel unimpeded until it reaches its target. Refer to Figure 2-17d.

In order to compare the photo-induced effects caused by illumination by different light sources we performed irradiance measurements to obtain a wavelength independent measure of the photon density incident on the sample. We used a thermal power sensor with a wavelength sensitivity covering a range starting at the near infrared and reaching the near ultraviolet with an optical power ranging from 0.1mW to 5W.

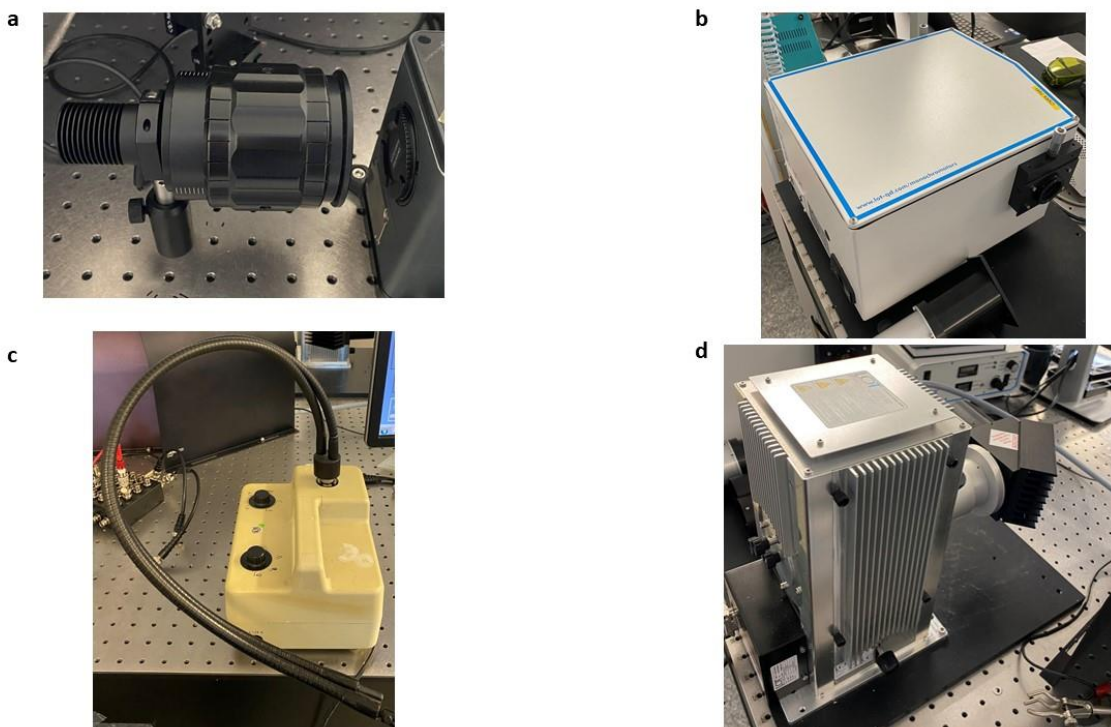


Figure 2-17: (a) Picture of a high power monochromatic LED assembled to its heat dump and collimator optics (b) Picture of the monochromator MSH-300F (c) Picture of the Halogen lamp with an optical fiber connected to the output (d) Picture of the Xe arc lamp connected to the beam turner assembly with dichroic mirror.

### 2.11.2) Heating

A common consequence of illumination is thermal heating. When photons incident on the sample are absorbed, some of the excess energy obtained is released in the form of heat causing the sample properties to change due to local changes in temperature. The process of illumination might also affect the sample environment such as the cryostat or the electrical contacts which might in turn affect the sample properties. These thermal changes in the sample properties might be erroneously interpreted as non-trivial electronic, phononic or structural processes if care is not taken to distinguish them from one another.

In this section we will describe how light induced heating might affect the various electrical properties of different samples and state what steps were taken in order to distinguish between nontrivial photo-induced changes and common heating induced changes.

Since most of the photo-induced effects studied in this work are persistent i.e. the changes in the sample properties caused by light remain constant even when the light is turned off, the first step we implemented was to perform measurements in dark after allowing the sample to be illuminated for a certain amount of time. The changes we then observe in the sample could not be caused by light induced heating since these relax rather quickly (typically a minute or two in our cryostat). However, this step does not allow us to eliminate changes caused by light on the sample environment.

For example, Figure 2-18a shows the temperature evolution (as measured by the cryostat thermometer situated on the cold finger) of the resistance of an oxygen deficient YBCO thin film after illumination. Figure 2-18b on the other hand shows the resistance measured across the YBCO as a function of the resistance measured across the Au bar. Note the change in the behaviour of the successive temperature cycles when plotted as a function of the cryostat temperature and the gold

resistance. This effect was attributed to a thermal lagging experienced by the cryostat thermometer caused by intense light illumination for long periods of time.

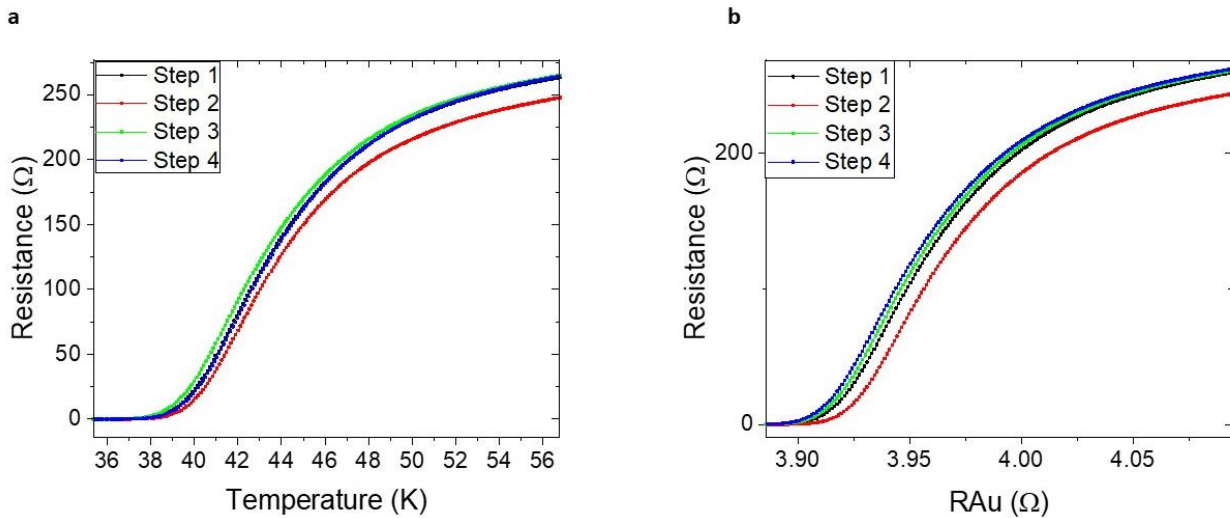


Figure 2-18 : (a) Temperature dependence of the resistance measured across an oxygen deficient YBCO bridge during successive temperature cycles labelled Step 1-4 in dark. (b) Resistance measured across the same YBCO bridge as a function of the resistance measured across the Au bar.

In order to accurately measure the sample temperature independently of how much itself and its environment are affected by the measurement procedure we decided to continuously measure the resistance across a gold bridge deposited on the sample substrate. Any resistance change measured across the Au bridge would have to be caused by a change in temperature experienced by both the Au and YBCO. This would allow us to distinguish between common heating induced changes and non-trivial photo-induced ones in the properties of YBCO.

This can be seen in Figure 2-19, showing the time dependence of the longitudinal resistance across the YBCO bridge and the one across measured across the Au bridge during illumination. As one can clearly see the initial increase in the resistance of the YBCO bridge is due to heating while the subsequent gradual decrease is clearly not.

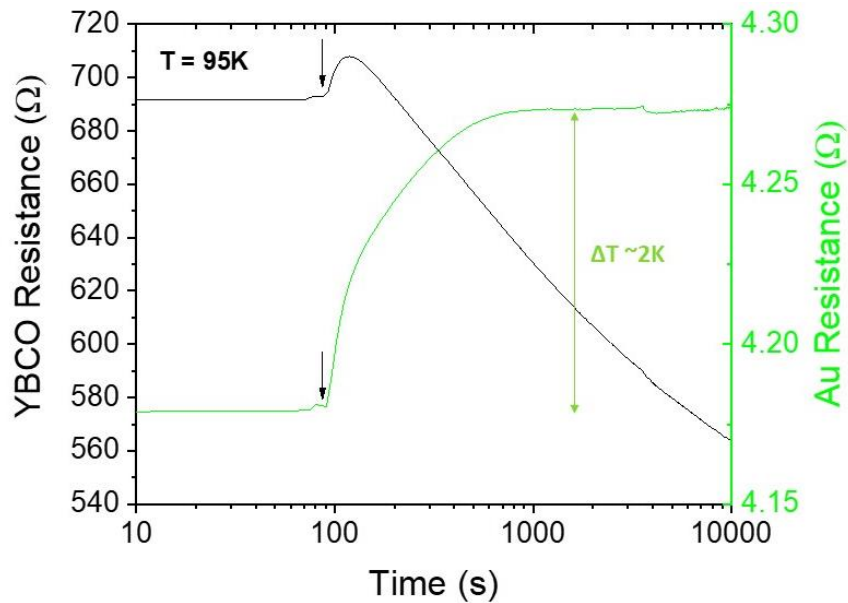
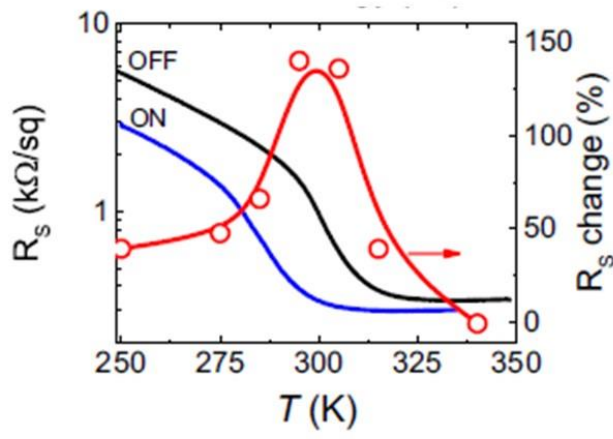


Figure 2-19: Time dependence of the resistance measured simultaneously across a YBCO bridge (black) and an Au bridge (green) during white light illumination at a temperature of 95K.

Figure 2-20 shows another example of the heating effect that usually accompanies illumination. These graphs are taken from (Liao *et al.*, 2018) and show the photo-induced effects on nickelate thin films whose metal-to-insulator transition has been tuned to lie around room temperature through the action of a tilt modulation layer, that is by acting on the bond angles. By fine tuning the MIT such that it approximately reaches room temperature it is possible to exploit the thermal effect of an illumination to trigger important electrical responses of the film. The graph on left shows the temperature dependence of the sheet resistance in dark and under illumination by visible light. On the right axis the sheet resistance change is shown as a function of temperature. This significant change in resistance however is due to a heating effect on the sample causing the measured temperature to be underestimated.

a



b

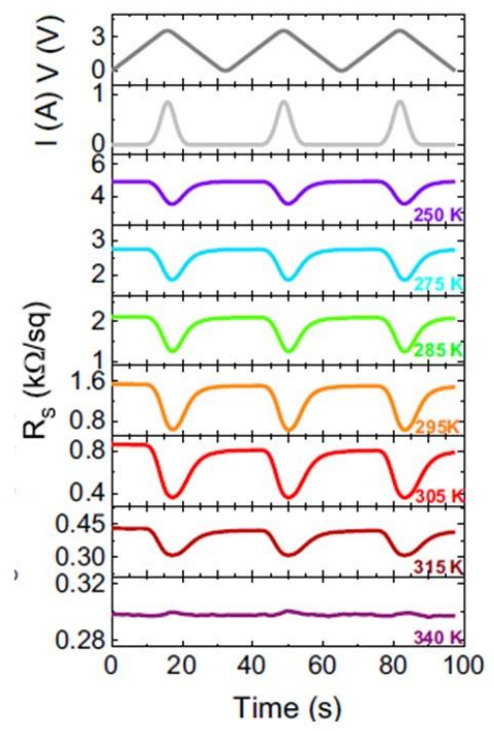


Figure 2-20: (a) Temperature dependence of the sheet resistance of a nickelate film before and during illumination with a LED (left axis) and relative photo-induced resistance of the film (right axis) (b) (Top) Voltage and current applied on the LED to illuminate the film. (Bottom) Time dependence of the resistance evolution of a nickelate film during illumination at different temperatures. Adapted from (Liao et al., 2018).

This can also be seen on the graph on the right showing the time dependence of the sheet resistance in dark and under illumination at different temperatures. The measured changes in the resistance are due to changes in the sample temperature by simple heating. The magnitude of the effect changes as a function of temperature because the response of the cryostat to external stimuli such as intense illumination differs for different temperatures and tends to be smallest around room temperature.

### 3) Photo-induced effects on $YBa_2Cu_3O_{7-\delta}$ films

#### Contents

3) Photo-induced effects on $YBa_2Cu_3O_{7-\delta}$ films.....	77
3.1) Motivation & key findings.....	78
3.2) Sample description .....	78
3.2.1) Oxygen deficient YBCO films.....	78
3.2.2) Ion Irradiated YBCO films.....	79
3.2.3) Comparison between the two sets of samples.....	80
3.3) Correlation between carrier density, carrier mobility and superconducting critical temperature.....	81
3.4) Temperature behaviour .....	81
3.5) Visible/UV light illumination .....	81
3.5.1) Basic effect.....	83
3.5.2) Dependence on irradiance.....	97
3.5.3) Doping dependence .....	97
3.6) Spectral dependence .....	99
3.7) Illumination of oxygen deficient vs ion irradiated samples .....	100
3.8) Summary .....	102
3.9) Relaxation .....	102
3.10) Resonant Inelastic Xray Scattering.....	105
3.11) Concluding remarks .....	107

### 3.1) Motivation & key findings

Transition metal oxides are characterized by an extremely rich phase diagram where a multitude of phases coexist in proximity to one another. For example, Figure 3-1 shows the typical phase diagram of a cuprate: YBCO. The parent phase of this material is an antiferromagnetic Mott insulator and by increasing the carrier density or doping the material exhibits different exotic phases such as pseudogap, high  $T_c$  superconductivity, strange metal and Fermi liquid (Keimer *et al.*, 2015). The complexity of this phase diagram reveals the intricacy of the mechanisms responsible for the appearance of these different phases. It is possible to explore it by using external stimuli such as electric fields (Crassous *et al.*, 2011), or light.

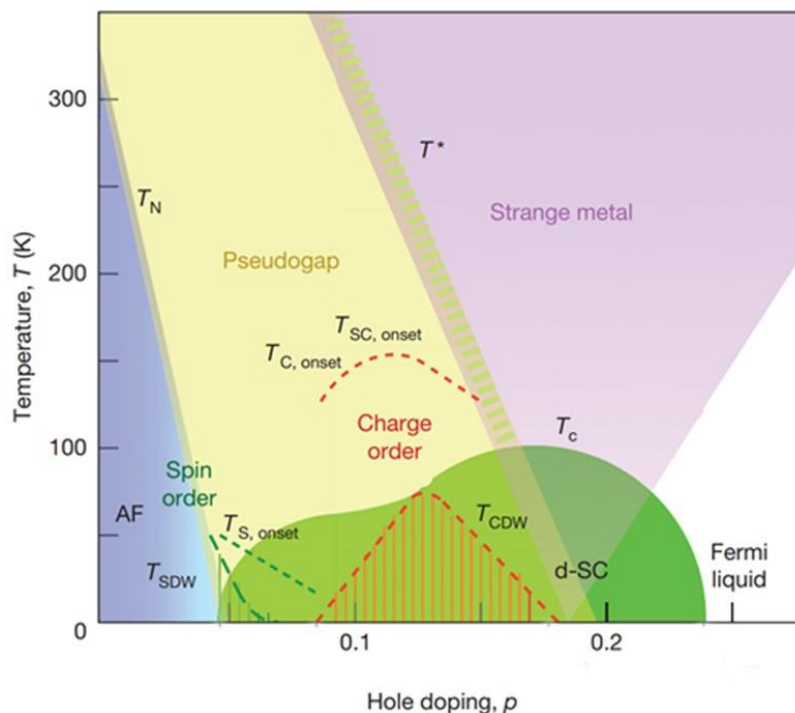


Figure 3-1: Typical temperature vs doping phase diagram of a cuprate oxide. The coexistence of multiple phases in competition with one another is visible. Adapted from (Keimer *et al.*, 2015)

In this chapter we investigate the changes in the electrical properties of YBCO thin films caused by visible and UV light illumination. This approach is based on the investigation of photo-induced changes in underdoped cuprates (Kudinov *et al.*, 1990) (Gilabert *et al.*, 2000) (Nieva *et al.*, 1992). Those experiments showed that, upon UV or visible light illumination, underdoped cuprate films show an increase of the charge carrier density, which is accompanied by an enhancement of its electrical and superconducting properties. These changes are consistent with a shift to the right on the cuprate phase diagram showed in Figure 1. However, a clear picture of photo-induced changes in cuprates has not emerged yet since the microscopic mechanisms behind the effect are still under debate. The two main scenarios are presented below:

1. A charge-transfer model where an electron-hole pair is created when a photon is absorbed by the material. The electron is trapped and the hole can participate to the conduction in the material. The traps can take the form of oxygen vacancies (Kudinov *et al.*, 1993) or pieces of CuO chain (Kudinov, 1994). As the hole density increases, this leads to an increase in the superconducting critical temperature.
2. A model based on the photo-assisted oxygen ordering in the CuO chains of the YBCO structure. The absorbed photon participates in a reordering of oxygen atoms in the structure such that

the average length of CuO chains increases (Osquiguil *et al.*, 1994)(Kudinov *et al.*, 1993). This affects the effective hole density in the CuO<sub>2</sub> planes and as such the superconducting critical temperature (Gauquelin *et al.*, 2014)(Ceder *et al.*, 1990)

The main objective of this part of the thesis was twofold. On the one hand, we characterised the illumination effects on our YBCO films, which is a pre-requisite before the more complex experiments described in Chapter 5) can be conducted and interpreted. On the other hand, we aim at contributing to the long-standing, unsettled debate on the origin of photo-induced effect in cuprates, via an original approach: comparing the effects of light illumination on oxygen deficient YBCO films with the effects on fully oxygenated films in which disorder (point defects) is introduced in a controlled manner.

Thus, light illumination experiments were performed on two sets of YBCO films: oxygen deficient samples and O<sup>+</sup> ion irradiated samples at high-energy (100keV) and variable fluence. We have observed that all the films exhibit a persistent photo-induced increase of the carrier concentration and a decrease of the normal-state resistivity. However, only oxygen deficient samples show changes in T<sub>c</sub>, when illuminated with UV or visible light, which is accompanied by an increase of the carrier mobility. The key finding is that, **contrary to what was expected from earlier work** (Keimer *et al.*, 2015)(Lee, Nagaosa and Wen, 2006), **the photo-induced changes measured in the superconducting critical temperature correlate with changes in the mobility of charge carriers rather than their density. This strongly supports the claim that light illumination produces structural changes, and that changes in the critical temperature cannot be explained based only on photo-doping. As will be discussed, this is further evidenced by the striking observation that the relaxation of photo-induced changes in the carrier density and mobility occur over different temperatures and time scales.**

The chapter is divided as follows. The first part of the chapter will be dedicated to the description of the sample properties. The heart of the chapter will start by a description of the photo-induced effect on both sets of samples before a comparison between the different types of illumination. The third part of the chapter will be dedicated to the relaxation of the photo-induced effects. We will then detail the preliminary resonant inelastic X-ray scattering (RIXS) measurements we performed on oxygen deficient YBCO samples. Finally, in the light of the previously drawn conclusions a hypothesis for the mechanism behind the observed photo-induced changes will be attempted before concluding the chapter.

### 3.2) Sample description

In order to understand the origin of photo-induced changes in YBCO films, two differently prepared sets of samples will be compared: an oxygen deficient set and an ion irradiated set. We will show that, although the processes used to obtain these samples are very different, they exhibit similar changes in properties making a comparison between both sets interesting.

#### 3.2.1) Oxygen deficient YBCO films

In order to obtain oxygen deficient YBCO films in a controlled manner, the samples are grown by sputtering and their oxygen stoichiometry is controlled through a post growth annealing step as described in section 2.3). It has been reported that this method mainly creates oxygen vacancies in a sub structure of YBCO: the b-axis CuO chains (Jorgensen *et al.*, 1990). This increase of oxygen vacancies in the chains leads to a decrease of the charge carrier density in the CuO<sub>2</sub> planes which in turn decreases the superconducting critical temperature  $T_c$  (Jorgensen *et al.*, 1990; Tallon *et al.*, 1995).

These changes of oxygen content also lead to changes in the YBCO structure. It has been demonstrated that a decrease in oxygen content leads to an increase in the c axis parameter (Cava *et al.*, 1990; Jorgensen *et al.*, 1990). A higher number of oxygen vacancies in the structure can cause an elongation of the YBCO unit cell along the c axis (Ye and Nakamura, 1993).

Figure 3-2a shows the temperature evolution of the resistance for several YBCO films with different oxygen stoichiometry. The samples shown in Figure 3-2 are colour coded. By decreasing the nominal oxygen content, we observe an increase in the normal state resistivity of the samples as well as a decrease of their superconducting critical temperature. Note that the shape of the resistance vs temperature curve is affected by the oxygen content of the sample. At optimal doping (which corresponds to an oxygen content of approximately 6.9 (Jorgensen *et al.*, 1990) the resistance in the normal state is linear with temperature from 300K down to  $T_c$ . However, as the oxygen content is decreased a downturn in the resistivity appears in the normal state. At low oxygen content, an additional upturn in the resistivity occurs before the onset of superconductivity below  $T_c$ . Finally, as the oxygen content reaches approximately 6.3, no superconducting phase is observed in the material and it seemingly undergoes a metal-to-insulator transition. These observations are consistent with what is reported in literature (Ando, Komiya, *et al.*, 2004).

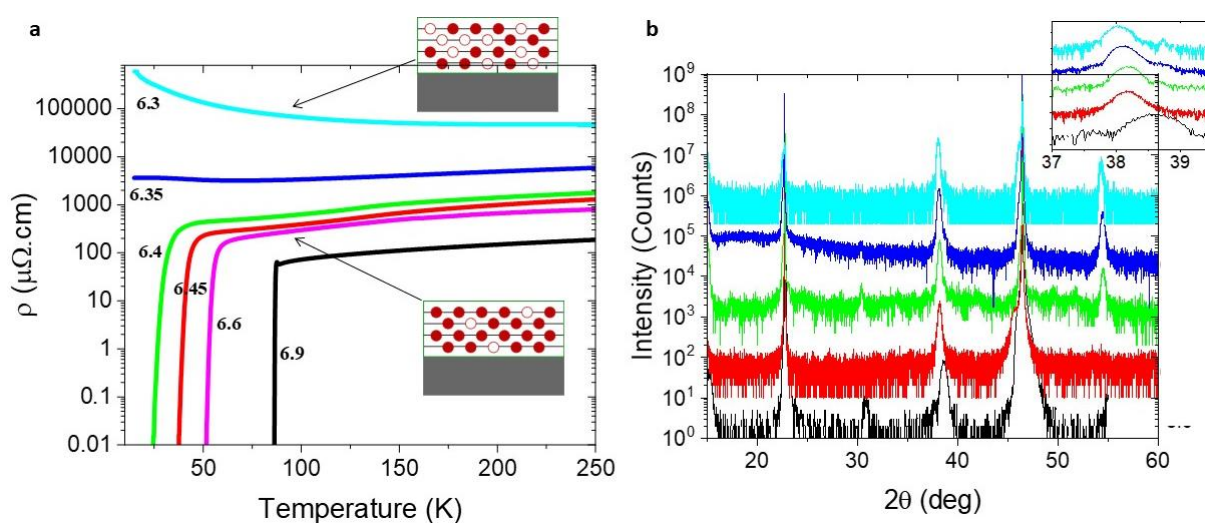


Figure 3-2: (a) Temperature dependence of the resistivity of YBCO films with different oxygen contents. The schemes represent the oxidation state of the YBCO films: The red circles represent oxygen atoms, the white oxygen vacancies. A decrease in the nominal oxygen content leads to a decrease in the superconducting critical temperature and an increase in the normal state resistivity of the films (b) X-ray diffraction spectra for an oxygen deficient YBCO film. The high intensity peaks around  $2\theta=23$  and  $2\theta=46$  arise from the STO substrate.

Figure 3-2b shows the XRD spectra of a typical oxygen deficient YBCO film. The presence of YBCO (00l) peaks shows that the integrity of the YBCO structure is conserved after the post growth annealing process. By looking at the position of the YBCO peaks we have noted that the peaks are shifted to smaller angles as the oxygen content is decreased which would correspond to an increase in the c-axis parameter (refer to Figure 3-4a in the next sections).

### 3.2.1.1) Oxygen content determination

Since we were unable to experimentally measure the exact oxygen content in our films we relied on the relationship between structural and electrical properties established previously in the literature to deduce it. Previous publications have established direct relationships between the measured c axis parameter and the oxygen content in YBCO films (Jorgensen *et al.*, 1990; Ye and Nakamura, 1993; Benzi, Bottizzo and Rizzi, 2004). Refer to section 2.3) for a more detailed discussion.

### 3.2.2) Ion Irradiated YBCO films

The second set of samples consists of ion irradiated YBCO films. The samples are initially optimally doped YBCO thin films that are then subjected to an irradiation by accelerated oxygen ions. The details of this process are explained in section 2.3). It has been shown that this process depresses the superconducting properties of YBCO films by creating pairs of interstitial/vacancy defects in the structure (Arias *et al.*, 2003)(Sirena *et al.*, 2007). The higher the number of defects in the structure the higher the effects on the superconducting and electrical properties of the samples.

Figure 3-3a shows the temperature dependence of the resistivity for several ion irradiated YBCO films. The samples shown in Figure 3-3 are colour coded. An increase in the resistivity in the normal state of 2 orders of magnitude is observed when the irradiation dose is increased from 0 to  $2 \times 10^{14} \text{ ions.cm}^{-2}$ . We note that by increasing the number of defects in the structure (which is illustrated by an increase of the ion irradiation dose c.f. section 2.3) the normal state resistivity of the samples increases and its superconducting transition temperature decreases. As the irradiation dose is increased, we observe a change in the shape of the resistivity curve. This is consistent with what is observed in literature (Arias *et al.*, 2003). These changes are interpreted as a change in the normal-state carrier density. This observation is consistent with the Hall effect measurements performed on these samples (shown later in section 3.3).

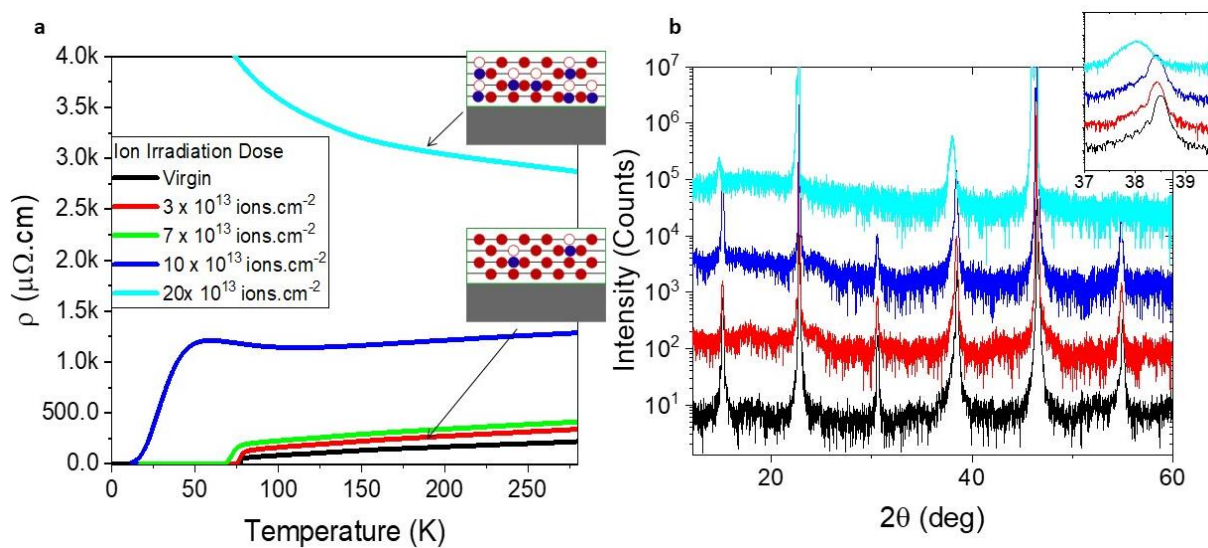


Figure 3-3: (a) Temperature dependence of the resistance for several ion irradiated YBCO films with doses ranging from  $3 \times 10^{13} \text{ ions.cm}^{-2}$  to  $2 \times 10^{14} \text{ ions.cm}^{-2}$ . The schemes represent the state of the YBCO film: The red circles are the oxygen

atoms and the blue ones are the irradiated defects (b) X-ray diffraction spectra for an irradiated YBCO film. The high intensity peaks around  $2\theta=23$  and  $2\theta=46$  arise from the STO substrate.

It has also been shown that structural changes are observed in ion irradiated YBCO films. The pairs of interstitial/vacancy created by the irradiation lead to an increase in the c-axis parameter of the YBCO unit cell (Navacerrada *et al.*, 2000).

Figure 3-3b shows a typical XRD spectra for in ion irradiated YBCO film. The presence of YBCO (00l) peaks in the spectra shows the conservation of the structural integrity of the YBCO structure after irradiation. As a matter of fact, based on the Full Width at Half Maximum (FWHM) of the diffraction peaks, and using the Scherrer formula  $\tau = \frac{0.9\lambda}{FWHM \times \cos\theta}$  we calculated that the structural coherence length  $\tau$  along the c-axis, in all samples showing a superconducting phase, is comparable to the film thickness. This implies that the neither the irradiation nor the deoxygenation compromises the structural coherence of the epitaxial films.

Similarly as in deoxygenated samples, by looking at the evolution of a YBCO peak we note a shift towards lower angles of the peak as the irradiation dose increases. This indicates an increase in the c-axis parameter as expected from literature (Navacerrada *et al.*, 2000).

### 3.2.3) Comparison between the two sets of samples

Figure 3-4 shows the evolution of the c-axis parameter, the resistivity in the normal state and the superconducting critical temperature for both sets of samples as a function of the nominal oxygen content shown in red and the ion irradiation dose shown in blue. Note that both sets of samples exhibit the same qualitative changes in their properties with decreasing oxygen content and increasing ion irradiation dose. The c axis parameter and the resistivity increase with both decreasing oxygen content and increasing ion irradiation dose, whereas the critical temperature decreases. This prompts us to compare the response of the two sets of samples to external stimuli such as illumination.

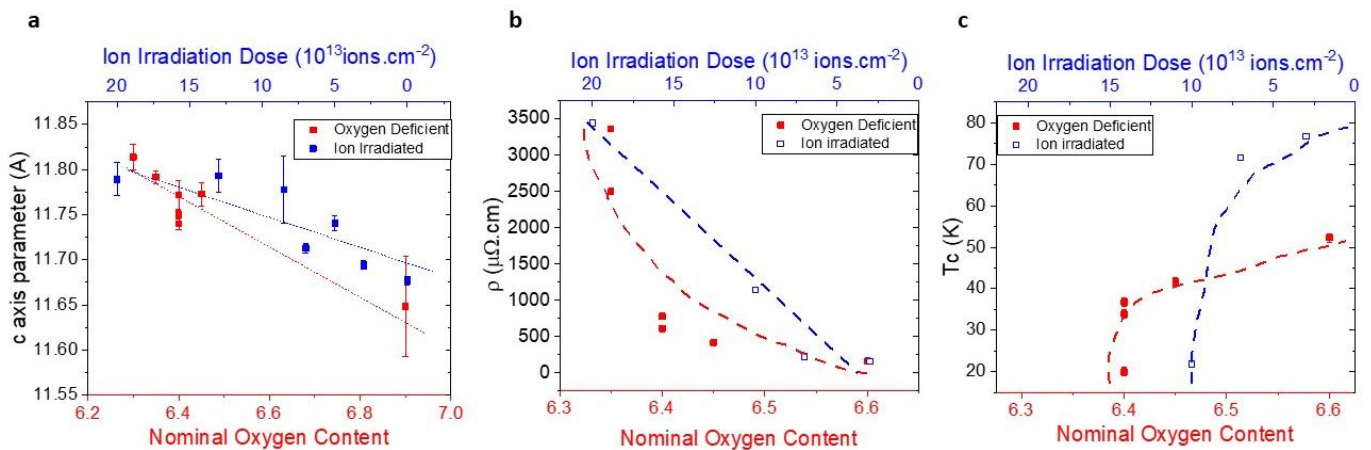


Figure 3-4: (a) c axis parameter, (b) resistivity and (c) superconducting critical temperature as a function of nominal oxygen content (closed symbols-down) and ion irradiation dose (open symbols-up) for the two sets of samples. Ion irradiation mimics the effects of oxygen deficiency: an increase in the c axis parameter and the normal state resistivity as well as a decrease in the superconducting critical temperature.

### 3.3) Correlation between carrier density, carrier mobility and superconducting critical temperature

In this section we will investigate the behaviour of the superconducting critical temperature of our samples with respect to their carrier density and their carrier mobility.

We have investigated the transport properties of our YBCO films using both longitudinal resistance and Hall effect measurements. For the latter, a transverse voltage is measured when an electrical current is injected along a YBCO bridge in the presence of a perpendicular magnetic field. The Hall coefficient is calculated by measuring the transverse voltage as a function of the applied magnetic field. Refer to section 2.10.5) and section 1.1.1.2) for a more detailed discussion. Thus to summarize, we have measured the resistivity, the Hall coefficient and the superconducting critical temperature, whose evolution we study as a function of the oxygen content and irradiation dose.

As was stated in previous sections, in the literature the parameter used to compare superconducting samples is usually the carrier density. It was shown that an increase in the carrier density of high T<sub>c</sub> superconductors leads to an increase in its critical temperature. Thus, for convenience, we will calculate the Hall number  $n$  as the inverse of the measured Hall coefficient c.f. Eq. 11, the carrier mobility  $\mu$  as the ratio between the Hall coefficient and the normal state resistivity, and the cotangent of the Hall angle as the inverse of the latter according to:

$$n = \frac{1}{R_H * e} = \frac{1}{slope * e} \quad 11$$

$$\mu = \frac{R_H}{\rho_{xx}} \quad 12$$

$$cot \theta_H \propto \frac{\rho_{xx}}{\rho_{xy}} = \frac{\rho_{xx}}{R_H * B} \quad 13$$

Where  $R_H$  is the Hall coefficient,  $e$  is the electric charge,  $t$  is the sample thickness,  $slope$  is the slope extracted from the transverse resistance vs applied magnetic field,  $\rho_{xx}$  the longitudinal resistivity,  $n$  the carrier density,  $\mu$  the carrier mobility and  $cot \theta_H$  the cotangent of the Hall angle.

Note that the Eq. 11 and Eq. 12 correspond to the Drude's free electron model, which does not accurately describe cuprates like YBCO (refer to section 1.5.5). For instance, the Hall number obtained through Eq. 11 is strongly temperature dependent in cuprates (Hussey, 2008), contrary to the case of ordinary metals. Yet, as discussed earlier (Anderson, 1991; Jones, Christen, Thompson, Feenstra, Zhu, *et al.*, 1993; Stockinger *et al.*, 1998), variations of the Hall number  $n$  obtained through Eq. 11 are a good approximation of the carrier density variation, for instance those produced upon light illuminations, provided that comparisons are made at a fixed temperature. Furthermore, it has been reported that in the underdoped region of the phase diagram and at low temperature (typically around 100K) the inverse Hall coefficient is proportional to the doping  $p$  which represents the number of charge carriers per Cu atom in the YBCO structure and typically ranges from 0 to 0.25 (Ando, Kurita, *et al.*, 2004) (Hussey, 2007). This is consistent with Figure 3-5a, in which the Hall number measured at 95 K is plotted vs the critical temperature for the two sets of samples, superposed by T<sub>c</sub> vs carrier density "dome" referred to in the literature (Ito, Takenaka and Uchida, 1993; Ando, Komiya, *et al.*, 2004; Segawa and Ando, 2004) (Carrington *et al.*, 1992) (dashed line). One can also see that the Hall number values are of the right order of magnitude when compared to literature. Thus, considering all of the above, the Hall number  $n$  and mobility  $\mu$  as defined per Eq. 11 and Eq. 12 constitute -in a good approximation- a meaningful set of quantities to monitor the deoxygenation, ion irradiation and light-illumination effects in the present experiments. In addition, we will also use the parameter  $cot \theta_H$  which does not imply any assumption or approximation and has been often used in the literature, thus allowing for a direct comparison.

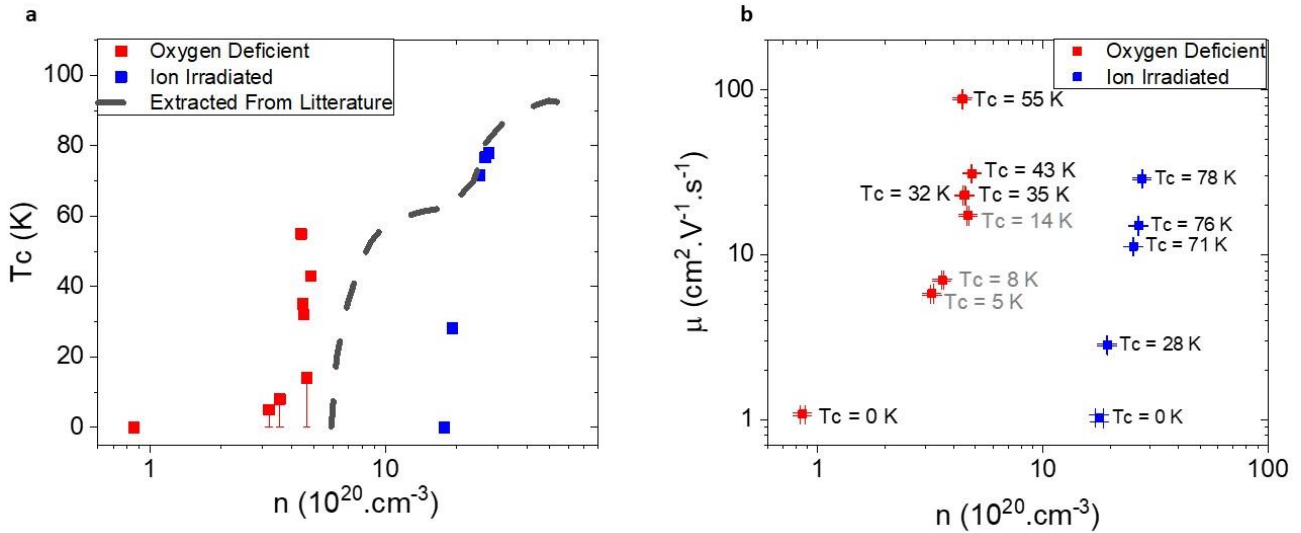


Figure 3-5: (a) Superconducting critical temperature as a function of the carrier density (deduced from Hall measurements from Eq.1) at  $T = 95\text{K}$  for both sets of samples. The dotted line represents the data extracted from literature (Ito, Takenaka and Uchida, 1993; Ando, Komiya, et al., 2004; Segawa and Ando, 2004)(Carrington et al., 1992) (b) Carrier mobility (deduced from Hall measurement from Eq.12) as a function of the carrier density (deduced from Hall measurement from Eq.11) for both sets of samples at  $T = 95\text{K}$ . The associated superconducting critical temperature of these films is shown in black on the graph. The grey text in the figure establishes the maximal estimate of  $T_c$  for some of the samples. The differences in critical temperature observed in samples with close carrier density can be understood in terms of differences in mobility.

A close look to Fig. 5a allows for an interesting observation: several samples have very similar carrier densities but very different superconducting critical temperatures. This is the case for oxygen deficient and irradiated samples. Additional insight concerning this situation can be obtained from Figure 3-5b where we show the calculated carrier mobility as a function of the carrier density for both sets of samples at a temperature of  $T = 95\text{K}$  in their virgin state. The labels on each point indicate the critical temperature associated with each sample. As is stated previously samples having very similar carrier density can have very different critical temperatures (c.f. Figure 3-5a), which interestingly correlate with very different carrier mobilities that span one order of magnitude (c.f. Figure 3-5b). This is especially clear for oxygen deficient samples with  $T_c$  between 14K and 55K. As the critical temperature of these samples increases, their carrier mobility is significantly enhanced, but the carrier density stays nearly constant.

In addition, we note that the ion irradiation affects both the carrier density and the mobility of YBCO thin films consistent with the description in section 3.2.2) and what is observed in literature (Arias et al., 2003). However, the carrier density is affected to a lesser extent, since it changes by a factor of  $\sim 2$  across the series of samples, while the mobility spans over more than an order of magnitude.

The above observations suggest that the carrier mobility is a very important parameter to monitor deoxygenation and ion irradiation effects, in addition to (or maybe to a higher degree than) the Hall coefficient.

### 3.4) Temperature behaviour

Figure 3-6 shows the temperature dependence of the resistivity, carrier density, carrier mobility and  $\cot\theta_H$  for an oxygen deficient YBCO sample (O content = 6.35) in its virgin state.

The temperature dependence of the resistivity shown in Figure 3-6a is the typical  $\rho$  vs  $T$  expected from underdoped cuprates. At temperatures higher than 300K (Barisic et al., 2013), the resistivity is a linear function of the temperature. However, as the temperature is decreased, a downturn in the resistivity is observed possibly due to the opening of a pseudogap(Ito, Takenaka and Uchida, 1993).

An upturn in the resistivity then appears at low temperature before it drops to 0 at the superconducting critical temperature. This results in a peculiar “S-shaped” resistivity vs temperature curve.

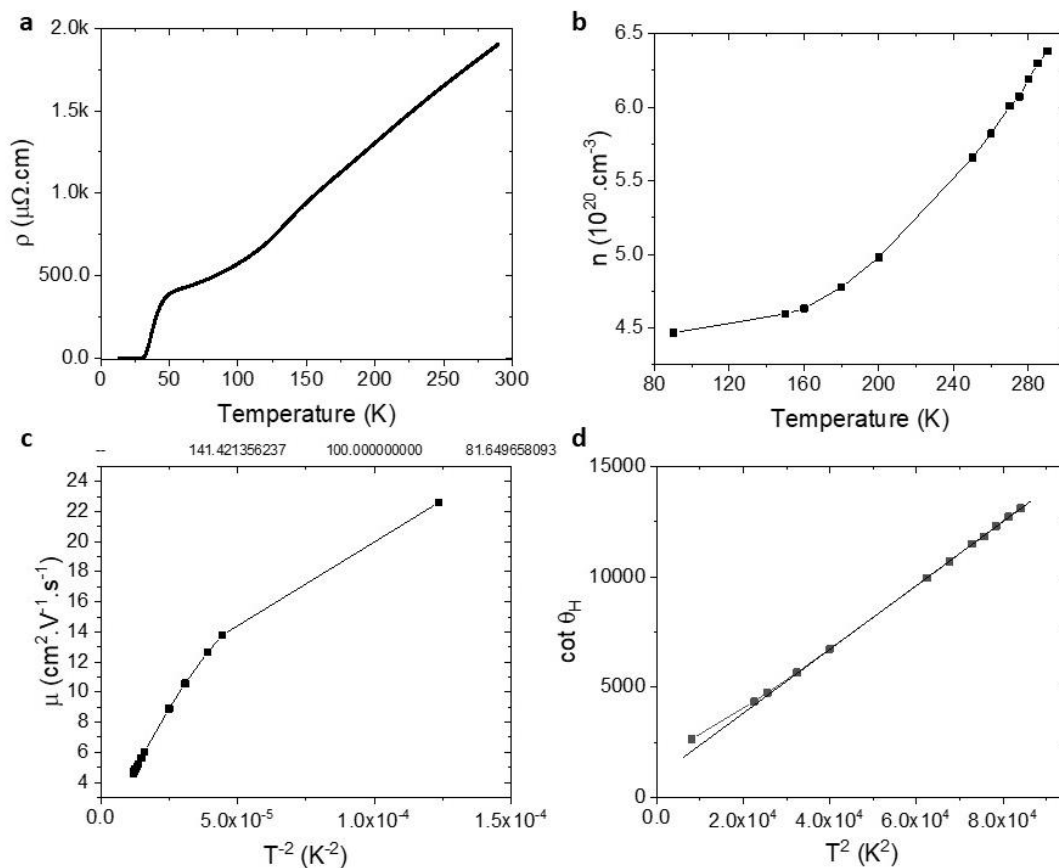


Figure 3-6: (a) Temperature dependence of the resistivity of an oxygen deficient YBCO film (b) Inverse Hall coefficient multiplied by the electric charge (carrier density) as a function of temperature (c) Hall coefficient divided by the resistivity (carrier mobility) as a function of the inverse square temperature, (d) Cotangent of the Hall angle as a function of the square temperature. The straight line is an extrapolation of the cotangent at high temperatures.

Figure 3-6b shows the temperature dependence of the carrier density as a function of temperature. We note a non-monotonous temperature dependence of the inverse Hall coefficient in the normal state. It decreases at high temperature and plateaus when the temperature reaches 160K. This behaviour has been widely reported in the literature (Wuyts *et al.*, 1993)(Hussey, 2008) and constitutes one of the open questions concerning cuprates. This behaviour is inconsistent with the standard Fermi liquid theory as one would expect  $R_H$  to present little to no variations as a function of temperature. Figure 3-6c shows the carrier mobility as a function of the inverse of the temperature squared.

The interpretation of the Hall coefficient as a measure of the carrier density in cuprates, **over the whole temperature and doping range**, has been challenged by the discovery of the relationship between the cotangent of the Hall angle and temperature (Chien, Wang and Ong, 1991). This straightforward relationship is also found in our data as shown in Figure 3-6d where the cotangent of the Hall angle is plotted against the temperature squared. Note that a deviation of the square relationship between the two quantities is observed around 100K. This overall behaviour has been observed in most cuprates in a wide range of temperature and doping (Hussey, 2007) except is some experiments with BSSCO which have found that the power exponent of the temperature changes from  $\sim 1.6$  to  $\sim 2$  with decreasing doping (Ando and Murayama, 1999).

### 3.5) Visible/UV light illumination

#### 3.5.1) Basic effect

In this section we will describe the photo-induced effects on the transport properties of our YBCO thin films. The experimental procedure followed in these measurements is detailed below: A resistivity vs temperature measurement is first performed on the film in dark. Then a Hall effect measurement is performed at a temperature of  $T = 95K$ . These measurements are labelled “Virgin State”. The light is then turned on and the sample is illuminated at a fixed temperature for a set amount of time (details of the illumination conditions are described below). The light is then turned off and the system is allowed to thermalize for about 30 minutes prior to performing a Hall measurement in dark. Finally, a resistivity vs. temperature measurement in dark is subsequently performed by first cooling down to 10K and then ramping to high temperature at an average rate of  $\sim 1 K/min$ . These measurements are labelled “After Light”.

The films were illuminated using different light sources detailed in section 2.11.1) with an optical power of  $P = 100mW.cm^{-2}$ , for a period of 2 hours and at a temperature of  $T = 95K$ . Unless stated otherwise these parameters were kept constant. The optical power corresponds to the maximal common optical power available on all light sources. The temperature and duration were chosen to maximize the magnitude of the photo-induced effect in the normal state (Stockinger *et al.*, 1998) while conserving some experimental practicality.

Figure 3-7(a-b) shows the temperature dependence of the resistance measured in oxygen deficient YBCO films in dark (virgin state) and after illumination. We note a persistent photoconductivity effect (PPC) on our film i.e. a decrease in the normal state resistance of approximately 1 order of magnitude. Additionally, we note a persistent photo-superconductivity (PPS) on our film i.e. the appearance of a superconducting critical temperature after illumination. The photo-induced effects are persistent as long as the sample is kept at low temperature. Conversely, one can recover the virgin state by increasing the film temperature to 300K in dark. Figure 3-7c shows a Hall effect measurement performed in dark (virgin state) and after illumination (after light). We note a decrease in the slope of the Hall resistance vs applied magnetic field after illumination. This is consistent with an increase in the charge carrier density  $n$ . These effects are consistent with what is observed in literature (Kirilyuk, Kreines and Kudinov, 1990; Nieva *et al.*, 1992; Markowitsch *et al.*, 1997; Gilabert *et al.*, 2000)

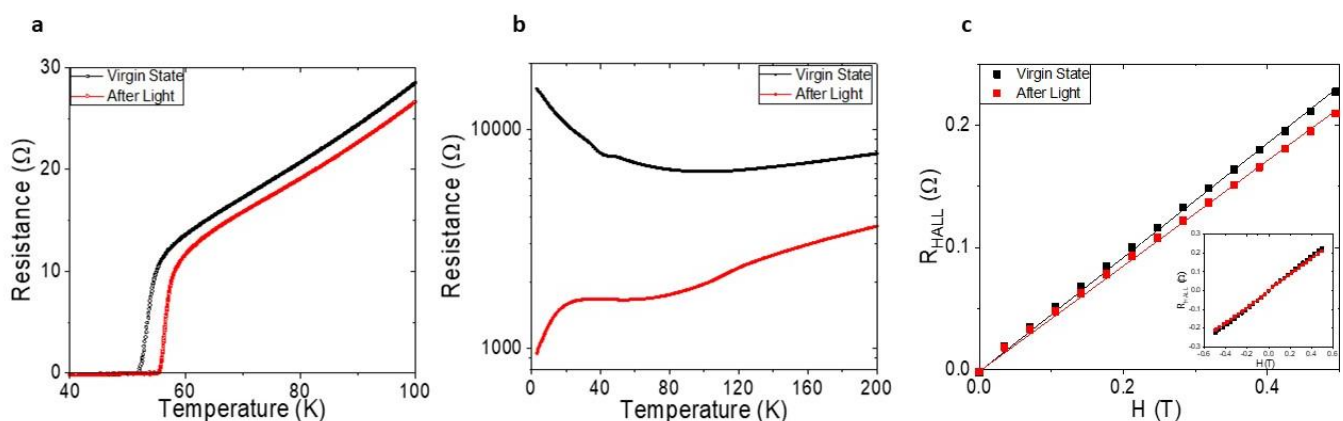


Figure 3-7: (a) Temperature dependence of the resistance of a YBCO film in its virgin state and after illumination with a white light. (b) Light induced superconductivity in an oxygen deficient YBCO film (O content = 6.3). The virgin state of this sample is insulating but after illumination an onset of superconductivity appears around a temperature of 30K (c) Field dependence of the Hall resistance for a YBCO film in its virgin state and after illumination with a white light. Solely positive values of the magnetic field are shown for clarity. The entire plot is shown in the inset.

### 3.5.2) Dependence on irradiance

A multitude of factors can influence the effect described in the previous section. These factors include the illumination time, the irradiance (optical power) or the wavelength of the light used. Figure 3-8 shows the changes measured in the inverse Hall coefficient and the resistivity at a temperature of 95K under illumination with different irradiance. We can see an increase in the size of the effect as a function of increasing irradiance. All the other factors were kept constant during this measurement. The scaling of the persistent photoconductivity with the incident photon dose  $Q = \frac{P \times t}{\hbar\omega}$  where  $P$  is the light irradiance and  $t$  is the time of illumination  $\hbar\omega$  is the photon energy suggests that the PPC observed in our films is a one photon process as is reported in literature (Kudinov *et al.*, 1993)(Endo *et al.*, 1996). Note that in the case shown in Figure 3-8, the illumination is performed using a white lamp with a finite wavelength bandwidth which complicates the estimation of a cumulative photon dose.

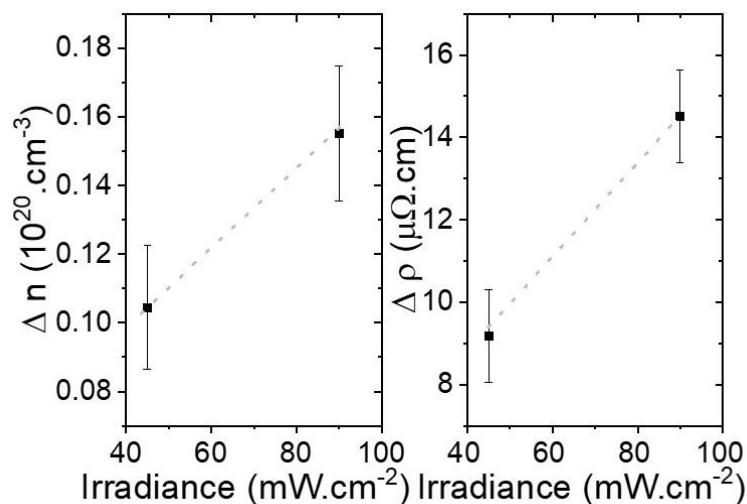


Figure 3-8: Photo-induced changes of the carrier density and the resistivity of an oxygen deficient YBCO film as a function of the light irradiance.

### 3.5.3) Doping dependence

A systematic study of the photo-induced effects as a function of the oxygen stoichiometry were performed on a series of  $YBCO_{7-\delta}$  thin films with  $0.4 < \delta < 0.7$ .

Figure 3-9 shows the photo-induced changes in the resistivity, carrier density and the carrier mobility at T=95K as well as the superconducting critical temperature as a function of  $\delta$  for the set of oxygen deficient YBCO films. The changes were calculated using a simple arithmetic difference between the values before and after illumination  $\Delta A = A_{after\ illumination} - A_{before\ illumination}$  with  $A$  as the measured quantity. The samples were illuminated using a LED with a wavelength of  $\lambda = 565nm$ .

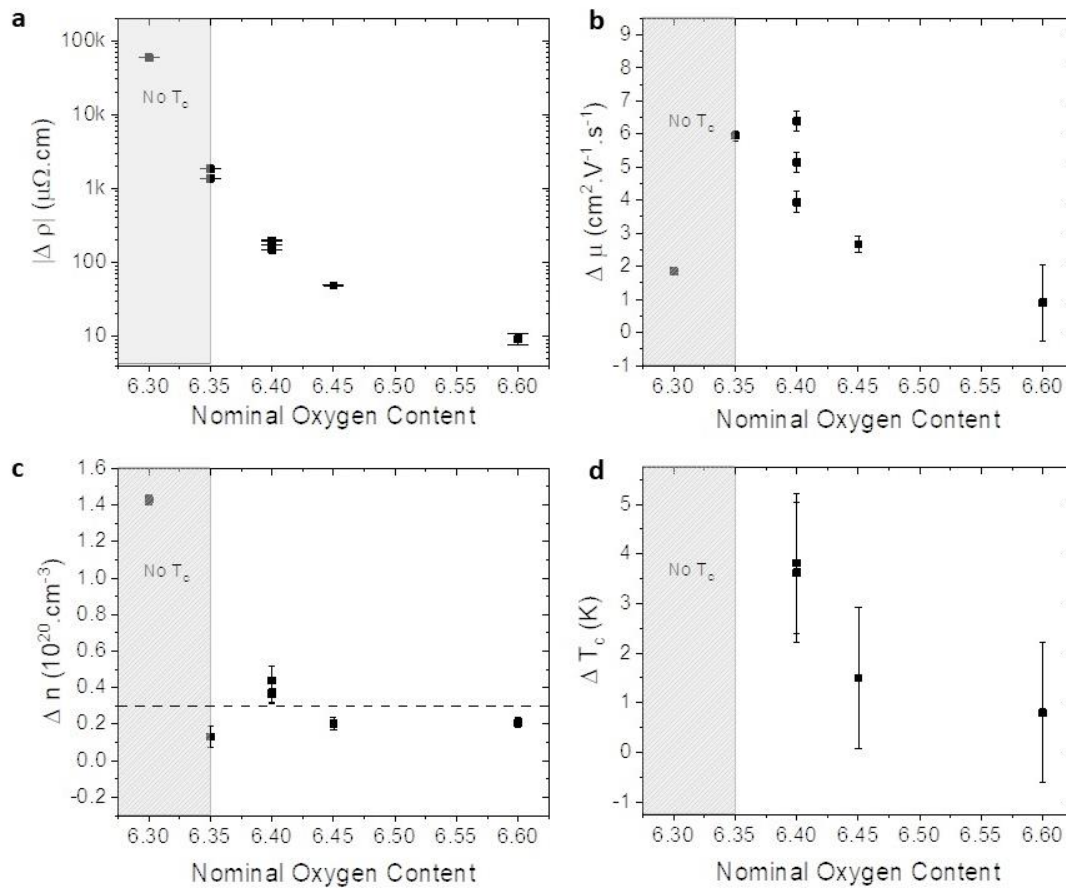


Figure 3-9: Photo-induced changes ( $\Delta A = A_{final} - A_{initial}$ ) with  $A$  as (a) resistivity, (b) carrier mobility, (c) carrier density and (d)  $T_c$  respectively as a function of the nominal oxygen content for the set of oxygen deficient YBCO films. The left side of the graphs (highlighted in grey) indicates the area of the phase diagram where superconductivity does not set in. Illumination was performed using a LED ( $\lambda = 565 \text{ nm} \approx 2.2 \text{ eV}$ ) at a temperature of 95K for duration of  $t = 4$  hours at an irradiance of  $100 \text{ mW.cm}^{-2}$ .

In Figure 3-9a we can see that the magnitude of the persistent photoconductivity (PPC) increases with decreasing oxygen content. This indicates that the efficiency of the PPC is closely related to the amount of oxygen vacancies in the structure. This is consistent with what is observed in literature (Hoffmann *et al.*, 1997). **As a matter of fact, studies have shown that the presence of oxygen vacancies in the YBCO structure is essential to observe the PPC. Changing the effective doping in a different manner such as rare earth doping is not sufficient to observe these effects (Lederman *et al.*, 1994).**

In order to obtain a better understanding of this effect we have looked at the changes in the carrier mobility and the carrier density as a function of  $\delta$  in Figure 3-9(b-c) respectively. We note that the photo-induced changes of the carrier density (c.f. Figure 3-9c) do not scale with the nominal oxygen content, but rather stays constant at approximately  $\sim 0.3 \times 10^{20} \text{ cm}^{-3}$  within experimental error. Only the sample with an oxygen content of 6.3, which is characterized by the absence of superconductivity, does not belong to the same trend. Contrary to the carrier density, the photo-induced changes measured in the mobility (Figure 3-9b) do correlate with the oxygen content, since the changes increase as the oxygen content decreases. Note that the changes in mobility measured on the sample with an oxygen content of 6.3 does not belong to the same trend.

The photo-induced changes observed in the superconducting critical temperature are shown in Figure 3-9d. Notice that the  $T_c$  changes correlate with the oxygen content in a way that resembles the

mobility behaviour: the photo-induced increase of  $T_c$ , known as persistent photo-superconductivity (PPS) in the literature, is larger the lower the oxygen content. This is consistent with previous reports (Osquiguil *et al.*, 1993).

**In view of the above observations, it is clear that the size of the photo-induced changes of the critical temperature scales with the photo-induced changes in the carrier mobility, but not with the photo-induced changes of the carrier density, which stays constant within the series of superconducting samples. The fact that these changes scale with a decreasing oxygen content highlights the importance of oxygen vacancies in these phenomena.**

As a reminder, two different scenarios have been presented to explain the PPC and PPS effects: a photo-increase of the carrier density through the absorption of a photon or a photo-assisted oxygen ordering in the charge reservoirs (more details can be found in section 3.1) and 1.7.3)).

We note that a promotion of photogenerated carriers to the conductance band would not be consistent with an increase in the mobility of charge carriers. An increase in carrier density would lead to smaller scattering length and thus lower mobility. On the other hand, a photo-assisted ordering of oxygen atoms in the YBCO structure could affect the scattering centres of charge carriers which would lead to an increase in their mobility.

#### 3.5.4) Spectral dependence

As is stated in the literature (Endo *et al.*, 1996)(Gilabert *et al.*, 2000)the PPC has a clear wavelength dependency. The magnitude of the effect is enhanced when the wavelength of the light used to illuminate is decreased from the visible towards the UV. The accepted argument is that the spectral efficiency of the PPC is enhanced in the UV region of the spectrum because of the presence of an absorption peak at 4eV (Endo *et al.*, 1996) related to an electronic transition of a  $Cu^{1+}$  atom present in CuO chains.

We performed a similar experiment where we monitored the evolution of several physical quantities after illuminating the samples with visible light ( $\lambda = 565nm$ ) and UV light( $\lambda \in [275,300] nm$ ). Note that contrary to the LED emitting in the visible range with a narrow bandwidth (20nm), the setup used to illuminate the samples with UV radiation allows for a small portion (4-5% of spectral weight) of visible light (refer to section 2.11.1) for more details).

The effect of wavelength on the magnitude of the persistent photoconductivity and persistent photosuperconductivity (PPS) were studied on a set of oxygen deficient YBCO samples with nominal oxygen content ranging from 6.4 to 6.6. We have used the same experimental protocol as described in the previous section.

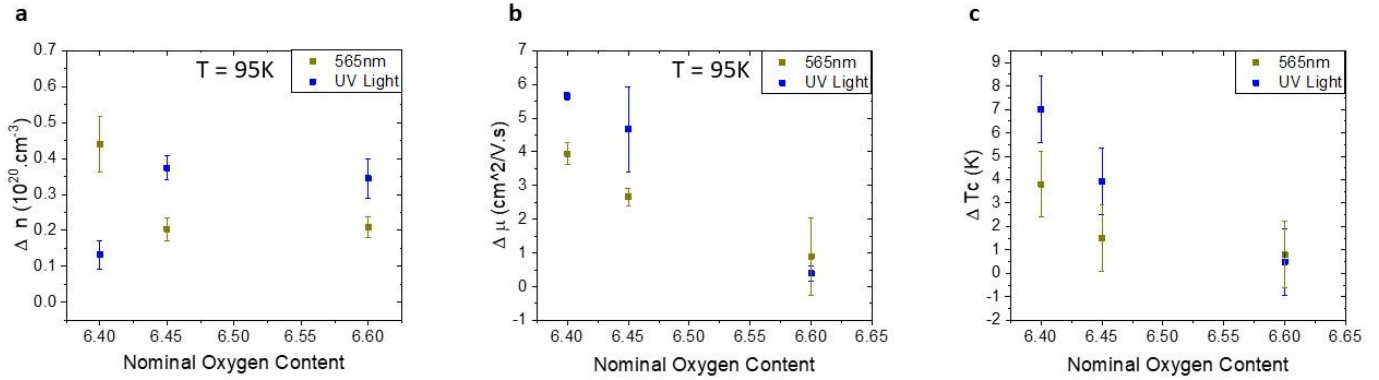


Figure 3-10: Photo-induced changes of the carrier density(a), the mobility (b) and the critical temperature(c) for the set of oxygen deficient YBCO films as a function of the nominal oxygen content after illumination with UV light (blue) and visible light (yellow). The irradiance was fixed at  $P = 100\text{mW.cm}^2$  for both illuminations at a temperature of  $T = 95K$  for  $t = 4\text{hours}$ .

Figure 3-10 shows the photo-induced changes of the carrier density, the mobility and the superconducting critical temperature respectively on a set of oxygen deficient YBCO thin films illuminated by visible and UV light at a fixed temperature of  $T = 95K$  as a function of the nominal oxygen content.

The photo-induced variation in carrier density does not scale with the nominal oxygen content. Rather they are constant as a function of  $\Delta$  for both illumination wavelengths and lie around  $\sim 0.3 \times 10^{20} \text{ cm}^{-3}$ . The changes are consistent with what is observed in literature, with relative changes of 4-5% in the Hall resistivity after illuminating at 100K (Stockinger *et al.*, 1998).

The photo-induced variations of the mobility do scale with decreasing oxygen content for both wavelengths. In particular, the mobility variation increases as the nominal oxygen content is decreased, and the trend is steeper for samples illuminated with UV light. The photo-induced changes in the superconducting critical temperature do scale with decreasing oxygen content for both wavelengths. Again, the  $T_c$  changes are more important when the samples are illuminated with UV light than visible light.

**The degree of correlation between the photo-induced changes in the superconducting critical temperature and the mobility is much more important than with the carrier density.** As was expected from literature the efficiency of both, the PPC and the PPS, are enhanced by illuminating with UV light rather than visible light. However, the fact that the mobility is affected by the illumination while the carrier density is not, constitutes a very interesting observation, which has gone unnoticed in the literature. That point further supports that the photo-induced changes in the critical temperature are linked to changes in the carrier mobility.

### 3.6) Illumination of oxygen deficient vs ion irradiated samples

To further explore the phenomena of photo-induced effects on cuprate thin films we have opted to compare the effects of visible light on oxygen deficient and ion irradiated YBCO thin films. The comparison between these two sets is interesting due to the similarities observed in their respective electrical and structural properties c.f. section 3.2.3).

The same experimental protocol described in the previous sections is followed where we monitored the photo-induced changes of various physical quantities. The ion irradiated samples considered in this section have been irradiated with doses ranging from  $3 \times 10^{13} \text{ ions.cm}^{-2}$  to  $1 \times 10^{14} \text{ ions.cm}^{-2}$ . Moreover, the oxygen deficient set of samples considered in this section have nominal oxygen contents ranging from 6.4 to 6.6. These correspond to the set of samples displaying a

measurable superconducting critical temperature since the purpose of this experiment is to correlate the changes observed in the electrical properties of the films to their superconducting ones.

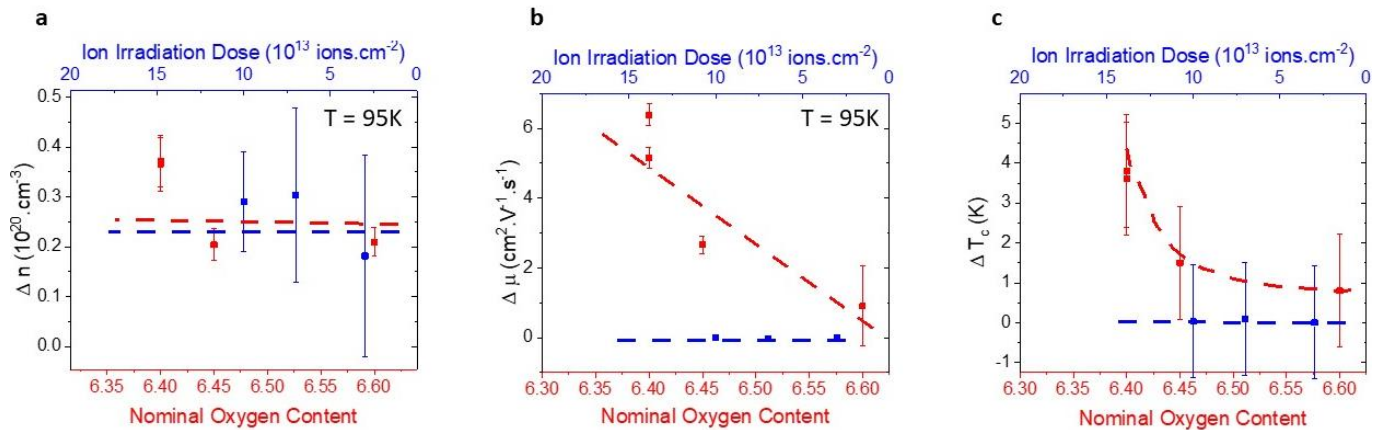


Figure 3-11: Photo-induced changes of carrier density, the carrier mobility and the critical temperature respectively from left to right for the set of oxygen deficient YBCO films as a function of the nominal oxygen content in red and for the set of irradiated YBCO films as a function of the irradiation dose in blue. The dotted lines are a guide to the eye.

Figure 3-11 shows the photo-induced changes of the carrier density (a), mobility (b) and superconducting critical temperature (c) as a function of the nominal oxygen content in red and the ion irradiation dose in blue, produced by illumination with visible light ( $\lambda = 565nm$ ).

The photo-induced changes in the carrier density  $\Delta n$  (Figure 3-11a) are comparable in the case of deoxygenated (red) and irradiated (blue) samples.  $\Delta n$  does not depend on the nominal oxygen content nor the ion irradiation dose, and approximately lies around  $\sim 0.3 \times 10^{20} cm^{-3}$ . The magnitude of  $\Delta n$  is consistent with what is observed in the literature for deoxygenated samples: a decrease of 4-5% in the Hall resistivity at 100K after several hours of illumination (Stockinger *et al.*, 1998)(Gilbert *et al.*, 2000).

Contrarily, the photo-induced changes in mobility differ significantly between the two sets of samples. The increase in mobility scales with decreasing oxygen content for the set of oxygen deficient YBCO films. These changes are consistent with what is observed in literature (Stockinger *et al.*, 1998): around 1-4% increase at 100K for samples with  $T_c \sim 50K$ . However, as the nominal oxygen content is decreased the changes in mobility are significantly increased and reach up to 30%. On the other hand, there are almost no photo-induced mobility changes for the set of ion irradiated YBCO thin films. This means that changes in their resistivity are solely caused by a change in the carrier density.

Finally, the photo-induced variations of the superconducting critical temperature scale with decreasing oxygen content for the set of oxygen deficient YBCO thin films, but they are non-existent for the set of ion irradiated set –despite both sets of samples displaying similar carrier density variation upon illumination. That is, a photo-induced increase of the carrier density is not enough to produce an increase of their superconducting critical temperature: photo-induced superconductivity occurs only in samples for which the carrier mobility is enhanced by light.

**All the above observations allow us to state that the photo-induced changes of the superconducting critical temperature correlate with changes in the mobility, rather than with changes in the carrier density.**

### 3.7) Summary

The previous sections have evidenced the correlation between the photo-induced changes of the superconducting critical temperature and the changes of the carrier mobility. It has also highlighted the independence of the former from photo-induced changes of the charge carrier density alone. This becomes clear in the data representation of this section.

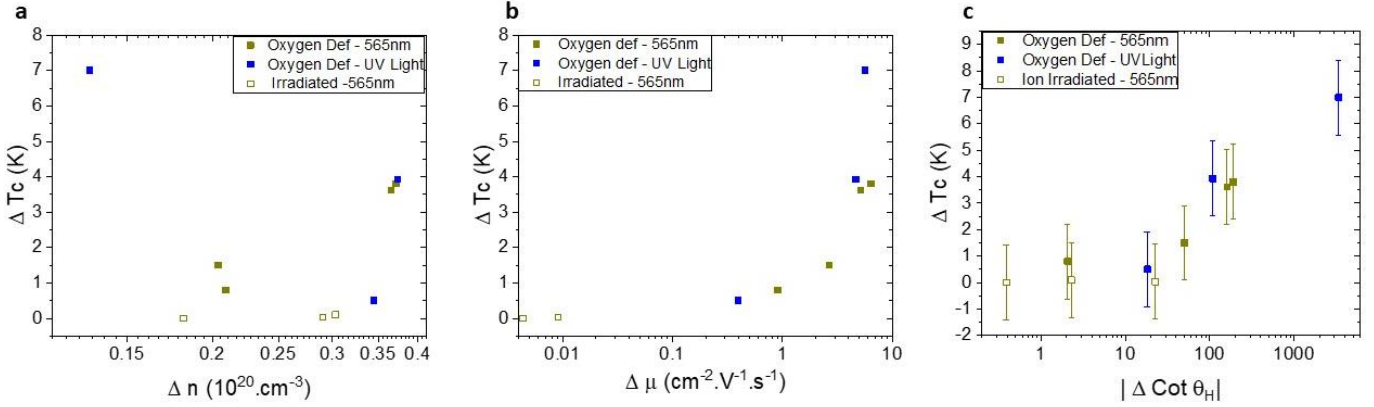


Figure 3-12: Photo-induced changes of the critical temperature as a function of the changes in carrier density(a) and mobility(b) and the cotangent of the Hall angle(c) at  $T = 95K$ .

Figure 3-12 shows the photo-induced changes of the superconducting critical temperature vs the photo-induced changes of the carrier density(a), the carrier mobility(b) and the cotangent of the Hall angle(c) for the previously mentioned measurements. The photo-induced changes observed in oxygen deficient YBCO and ion irradiated thin films after illuminating with visible light are shown in closed and open yellow symbols respectively. The photo-induced changes caused by UV illumination are shown in blue.

We can clearly see from these plots that the photo-induced changes of the critical temperature do not correlate with the changes in carrier density. On the other hand, the changes in superconducting critical temperature clearly scale with the mobility for all the different experimental configurations considered. This strengthens the claim that the mobility of carriers is closely related to the cuprate superconducting critical temperature.

Note that the cotangent is the inverse of the mobility, we thus expect the superconducting critical temperature's behaviour to show the same qualitative features, as it is actually observed in Figure 3-12c.

### 3.8) Relaxation

As stated previously the effects investigated in this chapter are persistent at low temperature. This means that the effects do not disappear when the light is turned off, and the excited state of the sample persists in time. In order to recover the virgin state the sample has to be heated up to high temperature, typically around 250K (Gilabert *et al.*, 2000) for a gradual relaxation to occur.

It has been shown that the resistivity relaxation dynamic at high temperature can be fitted to a stretched exponential function (Kudinov, Kirilyuk and Kreines, 1992)(Gilabert *et al.*, 2000) according to:

$$\rho(t) = \rho(\infty) + [\rho(0) - \rho(\infty)]e^{-[\frac{t}{\tau}]^\beta}$$

Where  $\rho(\infty)$  is the virgin state resistivity,  $\rho(0)$  is the initial resistivity (after illumination),  $\tau$  is the characteristic relaxation time and  $0 < \beta < 1$  is a dimensionless dispersion parameter. The use of such

a function assumes that the decay rate is not constant with time but decreases as  $t^{\beta-1}$ . Although this is mainly a phenomenological model with no real physical meaning to its parameters it has been widely used to model several systems such as glasses (Phillips, 1996).

The temperature dependence of the extracted relaxation time has been shown to follow a thermal activation process (Kudinov *et al.*, 1993):

$$\tau = \tau_0 e^{\frac{\Delta}{k_B T}}$$

Where  $\Delta$  is the energy barrier associated with the relaxation process.

The experimental protocol followed in this section is the following:

1. The resistance and Hall effect are measured in dark at several temperatures ranging from 100K to 300K.
2. The sample is cooled to 95K where the light is turned on for a fixed amount of time at a fixed irradiance of  $P = 100 \text{ mW} \cdot \text{cm}^{-2}$ .
3. The light is turned off and the sample is allowed to thermalize before warming it up to a specific temperature where the resistance and Hall effect are measured continuously as a function of time in the dark.

At the end of the measurement at a given temperature T, the sample is allowed to relax completely to the virgin state at room temperature before starting over from step 2. These steps allowed us to make sure that no relaxation took place during the illumination which would significantly complicate the analysis of the calculated physical quantities.

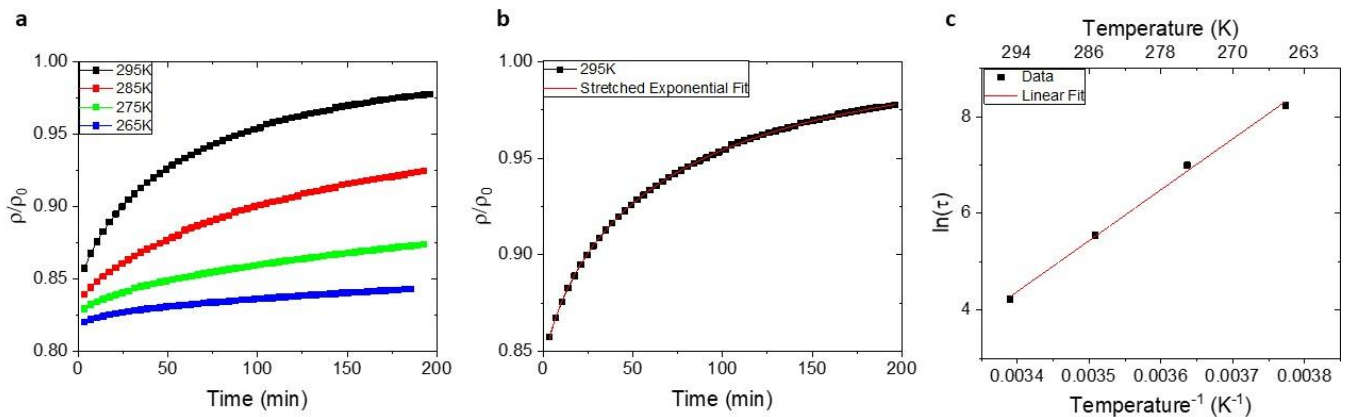


Figure 3-13: (a) Time dependence of a normalized resistivity relaxation temperatures measured in YBCO ( $O$  content = 6.4) (b) Stretched exponential fit of a resistivity vs time measurement in dark at a temperature of 295 K (c) Characteristic time of relaxation extracted from the stretched exponential fits vs the inverse of temperature fitted to a straight line.

Figure 3-13 shows relaxation measurements performed at high temperature on an oxygen deficient YBCO sample with a nominal oxygen content of 6.4 ( $T_c \sim 35K$ ). Figure 3-13a shows the time dependence of the normalized resistivity during relaxation in the dark at the temperature indicated in the legend. Figure 3-13b shows the time dependence of a normalized resistivity measured at 295K during relaxation in black as well as the stretched exponential fit function used to extract the time dependence. Figure 3-13c shows the inverse temperature dependence of the characteristic relaxation time as well as a linear fit used to extract the energy barrier associated with the process.

According to those fits we obtain an energy barrier  $\Delta = 0.9 \text{ eV}$ . This value is similar to what is reported in the literature where  $\Delta \approx 0.9 \pm 0.1 \text{ eV}$  (Kudinov *et al.*, 1993; Gilabert *et al.*, 2000) for YBCO films. Due to the similarity between the values obtained for the relaxation energy barrier ( $\sim 1.3 \text{ eV}$ ) (Tolpygo *et al.*, 1996) and the oxygen diffusion activation energy it has been suggested that the relaxation mechanism might be related to the motion of oxygen ions in the YBCO structure (Gilabert *et al.*, 2000). Note that the time constants  $\tau$  shown in Figure 3-13c are obtained with a fixed dimensionless parameter of  $\beta = 0.66$ . If  $\beta$  were left to vary it would decrease as a function of temperature and  $\Delta$  would increase by 12%.

In what follows we will present systematic relaxation measurements performed at different temperatures on an oxygen deficient YBCO thin film (*O content* = 6.35), by focusing not only on the evolution of the resistivity, but also on the mobility, the carrier density and the cotangent of the Hall angle.

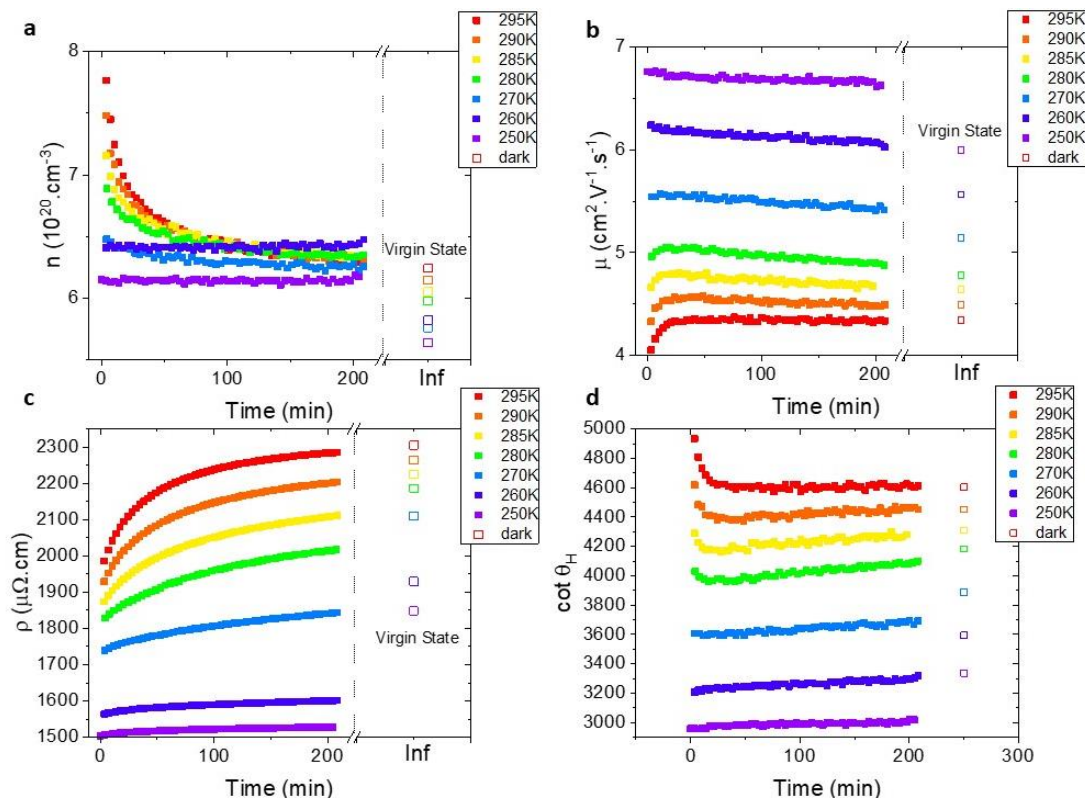


Figure 3-14: Time dependence of the carrier density(a), the mobility (b), the resistivity (c) and the cotangent of the Hall angle(d) during relaxation at different temperatures. The oxygen-deficient sample was illuminated for 4 hours at 95K at an irradiance of  $P = 100 \text{ mW} \cdot \text{cm}^{-2}$  with visible light ( $\lambda = 565 \text{ nm}$ ). These measurements were performed in dark. The open points represent the virgin state values measured before the illumination.

Figure 3-14 shows the time dependence of the carrier density(a), the mobility(b), the resistivity(c) and the cotangent of the Hall angle (d) during the relaxation process at different temperatures. The open dots represent the virgin state values of the measured/calculated quantities.

From Figure 3-14a we note that the Hall number does not relax at 250K, that is, it presents a characteristic time that tends to infinity. By increasing the temperature to 300K the characteristic time significantly decreases and at room temperature full relaxation is reached reaches in around 200 minutes.

The mobility on the other hand has a significantly different behaviour. We observe relaxation even at the lowest temperature (250K), note the quasi linear background that decreases slowly at low

temperatures. This is also clear at 260 K, where no relaxation exists for the carrier concentration. An inversion of the dynamic occurs at  $\sim 280\text{K}$ , where the mobility after illumination is lower than the virgin state value. This behaviour has also been reported in literature (Stockinger *et al.*, 1998; Markowitsch *et al.*, 2009) with a slight difference compared to our experiments (light was applied at different temperatures). We also noted that the relaxation characteristic time for the mobility is significantly shorter than that of the carrier concentration at high temperatures (300K), since the virgin state level is reached in  $\sim 10$  minutes for the mobility while the carrier concentration relaxes to the virgin state in around  $\sim 200$  minutes). This strengthens the claim that, although mobility and carrier density are both enhanced by light illumination, each is affected by a different mechanism.

The cotangent of the Hall angle, as stated previously, behaves as the inverse of the mobility. We thus expect its time dependency to be the inverse of the mobility as is indeed observed.

### 3.9) Resonant Inelastic Xray Scattering

In order to further investigate the PPC and PPS effects on cuprate thin films we have performed preliminary Xray absorption spectroscopy (XAS) and resonant inelastic Xray Scattering (RIXS) measurements. A description of these techniques can be found in section 2.8). These measurements were performed at the SEXTANT beamline of SOLEIL synchrotron.

The rationale of the experiments is to obtain a characterization of the samples in dark –comparing it to the existing literature– and then study the changes observed after visible light illumination. As a matter of fact, we expect RIXS spectra to show changes in the crystal field due to distortions of the oxygen octahedra, which would indicate that light induces changes in the oxygen ordering. Information concerning the electronic configuration of certain atoms can be extracted from typical RIXS spectra by looking at the cuprate dd excitations, as was shown by Magnuson *et al.* (Magnuson *et al.*, 2014) Furthermore, XAS measurements at the Cu L and O K-edges, would allow fingerprinting photo-induced charge transfer effects.

The films were illuminated using UV-blue light of the synchrotron for a duration of 4 hours. By opening the undulator gap and putting the monochromator on the 0<sup>th</sup> order, the visible light from the upstream bending magnet directly illuminates the sample at the exact position of the x-ray beam.

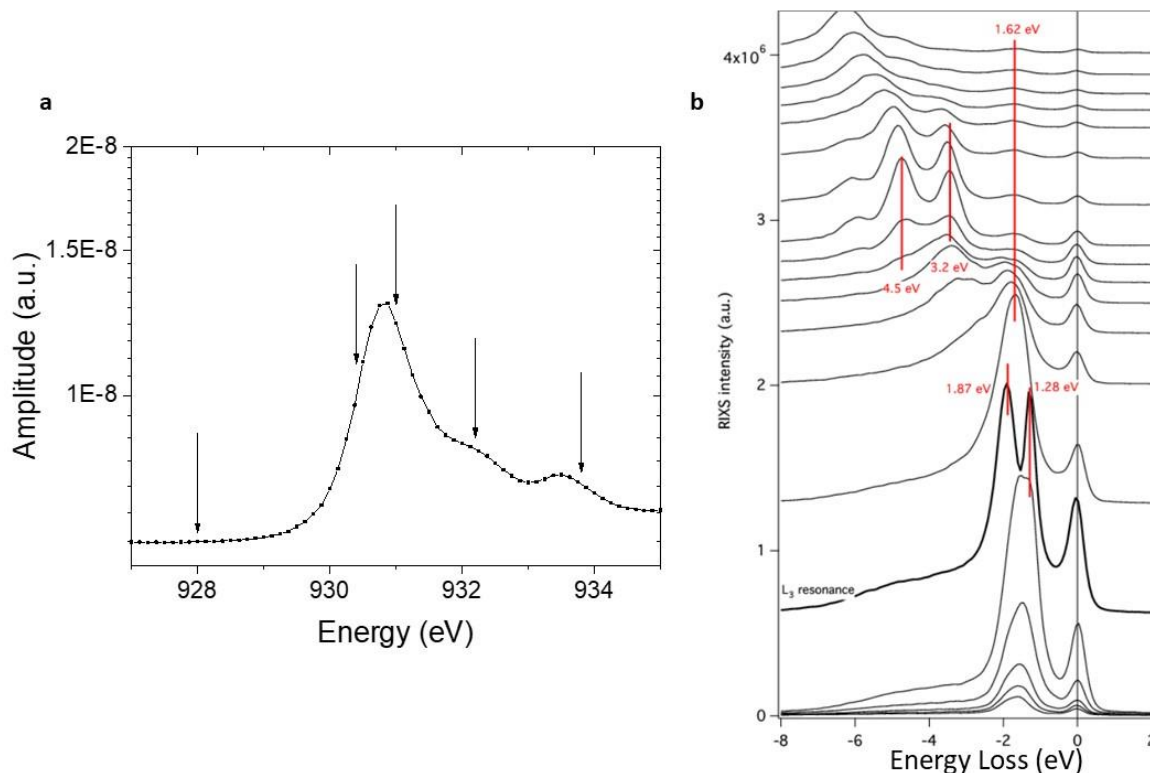


Figure 3-15: (a) XAS spectra at the Cu L edge at  $T = 300\text{K}$  on an oxygen deficient YBCO sample with a nominal oxygen content of 6.4. The black arrows indicate the energies at which RIXS measurements are performed (b) Multiple RIXS spectra obtained by incrementing the energy of the incident photons. The curves are shifted up for clarity. The red lines indicate the Raman peaks.

Figure 3-15a shows a XAS spectra obtained on an oxygen deficient YBCO sample in dark at room temperature at the Cu L edge. One can clearly note the main peak at 930.9eV indicating the presence of Cu atoms in the sample as well as small satellites at 932eV and 933.8eV that have been attributed to Cu atoms present in the planes and chains of YBCO respectively (Magnuson *et al.*, 2014)(Magnuson, Schmitt and Duda, 2018). The black arrows indicate the 5 energies at which a RIXS measurement was performed before and after illumination with visible light.

Figure 3-15b on the other hand shows several RIXS spectra taken at 10K obtained by incrementing the energy of the incident photons between 929.5eV and 935.5eV. This allows to determine the nature and position of the Raman and dd excitation peaks present in the spectra. The red lines indicate the position of Raman peaks that appear at a constant energy when the energy of the incident photon is changed.

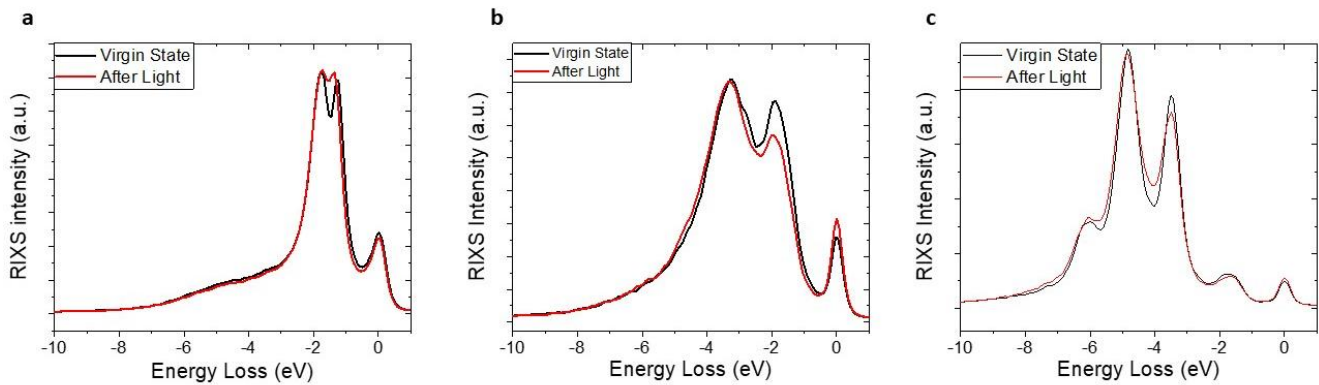


Figure 3-16: RIXS spectra taken on an oxygen deficient YBCO sample with a nominal oxygen content of 6.4 at  $T = 10\text{K}$  before and after illumination with visible light. The energy of the incident photon is (a) 931eV, 932.2eV (b), 933.8eV (c)

Figure 3-16 shows the RIXS spectra taken on an oxygen deficient YBCO film with a nominal oxygen content of 6.4 at  $T=10\text{K}$  before and after illumination with visible light. We notice several qualitative and quantitative changes in these spectra.

We note in Figure 3-16a a shift in the spectra after illumination. **This shift could be attributed to a change in the local symmetry of Cu atoms in the structure.** Furthermore, Figure 3-16b and Figure 3-16c taken at the **planes and chains satellite energies also display a spectral weight shift after illumination.**

However, despite the encouraging effects observed in these spectra, no definite interpretation is possible without further measurements. These would allow to more systematically characterize the changes observed in the spectra after illumination.

### 3.10) Concluding remarks

By investigating the effects of visible and UV light illumination on the two sets of YBCO thin films we have first noted that the mobility of charge carriers is an appropriate parameter to monitor in order to keep track of the deoxygenation and irradiation processes (refer to section 3.3)). Note that the different parameters studied in our films behave in a manner expected from previous work in the literature (refer to section 3.3) and 3.4)).

Furthermore, after illuminating our oxygen deficient samples with visible and UV light we have noted a clear correlation between the changes in the superconducting critical temperature and the changes in the carrier mobility rather than the carrier density refer to sections 3.5) and 3.5.4). On the other hand by comparing the effects of illumination on the two sets of samples we have noted that in order to observe a PPS a change in both the carrier mobility and the carrier density is required (a change in the carrier density alone is not sufficient) c.f. to section 3.6). These observations are summarized in section 3.7) and Figure 3-12.

We have also shown that recovering the virgin state of these samples is possible by allowing the samples to relax at temperatures  $\sim 260\text{K}$  and higher. The resistivity relaxes following a stretch exponential behaviour as is reported in literature. We have also noted that the relaxation of the carrier density and the carrier mobility are characterized by different behaviour as a function of time (refer to section 3.8).

In view of our experimental observations, we find that both microscopic scenarios detailed previously in the chapter, would occur after illumination. The different relaxation rates observed in the carrier density and mobility seem to indicate that, while both are affected by the illumination, their rate of

change is governed by different microscopic mechanisms. The fact that the photo-induced carrier density increase can be decorrelated from any mobility increase in ion irradiated samples, strengthens this claim. We have also shown that the photo-induced increases in mobility are directly correlated to the photo-induced changes in the superconducting properties of the films. This supports the claim that the superconducting changes induced by light arise from structural changes in the film that cannot solely be explained by a photodoping mechanism.

Our results show that it is unlikely that the changes in the mobility originate from a photodoping scenario through a change in the carrier effective mass in a Fermi liquid scenario. Another simple interpretation is that by reducing the scattering rate of carriers, via a photo-induced ordering of oxygen atoms in the CuO chains for example, their mobility would increase. This scenario would be consistent with the changes in the c axis parameter after illumination reported in literature (Lederman *et al.*, 1994), as well as a reduction of the well-known pair breaking scattering dominant in d-wave superconductor (Tolpygo *et al.*, 1996).

In addition, the preliminary RIXS and XAS results shown in section 3.9) hint at the fact that the mobility of carrier is affected by the motion of oxygen ions in the YBCO structure. The planned upcoming RIXS experiments will surely provide us with additional information on the matter.

# 4) Tunnel electroresistance in $YBa_2Cu_3O_{7-\delta}/BiFeO_3 - Mn/Mo_{80}Si_{20}$ vertical tunnel junctions

## Contents

4) Tunnel electroresistance in $YBa_2Cu_3O_{7-\delta}/BiFeO_3 - Mn/Mo_{80}Si_{20}$ vertical tunnel junctions.....	109
4.1) Motivation & key findings.....	110
4.2) Fabrication and structural characterization of the junctions .....	111
4.2.1) AFM & XRD characterization of YBCO/BFO heterostructures .....	112
4.2.2) PFM & CT-AFM characterization of YBCO/BFO heterostructures .....	112
4.2.3) Characterisation of superconducting properties of YBCO and MoSi.....	114
4.2.4) HAADF-EELS of YBCO/BFO/MoSi heterostructures .....	115
4.3) Electrical measurements on the junctions.....	116
4.3.1) Wiring.....	116
4.3.2) As-grown state .....	116
4.3.3) Poling.....	118
4.4) Thickness dependence of BFO layer .....	120
4.4.1) Conductance curves.....	121
4.4.2) Hysteresis loop.....	121
4.4.3) Temperature behaviour .....	122
4.4.4) Size effects .....	123
4.4.5) Effect of the duration of the $V_{pol}$ pulses.....	124
4.4.6) Changing the interlayer and the top electrode .....	125
4.4.7) Retention.....	126
4.4.8) Asymmetry in the poling voltages .....	127
4.5) Temperature and bias analysis of YBCO gap .....	128
4.5.1) BTK modelling of the conductance .....	130
4.6) Model.....	132
4.7) Conclusion.....	133

#### 4.1) Motivation & key findings

One of the objectives of this thesis is the investigation of ferroelectric tunnel electro resistance in superconductor/Ferroelectric/superconductor heterostructures. As described in section 1.6.5.2), one of the key mechanisms invoked to explain the tunnel electroresistance observed in ferroelectric junctions is that the reversal of the ferroelectric polarization modulates the average tunnelling barrier height, which is due to the asymmetric electric-field screening in the dissimilar electrodes that compose the junctions. The initial and primary motivation of this study was addressing a very fundamental question: how does superconductivity, which expectedly alters the electric-field screening, affect that mechanism? A second motivation is studying whether the coupling between the two superconductors through the ferroelectric polarization and the tunnelling of cooper pairs (rather than normal electrons) is affected by the ferroelectric switching (refer to Figure 4-1). Thus, by sandwiching a ferroelectric insulator between two superconducting electrodes, it would theoretically be possible to modulate the Josephson coupling and Josephson current between the two superconducting electrodes, in a reversible and non-volatile fashion. This is something long sought and investigated via different approaches with cuprate superconductors (Balasubramanian *et al.*, 2019)(Bergeal *et al.*, 2008). Theoretical work with ferroelectric barrier was published on the matter (Kittorov *et al.*, 1994) but no experimental work are reported in the literature to the best of our knowledge. Note that several reports have shown that it is possible to modulate the electrical properties of transition metal oxide thin film in a device with a planar geometry through the application of an electric field (Palau *et al.*, 2018; Gonzalez-Rosillo *et al.*, 2019).

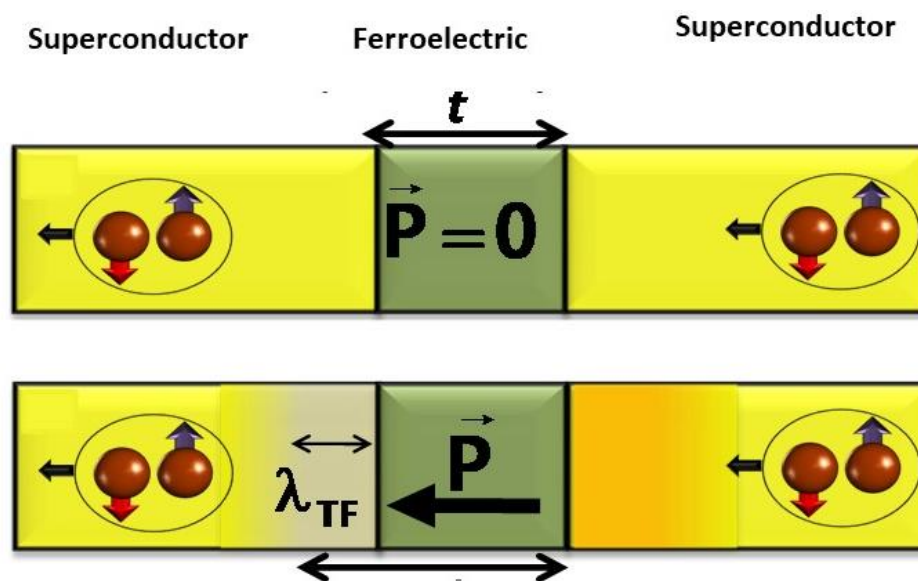


Figure 4-1: Schematic representation of ferroelectric tunnel junction combined with superconductor electrodes. Reversing the polarization of the ferroelectric allows to modulate the tunnelling of Cooper pair rather than normal electrons.

For our study, we have designed heterojunctions composed of  $YBa_1Cu_2O_{7-\delta}$  (superconductor) /  $BiFeO_3$  (ferroelectric) /  $Mo_{80}Si_{20}$  (superconductor). These heterojunctions were designed to boost tunnelling electroresistance mechanisms discussed above. On the one hand, previous work in the group (Bégon-Lours, 2017; Bégon-Lours *et al.*, 2018) shows that this material combination allows for high-quality heterostructures in which the modulation of superconductivity by ferroelectric field-effects (Ahn, Triscone and Mannhart, 2003) has been demonstrated earlier (Crassous *et al.*, 2011; Bégon-Lours *et al.*, 2018) –a priori an interesting ingredient to promote TER. On the other hand, YBCO and MoSi have very different carrier concentration –  $\sim 3 \cdot 10^{20} \text{ cm}^{-3}$  and  $\sim 3 \cdot 10^{22} \text{ cm}^{-3}$  respectively – and consequently the Thomas-Fermi screening length is shorter in MoSi ( $\sim \text{Å}$ ) than in YBCO ( $\sim \text{nm}$ ). Thus,

the pair of electrodes endow the junctions with the asymmetry that expectedly contributes to tunnelling electro-resistance of ferroelectric tunnel junctions.

We have observed a strong reversible modulation of the junction state by applying an external voltage ( $\sim V$ ) between at least two stable states characterized by differences in their conductance of several order of magnitude. However to our surprise, none of the usual microscopic mechanisms behind the ferroelectric tunnel electro resistance phenomena would comprehensively explain the differences observed in the junction behaviour. As a matter of fact, we have observed the same qualitative and quantitative behaviour in heterostructures lacking a ferroelectric barrier. The observed effect is interpreted in terms of an electrochemical reaction occurring at the electrode interfaces. The applied electric field leads to ionic motion (mostly oxygen vacancies) through the junction which alters the electrode ground state. We have observed an increase in the junction electro resistance (ER) between low and high bias measurements under a certain temperature interpreted as the opening of the YBCO superconductor gap. The high conductance state (ON state) is characterized by an optimally doped YBCO electrode however the low conductance state (OFF state) is characterized by an oxygen depleted YBCO electrode. The conductance at low bias in the low conductance state has been fitted according to Blonder-Tinkham-Klapwijk (BTK) theory and the tunnelling junction parameters extracted are consistent with these interpretations. However, the short YBCO c-axis coherence length and the high resistance of our junctions prevented us to observe a Josephson effect in our junctions. One way to remedy this issue would be designing junctions whose interface lies along the YBCO(a-b) crystallographic directions.

#### 4.2) Fabrication and structural characterization of the junctions

The junctions presented in this chapter were all conceived with the same architecture. They can be qualified as a superconductor/ferroelectric/superconductor heterostructure where a ferroelectric BFO layer is sandwiched between a cuprate high  $T_c$  superconductor  $YBa_2Cu_3O_{7-\delta}$  (bottom electrode) and a metallic superconductor  $Mo_{80}Si_{20}$  (top electrode). Figure 4-2 shows a schematic representation of the devices.

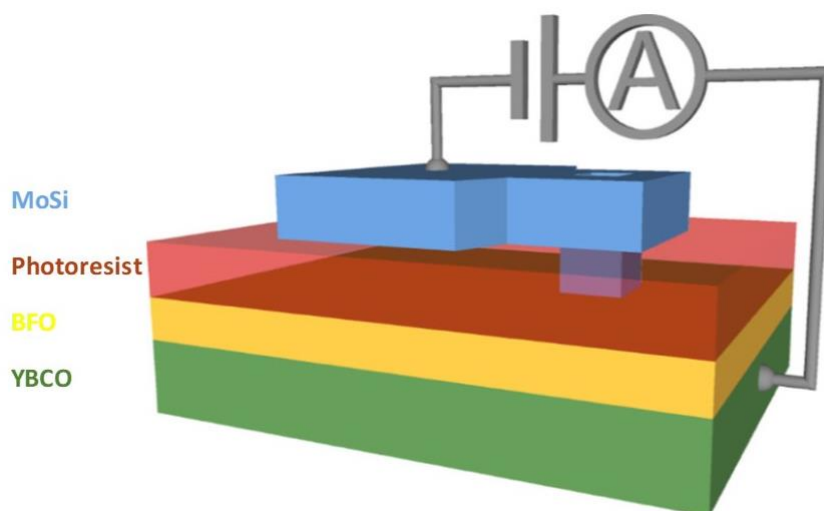


Figure 4-2: Scheme of a typical tunnelling superconductor/Ferroelectric/Superconductor Junction.

The high  $T_c$  superconductor  $YBa_2Cu_3O_{7-\delta}$  has been grown epitaxially by pulsed laser deposition (PLD) on a STO(001) substrate. The growth occurred at a temperature of  $695^\circ\text{C}$  in an  $O_2$  atmosphere of 0.36mbar, the target was ablated at a frequency of 1Hz. The growth of the BFO-Mn layer followed the YBCO growth in situ to ensure a clean interface is obtained between the two materials. Reports

have shown that doping the BFO with manganese (Mn) atoms reduces leakage currents without affecting its multiferroic properties (Kawae *et al.*, 2009). The BFO-Mn layer was grown at a temperature of 695°C in an  $O_2$  atmosphere of 0.36 mbars, the target was ablated at a frequency of 1Hz. An annealing in an  $O_2$  rich atmosphere (800 mbars) was then performed on the heterostructure to reach the targeted oxygen stoichiometries. Note that the growth optimization of these junctions was performed previously in our group. The thickness of the YBCO layer was fixed to 30nm (~30 unit cells) but the thickness of the BFO layer varied between samples typically ranging from 0 nm (no BFO) to 15nm. Once the growth of the BFO-Mn/YBCO bilayer completed, the samples were then taken out of the PLD chamber. The junctions were defined by an optical lithography process detailed in section 2.9.1). The deposition of the  $Mo_{80}Si_{20}$  top electrode was performed by DC sputtering. The MoSi layer was grown at room temperature in an  $2.5 \times 10^{-3}$  mbar atmosphere composed of Ar gas. A lift off step was then performed in order to define the design of the top electrode. In these conditions the MoSi grows in an amorphous manner but retains the electrical and superconducting properties necessary for our experiments.

#### 4.2.1) AFM & XRD characterization of YBCO/BFO heterostructures

Figure 4-3a shows an AFM image taken of the YBCO/BFO-Mn double layer after growth. This image shows the absence of precipitates at the surface of the BFO layer. The height contrast shown in the image is due to the formation of islands.

Figure 4-3b shows XRD spectra measured on the YBCO/BFO double layer. The visible (00l) YBCO family of peaks ensures the growth of a monodomain well defined YBCO phase. The (00l) BFO family of peaks also point to a monodomain growth of BFO-Mn.

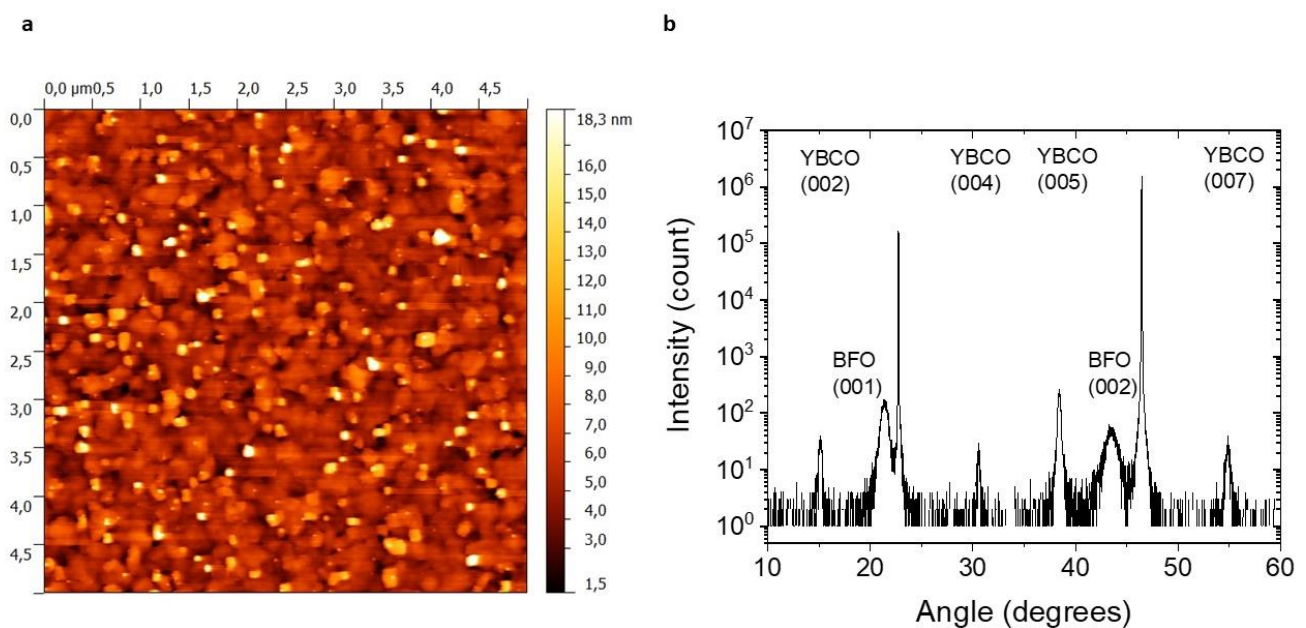


Figure 4-3: (a) AFM image of a BFO-Mn(15nm)/YBCO(30nm) double layer grown on an STO(001) substrate. (b) XRD spectra of a BFO-Mn(15nm)/YBCO(30nm) heterostructure grown on an STO(001) substrate.

#### 4.2.2) PFM & CT-AFM characterization of YBCO/BFO heterostructures

We have performed additional measurements such as PFM and CT-AFM on the YBCO/BFO-Mn bilayer to investigate the ferroelectric properties of the BFO-Mn film after the growth.

Piezoresponse force microscopy (PFM) is a very popular microscopy technique used to investigate the ferroelectric properties of thin films. By applying an AC voltage between the tip and the film one can

monitor both the local topography and ferroelectric properties of a sample. CT-AFM on the other hand, stands for conductive-tip AFM technique allowing to measure the local resistivity of a thin film by applying a voltage between the sample holder and the tip and measuring the corresponding current. A detailed description of these techniques can be found in sections 2.6.1) and 2.6.2) respectively.

Figure 4-4 shows PFM phase and amplitude images of  $YBCO/BFO - Mn$  heterostructures at room temperature with different BFO thicknesses. The protocol followed to obtain these images is the following: A square is first written by applying a positive voltage  $V_{write} > 0$  between the YBCO bottom layer and the PFM tip. This area is shown in Figure 4-4(a-c) in blue. Then a smaller concentric square is written by applying a negative voltage  $V_{write} < 0$  between the YBCO and the PFM tip (shown in yellow on the image).

The phase signal indicates the net polarity under the AFM tip:  $180^\circ$  if the ferroelectric polarization is pointing towards the YBCO layer and  $0^\circ$  if it is pointing outwards. The piezoresponse amplitude counterpart to the phase image is shown in Figure 4-4(b-d). One can note a contrast in the amplitude that corresponds to the written concentric squares. Bégon-Lours et al. (Bégon-Lours *et al.*, 2018) have shown that this implies that, as a positive bias is applied on the heterostructure, only a partial reversal of the BFO polarization (outwards) is achieved due to the pinning of ferroelectric domain walls or to a degradation of its ferroelectric properties. Reports in the literature show that ionic motion can occur in the ferroelectric structure under the influence of an electric field (Band *et al.*, 2020). Note that the ferroelectric properties of the BFO thin film would be affected by the oxygen ion migration resulting from the applied electric field (c.f. section 4.6)

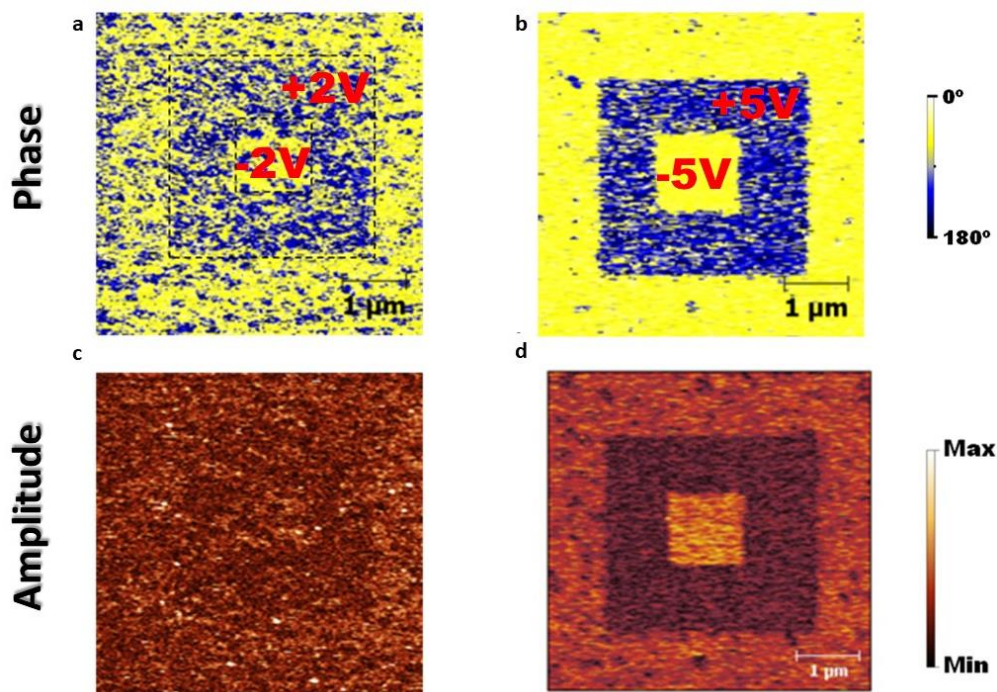


Figure 4-4: Piezoresponse phase and amplitude images of a  $STO(001)/YBCO/BFO(3nm)$  (a-c) and  $STO(001)/YBCO/BFO(15nm)$ (b-d) multilayer. The background represents the virgin state. A square with blue contrast is obtained by applying a writing DC voltage of  $V_{write} > 0$  between the YBCO and the AFM tip. A smaller concentric square (yellow) is obtained by applying a voltage with opposite polarity  $V_{write} < 0$

Figure 4-5a show a PFM phase image of a  $YBCO(30nm)/BFO - Mn(15nm)$  heterostructure. The colour scale indicates the polarity of the writing voltage used and thus the direction of the BFO polarization. Figure 4-5b shows a CT-AFM image taken on the same region of the heterostructure with a reading voltage  $V_{read} = 2V$ . The colour scale indicates the resistance measured across the heterostructure under the bias  $V_{read}$ . It is evident from the aforementioned plots that the resistance measured across the heterostructure greatly depends on the polarity of the writing voltage, which is as expected from the tunnelling electroresistance effect (Garcia *et al.*, 2009)

On the other hand, Figure 4-5c shows the resistance measured across the YBCO/BFO layer in the virgin state by CT-AFM for different thicknesses of BFO in log scale. The resistance measured across the heterostructures in the virgin state (before applying any writing voltage) scales linearly with the thickness of the BFO layer. This is consistent with a direct tunnelling transport regime occurring between the AFM tip, across the BFO-Mn layer and into the YBCO.

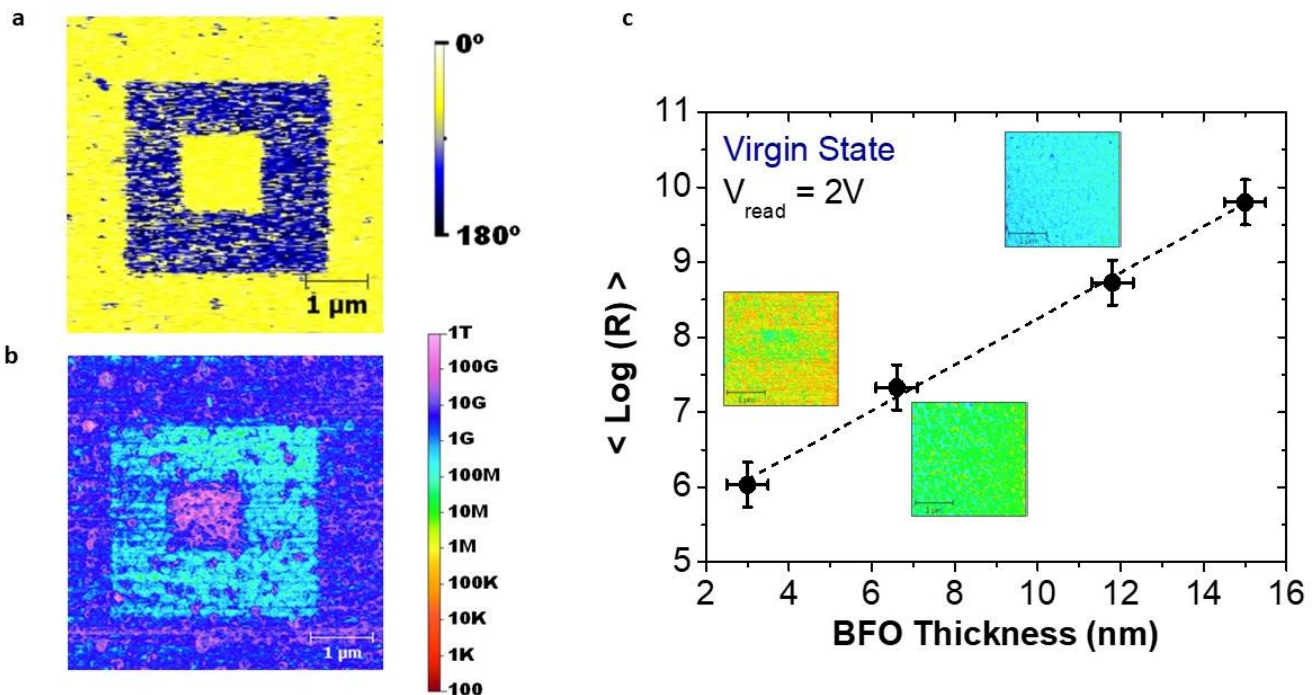


Figure 4-5: (a) PFM phase image of a  $BFO-Mn(15nm)/YBCO(30nm)/STO(001)$  heterostructures. (b) CT-AFM image of the same region on the sample, the colour scale indicates the measured resistance (in  $\Omega$ ) (c) Resistance measured across  $BFO-Mn(15nm)/YBCO(30nm)/STO(001)$  heterostructures as a function of the BFO thickness. The insets indicate the associated CT-AFM images.

#### 4.2.3) Characterisation of superconducting properties of YBCO and MoSi

We have checked the superconducting and transport properties of the various films used to define the junctions studied in this chapter.

Figure 4-6(a-b) show the temperature dependence of the resistance of a grown MoSi film and a YBCO film respectively. Both films present a superconducting transition temperature  $T_c \sim 90K$  for YBCO and  $T_c \sim 6.5K$  for MoSi as is widely observed in literature. Note that the YBCO transport properties were investigated after the junctions have been patterned on the films (following the experimental steps described in section 4.2).

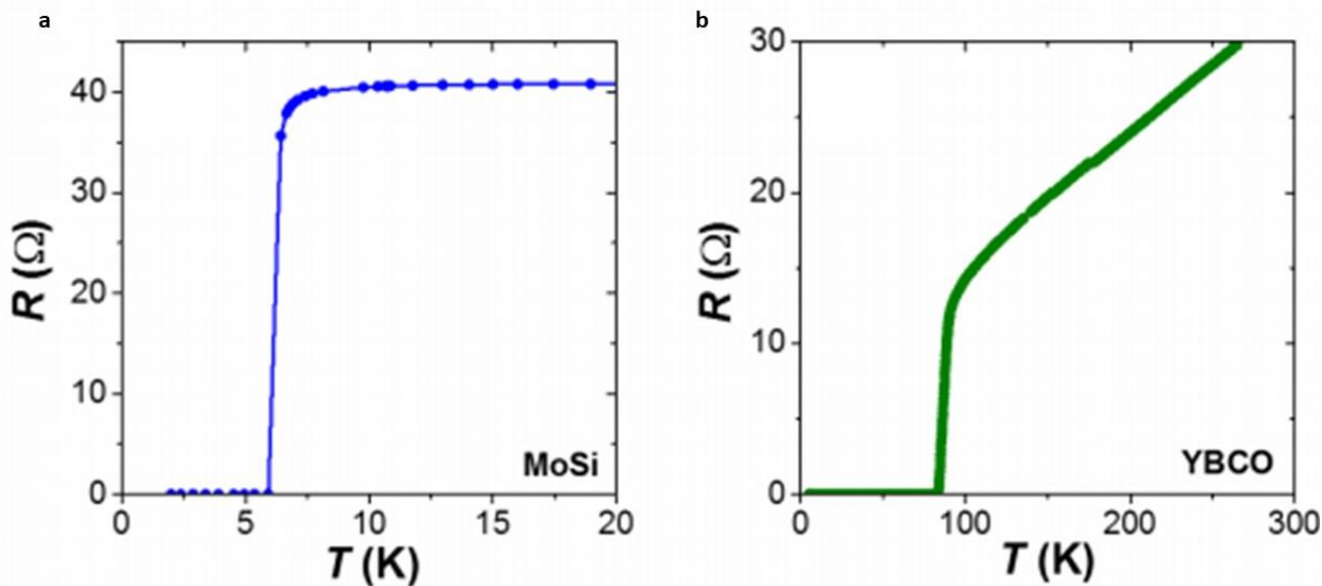


Figure 4-6: Temperature dependence of the resistance of the two superconducting electrodes (a) the top MoSi electrode (b) the bottom YBCO electrode. The measurements are performed using standard 4 point probe technique.

#### 4.2.4) HAADF-EELS of YBCO/BFO/MoSi heterostructures

Figure 4-7a shows a HAADF image of a typical junction in its as-grown state. It highlights the high epitaxial quality obtained in our junctions where one can identify clean and smooth interfaces between the different films.

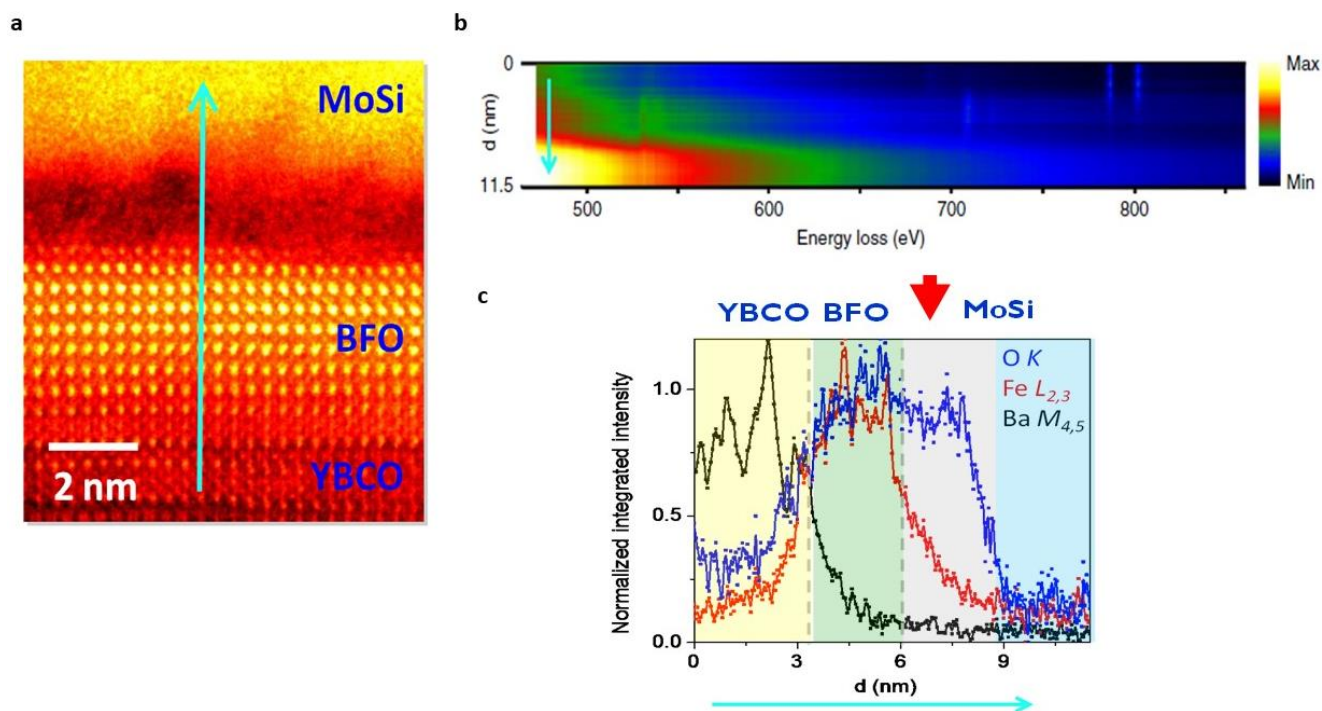


Figure 4-7: (a) Atomic resolution HAADF image of the YBCO/ BFO/ MoSi stack. The light blue arrow indicates the direction of the EELS scan (b) EELS linescan acquired by moving along the stacked sequence of material starting in the bottom YBCO electrode through the insulating BFO barrier and into the top MoSi electrode along the direction of the blue arrow. The edges considered are the O K edge at 528eV, Fe L<sub>2,3</sub> at 709eV and the Ba M<sub>4,5</sub> at 781eV (c) Normalized integrated intensities as a function of travelled distance for the O, Fe and Ba signals in blue, red and black, respectively. The starting point was the YBCO layer and the scan went through the BFO then the MoSi layers. The dashed lines represent the interfaces between the different layers.

Material	Reduction Reaction	Reduction potential $E_0$ (V)
YBCO	$\text{Cu}^{3+} + e^- \rightarrow \text{Cu}^{2+}$	2.4
BFO	$\text{Fe}^{3+} + e^- \rightarrow \text{Fe}^{2+}$	0.7
$\text{Mo}_{80}\text{Si}_{20}$	$\text{Mo}^{3+} + 3e^- \rightarrow \text{Mo}$	-0.2
$\text{Mo}_{80}\text{Si}_{20}$	$\text{Si}^{2+} + 2e^- \rightarrow \text{Si}$	-0.8
ITO ( $\text{In}_2\text{O}_3$ 98%/SnO <sub>2</sub> 2%)	$\text{In}^{3+} + e^- \rightarrow \text{In}^{2+}$	-0.49

Table 1: Reduction potentials of the junction materials. Obtained from (Milazzo and Carioli, 1978)

Analysis of the chemical composition of our junctions can be obtained on the nanoscale with electron energy loss spectroscopy measurements that can be seen in Figure 4-7(b-c). The normalized integrated intensities corresponding to the O K edge (blue), the Fe  $L_{2,3}$  edge and the Ba  $M_{4,5}$  edge is shown for a MoSi/BFO(3nm)/YBCO sample. The Fe and Ba edge allow us to distinguish between YBCO and BFO zones. The thickness of the Fe layer extracted from the Fe edge signal is consistent with the BFO film thickness. **One can note the existence of a rich O layer reaching 2-3nm into the MoSi layer. This hints at the existence of a nanometric highly oxidized MoSi layer present at the BFO interface.** Note that this layer does not extend all the way through the MoSi layer. This can be understood considering the reduction potential of the involved materials as is indicated in Table 1. YBCO has the highest reduction potential leading to a spontaneous oxidation occurring at the interface with the top electrode which would deplete it of oxygen ions. MoSi on the other hand, tends to attract oxygen due to the negative reduction potential of both Mo and Si.

### 4.3) Electrical measurements on the junctions

#### 4.3.1) Wiring

The YBCO bottom electrode was accessed by gently scratching the corners of the films with a diamond tip. It was then contacted with Aluminium (Al) wire and a drop of silver paste was deposited on the wire to ensure mechanical stability and to lower its contact resistance. We have chosen to access the YBCO bottom electrode in this manner in order to avoid an additional IBE (Ion Beam Etch) step since reports have shown that bombarding BFO-Mn with accelerated ions such as with an leads to a change in its transport properties (Begon-Lours, 2017). The top electrode was then contacted with an Aluminium wire as well.

#### 4.3.2) As-grown state

After the junctions have been wired the sample is inserted in the cryostat to perform transport measurements as a function of temperature. The as-grown-state (before applying any important external voltage) is investigated by applying a small bias voltage typically  $-200\text{mV} < V_{bias} < 200\text{mV}$  and the current flowing across the junction is measured. The measured current is then differentiated by the applied voltage to obtain the differential conductance  $G = dI/dV_{bias}$ .  $G$  is typically a square function of the applied bias voltage ( $V_{bias}$ ) indicating a direct tunnelling transport regime (Simmons, 1963) as will be detailed in the next section.

##### 4.3.2.1) BDR modelling of the conductance

A further quantitative analysis of our tunnel junctions was performed by fitting the conductance in the OFF state to a Brinkman, Dynes and Rowell (BDR) (Brinkman, Dynes and Rowell, 1970) model. The conductance depends on the applied voltage through the following expression:

$$\frac{G(V)}{G(0)} = 1 - \left( \frac{A_0 \Delta\phi}{16\phi^{\frac{3}{2}}} \right) eV + \left( \frac{9A_0^2}{128\phi} \right) (eV)^2$$

Where  $\Delta\phi$  is the barrier asymmetry,  $\phi$  is the average barrier height,  $A_0 = 4(2m)^{1/2} \frac{d}{3\hbar}$  where  $m$  is the rest electron mass and  $d$  the barrier thickness. This model assumes that the junction band structure varies slowly compared to the electron wavelength and supposes a trapezoid like barrier with  $\frac{\Delta\phi}{\phi} < 1$  (Brinkman, Dynes and Rowell, 1970). The fitting is performed up to a voltage bias of  $|V| = 100$  mV since the model breaks down for higher bias voltages.

Figure 4-8(a-b) show the fits performed on the conductance curves for a “0nm BFO” sample and a “3nm BFO” sample respectively. A good agreement between the fits and the experimental data is found. The extracted parameters are  $d = 5.0 \pm 0.2$  nm,  $\phi = 0.15 \pm 0.02$  eV and a 20% barrier asymmetry for the “0nm BFO” sample and  $d = 8.0 \pm 0.5$  nm,  $\phi = 0.53 \pm 0.03$  eV and a 13% barrier asymmetry for the “3nm BFO” sample. The barrier height difference between the two junctions is consistent with the BFO thickness. The barrier height  $\phi = 0.15$  in the absence of a BFO layer arises from the decrease of the YBCO work function through electron doping by oxygen vacancies. On the other hand in the case of BFO the barrier height  $\phi = 0.53$  comes from the difference in work functions between BFO ( $\sim 4.7$ eV)(You *et al.*, 2015) and YBCO ( $\sim 5.2$  eV) (Dedyk, Plotkina and Ter-Martirosyan, 1993). A schematic representation of the barrier is presented in Figure 4-8(c-d).

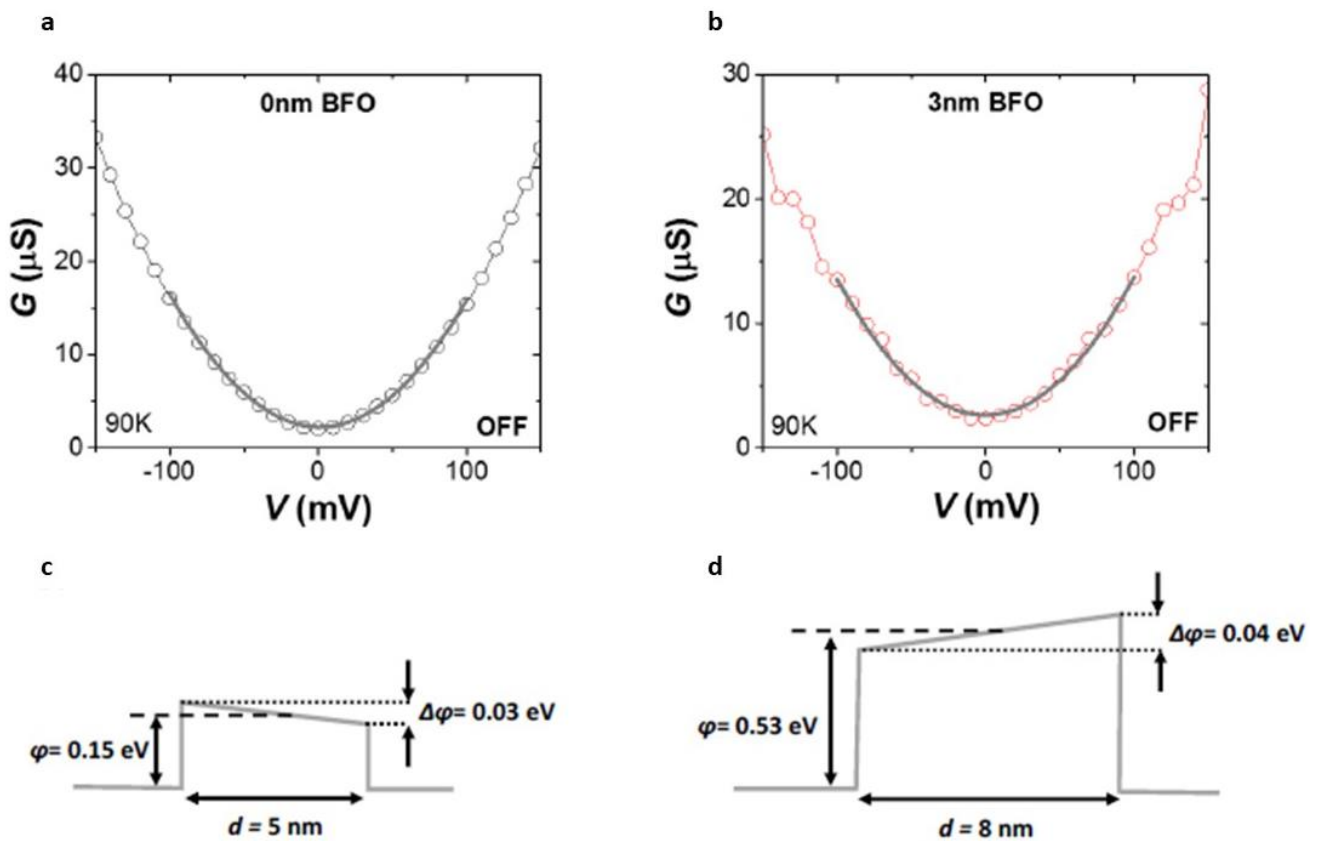


Figure 4-8: BDR fits of the conductance in the OFF state for two samples (a) “0nm BFO” sample and (b) “3nm BFO” sample. Schematic representation of the tunnel barrier for the (c) “0nm BFO” sample and (d) “3nm BFO” sample. The fit parameters  $d$ ,  $\Delta\phi$  and  $\phi$  are shown on the figures for each case.

### 4.3.3) Poling

The protocol followed in order to characterize the transport properties of the junctions is the following: a poling voltage (labelled  $V_{pol}$ ) of several volts is first applied on the junction to switch its resistive state then a smaller bias voltage  $V_{bias}$  is applied to measure its conductance. The poling voltage was applied gradually over tens of seconds: starting from 0V the voltage was increased until it reached the target  $V_{pol}$  followed by a gradual decrease to 0V. Figure 4-9(a-b) show the typical current (I) vs voltage curves during poling, measured for different maximum values of  $V_{pol}$  for positive and negative voltages respectively. The poling voltages did not exceed 6V in absolute value for these junctions. After applying the poling voltage  $V_{pol}$ , a low bias voltage (below 200 mV) is applied on the junction and the resulting current is measured from which G is calculated in a similar fashion than the virgin state measurements. Figure 4-9(c-d) show the differential conductance as a function of the bias voltage measured for after applying different values of  $V_{pol}$ . The maximal and minimal differential conductance (for  $V_{pol} = 4V$  and  $V_{pol} = -4V$ ) are labelled ON and OFF state respectively. In general, for the remainder of this manuscript the ON state will correspond to  $V_{pol} > 0$  and the OFF state to  $V_{pol} < 0$ .

The differential conductance curves corresponding to different poling voltage are significantly different. The ON state is characterized by a high conductance and a linear background. However, the OFF state is characterized by a conductance several order of magnitude lower and a roughly parabolic background. Note that the conductance measured for different poling voltage represents a remnant state since the effects studied are non-volatile and conserve their properties for as long as we can measure.

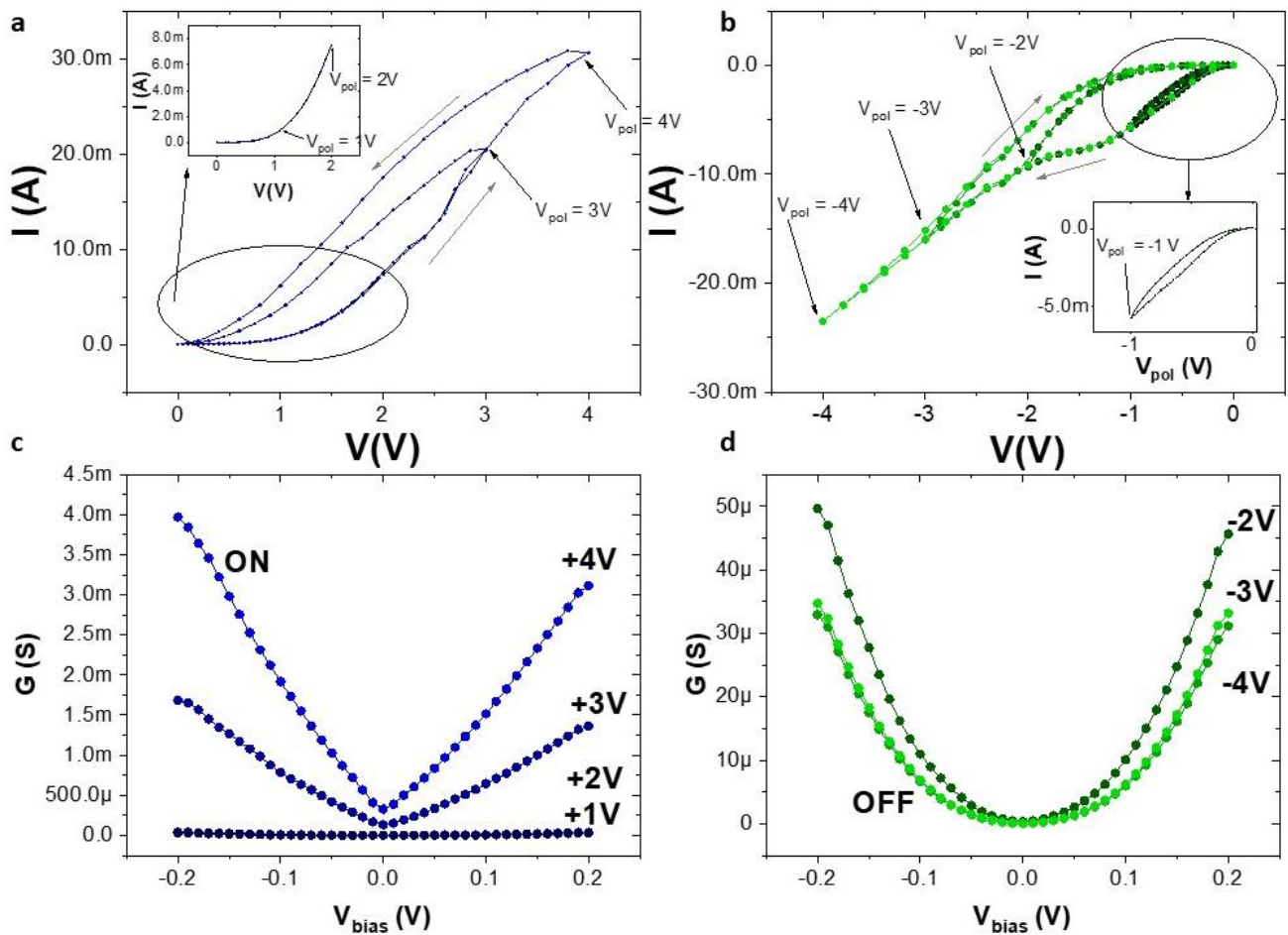


Figure 4-9: (a-b) Poling voltage dependence of the current measured across MoSi/BFO/YBCO junctions. The poling voltage is applied gradually from 0V to  $V_{pol}$  and back to 0V. The arrows indicate the hysteresis observed in the measured current (c-d) Bias voltage dependence (-200mV/200mV) of the differential conductance measured after each poling IV curve. The corresponding poling voltages are indicated next to each curve.

Figure 4-10a shows the differential conductance calculated at a bias voltage of 100mV in the remnant state as a function of the poling voltage for a YBCO/BFO(3nm)/MoSi junction at  $T = 3.2K$ . Note that these measurements are obtained after cycling from negative to positive poling voltages and vice versa to ensure the reproducibility of the switching mechanism. Full switching is obtained at values in the  $\sim V$  range and is asymmetric with respect to the polarity of the voltage. Typically switching from the OFF state to the ON state requires a higher voltage than vice versa.

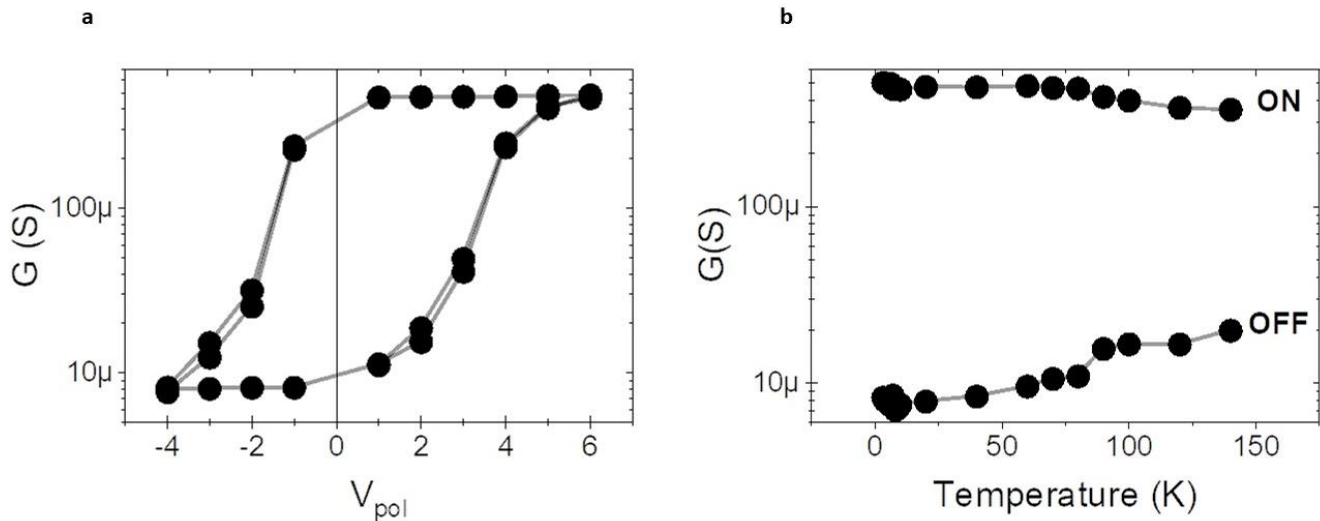


Figure 4-10: (a) Differential conductance vs poling voltage in a YBCO/BFO/MoSi junction at low temperature. Multiple cycles of the poling voltage are performed during this measurement (b) Temperature dependence of the differential conductance in a MoSi/BFO/YBCO junction in the ON and OFF states ( $V_{pol} = 4V$  and  $V_{pol} = -4V$ ). The poling voltage is applied at low temperature.

Finally, Figure 4-10b shows the temperature dependence of the differential conductance calculated at a bias voltage of 100mV in the remnant state after applying a polarization voltage at  $T = 3.2K$  for the ON and OFF states. We can see that the conductance in the ON and OFF states have different temperature behaviours. While in the ON state the conductance is nearly constant or slightly decreases over the whole temperature range, it increases steadily as a function of temperature in the OFF state. The conductance in the OFF state has an exponential dependence on the temperature which is reminiscent of a direct tunnelling regime. On the other hand, the temperature behaviour of the ON state is more complex and requires further analysis.

In summary, we have observed a fast, non-volatile and reversible change in the conductance state of YBCO/BFO/MoSi junctions upon the application of an external voltage of the order of a volt. This effect is similar both qualitatively and quantitatively to what is observed in ferroelectric tunnel junctions reported in the literature.

#### 4.4) Thickness dependence of BFO layer

In this section we will present the effect of the thickness of the BFO-Mn layer on the nature and magnitude of the TER effect. **We have varied the thickness of the ferroelectric from 15nm down to zero nm (without any ferroelectric barrier) and have observed the same qualitative features of the TER effect.** As previously stated, the possible mechanisms behind ferroelectric tunnel junctions in literature are three fold: the charge accumulation at the different interfaces leads to partial screening in the metallic electrodes (because of different Thomas-Fermi length) and thus to an asymmetric potential profile across the tunnelling barrier, orbital hybridization at the interface that might alter the tunnelling probability of electrons and the inverse piezoelectric profile that will affect the barrier characteristics (Tsymbol and Kohlsted, 2006)(Pantel and Alexe, 2010). To our surprise none of these mechanisms laid at the source of the TER effect observed in our YBCO/BFO/MoSi junctions since it was observed in the absence of any ferroelectric barrier. After presenting the different characteristic of the TER effect, we will describe the modified superconducting properties of the YBCO bottom electrode in the next section. We will then cover the microscopic model at the heart of this effect which is based on a reversible redox reaction.

#### 4.4.1) Conductance curves

Figure 4-11 presents the differential conductance  $G$  as a function of the bias voltage  $V_{bias}$  in the ON and OFF states at  $T = 3.2K$  for three different samples: A sample with a 15nm BFO barrier (blue), a sample with a 3nm BFO barrier (red) and a sample without any BFO (black). We can clearly see the existence of a significant TER effect in all three samples (differences in conductance are of many orders of magnitude). Note that the OFF state measured on the 15nm sample was too resistive and could not be accurately measured (its conductance is lower than the experimental resolution of  $10^{-8}$  S). We also note that the qualitative shape of the differential conductance is the same for the same state in all three samples: the linear background, high conductance and the visible dip in the conductance at low bias for the ON state and the parabolic background and low conductance for the OFF state.

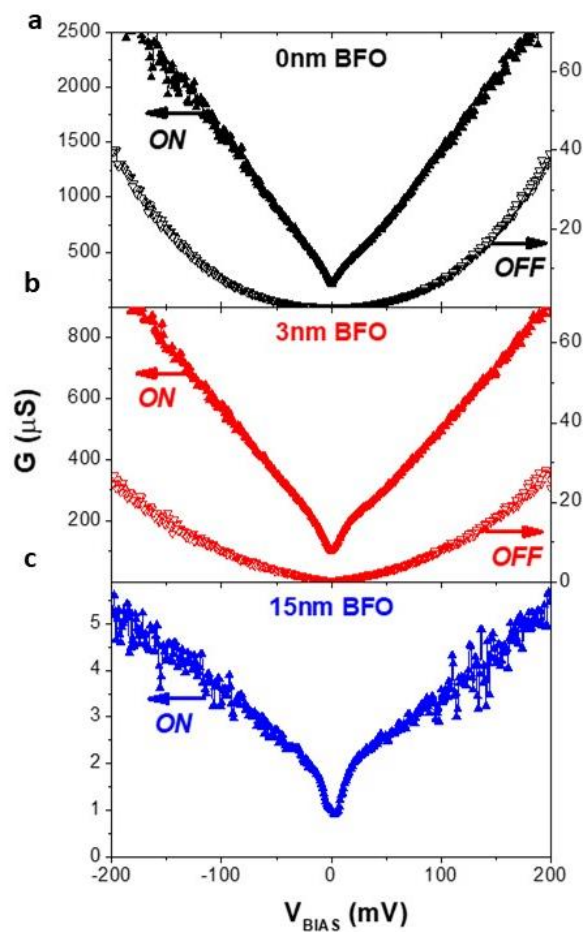


Figure 4-11: Differential conductance as a function of the bias voltage for samples of different BFO thicknesses at a temperature  $T = 3.2K$  for (a) no BFO-Mn, (b) 3nm BFO-Mn and (c) 15nm BFO-Mn. The OFF state in (c) is too resistive to measure.

#### 4.4.2) Hysteresis loop

Figure 4-12 shows the differential conductance at low temperature calculated at  $V_{bias} = 0$  mV and  $V_{bias} = 100$  mV, labelled  $G_0$  and  $G_{100}$  respectively, as a function of the poling voltage for the three samples stated previously. One can see that the asymmetry observed in the hysteresis loops of the samples with a BFO barrier is also present in the “0 nm BFO” sample i.e. the voltage required to polarize the junction from the OFF state to the ON state is higher than vice versa. We define the electroresistance ER as the ratio between the conductance in the ON state and the OFF state ( $ER \equiv G_{ON}/G_{OFF}$ ). Note that the tunnel electroresistance effect is most efficient at low bias voltage. One can clearly see from Figure 4-12a that  $ER_0 \sim 5000$  at  $V_{bias} = 0$  mV and  $ER_{100} \sim 150$  at  $V_{bias} =$

100 mV. The same can be said about the electroresistance measured in the 3nm BFO sample. It appears this increase in the electroresistance at low bias is connected to the superconductivity of the YBCO electrode as will be explained in section 4.5).

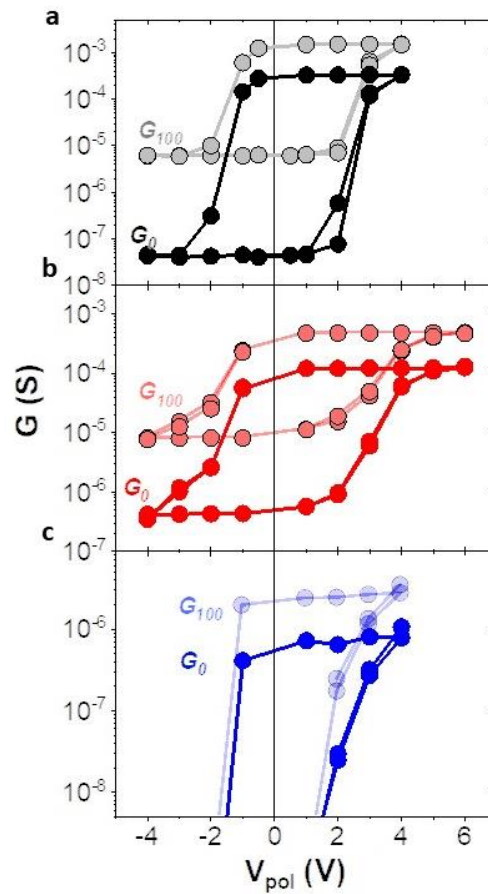


Figure 4-12: Differential conductance at a bias voltage of 100 mV vs poling voltage ( $V_{pol}$ ) for samples (a) no BFO-Mn, (b) 3nm BFO-Mn and (c) 15nm BFO-Mn at a temperature  $T = 3.2K$ .

#### 4.4.3) Temperature behaviour

We investigated the temperature dependence of the differential conductance of the three samples mentioned previously. The poling occurred at a temperature of  $T = 3.2K$  and the remnant state properties were measured subsequently as a function of temperature. Figure 4-13(a-c) shows the temperature behaviour of  $G_0$  and  $G_{100}$  in the ON and OFF states. One can see that the same qualitative behaviour is observed in the sample without a ferroelectric barrier when compared to the other two. The conductance in the ON state varies little over the temperature range contrary to the OFF state where it seems to follow an exponential behaviour at high temperature (highlighted by the straight lines drawn on the graph in log scale). The behaviour in the ON state is similar to what is observed in literature concerning ferroelectric tunnel junctions between metallic electrodes (Bruno *et al.*, 2016).

We can also see a difference in behaviour of the conductance as a function of the bias voltage. In the OFF state  $G_{100}$  seems to conserve the exponential behaviour down to low temperature but  $G_0$  on the other hand deviates from its high temperature behaviour at a temperature close to 85K. The green area highlights the deviation from its high temperature behaviour. The same temperature dependence can be seen for the 3nm sample (Figure 4-13b).

This behaviour can also be seen on the temperature behaviour of the ON state but is less striking. As a matter of fact, a small drop of  $G_0$  occurs under a temperature close to 80K. This can be seen from

Figure 4-13e which shows the behaviour of  $G_0$  as a function of temperature in the ON state for the 3nm BFO and 15 nm BFO samples. The linear scale used in the figure highlights the temperature at which the differential conductance departs from its high temperature behaviour.

Figure 4-13d shows the ratio of electroresistance between 0mV bias and 100mV bias calculated from the previous graphs as a function of temperature. Both curves show an increase in the ratio  $ER_0/ER_{100}$  below  $T \sim 80K$  with the highest upturn observed in the “0 nm BFO” sample where the ratio reaches approximately 30 at low temperature. The temperature behaviour of the ER hints at superconductivity being the source of this effect as we shall see in the section 4.5).

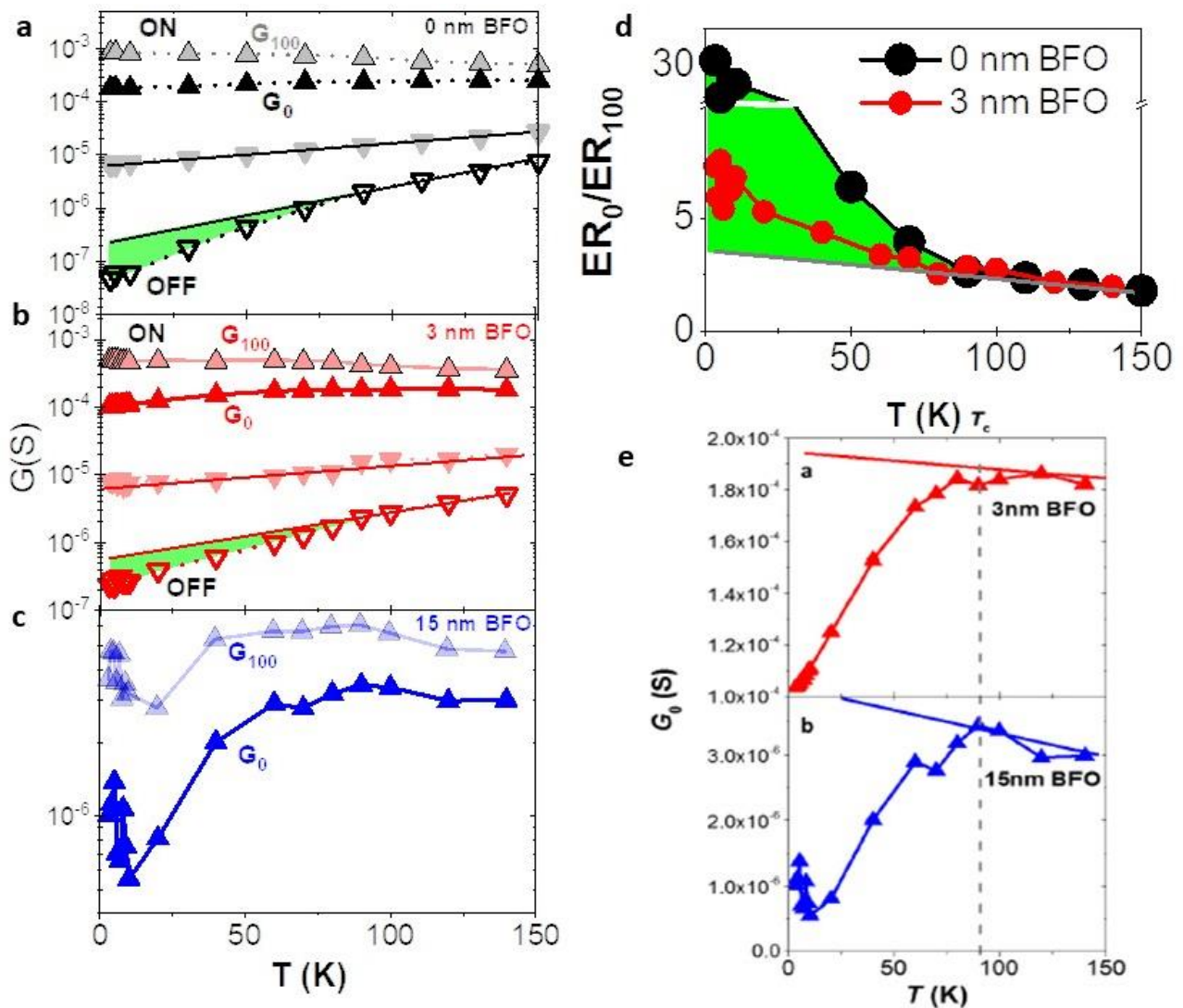


Figure 4-13: (a-c) Differential conductance vs temperature for both the ON and OFF states at  $V_{bias} = 100mV$  and  $V_{bias} = 0mV$ . The straight line in the OFF states are an extrapolation of the conductance at high temperature (d) Temperature dependence of the electroresistance at 0mV bias and 100mV bias for the first two samples. The green area highlights the deviation of the conductance at low temperature from its high temperature behaviour (e) Differential conductance vs temperature in the ON state for the 3nm and 15nm BFO samples in linear scale.

#### 4.4.4) Size effects

Transport measurements were performed on a series of junctions with different sizes ranging from  $1\mu m^2$  to approximately  $200\mu m^2$  square junctions. In Figure 4-14(a-c) we show the differential conductance calculated at 100mV ( $G_{100}$ ) normalized by the junction area in the ON and OFF states for the same samples shown previously. We note that the conductance in the OFF state is directly

proportional to the junction area whilst it is not in the ON state. This behaviour has been observed in ferroelectric tunnel junctions (Boyn *et al.*, 2016).

In the ON state the conductance scales with the perimeter of the junction as can be seen from Figure 4-14(d-f). This is also expected from the behaviour of ferroelectric tunnel junctions (Kohlstedt *et al.*, 2008)(Boyn *et al.*, 2016) since it has been previously shown that when applying the poling voltage the resulting electric field is highest at the junction periphery. The resistive switching thus occurs at the periphery of the junctions in the ON state rather than its centre. On the other hand, in the OFF state the conductance scales with the area suggesting that the conduction occurs over the junction as a whole. This scaling in the OFF state points to a tunnelling transport regime and rules point-like transport mechanisms such as filaments or pinholes (Gruverman *et al.*, 2009).

In addition, quantitative comparison between the ratios shown in Figure 4-14 ( $G_{100}/A \sim 10^{-8} S \cdot \mu m^{-2}$  and  $G_{100}/P \sim 10^{-5} S \cdot \mu m^{-1}$ ) and the values measured in standard ferroelectric tunnel junctions show comparable values (Boyn *et al.*, 2016).

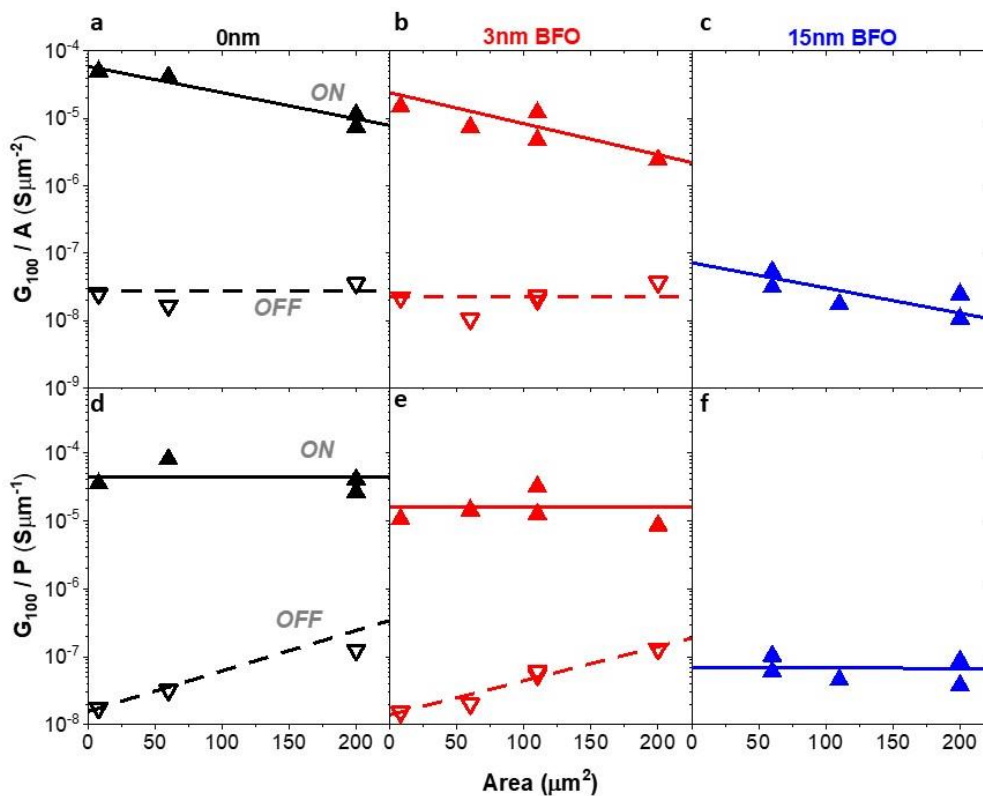


Figure 4-14: Area dependence of the normalized conductance at a bias voltage of 100mV normalized by the junction area (a)-(b)-(c) and by the junction perimeter (d)-(e)-(f) for samples with different BFO-Mn thicknesses in the ON and OFF states. The straight lines are added as a guide to the eye.

#### 4.4.5) Effect of the duration of the $V_{pol}$ pulses

We found no significant dependence of the above effect on the duration of the pulses  $V_{pol}$  used to produce the resistive switching. In Figure 4-15 we show the differential conductance as a function of the bias voltage for different samples at  $T = 3.2K$  in the ON and OFF states. The poling voltage ( $\sim V$ ) was applied in a single short pulse subsequently followed by the conductance measurements. The conductance measurements obtained after applying a DC pulse are shown for comparison. **A TER effect, i.e. a fast, non-volatile and reversible change in the conductance of the junction, is observed after applying the poling voltage  $V_{pol}$  in a nanosecond pulse.** The poling efficiency seems to be

conserved when the duration of the pulse is severely decreased down to the ns range as can be seen from Figure 4-15(a-b) where one can see that the same resistive switching occurs in the “3nm BFO” sample with a DC pulse and a 250ns pulse. On the other hand, in the “0nm BFO” sample the resistive switching occurs over three orders of magnitude during a DC pulse and over 2 orders of magnitude in a 500ns pulse. Note that an analogous behaviour can be seen in standard ferroelectric tunnel junctions (Garcia and Bibes, 2014)(Boyn *et al.*, 2016).

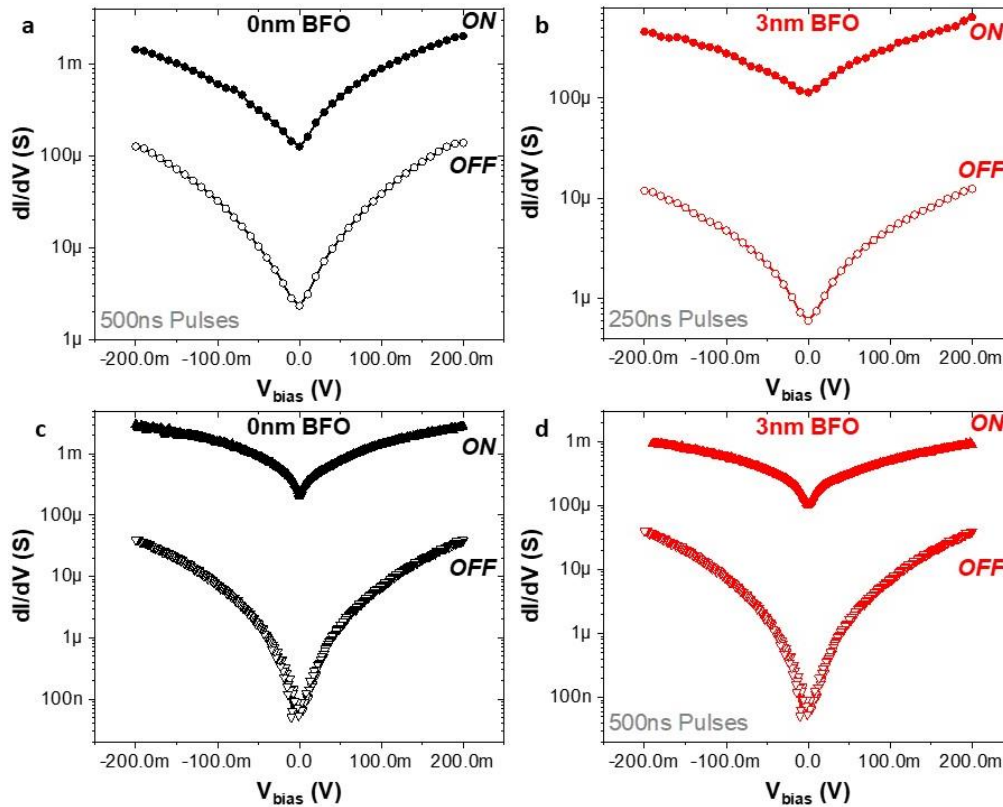


Figure 4-15: Differential conductance vs bias voltage on a « 0nm » BFO sample and a 3nm BFO sample, after applying the poling voltage during (a-b) short nanosecond pulses and (c-d) DC pulses. The differential conductance is calculated from the measured current while applying a bias voltage as previously explained.

#### 4.4.6) Changing the interlayer and the top electrode

In order to deepen our understanding of the mechanism behind these effects, we have performed resistive switching experiments on slightly different samples. In the first case we changed the ferroelectric interlayer BFO to a non-ferroelectric SrTiO<sub>3</sub> band insulator oxide. Figure 4-16(a-b) shows the ratio of differential conductance in the ON and OFF states calculated at a bias of 100mV as a function of the poling voltage for a BFO and an STO interlayer respectively. We can see that a resistive switching behaviour, quantitatively and qualitatively analogous to what is found in the literature, can be observed in a sample without a ferroelectric barrier. This shows that ferroelectricity does not play a major role in the resistive switching occurring in these junctions.

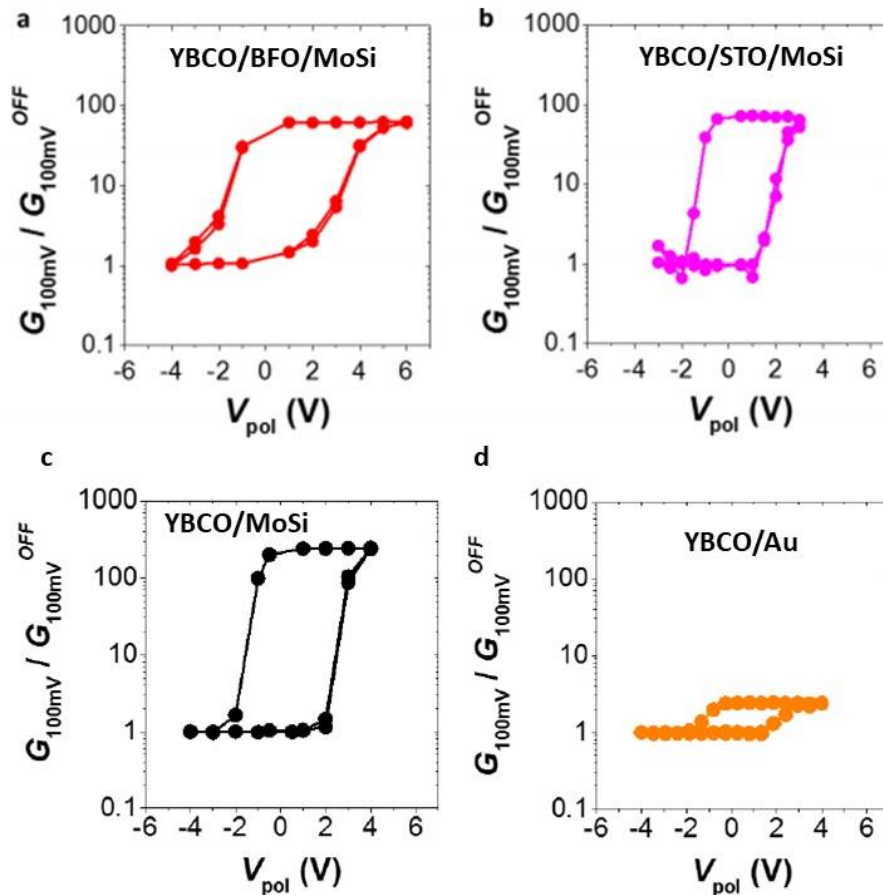


Figure 4-16: Differential conductance at a bias voltage of 100 mV normalized by the conductance at 100 mV of the OFF state as a function of the poling voltage for samples with different insulating barriers. (a) A junction with a ferroelectric barrier (MoSi/BFO(3nm)/YBCO), (b) a junction with a non-ferroelectric barrier (MoSi/STO(3nm)/YBCO) show the same qualitative and quantitative behaviour (c-d) junctions where the interface between the two materials is the barrier.

On the other hand, Figure 4-16(c-d) shows the ratio of differential conductance in the ON and OFF states calculated at a bias of 100mV as a function of the poling voltage for samples with different top electrodes. We note that by changing the top electrode to a noble metal such as gold (Au), a resistive switching effect is still observed but its efficiency is greatly diminished: from 2 orders of magnitude in a MoSi/YBCO sample to less than an order of magnitude for an Au/YBCO sample. Note that this behaviour was expected from literature (Plečenič *et al.*, 1998) since a resistive switching of the same order of magnitude is reported in YBCO/normal metal junctions. This shows that the use of a metal that tends to oxidize is necessary to observe a large resistive switching effect.

#### 4.4.7) Retention

As was stated earlier the TER effect observed in these junctions is reversible and non-volatile. Retention measurements were performed on different samples where positive and negative voltages are applied repeatedly on a given junction to switch between the ON and OFF states. Figure 4-17 shows the differential conductance calculated at a bias of 100mV in the ON and OFF states as a function of the number of cycles (switching from ON to OFF and then vice versa) for three different samples. We can see that the “0nm BFO” sample can be reversibly switched between ON and OFF states approximately 250 times before breakdown. No breakdown of the junction properties for the “3nm BFO” was observed for over 500 cycles. Note that when the top electrode was replaced from MoSi to Au, a much smaller resistive switching occurs that disappears after 100 cycles.

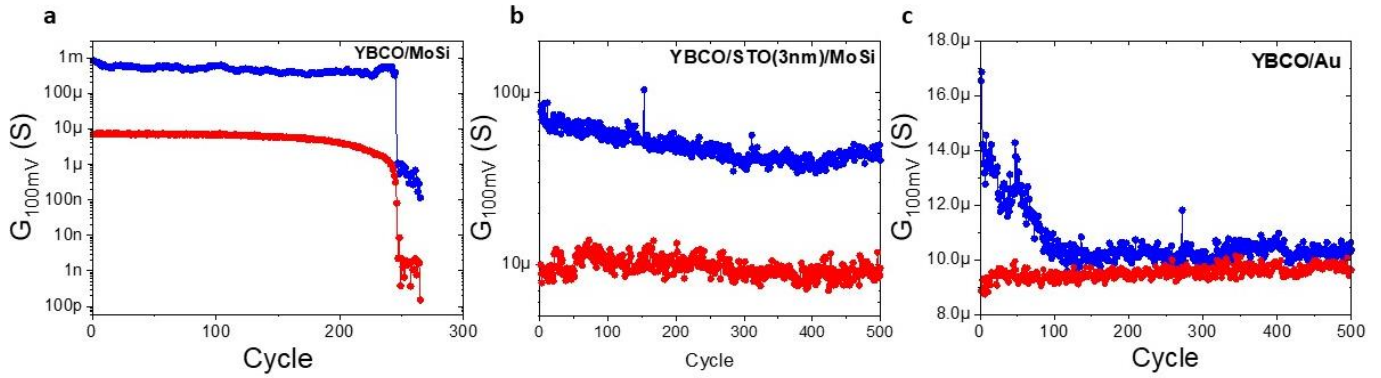


Figure 4-17: Differential conductance as a function of poling cycles for samples (a) YBCO/MoSi (b) YBCO/STO(3nm)/MoSi and (c) YBCO/Au junctions at a temperature of  $T = 3.2\text{K}$  in the ON (blue) and OFF states (red). The x axis represents the number of times the usual protocol (applying a poling voltage then a smaller bias voltage to calculate the differential conductance) is applied.

#### 4.4.8) Asymmetry in the poling voltages

Figure 4-18 shows the poling voltages required to switch between the ON and OFF states and vice versa for different samples. The samples that are depicted in this figure exhibit a resistive switching of approximately two orders of magnitude. The switching voltage has been defined as the voltage at which  $(G_{100} - G_{100}^{OFF})/G_{100}^{ON} = 0.5$ . The different samples include samples with direct contact between YBCO and MoSi, YBCO and  $\text{In}_2\text{O}_3$  98%/SnO<sub>2</sub> 2% (ITO) as well as samples with BFO and STO interlayers respectively sandwiched between YBCO and MoSi layers. The spread in the measurements shown in the figure arises from the fact that different devices are measured in each case. We note the asymmetry observed between the poling from ON to OFF ( $\sim 3.5\text{V}$ ) and vice versa ( $\sim -1\text{V}$ ). In addition, the poling voltages are rather similar for all samples indicating that their common denominator (the YBCO layer) plays an important role in the switching mechanism. As a matter of fact, the OFF to ON poling voltage is similar to the difference of reduction potential  $\Delta E_0$  calculated between different electrodes (c.f. Table 1) and represents the voltage required to reverse the spontaneous oxidation of the YBCO electrode.

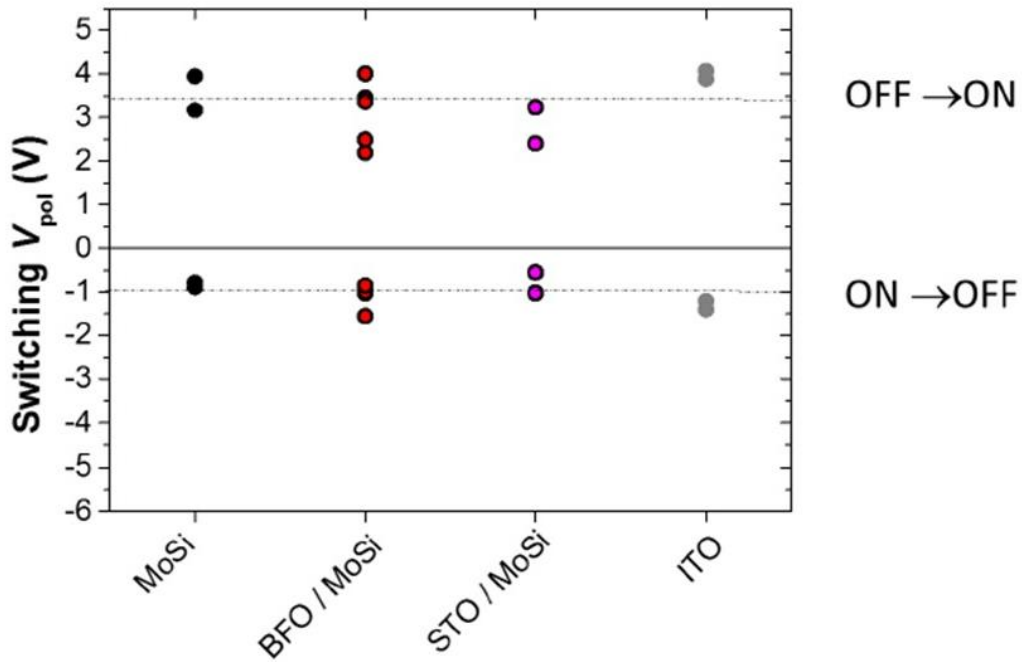


Figure 4-18: Poling Voltages required to switch between ON and OFF states for junctions with different top electrodes and different barrier materials. The switching amplitude is similar in all junctions (approximately 2 orders of magnitude). The switching voltage is defined as  $(G_{100} - G_{100}^{OFF})/G_{100}^{ON} = 0.5$ .

#### 4.5) Temperature and bias analysis of YBCO gap

As previously mentioned, we have observed an enhancement of the ER at low temperature in our junctions. The temperature behaviour of this enhancement hinted at a link between the behaviour of the conductance at low bias and the superconducting properties of the YBCO electrode. A systematic study of the differential conductance in the ON and OFF states as a function of the bias and the temperature is presented in this section.

Figure 4-19(a-b) shows the temperature dependence of the normalized differential conductance  $g$  (obtained by dividing the differential conductance by the conductance at  $V_{bias} = 60mV : G_{60mV}$ ) in the ON and OFF states of a MoSi/BFO(3nm)/YBCO junction. Note that the poling voltage was applied at low temperature. The qualitative features of these curves are similar to the ones reported in literature between a YBCO electrode and a metallic contact (Gurvitch *et al.*, 1989)(Plecenik *et al.*, 1998). As the temperature is decreased a dip in the conductance starts appearing at low bias in both the ON and OFF states. This dip in the conductance is directly related to the opening of a superconducting energy gap under  $T_c$ .

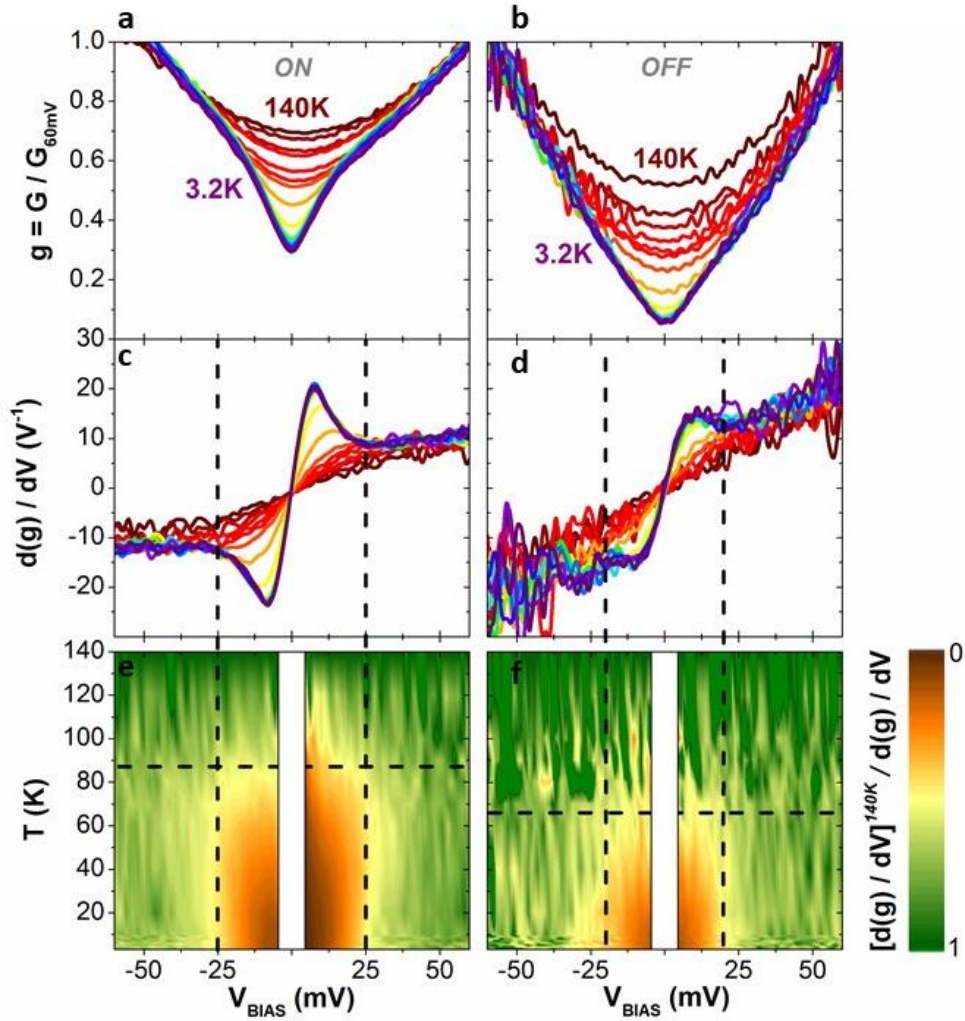


Figure 4-19: Differential conductance normalized to the conductance at 60 mV as a function of the bias voltage for different temperatures in the (a) ON and (d) OFF states for the 3nm BFO-Mn sample. Plots (b) and (e) show the derivative of the differential conductance with respect to the bias voltage in the ON and OFF states. Plots (c) and (f) show a color plot of the normalized derivative of the differential conductance as a function of the bias voltage and the temperature. The dotted lines represent the superconducting YBCO gap (vertical lines) and the superconducting transition temperature of YBCO (horizontal lines).

In order to characterize the temperature and bias dependence of this feature, the derivative of the differential conductance  $dg/dV_{bias}$  with respect to the applied bias is shown in Figure 4-19(c-d) and plotted in a normalized colour plot shown in Figure 4-19(e-f). The colour plot scale has been normalized to the value of that derivative at 140K thus a ratio of 1 corresponds to the high temperature trend shown in green. On the other hand, deviations from this value fall within the yellow and brown regions on the colour plot. This data representation allows us to estimate the superconducting critical temperature  $T_c$  (shown by the dotted horizontal lines) and the superconducting gap (shown by the vertical lines). By comparing Figure 4-19(e-d) we see that the gap region is defined between  $T_c \sim 90\text{K}$  and  $\Delta_{YBCO} \sim 25\text{meV}$  in the ON state and  $T_c \sim 70\text{K}$  and  $\Delta_{YBCO} \sim 20\text{meV}$  in the OFF state which correspond to values observed in both optimally doped and underdoped YBCO respectively.

Thus, by changing the conductance state of a MoSi/BFO/YBCO junction through the application of an external voltage we are able to change the ground state of the superconducting electrode. By reversing the conductance state from OFF to ON, the electrode ground state changes from a

depressed superconductive state to an optimal superconducting state and vice versa. The properties of a cuprate superconductor can be tuned through several means amongst which the control of its oxygen stoichiometry (Tallon *et al.*, 1995).

Note that no features corresponding to the MoSi gap have been observed in these junctions. It is of the order of 1 mV which renders features attributed to it below our experimental resolution.

#### 4.5.1) BTK modelling of the conductance

As was stated previously the superconducting energy gap of YBCO opens below  $T_c$  and this spectroscopic feature can be seen on the conductance curves shown previously. This event is closely related to the enhancement of the ER at low temperature and bias. The opening of a superconducting gap would lead to the majority of the tunnelling current at low bias being carried by quasiparticle excitations rather than normal electrons. The spectroscopic features arising from this change - observed in the conductance spectra- can be analysed through the lens of Blonder-Tinkham-Klapwijk theory (BTK) describing the interface between a normal metal (N) and a superconductor (S). More specifically the conductance can be analysed using a dimensionless parameter “Z” attributed to the barrier strength.  $Z = 0$  indicates a transparent interface and  $Z \gg 1$  a low transparency barrier (Blonder, Tinkham and Klapwijk, 1982).

The present analysis is made using a BTK formalism (see section 1.6.5.1) concerning c-axis tunnelling into a d-wave superconductor. (Wei *et al.*, 1998)(Kashiwaya *et al.*, 1995). The conductance in the superconducting state  $g_s$  is defined as the conductance at  $T = 3.2K$  and the conductance in the normal state  $g_n$  as the conductance at  $T = 90K$  and  $T = 70K$  in the ON and OFF states respectively. The parabolic background was subtracted from the curves (fitted the conductance curves between 30mV and 100mV) since the general BTK model used does not consider the background conductance. Finite quasiparticles are introduced into the model by the dimensionless parameter  $\Gamma$  (Dynes, Narayanamurti and Garno, 1978) and inhomogeneities present in the superconductor (Feigel’Man and Skvortsov, 2012) were considered to account for broadening effects on the conductance.

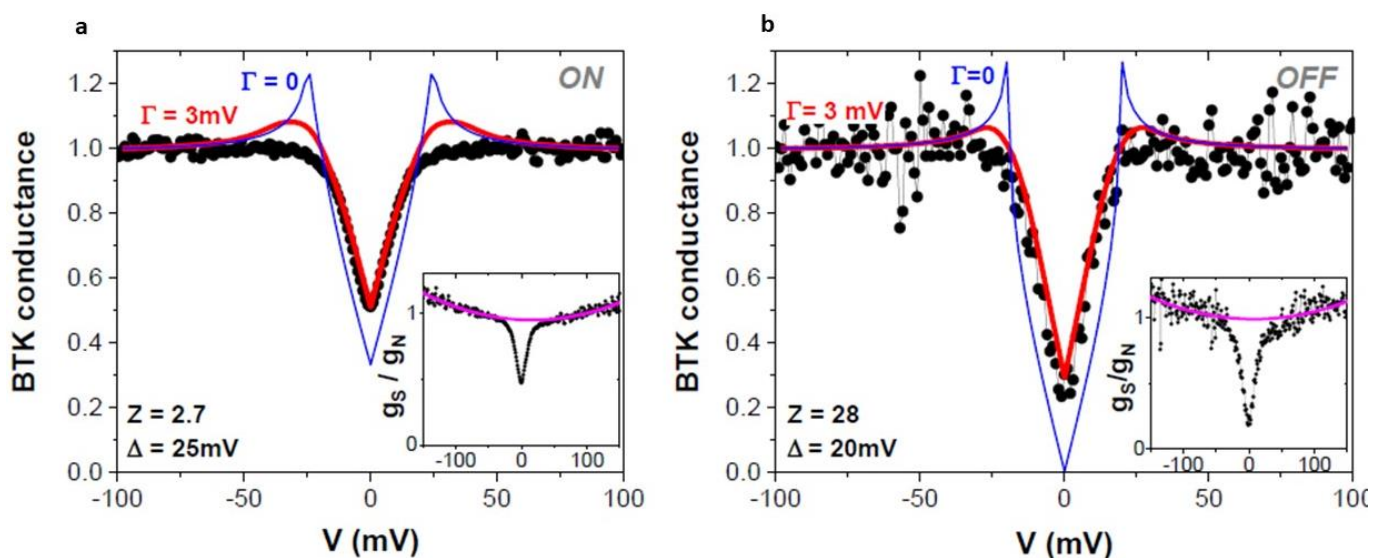


Figure 4-20: Conductance vs bias voltage in the (a) ON state and (b) OFF state. The black curves are the experimental measurements and the blue and red ones are the BTK calculations. The Z and Delta parameters are indicated in the legend for both plots. The inset shows the normalized conductance  $g_s/g_n$  for each of the conductance states. The pink line highlights the parabolic background subtracted from the main curves. It was fitted to a quadratic polynomial function between the range  $30\text{mV} < |V| < 100\text{mV}$ .

Figure 4-20 shows the calculated conductance curves (shown in colour) compared to the experimental data shown in black for the ON and OFF states. Note the effect of  $\Gamma$  on the smearing of the modeled curves that leads to a better fit of the experimental data, the value used are coherent with the ones found in literature (Plećenik *et al.*, 1994).

From the fits of the normalized conductance in both the ON and OFF states we extract the  $Z$  parameter displaying the strength of the barrier. The transparency is significantly increased in the ON state ( $Z \approx 3$ ) compared to the OFF state ( $Z \approx 30$ ) which is consistent with the resistive behaviour of the junctions in the two states. The YBCO gap values are extracted from the fits and we find  $\Delta = 25\text{mV}$  and  $\Delta = 20\text{mV}$  in the ON and OFF states respectively. The extracted value of the superconducting gap was used and averaged over 50 simulations with a standard deviation of  $5\text{meV}$  to simulate inhomogeneity in the sample.

Calculations of the normalized conductance as a function of temperature were performed using the expression for the temperature behaviour of a d-wave SC gap (Park *et al.*, 2005)  $\Delta(T) = \Delta_0 \tanh(2.06\sqrt{T_c/T - 1})$  and Fermi-Dirac statistics. Note that  $\Gamma$  is taken to be temperature independent as elsewhere. Figure 4-21a shows different conductance spectra calculated at different temperatures where the conductance at  $0\text{mV}$  bias  $G_0$  and the one at  $100\text{mV}$  bias  $G_{100}$  are highlighted. Figure 4-21b shows the temperature dependence of  $G_0$  and  $G_{100}$  in the ON and OFF states. The deviation of the high temperature of  $G_0$  is highlighted by the green area for both states. We note however a stronger drop in  $G_0$  in the OFF state compared to the ON state, which can be accounted for by the fact that the transparency is lower in the OFF state. This causes the ratio  $ER = G_0^{ON}/G_0^{OFF}$  to increase as the temperature is decreased below  $T_c$  since the conductance at high bias is unaffected by the quasiparticle population. The inset of Figure 4-21b shows the temperature dependence of the calculated  $ER$  which mainly reproduces the experimental data shown in Figure 4-13d. Note that discrepancies between the theory and the experimental data arise from the fact that the BTK theory does not consider the temperature and bias dependence of the background conductance. It is thus impossible to completely reproduce the experimental  $ER$  vs  $T$  curve.

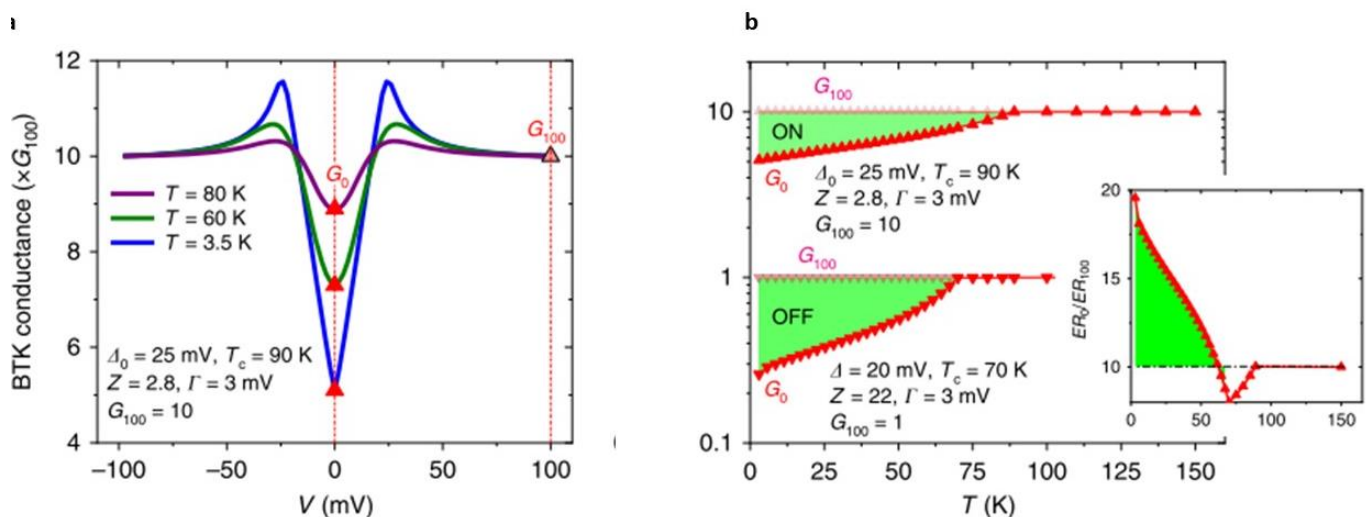


Figure 4-21: (a) ON state conductance curves calculated by BTK at different temperatures for a particular set of parameters (indicated in the legend).  $G_0$  and  $G_{100}$  (the conductance at  $0\text{ mV}$  bias and  $100\text{ mV}$  bias) are indicated on the figure as the dark and open triangles (b) Temperature behaviour of  $G_0$  and  $G_{100}$  calculated by BTK in the ON and OFF states for a set of parameters indicated in the legend. The inset shows the temperature behaviour of the electroresistance ratio at  $0\text{mV}$  and  $100\text{mV}$  bias.

#### 4.6) Model

The changes observed in the resistive properties of these tunnel junctions (both in the presence of a ferroelectric BFO layer and in its absence) as well as a change in the ground state properties of the bottom YBCO electrode upon the application of an external electric field were explained through the lens of a reversible electrochemical reaction occurring between the junction electrodes. Upon the application of an electric field across the junction a redox reaction occurs between the bottom and top electrodes leading to the motion of oxygen ions across the junction. This drastically changes the tunnelling properties of the junction (from a qualitative and quantitative perspective) along with a significant change in the ground state properties of the superconducting bottom electrode.

Let us start with the case of a “0nm BFO” sample where direct contact exists between the YBCO oxide and the MoSi metallic layer. The TEM of Figure 4-7 showed the existence of an oxidized MoSi layer at its bottom interface. This can be understood because of the high reduction potential of the YBCO layer (cuprates tend to lose oxygen easily) c.f. Table 1. Upon the deposition of MoSi, an oxidized layer forms at the MoSi interface thus depleting the YBCO layer from its oxygen. This depresses the superconducting properties of the YBCO layer creating a low transparency junction at the interface between the two layers. The ground state properties can be reversed by applying an external poling voltage  $V_{pol} > 0$  which severely thins down the oxidized MoSi layer at the interface at the expense of the YBCO layer c.f. Figure 4-22(a-b). The superconducting properties of YBCO are enhanced causing an increase of the interface transparency which yields an increase in the conductance. Upon the application of  $V_{pol} < 0$  the system returns to its ground state where an oxidized layer of MoSi is reformed at the interface.

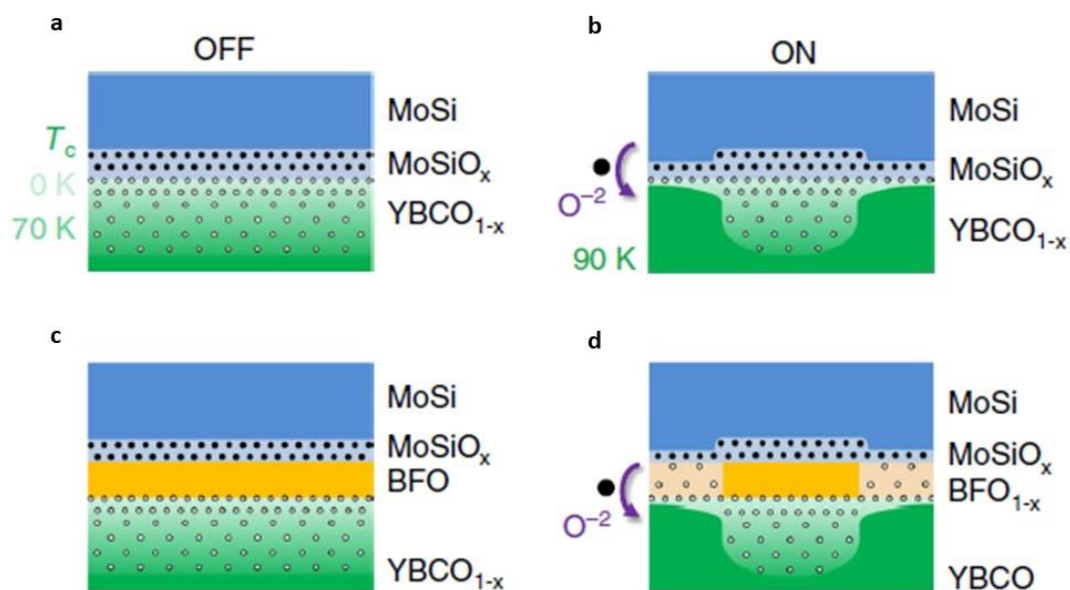


Figure 4-22: Schematic representation of the different scenarios observed in samples with and without a BFO layer (a) and (c) represent the low conductance (OFF states) for samples with and without BFO respectively. (b) and (d) represent the high conductance (ON states) for samples with and without BFO respectively (a) The oxygen anions (black dots) fill the MoSi layer near the interface thus gradually filling the YBCO layer with oxygen vacancies (or depleting it of oxygen ions) and depresses its superconducting properties (b) When a positive poling voltage is applied on the junction, the electric field is strongest along the periphery of the junction causing oxygen atoms to migrate from the top towards the bottom layer partially doping the YBCO layer and increasing its superconducting properties (c) The OFF state in the presence of a BFO layer has a depleted bottom YBCO layer and an oxygenated top MoSi layer. The BFO layer is not oxygen depleted in the OFF state (d) When a positive poling voltage is applied oxygen migrates from the both the MoSi and the BFO layers towards the bottom YBCO layer leading to a more superconducting YBCO layer and a more conducting BFO layer.

When a BFO layer (or another oxide) is inserted between the two electrodes the resistive switching occurring can be explained by the same mechanism where the ion transport occurs across this material c.f. Figure 4-22(c-d). Note that the voltage required to switch the junction from the ON to the OFF state is similar for junctions with and without BFO ( $V_{pol} \sim 3V$ ) because the reaction is mostly due to the high YBCO reduction potential. In addition, the fact that all junctions show the same poling voltage required to cross from the ON to the OFF state ( $V_{pol} \sim -1V$ ) c.f. Figure 4-18 hints at the barrier for ion transport being localized at the YBCO interface (the only common element in all junctions)

#### 4.7) Conclusion

In this chapter we have observed a tunnel electro resistance (TER) effect in junctions combining a high  $T_c$  superconductor YBCO and a low  $T_c$  superconductor MoSi. This effect is qualitatively and quantitatively similar to the ferroelectric tunnel electroresistance effect reported in the literature for ferroelectric barrier sandwiched between two metallic electrodes. As a matter of fact, we have demonstrated the existence of a fast, non-volatile and reversible change in the conductance state of two sets of tunnel junctions: junctions including a BFO ferroelectric barrier and others lacking a ferroelectric layer. We have observed an increase in the junction electroresistance between low and high bias measurements appearing under a certain temperature. This effect is interpreted as the opening of a superconducting gap under the critical temperature of YBCO. The spectroscopic features of the conductance is analysed and interpreted using BTK formalism where the modelling of the junction conductance is performed according to the junction transparency  $Z$ . The TER effect is interpreted as an electric field induced electrochemical reaction occurring at the interface between the two electrodes. The high poling voltage causes the migration of ionic species (mostly oxygen vacancies) across the junction which in turn affects both the electrode ground state and the tunnelling barrier characteristics. Note however, that no Josephson coupling between the two superconductors has been observed in these junctions. This might be due to insufficient coupling between the two superconducting electrodes. The YBCO coherence length is strongly anisotropic and its component on the  $c$  axis is  $3 \text{ \AA}$  which is smaller than the insulating barrier. By substituting the YBCO(001) of our junctions by YBCO(103) or YBCO(100) i.e. by changing the major crystallographic direction along the device interface we can obtain an enhanced coupling between the two superconducting electrodes

# 5) Interplay between field effect and light induced effects in $YBa_1Cu_2O_{7-\delta}/ITO$ vertical tunnel junctions

## Contents

5) Interplay between field effect and light induced effects in $YBa_1Cu_2O_{7-\delta}/ITO$ vertical tunnel junctions.....	133
5.1) Motivation & main results .....	136
5.2) Growth and characterization .....	136
5.3) Optical properties of top electrodes.....	137
5.4) Electric poling and transport measurements .....	138
5.5) Temperature dependence of the conductance .....	139
5.6) Thermally activated relaxation .....	140
5.7) Illumination effects: general portrait.....	141
5.8) Volatile illumination effects: photovoltage .....	143
5.8.1) Dependence of $V_{oc}$ on temperature.....	143
5.8.2) Dependence of $V_{oc}$ on optical power .....	145
5.8.3) Dependence of $V_{oc}$ on the junction conductance .....	145
5.9) Persistent illumination effects in the ON state.....	146
5.9.1) Temperature vs photon induced effects.....	148
5.9.2) Spectral Response .....	149
5.9.3) Time dependence.....	150
5.9.4) Temperature dependence .....	151
5.10) Persistent illumination effects in the OFF state.....	152
5.10.1) Time dependence.....	153
5.10.2) Temperature dependence .....	154
5.11) Illumination effects in intermediate junction states .....	155
5.11.1) Characteristic behaviour across the OFF to ON branch of the hysteresis loop .....	155
5.11.2) Characteristic behaviour across the ON to OFF branch of the hysteresis loop .....	156
5.11.3) Similarity between Persistent changes in conductance and photovoltage $V_{oc}$ .....	157
5.12) Model.....	161
5.12.1) Photovoltaic effect.....	161
5.12.2) Illumination effects in the ON state.....	162
5.12.3) Illumination effects in the OFF state.....	164
5.12.4) Illumination effect in intermediate conductance states.....	165
5.13) Conclusion.....	168

5.14)	Supplementary measurements.....	169
5.14.1)	Thermal vs photo-induced effects .....	169
5.14.2)	Absence of effects under infrared illumination .....	169
5.14.3)	Light induced fatigue.....	170
5.14.4)	Aluminium vs Gold wires .....	171

## 5.1) Motivation & main results

In the previous chapters we have shown that cuprate thin films and heterostructures are sensitive to external stimuli such as illumination by visible or UV light (Chapter 3) or field effect (Chapter 4). This chapter is dedicated to the study of the combination of both stimuli on a system composed of a high  $T_c$  superconductor (YBCO) and a transparent n-doped semiconductor (ITO) as a top electrode. In this system, we observe a similar tunnel electroresistance (TER) effect as the one observed on YBCO/BFO/MoSi junctions. These states can be switched by the application of an external electric field. On the other hand, due to the transparent nature of the top electrode, these systems allow us to investigate their response to light stimuli as well. As a matter of fact, we have shown a non-volatile light induced resistive switching between different conductance states of a junction.

In particular we have shown in Chapter 3) that persistent photo-induced effects are observed in underdoped YBCO thin films. These changes seem to be connected to the motion of oxygen ions in the YBCO structure. Given the role of redox reactions at oxide interfaces and their effect on the electrode ground state, it seems natural to investigate the photo-induced effects at an interface between an underdoped cuprate and a metallic oxide.

To our surprise, we have found that light confers unique behaviours in several strong photo-induced effects in these junctions. Very interestingly, the photo-response of the junction depends on conductance state prior to illumination. If the sample is set in the ON state, light induces a decrease in the conductance towards the OFF state. The photo-induced conductance decrease is non-volatile and the response cumulative: the conductance drop is proportional to the number of photons shone on the sample. Strikingly, if the junction is initially set in the OFF state, the opposite behaviour is observed: an increase of its conductance is obtained upon illumination. This effect is also non-volatile. In addition to the non-volatile effect described above, junctions also show an unusually strong photovoltaic effect, which appears only in the low conductance OFF state.

The different photo-induced effects in the ON and OFF states are associated to different microscopic mechanisms. In the ON state, the observed effects are explained through the lens of a photo-assisted electrochemical reaction leading to oxygen exchange *between* the two electrodes. In the OFF state, instead, the band bending at the interface between the interfacial oxygen-depleted YBCO and the ITO drives the separation of photo-created electron-hole pairs, which results in the appearance of a photovoltage which induces a redistribution of oxygen vacancies *within* the YBCO electrode.

Besides the fundamental significance of these findings, the ability to continuously manipulate the electronic state of the junctions using external knobs such as electric field pulses or light irradiation can be exploited in a variety of applications in the field of multi-state electronic nanodevices for neuromorphic computing, solid state memories or light sensors.

We will start by describing the growth and characterization of the films as well as the transport characterization performed on the junctions. We will then highlight the light induced effects observed in YBCO/ITO junctions. The next three sections will cover the details of the effects observed after illuminating the junction in the ON, the OFF and intermediate conductance states. A model accounting for all observed behaviours will be proposed.

## 5.2) Growth and characterization

The junctions presented in this chapter are designed following the methods previously described in Chapter 4). A 30nm optimally doped YBCO film is grown by PLD. A photolithography step is used to define the junctions and the top electrode is deposited by sputtering followed by a standard lift-off process. The choice of the top electrode was defined by two parameters: its transparency to the range

of wavelength chosen for the illumination experiments and a low surface resistivity to allow for efficient electric poling.

We have chosen a solid solution ternary oxide  $\text{In}_2\text{O}_3:\text{SnO}_2$  Indium Tin Oxide (ITO) that was deposited by sputtering at the “Laboratoire de Physique des Interfaces et des Couches Minces” (LPICM) by DC sputtering with a base vacuum of  $\sim 5 \times 10^{-7} \text{ mbar}$  and a deposition pressure of  $6 \times 10^{-3} \text{ mbar}$  of a mixture of Argon and oxygen gas (Ar: 43 sccm/  $\text{O}_2$ : 3 sccm) at room temperature. The sputtering power is 200W using a commercial target of  $\text{In}_2\text{O}_3$  98%/  $\text{SnO}_2$  2%.

Figure 5-1a and Figure 5-1b show a schematic of the devices and a picture of the sample after the junctions have been contacted.

Figure 5-1c shows the temperature dependence of the resistance across the YBCO layer after the lithography steps have been performed. The resistance decreases as a function of temperature until it abruptly falls to 0 at a superconducting critical temperature of  $T_c = 80\text{K}$ . This shows that despite the various lithography steps the YBCO films retain satisfactory superconducting properties.

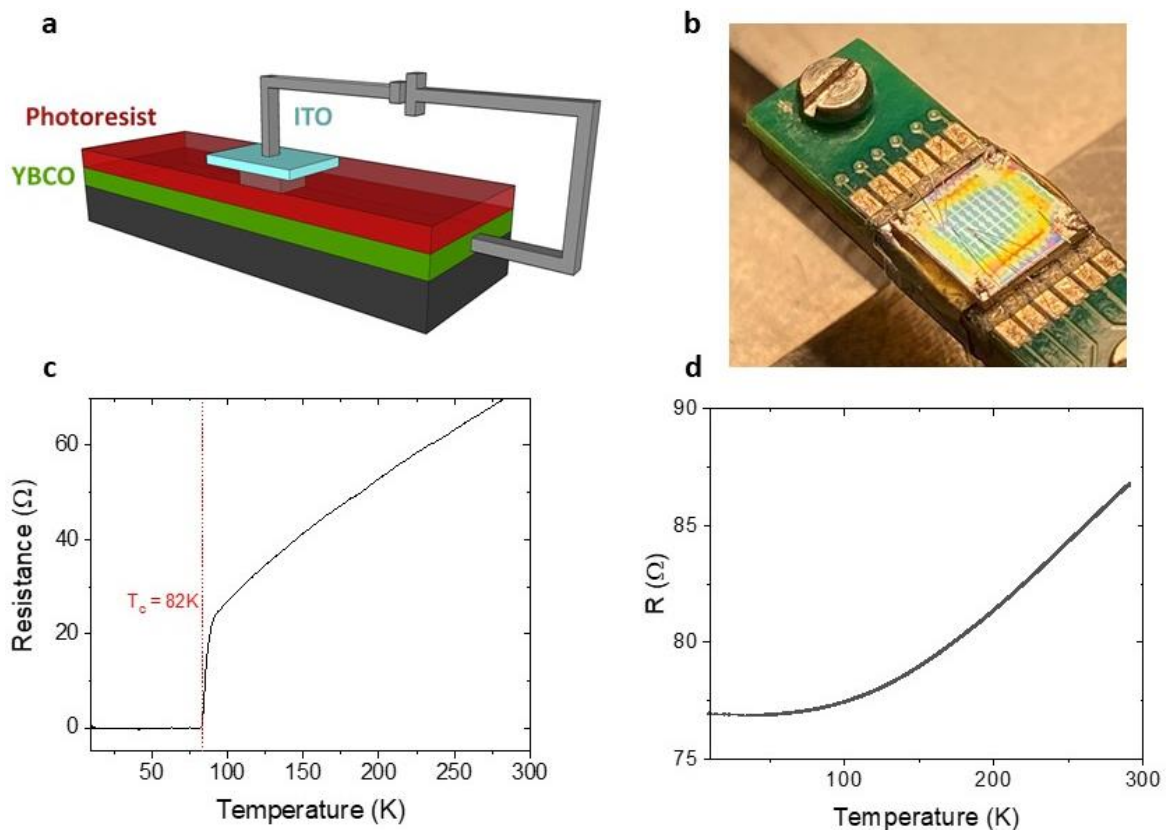


Figure 5-1: (a) Schematic representation of the devices built (b) Picture of the sample on its sample holder (c) Temperature dependence of a 4 point measurement of the resistance across the YBCO layer (d) Temperature dependence of a 2 point measurement of the resistance across an ITO electrode. The measurements were performed on the patterned sample.

The post-growth sheet resistance of an ITO film is found to be  $R_s \approx 40 \Omega/\square$  (using a 4 point measurement at room temperature). In addition, the temperature dependence of the resistance of the ITO on a single junction, in a two-point probe measurement, is seen in Figure 5-1d.

### 5.3) Optical properties of top electrodes

Unless otherwise stated, aluminium wires are used to contact the top and bottom electrodes. The YBCO layer is accessed by scratching the corners of sample and a drop of silver paint is added to minimize the contact resistance. The sample is placed in the cryostat facing the optical window. In

order to maximize the efficiency of our measurements a shadow mask is engineered on the sample by covering a section of the window with aluminium tape as can be seen from Figure 5-2a. This allows us to ensure that a portion of the junctions is protected from the illumination. We can thus discriminate between effects that are due to illumination exclusively and effects due to a combination of other factors on the same sample.

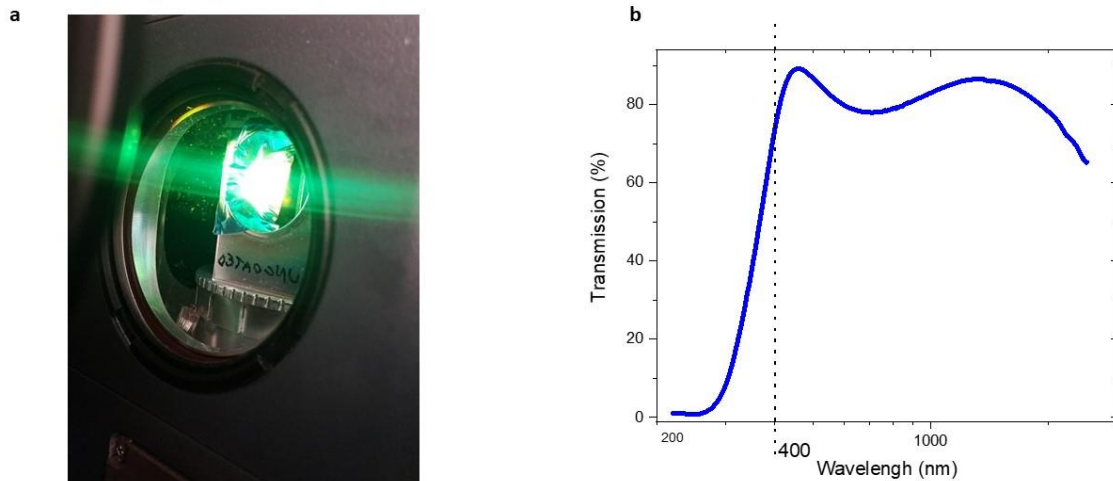


Figure 5-2: (a) Picture taken through the cryostat primary window showing the aluminium tape used to create a shadow (b) wavelength dependence of the transmission across ITO thin films.

Figure 5-2b shows the transmission percentage of photons across a thin film of ITO grown on a glass substrate -in the same conditions stated above- as a function of the photon wavelength. We note that the transmission percentage is quite high, around 80% in the range 400-800nm of the visible spectrum. However, the signal drops rapidly when wavelength is reduced below 400nm. This shows that our top electrode is mostly transparent to visible radiation and does not contribute to absorption in our experiments.

#### 5.4) Electric poling and transport measurements

Once the junctions are contacted, the sample is introduced in the cryostat and cooled down to 3K to perform standard transport measurements. The junctions are biased in voltage ( $-200\text{mV} < V_{bias} < 200\text{mV}$ ) and the current flowing through it is measured with a Keithley 2450 Sourcemeter. The voltage drop across the junction is simultaneously measured using a Keithley 2182 Nanovoltmeter. The junctions are then characterized by their differential conductance  $G(V) \equiv dI/dV$  obtained through the numerical derivation from the measured  $I(V)$ .

In order to switch the resistive state of the junction, a poling voltage (a couple of Volts) is applied to the junction. The poling voltage was applied in a ramp over tens of seconds: starting from 0V the

voltage was gradually increased until it reached the target  $V_{pol}$  followed by a gradual decrease to 0V. The bias voltage  $V_{bias}$  is then applied to the corresponding measure the differential conductance.

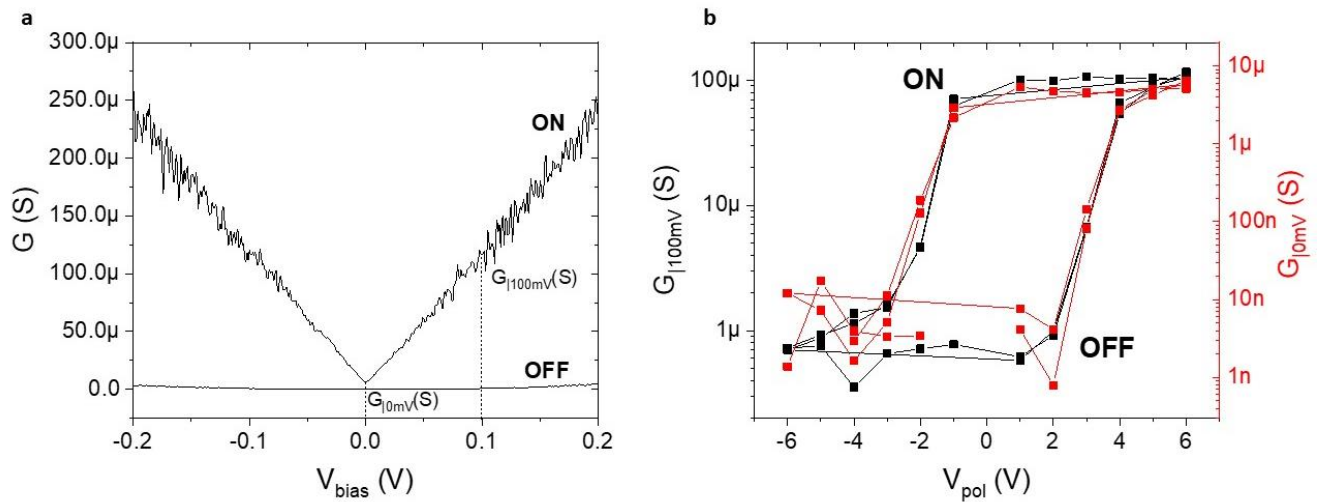


Figure 5-3: Differential conductance of the ON and OFF states as a function of the bias voltage measured at a temperature of  $T = 3K$  of a YBCO/ITO junction (b) Differential conductance as a function of the poling voltage at a temperature  $T = 3K$  calculated at a bias voltage of 100mV (left axis black) and at a bias of 0mV (right axis red) highlighting the switching between the high conductance (ON state) and the low conductance (OFF) state.

Figure 5-3a shows the differential conductance as a function of the bias voltage at a temperature of  $T = 4K$ . The high conductance state is labelled ON and is obtained after applying a poling voltage  $V_{pol} \sim 6V$ . On the other hand, the low conductance state is labelled OFF and is obtained after applying a poling voltage  $V_{pol} \sim -4V$ . The differential conductance in the ON/OFF state is characterized by a quasilinear/quadratic background at high bias. This effect is called Tunnel Electroresistance effect (TER) and consists in reversibly switching between several resistive states through the application of an electric field across the junctions. This effect has been already discussed in section 4.3).

Figure 5-3b shows the differential conductance measured at a bias voltage  $V_{bias} = 100mV$  and  $V_{bias} = 0mV$  in black(left axis) and red (right axis) respectively as a function of the poling voltage  $V_{pol}$  for a YBCO/ITO junction at a temperature of  $T = 3K$ . The hysteresis loop obtained also resembles the ones shown in chapter 4). This graph highlights the reversibility of the electrical switching effect since multiple loops fall on top of each other. We also note that the magnitude of the Electroresistance ( $ER \equiv \frac{G_{ON}}{G_{OFF}}$ ) is higher at a bias voltage of 0mV where  $ER = 1000$  than at 100mV where  $ER = 150$ . This difference has been attributed to the contribution of the YBCO superconducting gap (Rouco *et al.*, 2020) to the electroresistance.

### 5.5) Temperature dependence of the conductance

In order to measure the temperature dependence of the ON and OFF states, the junction was set in the corresponding conductance state at  $T = 4K$  before sweeping temperature.

Figure 5-4 shows the temperature dependence of the conductance in the ON(up triangles) and OFF(down triangles) states measured at a bias of  $V_{bias} = 100mV$  (closed symbols) and  $V_{bias} = 0mV$  (open symbols) of a YBCO/ITO junction. In the ON state and at a bias of 100mV, the conductance remains more or less constant over the whole temperature range. At a bias of 0mV however, a deviation from its high temperature behaviour occurs at  $T \approx 90K$ . In the OFF state the conductance increases exponentially with increasing temperature hinting at a temperature dependent tunnel

barrier. The deviation of the conductance, in the OFF state, at a bias of 0mV from its high temperature behaviour occurs at a temperature  $T \approx 80K$ .

We note the similarities between the temperature behaviour of a YBCO/ITO junction and that of a YBCO/MoSi junction presented in section (4.4.3).

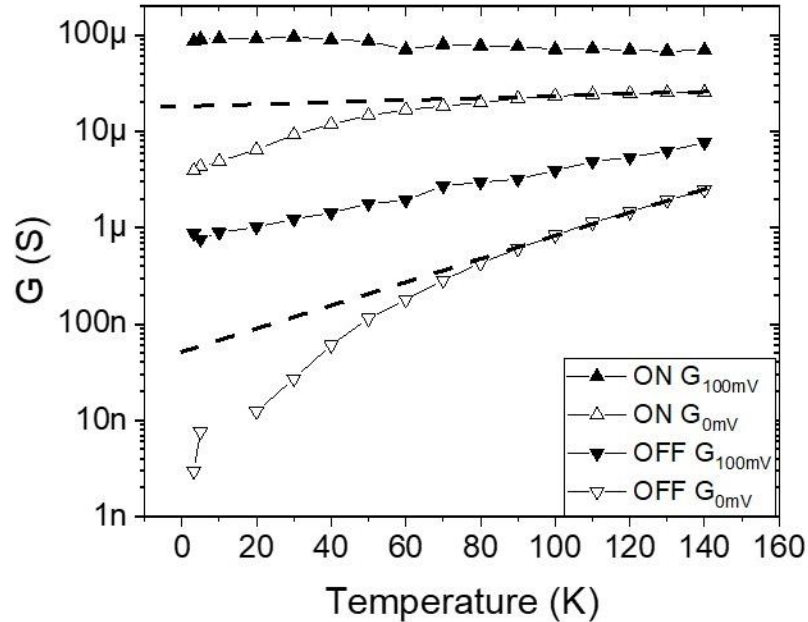


Figure 5-4: Temperature dependence of the differential conductance of a YBCO/ITO junction in the ON and OFF states, calculated at a bias of 100mV and 0mV. The dashed lines are guides to the eye and highlight the high temperature behaviour of the conductance.

### 5.6) Thermally activated relaxation

We have observed a thermally activated relaxation of the conductance of our YBCO/ITO junctions **in the absence of illumination and when the junction is set in the ON state**. Figure 5-5a shows the time evolution of the normalized differential conductance  $((G - G_{OFF})/G_{ON}|_{t=0min})$  of a YBCO/ITO junction after poling it in the ON state as a function of temperature. The factor  $G_{ON}|_{t=0min}$  in the normalization considers the first differential conductance measurement performed once the temperature reaches the target value. The junction was reset by poling to the OFF and then back to the ON state at a temperature of  $T = 3K$  between each relaxation measurement. While the differential conductance in both ON and OFF states are constant in dark at low temperature, we have observed a slow decrease of the conductance in the ON state approaching the OFF state as the temperature increases. No evolution of the conductance in the OFF state is observed up to temperatures of 300K. We note a stretched exponential behaviour of the relaxation dynamics consisting of a sharp decrease in the beginning followed by a long tail. At a fixed temperature, the conductance does not seem to relax all the way to the OFF state but to plateaus at intermediate levels. As the temperature is increased the amplitude of the conductance relaxation seems to increase.

In order to obtain a quantitative measure of this relaxation we have performed a numerical fit of the normalized conductance. The data were fitted to a stretched exponential function of the form:

$$G = A * e^{\left(-\frac{t+t_0}{\tau}\right)^\beta}.$$

A is the amplitude of the relaxation,  $t_0$  is a parameter added to account for the elapsed time before the measurement is started,  $\tau$  is the characteristic time of the relaxation and  $0 < \beta < 1$  is a dimensionless parameter that dictates the degree of the stretched attribute of the exponential.

In this analysis we have allowed both  $\beta$  and  $\tau$  to evolve with temperature since fixing  $\beta$  to a specific value maintains the same qualitative temperature behaviour of the  $\tau$  parameter with a bigger dispersion. Figure 5-5b shows the inverse temperature behaviour of the characteristic relaxation time (black dots)  $\tau$  in log scale fitted to a linear function (red line). The upper axis shows the corresponding temperature values for clarity. We note a linear relationship between the logarithm of the characteristic time and the inverse temperature.

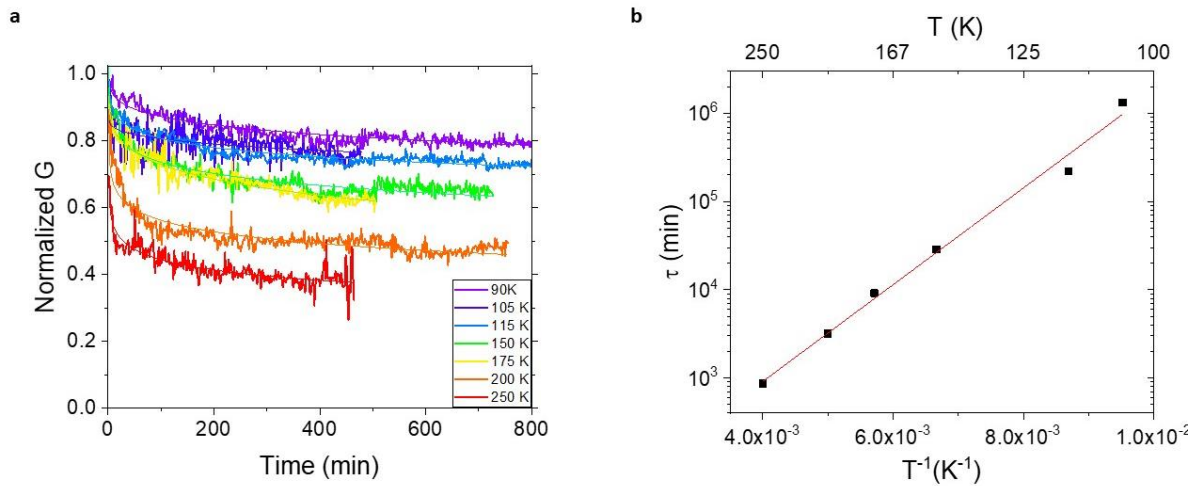


Figure 5-5: (a) Time dependence of the normalized differential conductance during relaxation as a function of temperature. The straight lines are the fitted stretched exponential functions. (b) Inverse temperature dependence of the relaxation characteristic time in log scale. The straight line is a linear fit to the data. The upper axis shows the corresponding temperature values for clarity.

We can model the temperature behaviour of  $\tau$  by an exponential function of the form :

$$\tau \propto e^{-E_a/k_B T}$$

Where  $E_a$  is the relaxation associated energy barrier and  $k_B T$  is a thermal energy. From this linear fit we can extract the energy barrier that governs the relaxation process  $E_a = 0.11 eV$ .

The high reduction potential of copper in YBCO leads to the instantaneous reduction of the YBCO layer at the expense of the ITO layer. (c.f. Table 1 in chapter 4) The ground state of the system is thus its low conductance state. By applying a positive voltage pulse, the system can be driven to a metastable state. At high enough temperature we note a **gradual temperature dependent relaxation from the metastable (ON) state towards the system ground state (OFF) in the absence of illumination.**

### 5.7) Illumination effects: general portrait

As stated previously, one of the major objectives of this thesis is the investigation of the effects of light on the properties of the vertical tunnel junctions composed of at least one transition metal oxide. This section will briefly summarize the different types of light induced effects observed on the transport properties of YBCO/ITO tunnel junctions. These will be subsequently detailed in the following sections. Finally, their microscopic origin will be discussed in the "Model" section.

These effects are portrayed in Figure 5-6(a-b) that shows the differential conductance as a function of the bias voltage in the ON and OFF states and after illumination. The junction was previously set in the

ON state in Figure 5-6a and in the OFF state in Figure 5-6b. We clearly note a difference in the sign and magnitude of the photo-induced effect that depends on the state of the junction prior to the illumination. If the junction is set in the ON state, a permanent decrease in the differential conductance of the junction after illumination is observed. However, if the junction is set in the OFF state, an increase in its differential conductance is noted after illumination.

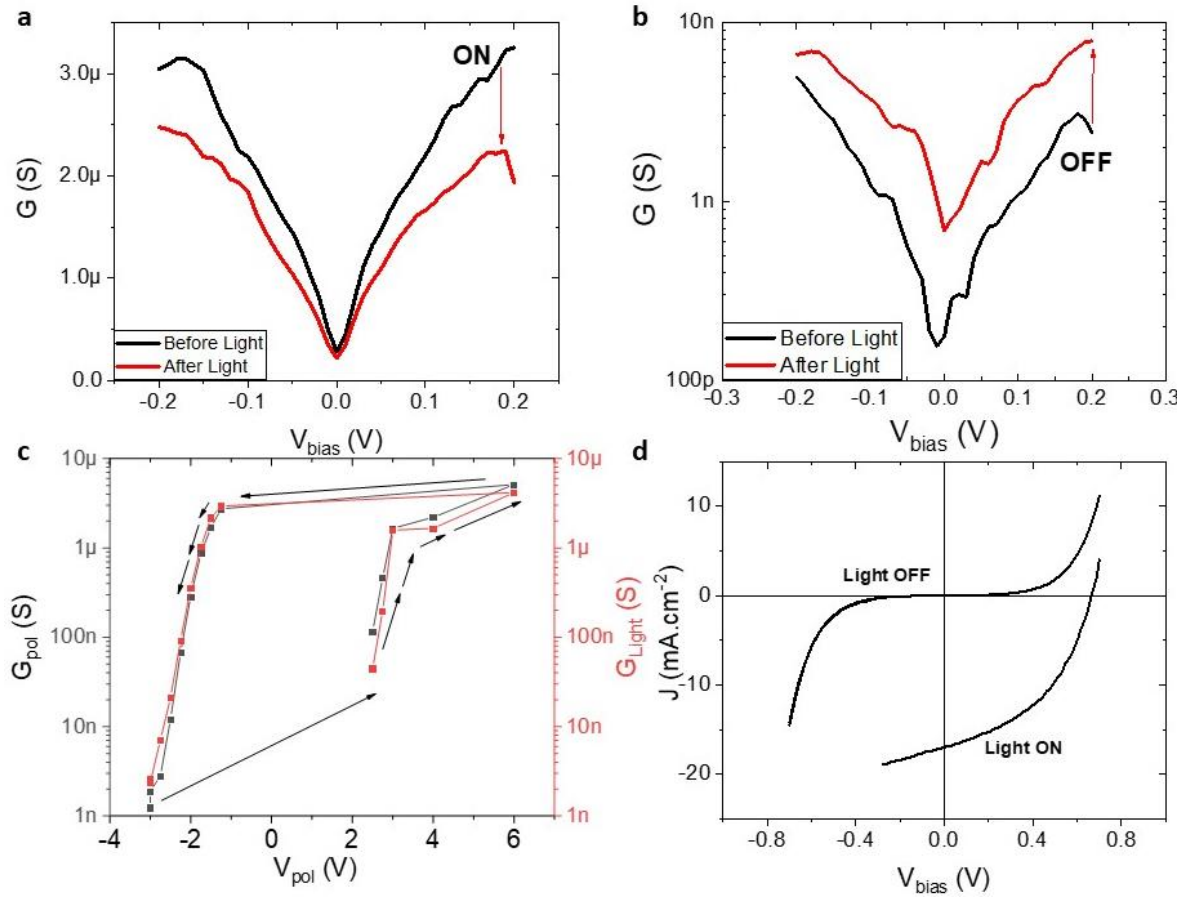


Figure 5-6: Differential conductance as a function of the bias voltage at a temperature of  $T = 4K$  in the ON and OFF states in dark and after illumination. The junction was set in the (a) ON / (b) OFF state prior to the illumination. (c) Differential conductance calculated at a bias of  $100mV$  as a function of the poling voltage before (black) and after (illumination) (red). (d) Current density - Voltage characteristic of a YBCO/ITO junction in dark and under illumination by UV/visible light.

A more systematic study, as a function of the conductance state of the junction, provides additional insights into the nature of these photo-induced effects. As a matter of fact, light affects the transport properties of the junction in the intermediate states available between the ON and OFF states.

The main results are depicted in Figure 5-6c that shows the differential conductance measured at a temperature of  $T = 4K$  at a bias of  $V_{bias} = 100mV$  as a function of the poling voltage  $V_{pol}$  before (black dots) and after illumination (red dots). The photo-induced increase in the conductance can be observed in all of the intermediate states accessible by gradually poling from the ON to the OFF state (left hand side of the hysteresis loop). On the other hand, the photo-induced decrease in the conductance can be observed in all the intermediated states accessible by gradually poling from the OFF to the ON state (right hand side of the hysteresis loop).

In addition to the persistent photo-induced changes in the junction conductance we have noted the appearance of a significant photovoltage only under illumination –it disappears once the light is turned off. Figure 5-6d shows the Current-Voltage (I-V) characteristic of a YBCO/ITO junction, in dark

and under illumination at a temperature of  $T = 4K$ . The illumination was performed using a monochromatic LED with a wavelength  $\lambda = 405nm$  and at an irradiance of  $P = 155mW.cm^{-2}$ . We note a shift in the I-V characteristic of the junction under illumination. As will be described in more detail later, the appearance of this photovoltaic effect is related to the conductance level of the junction and as such is more prominent in the OFF state than the ON state.

The next section will detail the instantaneous photovoltage measured across the junction under illumination. The subsequent sections will be dedicated to a description of the photo-induced effects observed on the ON state, then those observed on the OFF state and finally the light effects observed in intermediate conductance states. Finally, we will describe a model that accounts for all observations.

### 5.8) Volatile illumination effects: photovoltage

We have observed a volatile photovoltaic effect (PVE) in our YBCO/ITO junctions under illumination by visible light. Figure 5-7a shows the IV characteristic measured at a temperature of  $T = 4K$  in dark and under illumination by a monochromatic LED with a wavelength of  $\lambda = 405nm$ . We note the instantaneous response of the junction to the switching on/off of the light indicated in the figure by an arrow. The characteristic time associated with this effect is considerably smaller than the time resolution of our apparatus ( $\sim$ seconds) which is incompatible with the thermal induced effects described in this thesis. The open-circuit voltage  $V_{oc}$  and the short-circuit current  $I_{sc}$  are defined respectively as the photovoltage at 0 current bias and the photocurrent at 0 voltage bias and are indicated in the figure. Figure 5-7b shows the extracted photocurrent density (black) and the photo-power (red) extracted from the cell as a function of the photovoltage measured across the junction under illumination. While the  $V_{oc}$  measured in these devices is of the same order of magnitude than what is seen in literature ( $\sim 0.5V$ ) in cuprate based photovoltaic heterostructures, the photocurrent density is several orders of magnitude higher than what is reported in literature (Yang, Han and Chang, 2015; Hao *et al.*, 2016). in similar devices and comparable to what is measured in silicon-based photovoltaic cells (Xie *et al.*, 2019).

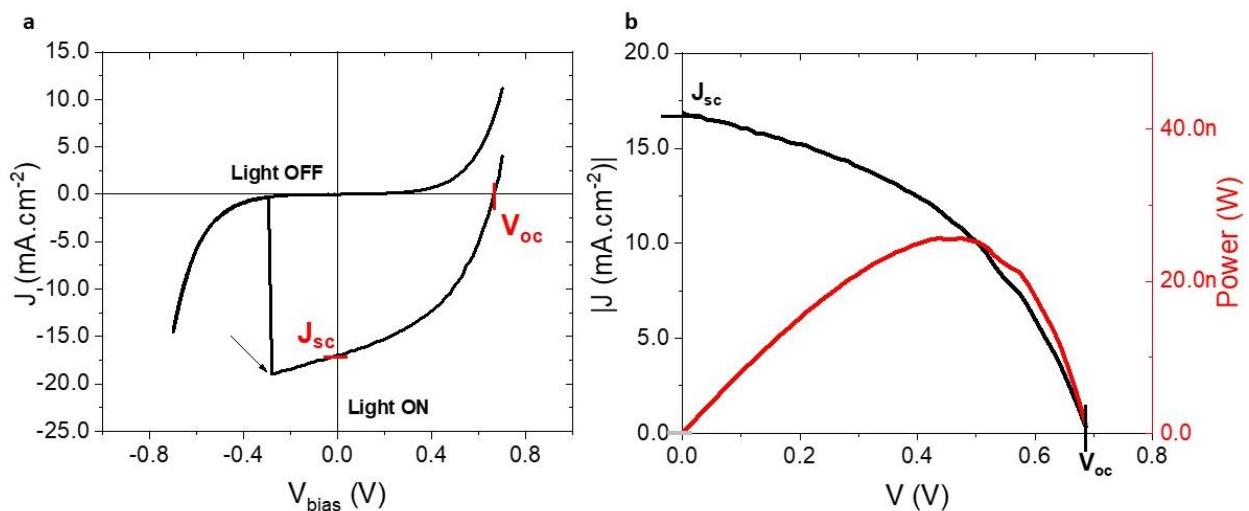


Figure 5-7: (a) Current density -Voltage ( $J$ - $V$ ) curve of a YBCO/ITO junction in dark and under illumination by UV/visible light, the arrow indicates the moment the light was turned off. (b)  $J$ - $V$  curve of the junction under illumination. The open-circuit voltage  $V_{oc}$  and short-circuit current  $J_{sc}$  are highlighted in the figure.

#### 5.8.1) Dependence of $V_{oc}$ on temperature

We have investigated the temperature dependence of the PVE by measuring IV characteristics across a YBCO/ITO junction under illumination at different temperatures.

Figure 5-8a shows the measured  $V_{oc}$  as a function of temperature in an open-circuit measurement. A Keithley 2182 nanovoltmeter was used to measure the voltage across the junction with no external bias under illumination as a function of temperature. The junction was illuminated by a monochromatic LED with a wavelength of  $\lambda = 405nm$  and an optical power of  $P = 155mW.cm^{-2}$ .

The voltage measured in this configuration is negative, which is consistent with the positive  $V_{oc}$  measured in the previous plot. For clarity, the absolute value of the measured photovoltage is plotted. The open-circuit voltage decreases gradually with increasing temperature. Notice that there is a fast steady decay up to  $T \sim 60K$  followed by a much slower decay trend above that temperature as is highlighted by the dashed line in the figure.

Note that the temperature shown in the x-axis represents the actual sample temperature under illumination measured by adjusting for the heating effects of the illumination as is described in section 5.14.1).

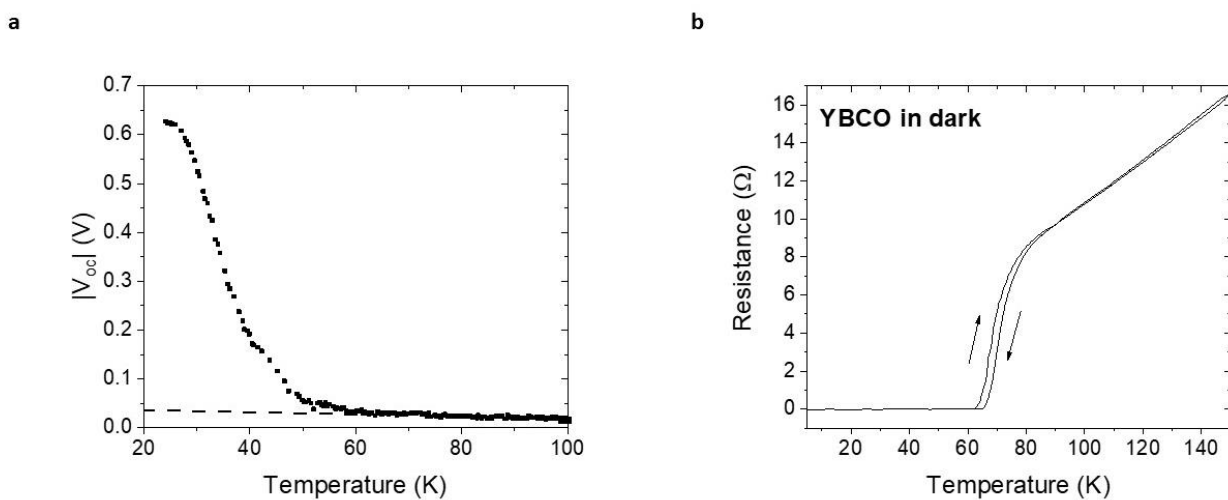


Figure 5-8: Temperature dependence of the absolute value of the open-circuit voltage measured under illumination under illumination. (b) Temperature dependence of the resistance measured across the YBCO film in a 4 pts configuration performed after the measurement shown in (a).

The open-circuit voltage in solar cells based on p-n like junctions is known to decrease with increasing temperature. This decrease is due to a higher recombination rate leading to an increased leakage current. This is translated into a decreased of the open-circuit voltage. Similar qualitative behaviours of  $V_{oc}$  versus temperature in transition metal oxide heterostructures have been reported in literature (Sun *et al.*, 2004; Hao *et al.*, 2016) but over temperature ranges reaching 250K and have been attributed to structural origin. Other reports have shown a non-monotonous behaviour of  $V_{oc}$  as a function of temperature where a change in behaviour seems to occur at the superconducting critical temperature (Yang, Han and Chang, 2015; Chu *et al.*, 2017).

Figure 5-8b shows the temperature dependence of the resistance across the YBCO film measured right after the previous measurement. One can see that the superconducting critical temperature has sharply decreased from its expected value of 80K (c.f. Figure 5-1c) to approximately 60K. This could have been caused by the numerous temperature and electrical cycles the sample was subjected too during the measurements. One has to note however the correlation between the apparent  $T_c$  of YBCO and the temperature at which the change of rate occurs in the previous plot.

### 5.8.2) Dependence of $V_{oc}$ on optical power

We have investigated the dependence of  $V_{oc}$  on the optical power of the light. We have performed this experiment in an open-circuit configuration by following the same experimental procedure described in the previous section and the result is shown in Figure 5-9. We clearly distinguish two regimes. As the power increases from  $0\text{mW}\cdot\text{cm}^{-2}$  to  $180\text{mW}\cdot\text{cm}^{-2}$  the measured  $V_{oc}$  increases quickly then peaks at a value of 0.65. As the power increases,  $V_{oc}$  decreases sharply at first before slowly decreasing once the optical power reaches  $\sim 400\text{mW}\cdot\text{cm}^{-2}$ . One usually expects the open-circuit voltage to depend exponentially on the optical power as it is reported in literature (Sun *et al.*, 2015). However, the behaviour at low power shown in Figure 5-9 does not follow this trend as the increase of the open-circuit voltage with optical power is more pronounced until power reaches  $180\text{mW}\cdot\text{cm}^{-2}$ .

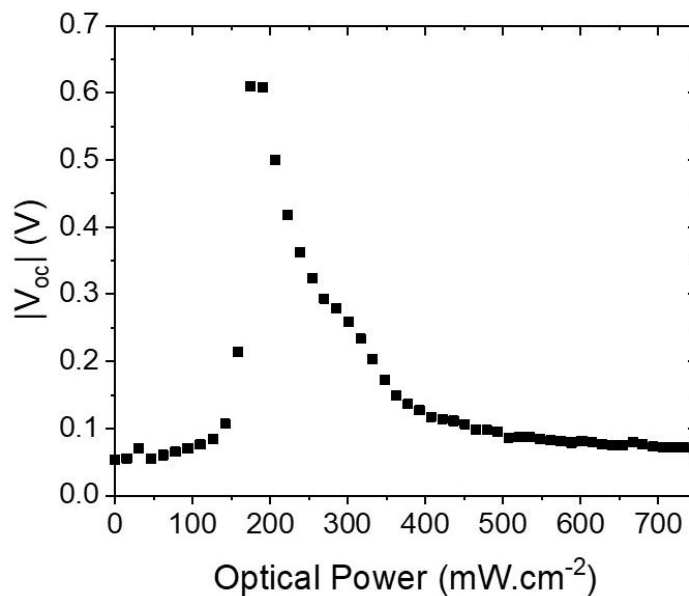


Figure 5-9: Optical Power dependence of the open-circuit voltage under illumination.

As is described in section 5.14.1), we have measured the sample temperature under illumination by measuring a junction resistance. We can conclude from this measurement that the actual temperature of the sample reaches around 55K when illuminated with an optical power of  $400\text{mW}\cdot\text{cm}^{-2}$ . Thermal heating seems to play an important role, and thus the behaviour of  $V_{oc}$  in this experiment cannot be attributed to a pure optical effect, since the temperature of the sample is affected as well. Indeed, one can consider that  $V_{oc}$  decreases as the optical power is increased because of the associated temperature increase.

### 5.8.3) Dependence of $V_{oc}$ on the junction conductance

The magnitude of the photovoltaic effect observed in these junctions depends on its resistive state. As a matter of fact, we have observed a clear correlation between the value of  $V_{oc}$  and the differential conductance of the junction before illumination.

In this section we will present the behaviour of  $V_{oc}$  as a function of the applied poling voltage across the junction for different optical powers at low temperature. The junction was set in a different conductance state prior to the illumination, by applying poling voltages in a manner similar to the electrical hysteresis loop measurement shown in Figure 5-3b. The junction was illuminated at  $T = 4\text{K}$  with  $\lambda = 405\text{nm}$  for each conductance state.

Figure 5-10 shows the open-circuit voltage  $V_{oc}$  as a function of the junction conductance before the illumination  $G_{pol}$ . The junction was illuminated with an optical power of  $P = 158 \text{ mW.cm}^{-2}$  (black),  $P = 733 \text{ mW.cm}^{-2}$  (red).

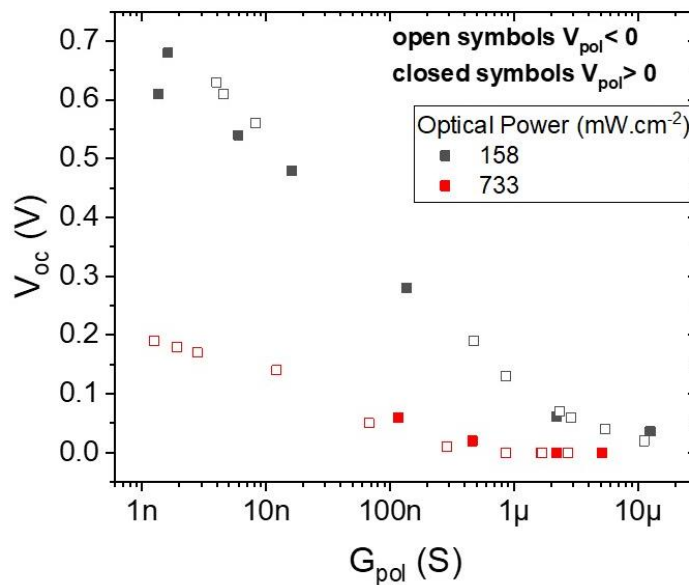


Figure 5-10: The dependence of the open-circuit voltage on the junction conductance before illumination with  $P = 158 \text{ mW.cm}^{-2}$  (black) and  $P = 733 \text{ mW.cm}^{-2}$  (red). The open/closed symbols represent the left/right hand side of the hysteresis loop for  $V_{pol} < 0/V_{pol} > 0$ .

We note a clear dependence of the open-circuit voltage on the differential conductance of the junction irrespective of the direction of poling. Meaning the open-circuit voltage only depends on the junction conductance and not its electrical history.

In addition, the maximal open-circuit voltage is obtained under an illumination of  $P = 158 \text{ mW.cm}^{-2}$  and decreases for an illumination of  $P = 733 \text{ mW.cm}^{-2}$ . This is consistent with what is presented in section 5.8.1) where the efficiency of the PVE decreases with an increasing temperature. The temperature of the sample increases significantly under illumination which we cannot avoid in our set up but we can fully characterize as shown in the supplementary section 5.14.1)

### 5.9) Persistent illumination effects in the ON state

We have observed a permanent, cumulative and reversible decrease in the differential conductance of a YBCO/ITO junction after illumination with visible light for several hours.

The experimental protocol adopted for this measurement and for the remainder of this section (unless stated otherwise) is the following: the junction is first poled from the low conductance state (labelled “OFF state”) to the high conductance state (labelled “ON state”) at  $T = 3K$ , the sample is then heated up to  $T = 100K$  where the illumination took place. The light is then turned off and the sample is cooled down to  $T = 3K$  where another differential conductance measurement is performed (labelled “after light”).

The junction was illuminated using a monochromatic LED with a wavelength  $\lambda = 405nm$  at a temperature of  $T = 95K$ , for a period of  $t = 2 \text{ hrs}$  and with an optical power of  $P \approx 700 \text{ mW.cm}^{-2}$ . Any change from these conditions will be explicitly stated.

Figure 5-11a shows the differential conductance as a function of the bias voltage for a YBCO/ITO junction at  $T = 3K$  before and after illumination. A sharp decrease in the conductance of the junction

is observed after the illumination. This highlights the non-volatile attribute of this effect since all the differential conductance measurements were performed in dark, before and after the illumination.

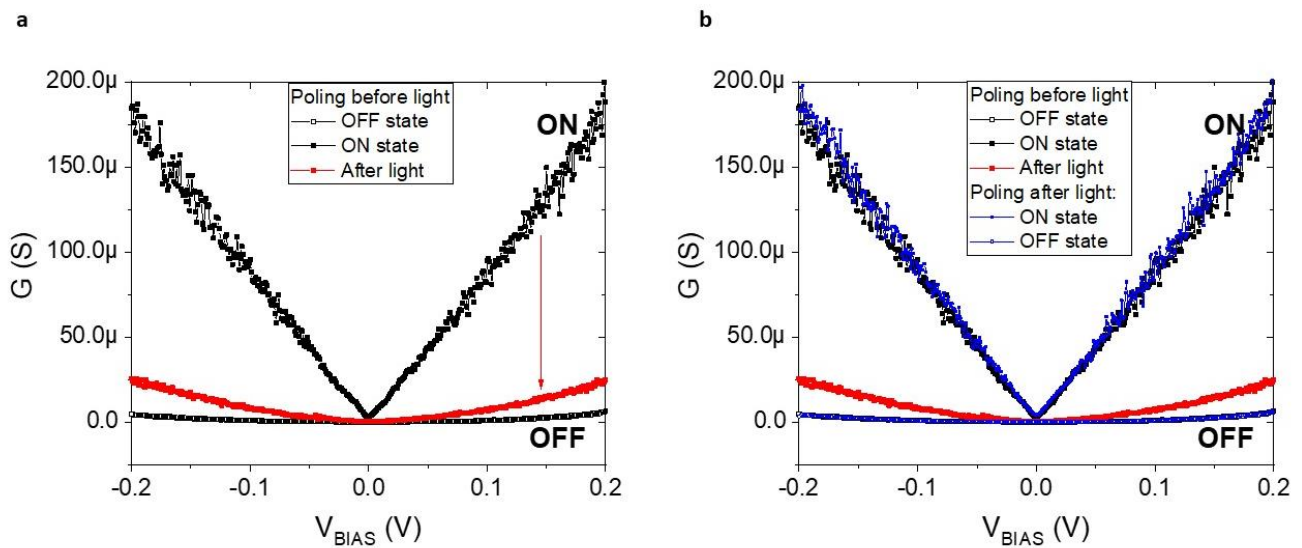


Figure 5-11: Differential conductance as a function of the bias voltage at a temperature  $T = 3K$  in the ON and OFF states before illumination and after illumination. (b) The ON and OFF states are recovered after the illumination by electrical poling.

**This effect is reversible since the initial states of the junctions can be recovered by applying a poling voltage across the junction.** This can clearly be seen in Figure 5-11b showing both the high conductance ON state and low conductance OFF states recovered after illuminating. The electric field required to recover the initial states of the junction are similar to the ones used before the illumination.

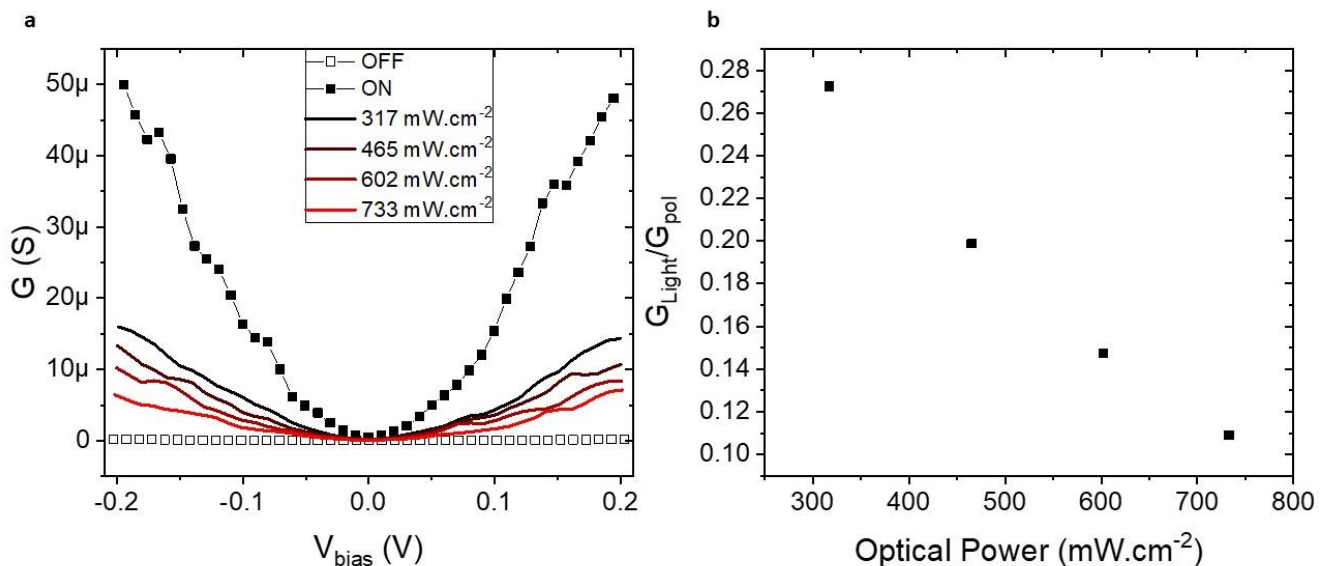


Figure 5-12: (a) Differential conductance as a function of the bias voltage at a temperature of  $T = 3K$  in the ON and OFF state and after illumination with different optical power. (b) Ratio between the conductance after and before light  $G_{Light}/G_{pol}$  as a function of the optical power of the light source.

Figure 5-12a shows the differential conductance as a function of the bias voltage at a temperature of  $T = 3K$  in the ON and OFF states before illumination and after illumination with several optical powers. Before each illumination, a poling voltage is applied across the junction to polarize it in the

OFF then the ON state at  $T = 3K$ . We note a gradual decrease of the conductance after illumination as the optical power of the light is increased.

Figure 5-12b describes the ratio between the conductance after and before illumination  $\frac{G_{Light}}{G_{pol}}$  as a function of the optical power of the monochromatic LED at  $T = 4K$ . The lower the ratio, the more efficient the light effect is. This highlights the cumulative property of this effect since the relative decrease in conductance increases as the dose of incident photons increases.

As stated previously we have accounted for the heating effect that occurs during illumination by measuring the sample temperature accurately during illumination c.f. section 5.14.1). We have also described the thermally activated relaxation that occurs in the absence of light, when the junction conductance gradually relaxes from the metastable ON state to the OFF state c.f. section 5.6). It is thus natural that we compare and then differentiate between the effects that are directly due to the increase in temperature and those that are due to an optical phenomenon. Such a measurement is presented in the next section.

### 5.9.1) Temperature vs photon induced effects

We have characterized the effects of the thermal relaxation at high temperature on the differential conductance at  $T = 4K$ . Figure 5-13a shows the evolution of the differential conductance at a temperature of  $T = 4K$  after allowing for a thermal relaxation of  $t = 4$  hours at different temperatures. The junctions were polarized in the OFF than in the ON state between each measurement. We note that as the temperature of the relaxation increases the relaxation rate increases and the resistive state of the junction gets closer to the OFF state.

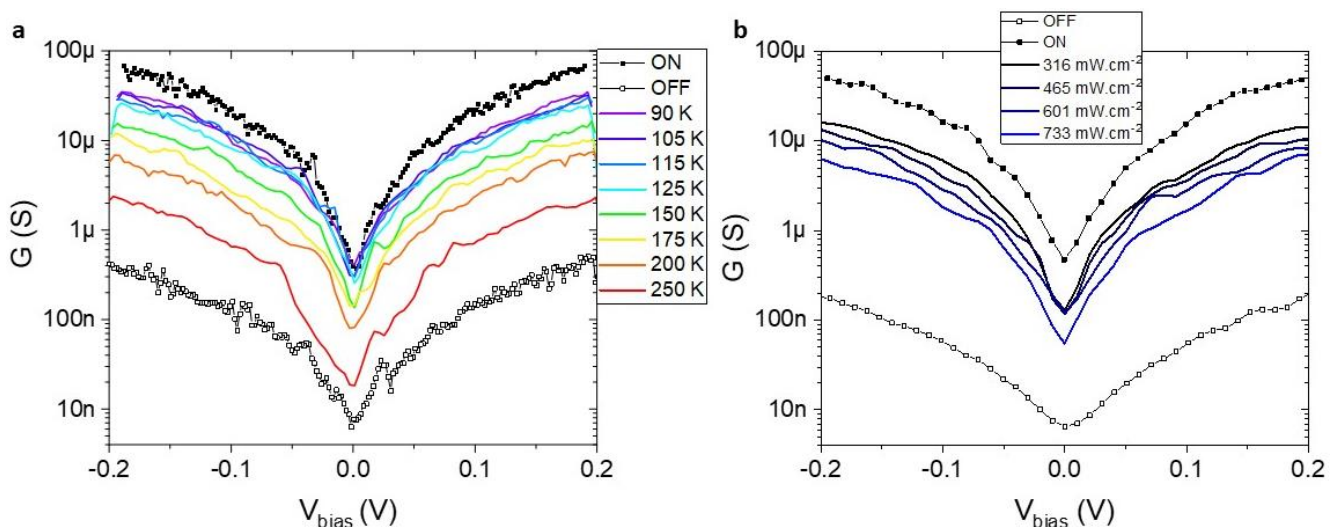


Figure 5-13: Differential conductance as a function of the bias voltage in the ON and OFF states at a temperature of  $T = 4K$  as well as (a) after a thermal relaxation occurred at different temperatures for  $t = 4$  hours and (b) after an illumination took place at  $T = 95K$  for  $t = 4$  hours with different optical powers.

The next step was to measure the effect of the photo-induced change in the conductance as a function of the optical power and then compare the observed conductance decrease to the equivalent conductance decrease induced by thermal relaxation. Figure 5-13b shows the differential conductance as a function of the bias voltage measured at a temperature of  $T = 4K$  after illuminating the sample at  $T = 95K$  with various optical powers.

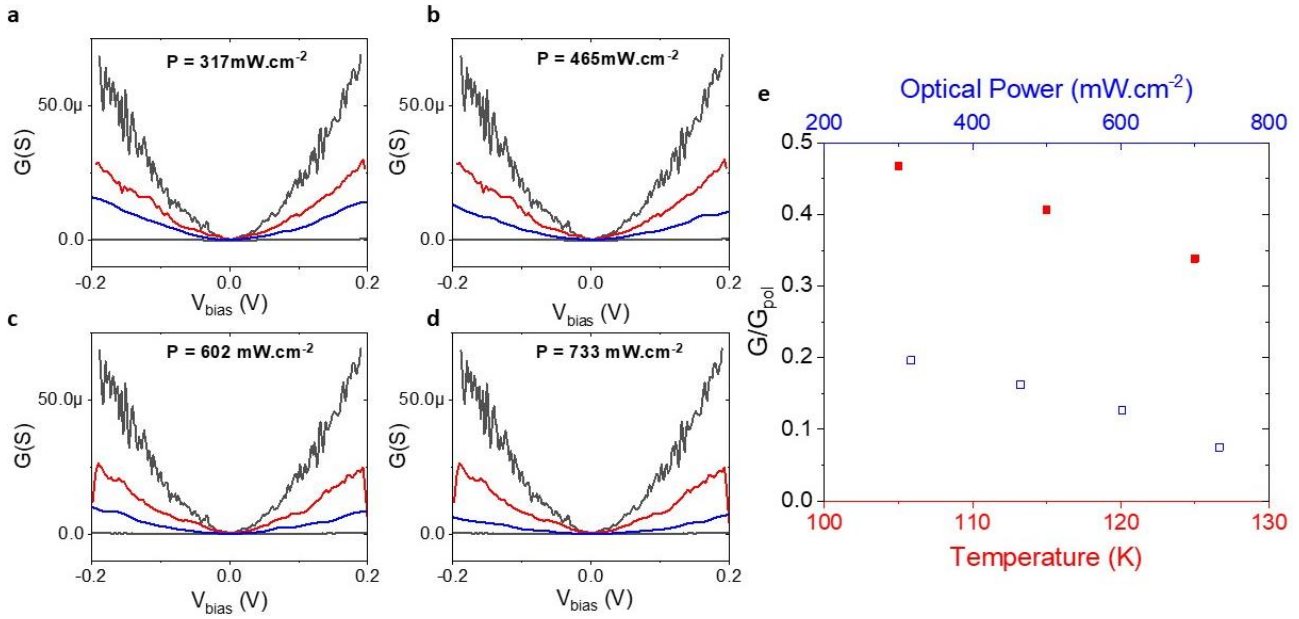


Figure 5-14: Differential conductance as a function of the bias voltage at a temperature of  $T=4K$  in the ON and OFF states before illumination (shown in dark), after an illumination (shown in blue) with an optical power of (a)  $P = 317\text{mW.cm}^{-2}$ , (b)  $P = 465\text{mW.cm}^{-2}$ , (c)  $P = 602\text{mW.cm}^{-2}$ , (d)  $P = 733\text{mW.cm}^{-2}$  and after a relaxation in dark (shown in red) at the corresponding temperature. (e) Ratio of the conductance after Light(blue)/Relaxation(red) as a function of the temperature and optical power.

In Figure 5-14(a) we compare the differential conductance at  $T = 4K$  obtained after illuminating with an optical power of  $P = 317\text{mW.cm}^{-2}$  (in blue) at a temperature of  $T = 95K$  for  $t = 4$  hours and the differential conductance obtained after a relaxation in dark at the corresponding temperature (in red) as well as the ON and OFF states for a clearer comparison. Figure 5-14(b-c-d) show the same comparison for the other optical powers that were used in this experiment. We can clearly see that for all the optical powers used in this experiment the conductance decreases due to the illumination are more pronounced than those obtained by thermal relaxation only. Figure 5-14e shows the ratio of the conductance after illumination(blue)/relaxation(red) and before illumination as a function of temperature and optical power. We can see that the ratio decreases as a function of increasing temperature and optical power. However, the changes obtained after illumination are consistently larger than the ones obtained after relaxation. This indicates that under illumination, the conductance change is enhanced beyond the effects of simple heating.

However, the relationship of these two phenomena and how they regulate the dynamics of the conductance evolution is unclear from these measurements since it is difficult to disentangle one from the other.

We have shown that the photo-induced decrease in differential conductance is dependent on the incident dose of photons. **When the junction is illuminated in its ON state, light enhances the thermal relaxation as a higher dose of photon leads to a greater decrease in the conductance.**

### 5.9.2) Spectral Response

In order to gain additional information on the photo-induced effect observed in our junctions we have investigated its spectral efficiency. To do so we have used three different LEDs emitting at different wavelengths in the visible range ( $\lambda = 405\text{nm}$ ,  $\lambda = 565\text{nm}$  and  $\lambda = 625\text{nm}$ ). The optical power of the LEDs used for this experiment was  $P \approx 200 \text{ mW.cm}^{-2}$  since this is the maximal common output to all three LEDs.

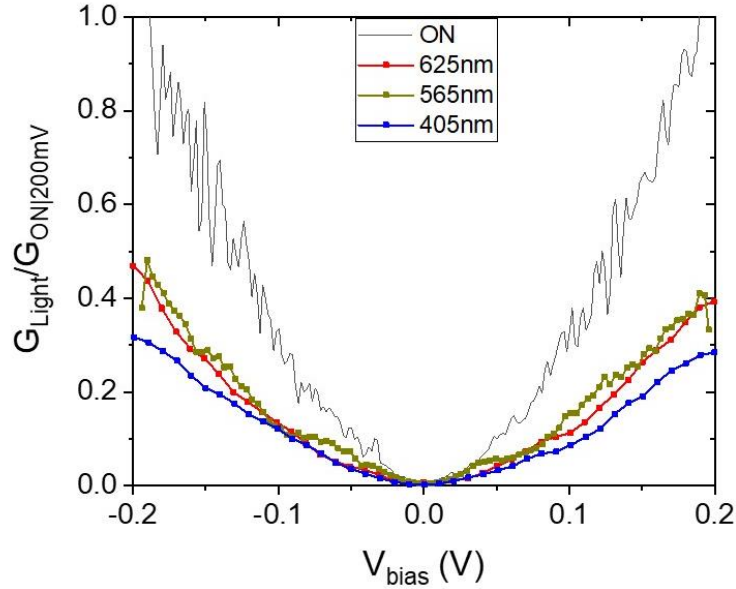


Figure 5-15: Normalized differential conductance  $G/G_{pol|200mV}$  as a function of the bias voltage measured at a temperature of  $T = 4K$  after an illumination with different wavelengths at a temperature of  $T = 95K$ .

Figure 5-15 shows the normalized differential conductance after illumination normalized by the conductance before illumination calculated at a bias of  $V_{bias} = 200mV$  as a function of the bias voltage before and after illumination with three different wavelengths. In this graph the bigger the decrease in conductance, the higher the effect of the wavelength used. **We can see that although the difference between the curves is small, the conductance decrease is highest for a wavelength of  $\lambda = 405nm$ .**

### 5.9.3) Time dependence

In this section we will describe the time dependence of the differential conductance evolution during illumination.

The sample was illuminated for a specific time  $t$  at  $T = 95K$  before the light was turned off and its conductance measured at  $4K$ . The illumination was then resumed without resetting the state of the junction.

Figure 5-16a shows the differential conductance as a function of the bias voltage in the ON and OFF states as well as after different sequences of illumination. The decrease in conductance is investigated as a function of the illumination time for an illumination with an optical power of  $P = 465mW \cdot cm^{-2}$  with a wavelength  $\lambda = 405nm$ .

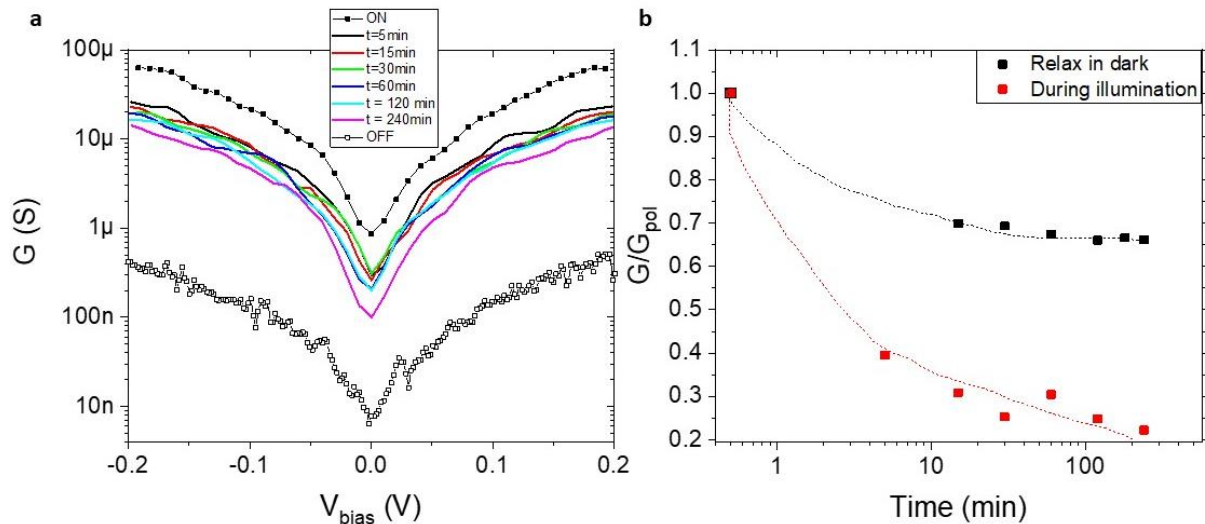


Figure 5-16: (a) Differential conductance as a function of the bias voltage in the ON and OFF states as well as after illumination at a temperature of  $T = 95K$  with an optical power of  $P = 465mW.cm^{-2}$  with a wavelength  $\lambda = 405nm$ . The illumination time was varied between 5min and 240 min. (b) Time dependence of the normalized differential conductivity  $G_{Light}/G_{pol|100mV}$  calculated at a bias voltage of  $V_{bias} = 100mV$  in dark prior (black) and after illumination (red). These data are extracted from (a).

Figure 5-16b shows the normalized conductance  $G_{Light}/G_{pol|100mV}$  at a voltage bias of  $V_{bias} = 100mV$  as a function of the illumination time at a temperature of  $T = 4K$ . Note that the data point at 0.1 min is calculated from the conductance after poling in the ON state and serves as a reference. We note that the conductance decrease is continuous over a time period of several hundreds of minutes at least with the strongest decrease however occurring over the first ten minutes.

As a means of comparison, the evolution of the conductance in dark at a temperature of  $130K$  is also shown in this graph. Note that the temperature of relaxation was chosen such that it corresponds to the actual temperature of the sample during illumination due to light induce heating, as is explained in section 5.14.1). We note that the conductance seems to saturate in dark to approximately 68% of its initial value over the time period of the measurement. **However, under illumination, the conductance decreases faster than in dark and does not saturate over the time period of the measurement.**

#### 5.9.4) Temperature dependence

We have investigated the temperature dependence of the photo-induced decrease in conductance on YBCO/ITO junctions. We have compared the magnitude of the conductance decrease after illuminating the junction at several temperatures.

Figure 5-17a shows the conductance vs. bias after illumination, normalized to the conductance before illumination calculated at a bias of  $200mV$  and  $T = 4K$ , measured at  $4K, 50K$  and  $100K$ . We note that the efficiency of the photo-induced conductance drop increases monotonously as the temperature of illumination increases.

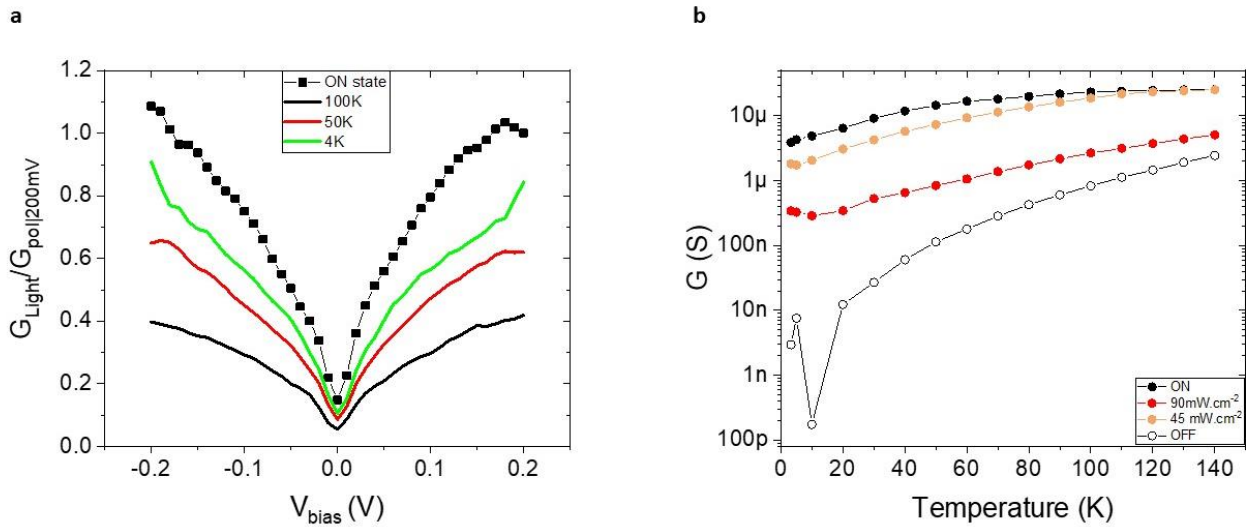


Figure 5-17: (a) Differential conductance calculated at a bias of 200mV normalized by the conductance before illumination  $G_{\text{Light}}/G_{\text{pol}|200\text{mV}}$  measured at a temperature of  $T = 4\text{K}$  after illuminating at different temperatures. (b) Temperature dependence of the conductance calculated at a bias of 0 mV in the ON and OFF states before illumination and after illumination with different optical powers.

Figure 5-17b shows the temperature behaviour of the differential conductance calculated at a bias of 0mV before illumination in the ON and OFF states as well as after illumination with two different optical powers. In this experiment, the illumination occurred at a temperature of  $T = 95\text{K}$  before turning the light off and cooling the sample down to the base temperature of the cryostat. The temperature was then gradually increased to 150K while measuring the conductance.

We note that the higher the optical power of the illumination the closer the qualitative behaviour of the conductance state is to the behaviour in the OFF state. We also note that the same deviation from the high temperature behaviour is observed in the states obtained after illumination. This comforts the observations made in the previous section about the cumulative nature of this effect.

As stated previously, the system's ground state is its low conductance OFF state and by applying a positive voltage pulse one can drive it towards the metastable ON state. At high temperature we have noted a gradual decrease of the conductance from the metastable state towards the system ground state in the absence of illumination. **We have shown that illuminating the sample increases its temperature and accelerates the relaxation towards the ground state. In addition, we have also shown that a light-only induced increase in temperature is not sufficient to explain the magnitude of the conductance change under illumination. Instead, one has to consider an additional optical effect that is not related to temperature change. One can thus conclude that light activates the relaxation into the ground state.**

### 5.10) Persistent illumination effects in the OFF state

As stated previously in section 5.7), we have observed a permanent photo-induced increase in the conductance of a junction after visible light illumination. The measurements described in this section are all performed in dark, after the light is turned off. We have maintained the same experimental procedure described in section 5.9), where persistent illumination effects in the ON state are presented. The junction was illuminated using a monochromatic LED with  $\lambda = 405\text{nm}$ , at a temperature of  $T = 4\text{K}$ , with an optical power of  $P = 158\text{mW.cm}^{-2}$  and for a duration of  $t = 2\text{hrs}$ . Any change from these conditions will be explicitly stated.

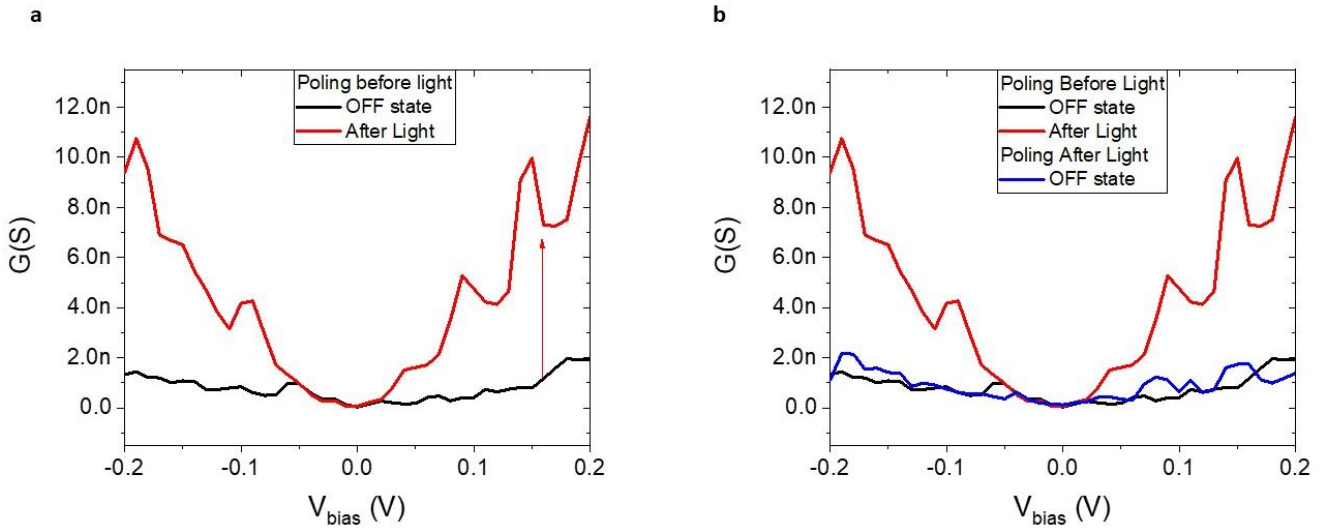


Figure 5-18: (a) Differential conductance of a YBCO/ITO junction in the OFF state at a temperature of 4K before (black) and after (red) illumination. (b) Differential conductance of the junction after applying a poling voltage of  $V_{pol} = -4V$  after the illumination.

Figure 5-18a shows the differential conductance of the junction as a function of the bias voltage at a temperature of  $T = 4K$  before and after illumination. A poling voltage of  $-4V$  was applied on the junction prior to the illumination for it to effectively reach the low conductance OFF state. The differential conductance of the junction increases by approximately a factor 4 at a bias of 100mV. Figure 5-18b shows the differential conductance of the junction after applying a poling voltage of  $-4V$  after the illumination. **This highlights the reversible nature of the light induced changes in the OFF state.**

### 5.10.1) Time dependence

We have also investigated the time dependence of the photo-induced increase of the junction conductance after illumination. The junction was first set in the low conductance OFF state at a temperature of  $T = 4K$  by applying a poling voltage of  $V_{pol} \sim -4V$ . The junction was then illuminated for a pre-set amount of time  $t$  before its differential conductance is measured in dark. The illumination was then resumed without resetting the conductance state of the junction.

Figure 5-19a shows the conductance of the junction calculated at a bias of 100mV as a function of illumination time. The point at  $t = 0min$  indicates the conductance in the OFF state prior to the illumination. Figure 5-19b on the other hand, shows the ratio between the conductance after and before illumination  $G_{Light}/G_{pol}$  calculated at a bias of 100mV as a function of illumination time in log-log scale.

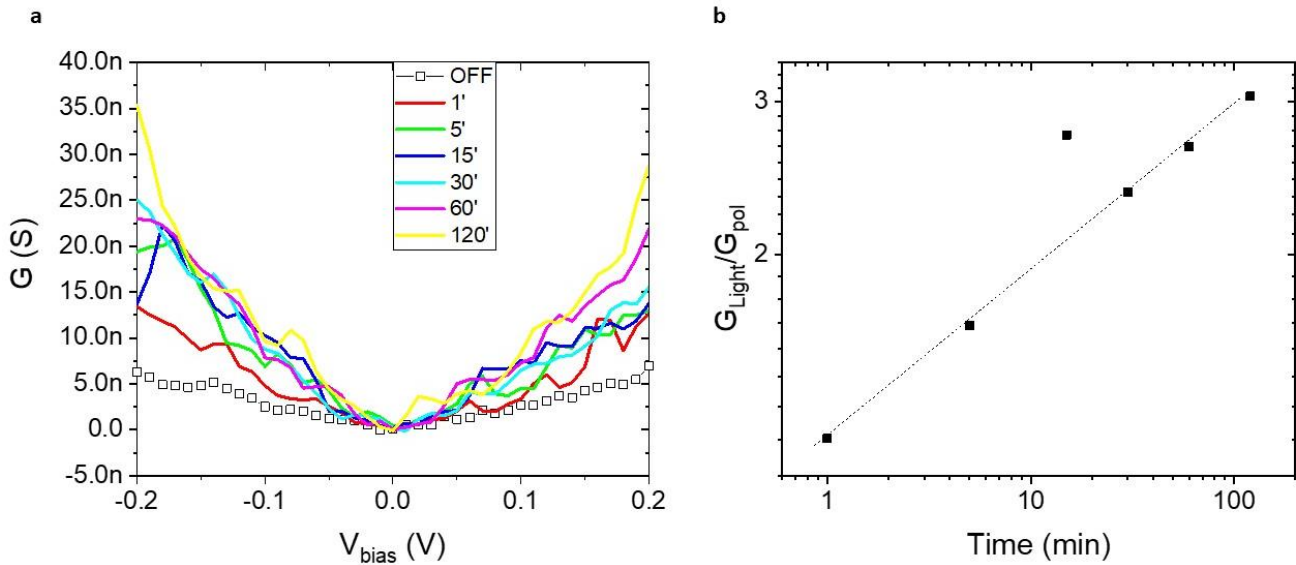


Figure 5-19: (a) Differential conductance as a function of the bias voltage in the OFF state and as a function of time after illumination. (b) The ratio  $G_{\text{Light}}/G_{\text{pol}}$  calculated at a bias of 100mV as a function of time after illumination.

The increase in conductance mostly occurs over a small period of time  $t \sim 10\text{min}$  after which the changes are significantly slower. Note the power relationship between the conductance increase and the illumination time characterized by a straight line in the log-log plot.

### 5.10.2) Temperature dependence

We have investigated the temperature dependence of the photo-induced changes in the conductance of our junctions after illumination. The junction was poled in the OFF state (by applying a poling voltage  $V_{\text{pol}} \sim -4\text{V}$ ) prior to each illumination. The temperature of illumination was then gradually varied from 4K to 100K.

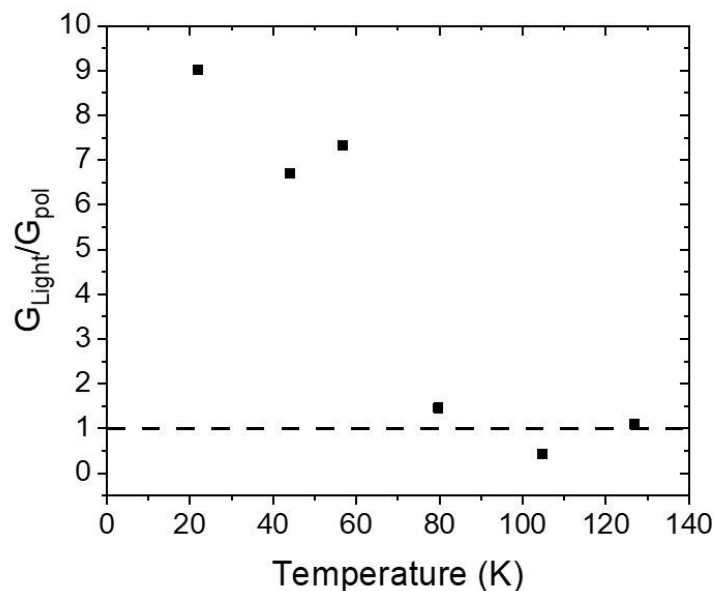


Figure 5-20: Temperature dependence of the ratio of the conductance after illumination to the one before illumination  $G_{\text{Light}}/G_{\text{pol}}$  calculated at a bias of 100mV at a temperature of  $T=4\text{K}$  after illuminating at several temperatures. The x axis was corrected for the actual temperature of the sample.

Figure 5-20 shows the ratio between the conductance after and before illumination  $G_{Light}/G_{pol}$  calculated at a bias of 100mV at  $T = 4K$  after illuminating at different temperatures as a function of the sample temperature. Note that the temperature shown in the x-axis represents the actual sample temperature under illumination measured by adjusting for the heating effects of the illumination as is described in section 5.14.1).

**We clearly note that contrary to what happens in the ON state (see section 5.9), in the OFF state the efficiency of the photo-induced effect is highest at low temperature and decreases as the temperature increases.** Note that these photo-induced changes disappear above a temperature of 60K.

**It is worth highlighting the correlation between the temperature dependence of the photovoltage detailed in section 5.8.1) and the one shown in Figure 5-8. The dependence of both effects seem to be altered at the same temperature of  $T = 60K$ . In a subsequent section 5.11.3), we will provide conclusive evidence that the conductance enhancement near the OFF state is proportional to the photovoltage.**

### 5.11) Illumination effects in intermediate junction states

In intermediate resistance states (that is, when the junction is driven by voltage pulses from the ON into OFF state, or vice versa), the light induced effects are those characteristic of the ON and OFF state at extreme temperatures. In particular, the behaviour described above for the ON state is visible for any intermediate state as the system is driven from OFF to ON only at high temperatures. Conversely, at low temperature the photo-induced effect observed in most intermediate states resemble the one described when the sample is illuminated in the OFF state. The behaviour of the photo-induced effects at other temperature shows a crossover for both types of behaviours. This will be detailed in the subsequent section and its analysis will provide insight into the physics of the microscopic mechanism.

#### 5.11.1) Characteristic behaviour across the OFF-to-ON branch of the hysteresis loop

The efficiency of the photo-induced effect in the intermediate conductance states has been investigated. Starting in the OFF state we have applied increasingly positive biases on the junction until the ON state was reached and illuminated it at each of the intermediate steps. The poling voltage applied across the junction at a temperature of  $T = 4K$  ranged from 2.5V to 6V without resetting the electrical state of the junction before each illumination. The sample was illuminated at high temperature ( $T = 95K$ ) to maximize the size of the effect, following the observations of the experiments discussed above in section 5.9.4). Note that the experiment was started as soon as a non-negligible increase in the conductance was measured after applying a poling voltage.

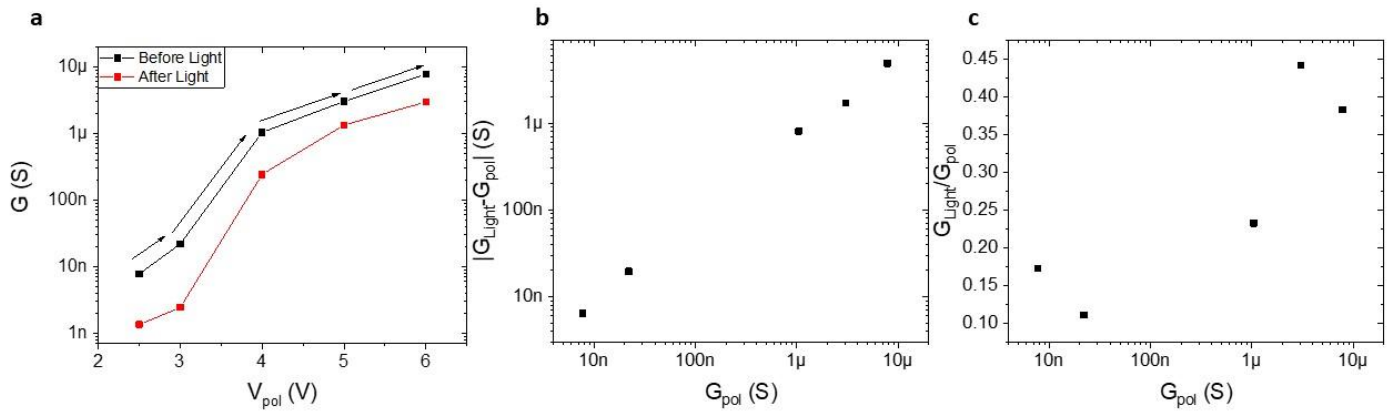


Figure 5-21: (a) Differential conductance calculated at a bias of 100mV measured before and after illumination as a function of the poling voltage applied across the junction before the illumination. (b) Absolute value of the difference between the conductance calculated at a bias of 100mV before and after illumination. (c) Ratio of the conductance before and after illumination calculated at a bias of 100mV. The data in (b) and (c) are extracted from (a).

Figure 5-21a shows the differential conductance calculated at a bias of  $V = 100\text{mV}$  at a temperature of  $T = 4\text{K}$  as a function of the poling voltage  $V_{pol}$  applied across the junction. The arrows indicate the change in conductance due to illumination. Figure 5-21(b-c) show the difference in conductance due to illumination  $G_{Light} - G_{pol}$  and the ratio between the conductance after and before light  $\frac{G_{Light}}{G_{pol}}$  respectively as a function of the conductance before illumination  $G_{pol}$ . In this experiment the conductance before illumination  $G_{pol}$  increases as the junction is switched from the OFF to the ON state. We note that after illumination, both  $G_{Light} - G_{pol}$  and  $\frac{G_{Light}}{G_{pol}}$  increase as  $G_{pol}$  increases.

This observation implies that the absolute photo-induced changes c.f. Figure 5-21b are the largest when the resistance state approaches that of the ON state. Contrarily, the relative photo-induced changes c.f. Figure 5-21c are the highest when the junction is close to the OFF state (with a ratio of close to 0.1) and decrease as its conductance increases (reaching a ratio of close to 0.4 in the ON state).

### 5.11.2) Characteristic behaviour across the ON-to-OFF branch of the hysteresis loop

Starting in the high conductance ON state we have applied increasingly negative biases on the junction until the OFF state was reached and illuminated it at each of the intermediate steps. The change in conductance at the intermediate resistive states is shown in Figure 5-22a showing the differential conductance calculated at a bias of 100mV as a function of the poling voltage before illumination (black) and after illumination (red) at 4K. In this experiment, the sample was illuminated at  $T = 4\text{K}$  to maximize the size of the effect in the ON state, following the observations of section 5.10.2).

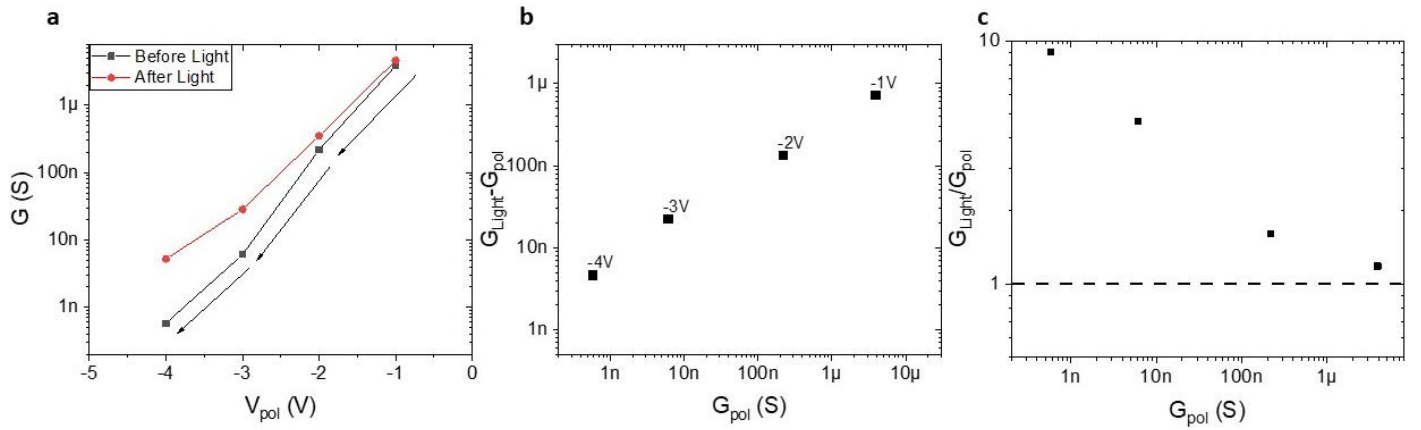


Figure 5-22: (a) Differential conductance of a YBCO/ITO junction before (black) and after (red) illumination as a function of the poling voltage  $V_{pol}$  on the left hand side of the hysteresis loop (from ON to OFF). (b) Absolute difference of the conductance before and after illumination  $G_{Light} - G_{pol}$  as a function of the conductance before illumination  $G_{pol}$ . (c) Ratio of the conductance before and after illumination  $G_{Light}/G_{pol}$  as a function of the conductance before illumination. The dashed line indicates a ratio of 1. The data are extracted from (a).

Figure 5-22(b-c) shows both the absolute difference and the ratio between the conductance after and before light ( $G_{Light} - G_{pol}$ ) and  $\frac{G_{Light}}{G_{pol}}$  respectively as a function of the conductance before illumination  $G_{pol}$ . ( $G_{Light} - G_{pol}$ ) decreases as the conductance decreases however, the ratio  $\frac{G_{Light}}{G_{pol}}$  displays the opposite trend and increases from a factor 1 to approximately 10 as the conductance of the junction decreases. As in the previous section, the relative changes are the largest at low conductance since the conductance increases by a factor 10 (as can be seen from Figure 5-22) and decreases by a factor 10 (as can be seen from Figure 5-21).

### 5.11.3) Similarity between persistent photoinduced changes in conductance and photovoltage $V_{oc}$

In this section we will highlight the differences and similarities between the persistent photo-induced changes in the conductance after illumination and the appearance of a photovoltage across the junction during the illumination.

We have investigated the correlation between  $V_{oc}$  and  $G_{Light}/G_{pol}$  across the hysteresis loop of the junction. Figure 5-23a shows the hysteresis loop of the conductance calculated at a bias of 100mV at  $T = 4K$  as a function of the poling voltage  $V_{pol}$ . The junction is illuminated at several points in the intermediate conductance states between the ON and OFF states at  $T = 4K$  with an optical power of  $P = 158mW.cm^{-2}$ .

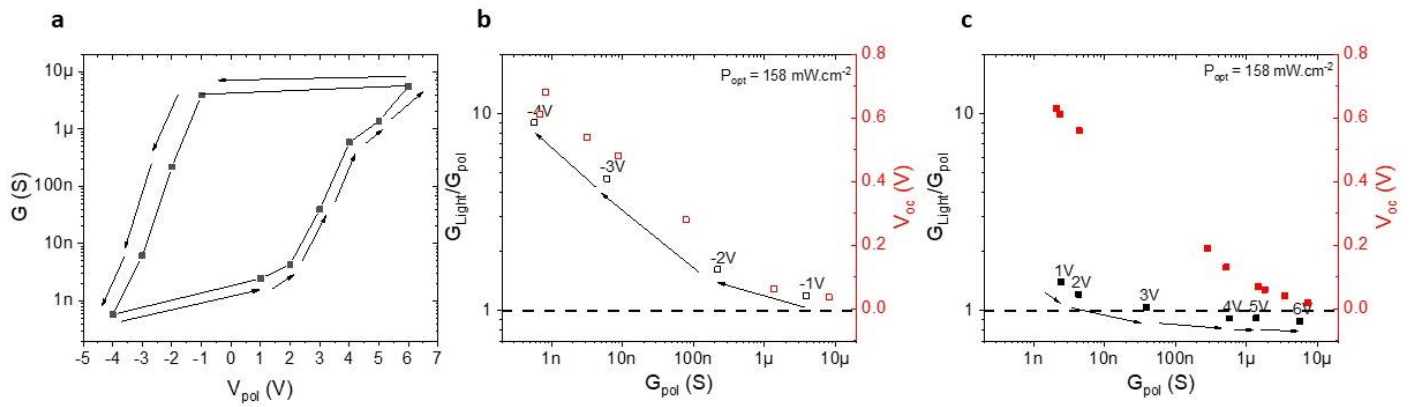


Figure 5-23: (a) Hysteresis loop showing the differential conductance calculated at a bias of 100mV as a function of the poling voltage. (b) Ratio of conductance ( $G_{Light}/G_{pol}$ )(black) and open-circuit voltage  $V_{oc}$ (red) as a function of the conductance before illumination on the (b)left/(c)right part of the hysteresis loop. The numbers indicate the corresponding  $V_{pol}$ . The sample was illuminated with an optical power of  $P = 158mW.cm^{-2}$ . The arrows indicate the direction of the poling sweep.

Figure 5-23b shows the ratio of conductance  $G_{Light}/G_{pol}$ (black) and  $V_{oc}$  (red) as a function of the conductance before illumination  $G_{pol}$ , for the left section of the hysteresis loop (that is, when the junction is electrically driven from the ON into the OFF state by application of  $V_{pol}$ ). The junction was first set in the ON state by applying a voltage of  $V_{pol} \sim 6V$ . The  $V_{pol}$  subsequently applied are indicated by the labels near the data points, following the order indicated by the arrows. **One can see that both  $G_{Light}/G_{pol}$  and  $V_{oc}$  increase as  $|V_{pol}|$  is increased and the junction conductance drops.** The relative conductance variation  $G_{Light}/G_{pol}$  increases by an order of magnitude as  $V_{pol} = -4V$  is applied, for which the junction switches completely to the OFF state. Meanwhile,  $V_{oc}$  (red dots) increases monotonically from 36mV to  $\sim 0.65V$  along the same sequence of poling voltages.

Figure 5-23c shows the ratio of conductance  $G_{Light}/G_{pol}$  (black) and  $V_{oc}$  (red) as a function of the conductance before illumination  $G_{pol}$ , this time for the right branch of the hysteresis loop (as indicated by the arrows, the junction is thus progressively poled back from the OFF to the ON state by applying a sequence of increasing  $V_{pol}$  (labels near the data points). We note that the conductance is enhanced upon illumination until a poling voltage of 4V is applied. The conductance increase is much smaller than in the negative branch of the hysteresis loop (Fig. 23b). That is, the ratio  $G_{Light}/G_{pol}$  significantly decreases after applying small positive  $V_{pol}$  (in the early stages of the OFF to ON branch) as compared to the late stages of the ON to OFF branch. Above  $V_{pol} \sim 4V$ , the ratio becomes smaller than 1. This means that the conductance *decreases* upon illuminating. Meanwhile, and despite the very different behaviour of  $G_{Light}/G_{pol}$  when comparing the left and right branches of the hysteresis loop (Figure 5-23b and Figure 5-23c), the behaviour of  $V_{oc}$  (red dots) is essentially the same for both branches: it decreases gradually from its maximal value of  $\sim 0.6V$  in the OFF state as the poling voltage is increased and the junction reaches the ON state.

In order to obtain additional insight into the crossover between the two photo-induced effects, we have performed the same experiment by illuminating the sample with a higher optical power.

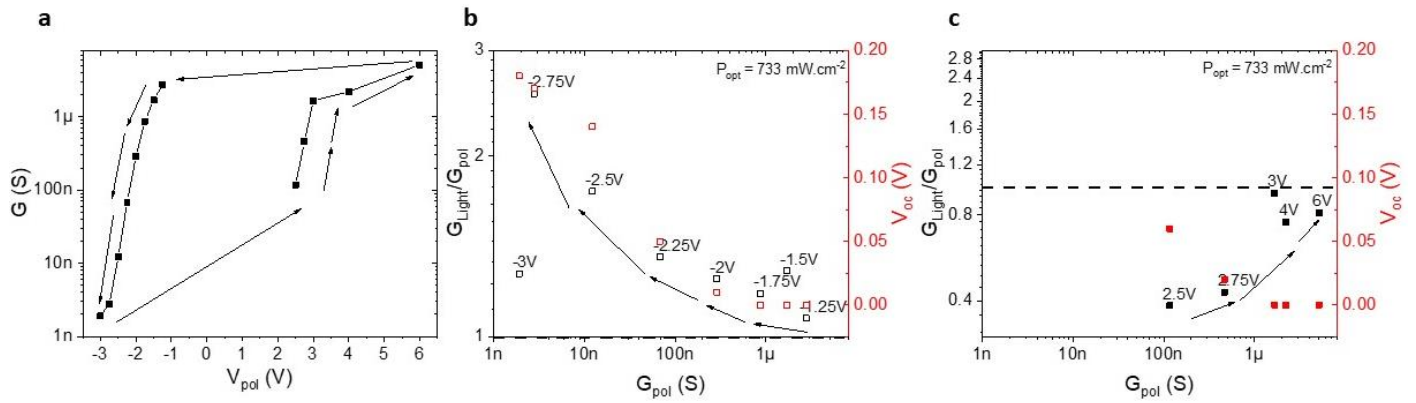


Figure 5-24: (a) Hysteresis loop showing the differential conductance calculated at a bias of 100mV as a function of the poling voltage. Ratio of conductance ( $G_{Light}/G_{pol}$ ) (black) and open-circuit voltage  $V_{oc}$  (red) as a function of the conductance before illumination on the (b) left/(c) right branch of the hysteresis loop. The numbers indicate the corresponding  $V_{pol}$ . The sample was illuminated with an optical power of  $P = 733 \text{ mW.cm}^{-2}$ . The arrows indicate the direction of the poling sweep.

Figure 5-24a and Figure 5-24b show the same experiments as Figure 5-23b and Figure 5-23c, only the optical power has been increased to  $P = 733 \text{ mW.cm}^{-2}$ . In the left branch of the hysteresis loop (Figure 5-24a) we observe the same qualitative behaviour as in Figure 5-23b. Quantitatively, however, the relative conductance increase  $G_{Light}/G_{pol}$  and photovoltage are both smaller than at lower optical power. This further supports that the light induced conductance increase across the ON to OFF switching and photovoltage have both the same microscopic origin. Furthermore, we can infer that both the conductance increase and the photovoltage are weaker here because the temperature of the sample increases significantly under an illumination with an optical power of  $733 \text{ mW.cm}^{-2}$  (as demonstrated in section 5.14.1), with this power we expect the temperature to reach approximately 70K and this drastically diminishes the photovoltage (see section 5.8.1). The opposite effect is observed in the right branch (across the OFF to ON switching), see Figure 5-24b. When illuminated with a higher optical power, the photo-induced conductance decrease is stronger (the ratio of conductance drops well below 1 in the early stages of the OFF to ON branch). That is, at higher optical power, the conductance decreases upon illumination over the entire right branch of the hysteresis loop. This suggests that the mechanism responsible for the conductance decrease is not related to the photo-voltage, and that it is favoured by the temperature increase. This is further supported by Figure 5-25

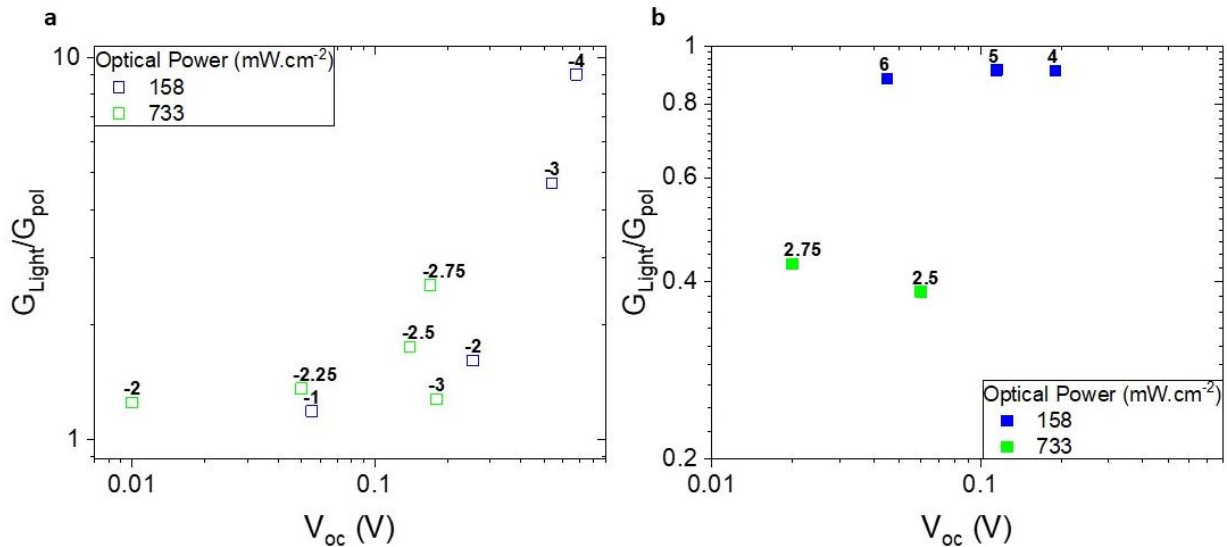


Figure 5-25: Ratio between the conductance before and after illumination  $G_{Light}/G_{pol}$  as a function of the open-circuit voltage  $V_{oc}$  illumination occurring on the (a)left/(b)right hand side of the hysteresis loop

Figure 5-25 shows the relative conductance variation after illumination,  $G_{Light}/G_{pol}$ , as a function of the photovoltage measured during illumination,  $V_{oc}$ , both for the left (Figure 5-25a) and right (Figure 5-25b) branches of the hysteresis loop. Data for the two used optical powers are included. One can see that the conductance increase observed in the left branch scales with the induced photovoltage. This is not the case of the right branch.

In summary, the key learnings from this section are:

- 1) In the OFF state, and all across the ON to OFF branch of the hysteresis loop, the conductance is persistently enhanced by illumination, and the relative variation  $G_{Light}/G_{pol}$  is proportional to the photovoltage  $V_{oc}$ . Both  $G_{Light}/G_{pol}$  and  $V_{oc}$  diminish with increasing optical power, which can be quantitatively understood by considering the temperature increase produced by the illumination.
- 2) In the ON state, the illumination effect is completely different: we observe a conductance decrease which scales with the light power and is stronger the higher the temperature. Contrary to 1), there is no correlation with  $V_{oc}$ .
- 3) In the OFF to ON switching branch, the behaviour resembles 1) or 2) depending on the temperature, optical power and junction resistance, which suggests that effects 1) and 2) compete as otherwise expected from their opposite dependence on temperature and optical power.
- 4) A crucial element to be considered is that the photovoltage depends itself only on the junction conductance -as is shown in Figure 5-10,  $V_{oc}$  scales with the logarithm of the junction conductance and is independent of the poling history.

A corollary for the above conclusions is that there exists an asymmetry in the photo-induced effects: they are opposite in the "ON to OFF" and "OFF to ON" branches. For a given junction conductance level, the illumination yields exactly the same photovoltage  $V_{oc}$  over both branches. However, in one case (left branch) that is associated to a persistent increase of the conductance after illumination, while in the other case (right branch) there is a persistent decrease of the conductance after illumination. This suggests that the interfacial distribution of oxygen vacancies, which explain the resistance switching effects, are different in each branch. This is discussed in detail in the next section.

## 5.12) Model

We have observed a persistent change in the differential conductance of a YBCO/ITO junction after illumination described in sections 5.9) and 5.10) with visible light as well as the appearance of a photovoltaic effect at low temperature described in section 5.8). The nature of the photo-induced change in the conductance depends on whether the junction is set in the ON state or the OFF state prior to illumination. **These effects can be explained based on two different light-mediated oxygen redistribution effects occurring near the junction interface. Depending on history and sample temperature, either 1) a change of the oxygen distribution *within* the YBCO only, or 2) an exchange of oxygen (redox reaction) with the ITO is favoured, which leads to different changes in the junction conductance.** For clarity purposes we will subsequently detail the mechanisms behind the appearance of a photovoltaic effect, the illumination on the ON state, those in the OFF state and finally those in intermediate conductance states.

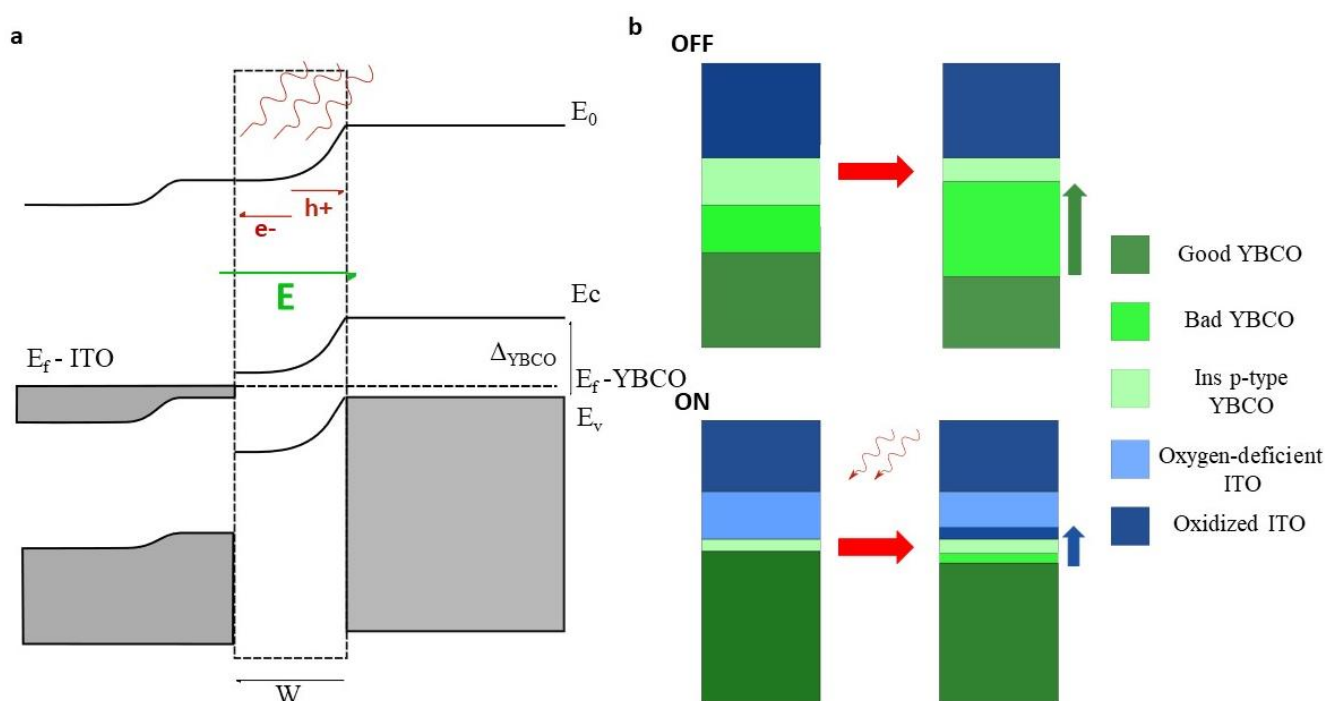


Figure 5-26: (a) Schematic band diagram of the YBCO/ITO interface. A band bending occurs at the interface. The green arrow represents the built-in electric field, the red arrows the photo-charges. (b) Schematic representation of the different scenarios occurring under illumination when the junction is in the (upper scheme) OFF / (lower scheme) ON state prior to the illumination. The blue and green arrows indicate the movement of oxygen ions due to light in both cases.

### 5.12.1) Photovoltaic effect

The measured photovoltage arises from a mechanism analogous to the photovoltaic effect observed in a p-n junction (Yang, Han and Chang, 2015; Xie *et al.*, 2019), which here forms at the interface between the ITO and the YBCO. Figure 5-26a shows a schematic representation of the interface between the two materials. Severely underdoped (oxygen depleted) c-axis YBCO plays a role of a tunnel barrier because of its low electrical conductivity, but for the band matching modelling it can be considered as a p-type semiconductor with an energy gap of approximately 1.25eV as reported in literature (Jagtap, Dégardin and Kreisler, 2012; Dadras and Ghavamipour, 2016). ITO as a n-type degenerate semi-conductor with its Fermi level lying in the conduction band (Kim *et al.*, 1999). A charge transfer will occur at the interface between these materials due to the different work functions ( $\phi_{\text{ITO}} = 4.5\text{eV}$  (Schlaf, Murata and Kafafi, 2001) and  $\phi_{\text{YBCO}} \approx 5.5 - 6\text{eV}$  (Van Zalk *et al.*, 2010)): electrons will diffuse from the ITO into the oxygen-deficient YBCO, leading to negative charge accumulation, and to the appearance of an electric field across the interface as in the scheme of Figure

5-26a. Upon illumination, the absorbed photons create electron-hole pairs which will be separated by the built-in electric field as shown in the scheme of Fig 26a. Thus, a photocurrent arises due to the drift of these photo-carriers. The associated open-circuit voltage reaches up to 0.7V in the junctions with the lowest conductance. The signs of  $V_{oc}$  and  $I_{sc}$  shown in Figure 5-7a are consistent with a photocurrent flowing towards the YBCO.

The above scenario is quantitatively consistent with the model of the junction interface derived from the tunnel conductance measurements. The depletion region width can be estimated using (Pierret, 1996)

$$W = \sqrt{\frac{2 * \epsilon_s}{e} \left( \frac{N_A + N_D}{N_A * N_D} \right) * V_{bi}}$$

where  $N_A \sim 8 \times 10^{19} \text{ cm}^{-3}$  and  $N_D \sim 5 \times 10^{20} \text{ cm}^{-3}$  are the carrier densities in the insulating YBCO (Ito, Takenaka and Uchida, 1993)(section 3.3) and ITO (Kim *et al.*, 1999), and the built-in voltage  $V_{bi} \sim 1.5\text{V}$  is estimated as the difference of work functions of both materials (assuming most of the band bending occurs in the p-type YBCO). This yields  $W \sim 5 \text{ nm}$ , which agrees with the barrier width  $d \sim 5\text{nm}$  extracted from the BDR fit of section 4.3.2.1) in the junction OFF state. Note as well that the YBCO layer recovers metallic and superconducting properties further from the interface, as evidenced in section 4.6). This is accompanied by gradual increase of the carrier density, which goes up to  $N_A \sim 5 \times 10^{20} \text{ cm}^{-3}$  ( c.f. section 3.3). In this more highly doped YBCO the depletion region would be much narrower,  $W \sim 2 \text{ nm}$ . All of that further supports the conclusion that, essentially, the heavily oxygen-depleted interfacial layer that yields dictates the junction's conductance is the active layer that plays the photon absorber role for the discussed photovoltaic effects

In the ON state, that is, when the strongly depleted YBCO layer (tunnel barrier) is the thinnest and the junction conductance orders of magnitude higher, the photovoltaic effect vanishes. Indeed, as demonstrated in Figure 5-10, the open-circuit voltage  $V_{oc}$  decays  $\sim$  linearly when plotted as a function of the logarithm of the junction's conductance. This behaviour can be understood if one considers the well-known Shockley-Queisser relation for the photovoltaic effect in p-n junctions (Shockley and Queisser, 1961),

$$V_{oc} = \frac{k_b T}{\eta q} \ln\left(\frac{I_{sc}}{I_0} - 1\right)$$

where  $\eta$  is an ideality factor (typically ranging between 1 and 2),  $q$  is the electric charge,  $I_{sc}$  is the short-circuit photocurrent and  $I_0$  is the reverse saturation current in the dark. Because the junction's conductance and the saturation current are roughly proportional, the experimental results in Figure 5-10 are indeed essentially explained by the above relation, which does predict that the photovoltage vanishes as the junction conductance increases. In addition, we cannot exclude that, close to the ON state when the junction conductance is high, the severely underdoped YBCO layer that absorbs photons becomes very thin which contributes to reducing the photovoltage.

### 5.12.2) Illumination effects in the ON state

When the junction is set in the high conductance ON state, we observe a persistent decrease of the conductance after illumination with visible light. Note that, as described in section 5.6), a natural relaxation from the ON state towards the OFF state occurs in dark, the relaxation rate being temperature dependent. This is because the OFF state is the ground state of the system: as described in Chapter 4) Indium atoms in ITO have a much lower reduction potential than Cu atoms in YBCO, and therefore upon fabrication ITO grows fully oxygenated at the expense of oxygen depletion of the YBCO

surface. The ON state is therefore a metastable state, created by applying voltage that reverses the redox reaction that is spontaneous from the electrochemical point of view. As discussed in chapter 4), the ON state (represented in Figure 5-26b) consists of a YBCO layer with an optimal oxygen stoichiometry (labelled “good YBCO”) separated from the oxygen deficient ITO layer by thin (~3 nm, see section 4.6) severely oxygen depleted insulating YBCO which behaves as the electron tunnelling barrier. Relaxation from the ON state into the OFF (ground) state requires overcoming a small energy barrier which is related to the diffusion of oxygen ions across the interface (c.f. Figure 5-27). This is why the relaxation rate is increased with increased temperature (section 5.6).

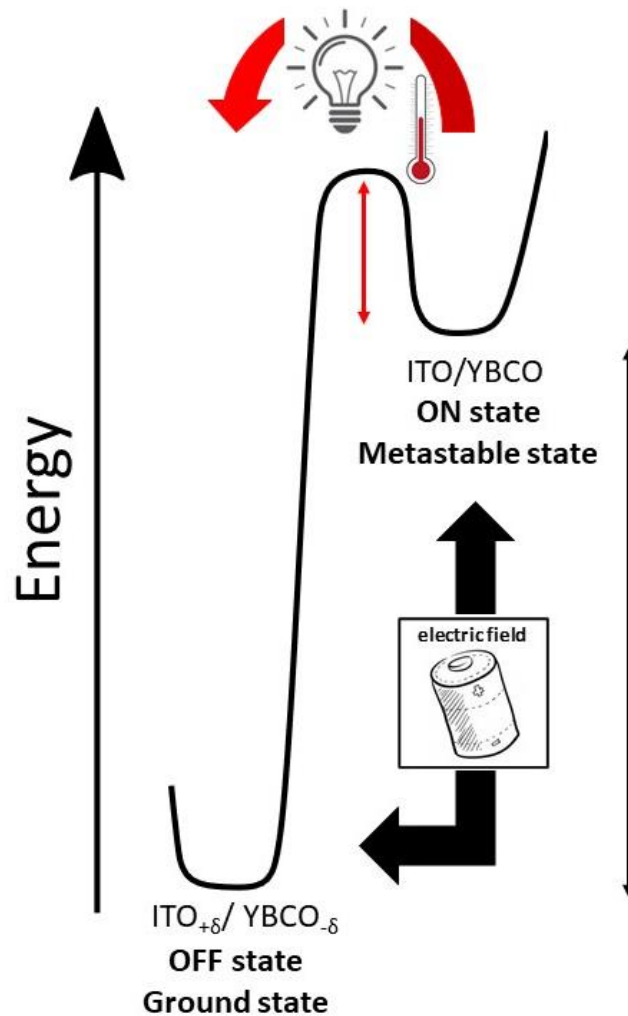


Figure 5-27: Schematic representation of an energy diagram representing the ground (OFF) and metastable (ON) states of a YBCO/ITO junction. The black and red arrows indicate the energy required to overcome the reduction potential difference (electrochemical) barrier and the barrier associated with ion diffusion across the surface respectively. The latter can be overcome through a voltage pulse, thermal activation or light illumination.

**By illuminating the junction, the relaxation from the ON into the OFF (ground) state is activated. This makes the relaxation (and the associated conductance decrease) much faster than in the dark.** Note however that, as demonstrated in section 5.9.1), the illumination effect is *not* just a consequence of heating. Light itself (and not only the collateral heating) activates the oxygen diffusion from the YBCO into the ITO, and thus acts as a catalyser of the redox reaction that leads to oxidation of indium in ITO and the reduction of copper atoms in YBCO. That is, photon absorption assist oxygen atoms in overcoming the energy barrier for ion diffusion and allows oxygen to cross the interface from the YBCO (which is oxygen-rich before the illumination) to the ITO layer (which is depleted in oxygen

before the illumination). This is represented by a blue arrow in Figure 5-26b. That process results in the thickening of the oxygen-depleted YBCO layer (a thickening tunnelling barrier), and thus to a conductance decrease. This process is of course also thermally activated, as evidenced by the temperature dependence of the effect in section 5.9.4).

In addition, the observations made in Figure 5-15 indicate that the efficiency of the light induced effect is wavelength dependent, i.e. for similar optical power shorter wavelengths produce stronger effects. This further proves that light plays an active role in activating the redox reaction occurring at the interface (not only through collateral heating). The spectral response of this effect calls to mind the enhanced photo-induced effects observed in underdoped YBCO thin films under UV illumination that are detailed in Chapter 3).

**In summary, light induced effects in the ON state result from the photon-assisted migration of oxygen from YBCO into ITO. The photon energy allows to overcome the energy barrier associated with oxygen diffusion across the barrier and allows the expected redox reaction (from electrochemical arguments) to take place.**

### 5.12.3) Illumination effects in the OFF state

Contrary to what happens in the ON state, when the junction is in the OFF state, we have observed a persistent increase in the conductance after illumination with UV/visible light. The OFF state corresponds to the virgin and ground state, in which the ITO layer is fully oxidized at the expense of the oxygen in the YBCO near the interface. This leads to a thick tunnelling barrier (primarily composed of insulating YBCO) and yields a low tunnelling conductance. As one moves away from the interface, the oxygen stoichiometry of the YBCO layer gradually increases back to its optimal concentration. This is schematized by the “bad YBCO layer” that is displayed in bright green in Figure 5-26a. As shown in Chapter 4), this intermediate layer (between the optimally doped YBCO and the oxygen depleted YBCO tunnelling barrier) presents depressed superconducting properties. In summary, in the OFF state we expect a strong gradient of oxygen content across the YBCO layer.

In this state, and indeed at every state across the switching between the ON and OFF states, the conductance of the junction increases after illumination, which denotes a narrowing of the tunnelling barrier (insulating YBCO layer). We showed in section 5.11.3) that the size of this effect scales with the size of the photovoltage under illumination, and thus has the same temperature dependence as the photovoltage. As just discussed in section 5.12.1), the photovoltage indicates the interfacial accumulation of photo-excited holes in the YBCO layer. **The key to understand the illumination in the OFF state is that this hole accumulation drives the re-oxidation of the YBCO near the interface. This occurs by oxygen migration from in-depth the YBCO layer and leads to widening of the “bad YBCO” (bright green) layer and to a narrowing of the insulating YBCO thickness (tunnel barrier).** This process is analogous to the photocatalytic effect in oxides discussed for many years in the literature (Mills and Le Hunten, 1997; Bora and Mewada, 2017). In other words, the main illumination effect in the OFF state is that it smoothens the strong oxygen content gradient across the YBCO layer, leading to a thickening of the “bad YBCO” while thinning out the “good YBCO” and “insulating YBCO” layers. The latter yields the observed conductance increase. A schematic representation of the interface after illumination is shown in Figure 5-26b where the light-induced motion of oxygen is represented as a green arrow. The efficiency of this reaction depends on the magnitude of the photovoltage, because as in p-n junction this is proportional to the photo-induced hole accumulation, and thus to the oxygen migration towards the interface from the bulk of the YBCO layer.

**In summary, light induced effects in the OFF state result from the photon-assisted migration of oxygen *within* YBCO. As in the ON state, illumination activates oxygen moves “up” in the structure.**

**The photon energy is used in creating a hole accumulation near the interface, which is widely discussed in the literature (Shifu *et al.*, 2009; Bora and Mewada, 2017) of photocatalytic reactions in oxides to help re-oxidizing the interface. The use of a p-n like structure coupled to an efficient light absorber allows a more efficient charge separation and a decrease in charge recombination to allow for enhanced photocatalytic behaviour.**

#### 5.12.4) Illumination effect in intermediate conductance states

At intermediated conductance states, the illumination effects are governed by a crossover of the two different mechanisms described above in the ON and OFF state. The balance between these two competing mechanisms depends on temperature and electrical history. The latter implies an asymmetry in the ON/OFF electrical switching process, which occurs through a different sequence of intermediate states, as described below.

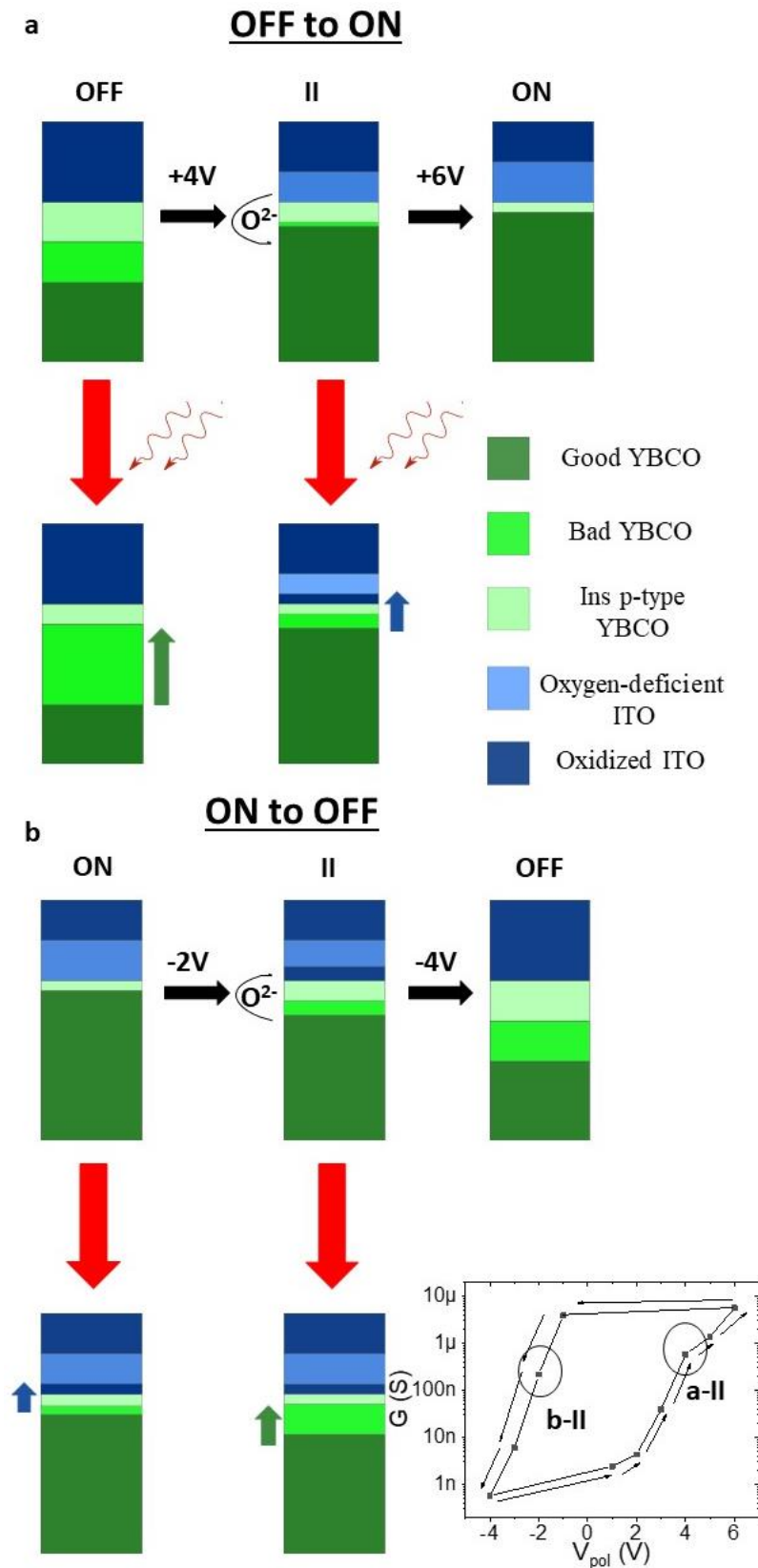


Figure 5-28: (a) Schematic representation of the YBCO/ITO interface during the electrical poling required to drive the junction (a) from the OFF to the ON state and (b) vice versa as well as the effects of illumination on some of the intermediate states. The black arrows and the voltages represent the applied poling voltage and the corresponding oxygen ion motion. The green/blue arrow represents the motion of oxygen within the YBCO layer and across the YBCO/ITO interface respectively. On the hysteresis loop in the inset the two intermediate states with similar junction conductance are highlighted.

This is highlighted in Figure 5-28a and Figure 5-28b, which respectively represent a cartoon of the YBCO/ITO interface across the ON to OFF (left) and OFF to ON (right) branches of the hysteresis loop, together with their corresponding illumination effects.

As was stated earlier, for a given junction conductance level (represented by the highlighted conductance states in the hysteresis loop of Figure 5-28), the illumination yields exactly the same photovoltage  $V_{oc}$  over both branches. However, in one case (ON to OFF) that is associated to a persistent increase of the conductance after illumination, while in the other case (OFF to ON) there is a persistent conductance decrease after illumination.

The electrical switching from the OFF into the ON state occurs by gradual oxygen depletion of the ITO layer, which allows filling up the YBCO layer. The applied voltage allows the redox reaction between the YBCO and ITO, which in the absence of applied voltage would go in the opposite direction due to the difference of reduction potentials. Both ITO and bad/good YBCO are metallic, and the applied voltage drops across the insulating YBCO. In the late stages of the switching, represented by a-II), the YBCO layer is fully replenished with oxygen almost at optimal stoichiometry near the interface (this is illustrated by a very thin “bad YBCO” layer at the interface) at the expense of the oxygen depletion within an important portion of the ITO layer. Notice that oxygen depleted ITO is metallic (Kim *et al.*, 1999). The illumination effects vary across the different states, from that characteristic of the OFF state (see section 5.12.3) above) to that characteristic of the ON state, because the interface **gradually** changes from one that resembles the OFF state (an oxygen rich ITO layer and the presence of an important “bad” YBCO layer) to one that resembles the ON state (an important oxygen deficiency in the ITO layer and an oxygen rich YBCO layer separated by a very thin insulating YBCO layer).

The electrical switching from the ON into the OFF state gradually depletes oxygen from the YBCO layer (yielding “bad YBCO” at the interface) and fills the ITO layer. This process goes as dictated by the difference of electrochemical potentials of YBCO and ITO, and in this sense it is spontaneous. However, it has slow dynamics due to the energy barrier for oxygen diffusion from one material to the other. The dynamic is accelerated by thermal activation (see section 5.6) but also electrically as the applied voltage helps overcoming the barrier for oxygen diffusion (notice that oxygen vacancies are charged defects). In the early stages, the redox-reaction takes oxygen from the fully oxygenated interfacial YBCO (dark green) and moves it to the interfacial ITO at the other side of the tunnelling barrier. Thus, from the very first stages, a “bad YBCO” interfacial layers forms, and the interfacial ITO is re-oxygenated. This is shown in case b-II in Figure 5-28b. Notice that at this early stage the layering is already similar to that in the OFF state, in the sense that an interfacial “bad YBCO” layer is present and the ITO is oxygenated at the interface with the tunnelling barrier (dark blue). The switching evolves as more oxygen moves to the ITO at the expense of further depleting YBCO. In the final stages, a thick “bad YBCO” layer has formed and the “insulating” YBCO layer has also thickened, while the ITO layer is oxygen rich. During this process, the illumination effect rapidly evolves from that characteristic of the ON state to that characteristic of the OFF state, because of the strong gradient of oxygen content within the YBCO and the fully oxygenated interfacial ITO that forms rapidly.

This model allows to explain the asymmetry in light induced effects observed across the hysteresis loop: Two similar intermediate resistance states (on the left and right branches of the hysteresis loop with the same conductance) are characterized by different light induced effects c.f. Figure 5-23 and Figure 5-24. This is portrayed by the cases (a-II) and (b-II) in Figure 5-28 showing a similar insulating YBCO layer (corresponding to the tunnelling barrier width of the junction) and as such very similar  $V_{oc}$ . The presence of an oxygen rich YBCO layer as well as an oxygen deficient ITO layer before

illumination **near the interface** in case a-III drives the light induced electrochemical reaction characteristic of the ON state. Conversely, the presence of a “bad YBCO” layer as well as an oxygen-rich ITO layer **near the interface** drive the characteristic light induced electrochemical reaction of the OFF state.

As temperature increases however, the energetic landscape of these two reactions changes dramatically. The characteristic behaviour observed in the ON state is largely preferred over the one observed in the OFF state in the intermediate resistance states as is detailed in section 5.9.4), section 5.10.2) and Figure 5-24.

### 5.13) Conclusion

We have measured a TER effect of several orders of magnitude in YBCO/ITO junctions similar to the one described in Chapter 4). Additionally, we have observed a persistent, reversible and history-dependent light-induced change in the conductance of our junctions under UV/visible illumination. The differential conductance increases after illumination if the junction is set in the OFF state and decreases if the junction is set in the ON state. We have also measured a photovoltaic effect across the junction under UV/visible illumination ( $\lambda = 405\text{nm}$ ) leading to a  $V_{oc} \approx 0.7\text{V}$  and a  $J_{sc} \approx 17 \text{ mA} \cdot \text{cm}^{-2}$ .

These effects have been interpreted through the lens of a light-assisted electrochemical reaction occurring at the interface between the two electrodes. In the ON state, light accelerates the natural relaxation towards the system ground state leading to the reduction of the YBCO electrode at the expense of the ITO. On the other hand, in the OFF state, photocarriers resulting from the absorption of photons are separated at the interface and participate in the oxidation of the YBCO layer near the interface. This leads to a decrease in the barrier height and an increase in the conductance of the junction.

The peculiar behaviour of our junctions in response to external stimuli pave the road to a versatile applicability in the field of electronics. The dual control of the resistive state of our junctions (in both directions) through the use of electric fields and light irradiation widens the field of applications in neuromorphic computing as multi-state memristors or even in light sensing technology.

## 5.14) Supplementary measurements

The present section will cover additional experiments that were performed on these junctions to rule out experimental artefacts. They have been referred to along the chapter and have been placed here for clarity and to avoid disrupting the flow of experiments and discussions.

### 5.14.1) Thermal vs photo-induced effects

Since both the photo-induced effects observed when the junction is in the ON state and the thermal relaxation lead to a decrease in the differential conductance of the junction, we needed a way to differentiate between the two effects. We needed to first characterize the heating power of the LEDs during the illumination experiment on the sample. Figure 5-29a shows the time dependence of the resistance measured across the YBCO film (in a 4-point probe configuration) while the temperature of the cryostat was set to  $T = 95K$  before during and after illumination with a LED at different optical power. Figure 5-29b shows the temperature dependence of the resistance measured across the same YBCO layer in dark. A measure of the temperature of the sample during the illumination can thus be obtained from the values of the resistance measured. This allowed us to characterize the sample temperature under illumination for temperature higher than 80K.

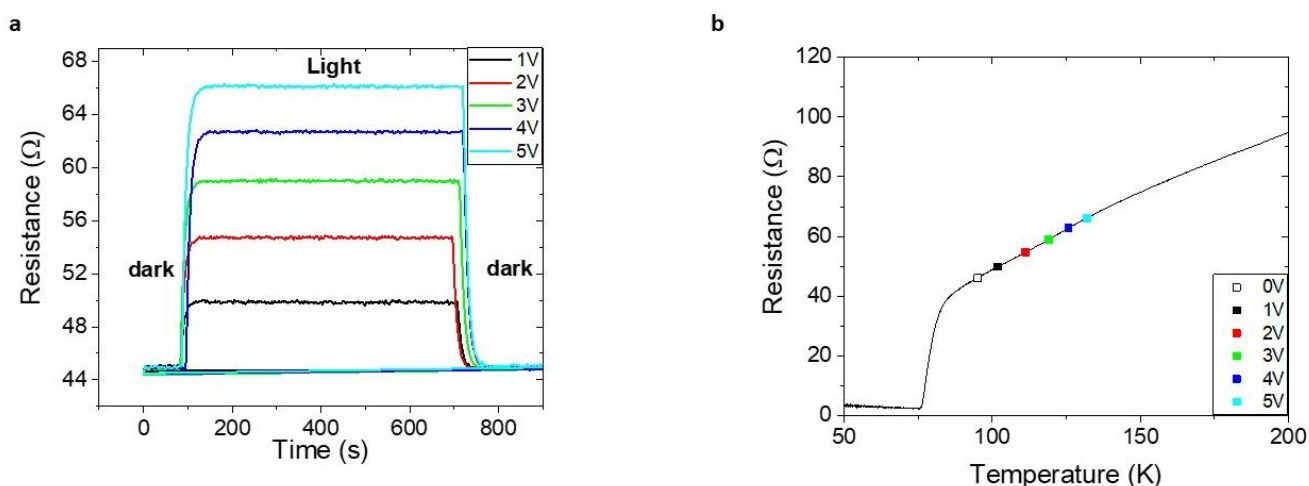


Figure 5-29: (a) Time dependence of the resistance measured in a 4 point configuration across the YBCO layer while the temperature is fixed at  $T = 95K$  before, during and after illumination with different optical powers. The wavelength of the light used is  $\lambda = 405 \text{ nm}$ . (b) Temperature dependence of the resistance measured in a 4 point configuration across the YBCO layer in dark. The highlighted coloured points represent the resistance measured across the YBCO layer during illumination.

We have measured the resistance across one of the YBCO/ITO junctions when the sample was illuminated below 80K. The particular junction is chosen such that its resistance is in the  $k\Omega$  range at low temperature and the current bias is chosen such that it maximizes the signal to noise ratio without damaging the junction. The experimental procedure used is the same than the one described previously. This allows us to accurately measure the sample temperature over the whole temperature range.

### 5.14.2) Absence of effects under infrared illumination

We have investigated the effects of infrared radiation on the transport properties of YBCO/ITO junctions. No photo-induced effects are observed on the junctions under infrared illumination. A monochromatic LED emitting at a wavelength of  $\lambda = 1050 \text{ nm}$  with an optical power of  $P \approx 100 \text{ mW} \cdot \text{cm}^{-2}$  was used to illuminate the junctions for a period of  $t = 2 \text{ hrs}$ . Figure 5-30a shows the IV curve measured during illumination at a temperature of  $T = 4K$  in the ON and OFF states. No apparent photovoltaic effect is observed in this measurement.

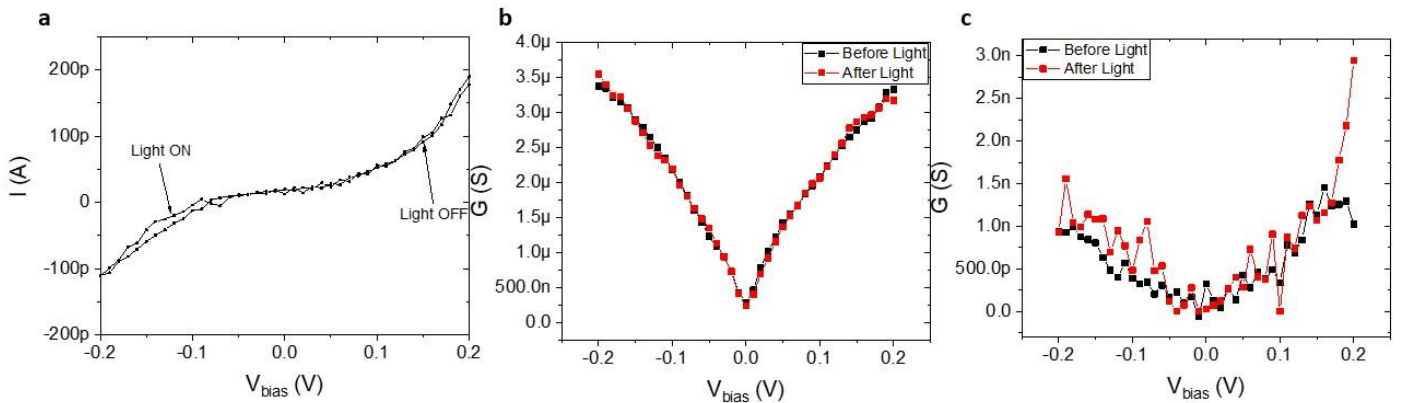


Figure 5-30: (a) IV curve measured in dark and under illumination with  $\lambda = 1050 \text{ nm}$  LED at a temperature of  $T = 4\text{K}$ . The junction was set in the OFF state prior the illumination. (b-c) Differential conductance as a function of the bias voltage measured in the ON state and after illumination that took place at temperature of  $T = 100\text{K}$  (c) in the OFF state before and after illumination that took place at  $T = 4\text{K}$

Figure 5-30 (b-c) also shows the differential conductance of these junctions before and after illumination in the ON and OFF states. No apparent change in the conductance is measured after illumination.

This would suggest there exists a threshold of at least 1.18eV in energy for all the effects described in the previous three sections.

### 5.14.3) Light induced fatigue

During our investigation of the photo-induced effects on YBCO/ITO junctions we encountered at least two distinct fatigue phenomena. The first one is a gradual decrease in the magnitude of the photo-induced effect after several long illuminations. This effect thwarted the progress of our systematic investigation of the light induced effects since the successive illuminations required to do so led to gradually smaller effects. The results shown in this section was set in the high conductance ON state prior to the illumination.

Figure 5-31 shows the differential conductance of a YBCO/ITO junction as a function of the bias voltage in the ON and OFF states as well as after three successive illuminations performed in the same conditions. The sample was successfully re-poled both in the OFF then ON states prior to each illumination. We clearly see a gradual decrease in the magnitude of the photo-induced effect as the number of successive illuminations increases. This can be seen from the decrease in the persistent conductance drop occurring after the illumination. Note that the efficiency of the electric poling seems to be unaffected by the light induced fatigue since the voltages required to recover the ON and OFF states remain unchanged. Several methods were used in order to cancel the fatigue and recover the full efficiency of the photo-induced effects such as repeated electrical poling or temperature cycles up to room temperature but to no avail.

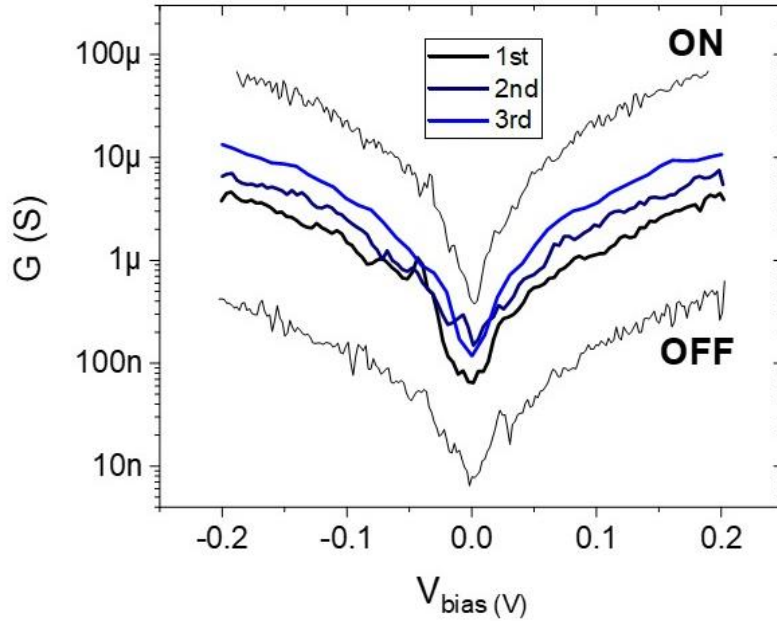


Figure 5-31: (a) Differential conductance as a function of the bias voltage in the ON and OFF states at a temperature of  $T = 4K$  as well as after three successive illuminations occurring under the same conditions. We note a gradual decrease in the efficiency of the photo-induced effect.

#### 5.14.4) Aluminium vs Gold wires

It may be of interest to note that a difference in behaviour was observed initially when the junctions were contacted using aluminium (Al) or gold (Au) wires. The majority of junctions measured during this thesis have been contacted using aluminium wire for its simpler implementation (the aluminium wires achieved a higher mechanical stability than the gold wires). We noted a gradual decrease of the conductance as a function of time once the junctions have been contacted with

aluminium wires.

Figure 5-32a shows the differential conductance as a function of the bias voltage measured across a YBCO/ITO junction contacted with Alu wire at room temperature over a period of 30 minutes. We clearly see a decrease of the conductance as a function of time. This evolution can reach several orders of magnitude if the samples are kept in a controlled atmosphere for a long period of time (typically around days).

However, this effect seems to disappear once the junctions are contacted using Au wires. Figure 5-32b shows the differential conductance measured across a YBCO/ITO junction contacted with an Au wire and of a similar size than the one presented in Figure 5-32a. We clearly note the absence of any variation of the conductance over a period of 30minutes.

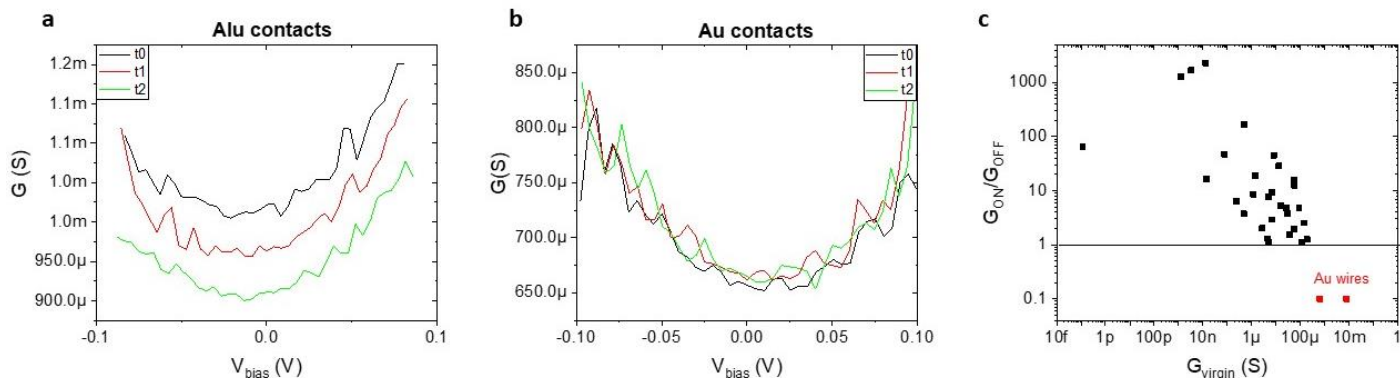


Figure 5-32: Differential conductance as a function of the bias voltage measured on YBCO/ITO junctions contacted with Aluminium wires (a) and Gold wires (b) at room temperature for a period of 30 minutes. (c) Electroresistance ( $ER = \frac{G_{\text{ON}}}{G_{\text{OFF}}}$ ) measured across YBCO/ITO junctions as a function of the virgin state conductance at a temperature of 4K. The black dots indicate the junctions contacted with Al and the red dots the ones contacted with Au.

A possible explanation of this effect lies in the reactivity of aluminium to YBCO. As a matter of fact, reports have shown that the optical and transport properties of YBCO are locally affected once contacted with aluminium wires (Begon-Lours, 2017). It has been postulated that this change in properties originates from the tendency of YBCO to lose its oxygen when in contact with a highly oxidizing material. In our junctions the presence of aluminium wires on top of ITO might exacerbate the redox reaction occurring at the interface between the ITO and the YBCO leading to a decrease of the conductance as a function of time.

Although it is clear that the dynamic of the conductance at room temperature is affected by the nature of the wire used to contact the junctions, its relevance to the magnitude of the electroresistance (ER) and the photo-induced effects is unclear. Figure 5-32c shows the ER as a function of the virgin state conductance measured at 4K. While some dispersion exists, the higher ER efficiency are achieved on junctions with a fairly low conductance in the virgin state. It is thus favourable for the sake of the effects studied in this chapter to use aluminium wires to contact the junctions.

# 6) Tunnel electroresistance observed in $NdNiO_3$ /MoSi vertical tunnel junctions

## Contents

6) Tunnel electroresistance observed in $NdNiO_3$ /MoSi vertical tunnel junctions.....	173
6.1) Motivation & main results .....	174
6.2) Nickelate structure.....	174
6.3) Film Growth and Device Fabrication.....	175
6.3.1) Film Characterization .....	176
6.3.2) Device Fabrication.....	177
6.4) Transport Measurement.....	178
6.4.1) Differential conductance in the ON (low resistance) and OFF (high resistance) states 178	
6.4.2) Influence of poling on MIT .....	180
6.5) Poling Efficiency as a function of Poling temperature .....	181
6.6) Relaxation dynamic.....	182
6.7) Model.....	184
6.8) Conclusion.....	185

## 6.1) Motivation & main results

Throughout this thesis we have studied the effect of field effect and illumination on a variety of different samples whose main component is the cuprate high  $T_c$  superconductor. The natural follow up would be to investigate these effects on a slightly different class of materials. Nickelates are the first candidates that come to mind. As a matter of fact, this class of materials belongs to the same family of oxides as cuprates and share a number of common properties such as metal-to-insulator transitions (Liao *et al.*, 2018) and superconductivity with a  $T_c$  vs. doping dome (Li *et al.*, 2019) in the infinite layer (strongly reduced) phase. In addition, replicating the experiments described in the previous chapters on nickelates might help to shed some light on the unexplained cuprate properties. On the other hand, nickelates are promising candidates for the creation of memristive devices because of their strong first order metal-to-insulator Transition (MIT) which is tuneable by external parameters (Guo *et al.*, 2020)(Nikulin *et al.*, 2004)(Heo *et al.*, 2017). They have been used to create Ferroelectric Tunnel Junctions (FTJ) that displayed a record millionfold resistive switching which is believed to originate from an electric field induced reversal of the ferroelectric polarization (Bruno *et al.*, 2016).

This is why we have fabricated tunnel electro-resistance (TER) devices by growing NdNiO<sub>3</sub> (NNO) thin films on a LAO substrate by PLD then depositing a MoSi counter electrode to define micrometre wide junctions following the recipes detailed in section 2.9.1). We observed the same qualitative behaviour in these junctions as the one described in the previous chapters of this thesis: in the absence of a ferroelectric layer and by applying voltage pulses ( $\sim V$ ) one can switch the resistance of these junctions by several orders of magnitude. In addition, we have found that the bulk metal-to-insulator transition temperature shows in these junctions' conductance, and that the MIT is different in the ON and OFF state of the junctions, indicating a change in the oxygen stoichiometry near the interface –similarly as in the case of cuprates, see Chapter 4). This indicates that the resistive switching observed in these devices is due to an electric-field induced oxygen migration across the interface between the MoSi and the nickelate. At variance with the case of cuprate junctions, while this junction's ON/OFF states are persistent at low temperatures., here the ON (high conductance state) relaxes into the OFF state much faster –following a stretched exponential law– as the temperature increases.

We will start this chapter by describing the properties of nickelates then detail the device fabrication techniques used to obtain the samples. We will then describe the transport measurements highlighting the TER effect observed in these junctions. The next two sections will cover the temperature efficiency of poling as well as the relaxation dynamic at high temperature. Finally, a model will be presented before concluding the chapter.

## 6.2) Nickelate structure

In this section we will describe the basic properties of nickelates required to place the results presented below in an adequate context.

Nickelates of the form RNiO<sub>3</sub> are characterized by a perovskite unit cell where the rare earth ion R sits at the centre of a cube formed by nickel atoms and surrounded by an oxygen octahedra (Chen *et al.*, 2018). At room temperature, nickelate crystals possess an orthorhombic structure whose lattice constant depend on the radii of the rare earth ion. These materials are characterized by a temperature dependent structural phase transition. The unit cell volume displays a sudden increase as the temperature is lowered as well as a hysteretic temperature behaviour (Medarde, 1997).

The most interesting attribute of these materials is certainly the temperature dependence of their electrical resistance. At high temperature they behave as metals but as the temperature decreases a transition into a semiconducting/insulator like behaviour occurs under a critical temperature (Obradors *et al.*, 1993). A hysteretic behaviour in the temperature dependence of the electrical

resistivity is also observed in these materials. It has been reported that the hysteresis behaviour of the transport properties emanates from the coexistence of metallic and insulating regions in a certain temperature range (Granados *et al.*, 1992). The temperature at which the transition in electrical transport occurs scales with the radius of the rare earth element (Torrance *et al.*, 1992) as well, as can be seen from Figure 6-1.

An additional magnetic phase transition occurs at a Neel Temperature  $T_N$ , where the material transitions from a paramagnetic phase to an antiferromagnetic phase as the temperature decreases. Moreover, the Neel temperature has been shown to scale with the average angle of superexchange in the RNiO<sub>3</sub> series of materials (Medarde, 1997).

The investigation of nickelate thin films rather than single crystals leads to additional properties to consider. Reports of nickelate thin films grown by PLD, sputtering or molecular beam epitaxy have been published in literature. The choice of substrate, unto which the nickelate film is grown, plays an important role in the tuning of transport properties. Reports in the literature show that compressive strain can lower the MIT and Neel temperature of SmNiO<sub>3</sub> (Catalano *et al.*, 2014) for example. The electronic transition is coupled to a structural phase transition from a orthorhombic phase to a monoclinic phase (Freeland, Van Veenendaal and Chakhalian, 2016). These transitions can be tuned by changing the rare earth element or by strain (Wang *et al.*, 2015). Note that the microscopic mechanisms behind the plethora of phases previously described are still under debate.

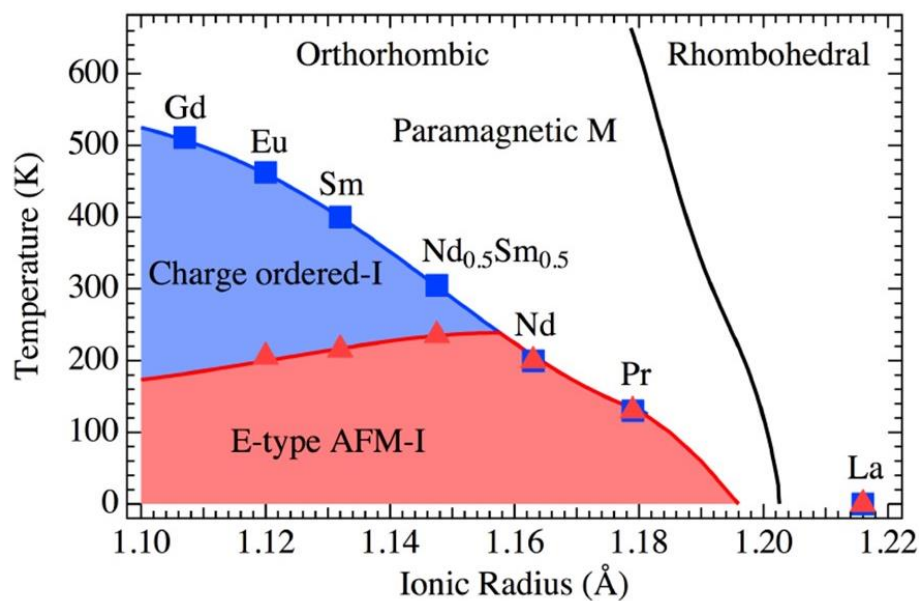


Figure 6-1: Phase diagram of nickelates showing the different electronic, magnetic and structural phases as a function of the ionic radius of the rare earth element. Adapted from (Freeland, Van Veenendaal and Chakhalian, 2016)

### 6.3) Film Growth and Device Fabrication

NdNiO<sub>3</sub>(NNO) films were grown by PLD onto LaAlO<sub>3</sub> (LAO) single crystals by Daniele Preziosi at the “Institut de Physique et de Chimie des Matériaux de Strasbourg”.

The LAO single crystals substrates were annealed in air for 10 hours at 1200°C to show single-phase surface termination. The NNO films were grown by ablating a single phase ceramic target (Toshiba Manufacturing Co.) with a KrF excimer laser at a frequency of 2 Hz and with a fluence of  $\sim 4 \text{ J/cm}^2$ . The

deposition took place in an oxygen partial pressure of 0.15 mbar of O<sub>2</sub> at a temperature of 675°C. After growth the samples were cooled down at a rate of 5°C/min in the same oxygen partial pressure.

### 6.3.1) Film Characterization

Reflection high energy electron diffraction measurements (RHEED) shown in Figure 6-2a indicate a layer by layer growth of a 10nm layer of NdNiO<sub>3</sub>. The diffraction pattern shown in the inset of the figure also indicates the growth of an epitaxial growth of the NNO layer on the LAO substrate.

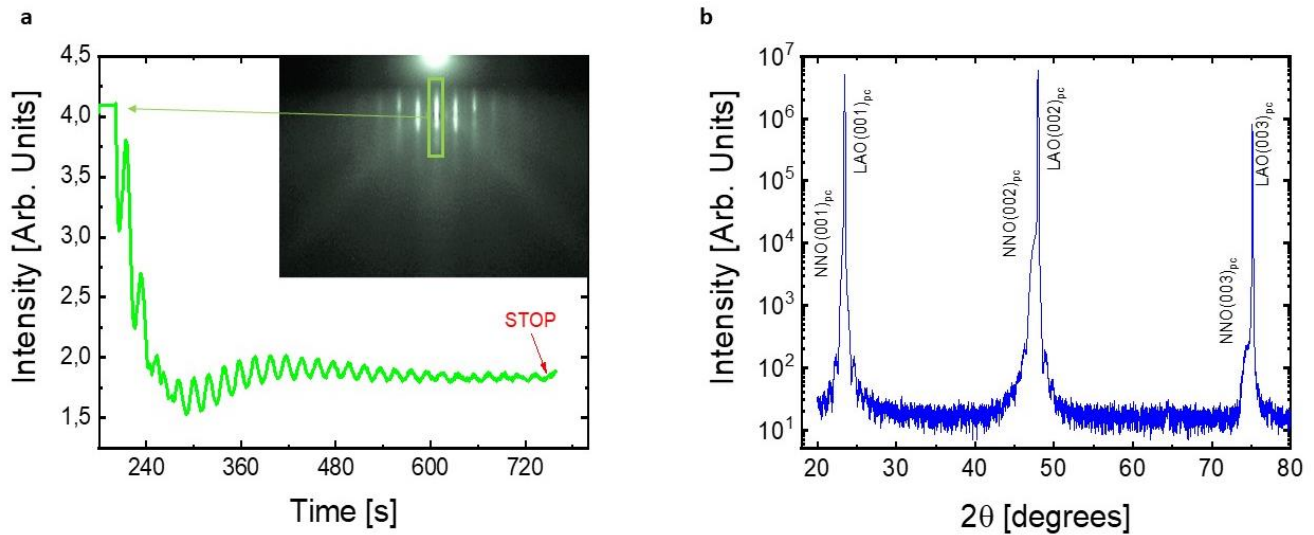


Figure 6-2: (a) RHEED oscillations obtained during the growth of NdNiO<sub>3</sub>(NNO) on an LaAlO<sub>3</sub>(LAO) substrate by PLD. The inset shows the diffraction pattern obtained during the growth. (b) XRD diffraction pattern of the NNO/LAO sample.

Figure 6-2b shows the XRD spectra obtained on the NNO/LAO film and further corroborates the single phase epitaxial growth of NNO on LAO. Furthermore, the slight difference (-0.51%) in in-plane lattice parameter (0.381nm and 0.379nm for NNO and LAO, respectively) lead to an in-plane compressive strain on the nickelate film.

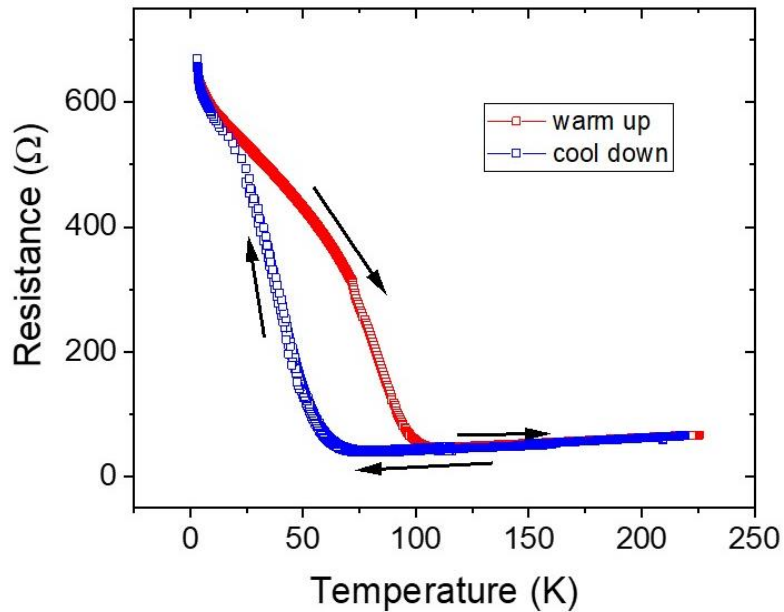


Figure 6-3: Temperature dependence of the resistance measured in a 4 point configuration across the NNO film during the cool down (blue) and the heat up (red). The measurement was performed on the chip unto which the junctions were fabricated.

Figure 6-3 shows a typical resistance vs temperature measurement of the NNO when grown on a LAO substrate. The film is metallic at high temperature (resistance decreases as a function of temperature) then undergoes a first order phase transition to an insulating phase at a temperature of approximately 50K. This can be clearly seen from the sudden increase in resistance of more than an order of magnitude close to this temperature. A hysteresis of approximately 25K is observed when comparing the resistance measurements obtained while the temperature is decreased (blue curve) to the one obtained when the temperature is increased (red curve). Note that the resistance measurement shown in Figure 6-3 was performed on the same chip where the vertical junctions were fabricated using standard 4-point probe measurement technique.

### 6.3.2) Device Fabrication

Once the films have been grown and characterized, we proceeded to fabricate the vertical junctions following the recipe described in section 2.9.1). The  $Mo_{80}Si_{20}$  top electrode was deposited by DC sputtering at room temperature. In these conditions the MoSi grows in an amorphous manner but retains its metallic and superconducting properties. In a subsequent step a lift off has been performed in order to define the design of the top electrode.

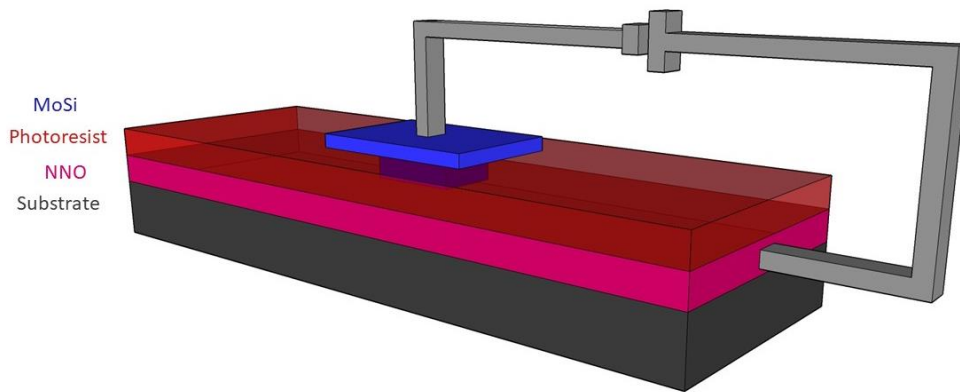


Figure 6-4: Schematic representation of the vertical junctions measured in this chapter.

Figure 6-4 shows a schematic representation of the resulting vertical junctions. To clarify, the actual junction is the interface between the nickelate and the metallic superconductor MoSi.

#### 6.4) Transport Measurement

Once the lift-off step completed the junctions were contacted using Aluminium wires and measured using a conventional Keithley 2450 Sourcemeter and Keithley 2182 Nanovoltmeter. The current voltage characteristics of the junctions were measured by biasing in voltage with a small voltage drop labelled  $V_{bias}$  and measuring the corresponding current flowing through the junction using the Keithley 2450. The bias voltage did not exceed 200mV in order to avoid resistance switching effects. The voltage drop across the junction was simultaneously measured using the Keithley 2182 to obtain a 4-point measurement. The junctions were characterized by their differential conductance calculated by performing a numerical differentiation of the current by the voltage drop.

A poling voltage labelled  $V_{pol}$ , typically a couple of volts, is applied across the junction to switch its resistive state. The voltage is gradually ramped up to the desired value before gradually decreasing back to 0 over thirty seconds approximately. The current flowing through the junction is measured with the Keithley 2450 and the voltage drop during the poling is measured using the Keithley 2182.

##### 6.4.1) Differential conductance in the ON (low resistance) and OFF (high resistance) states

By applying a positive poling voltage ( $\sim 2.2V$ ) on the junction we can decrease its resistance by more than two orders of magnitude. By reversing the polarity of the applied poling voltage ( $\sim -1.5V$ ) the junction switches to its high resistance state. Figure 6-5a displays the differential conductance  $G$  of a NNO/LAO junction at 100K as a function of the bias voltage in its as grown state (black), its ON state (low resistance) and in its OFF state (high resistance). Note that the OFF and the virgin state are almost identical and their conductance is a quadratic function of the applied bias voltage. The ON state on the other hand is characterized by a linear background at high bias voltage and an important asymmetry. These properties are reminiscent of the YBCO/MoSi junctions presented in Chapter 4).

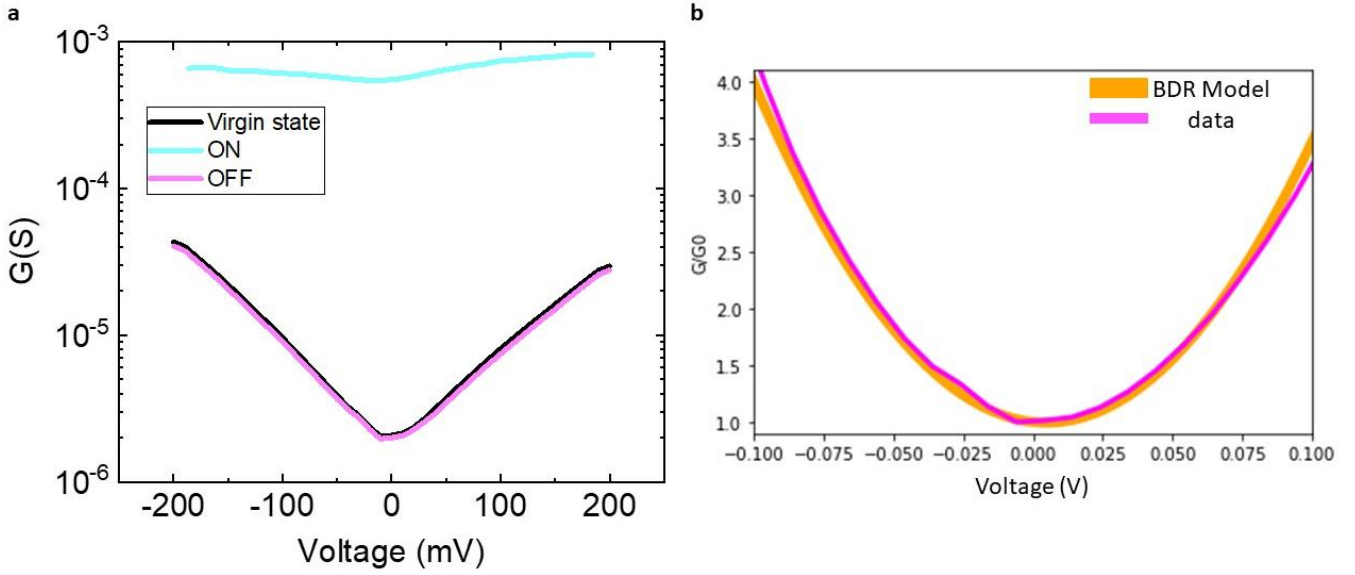


Figure 6-5: Differential conductance as a function of the bias voltage in the as grown state (black), OFF state (pink) after applying a poling voltage of  $V_{pol} = -1.5V$  and in the ON state (blue) after applying a poling voltage of  $V_{pol} = +2.2V$ . (b) BDR fit of the conductance in the OFF state at a temperature of  $T = 100K$ .

The conductance in the OFF state can be fitted to a Brinkman, Dynes and Rowell (BDR) model. This model assumes the following relationship between the conductance and the bias voltage:

$$\frac{G(V)}{G(0)} = 1 - \left( \frac{A_0 \Delta \varphi}{16 \varphi^{\frac{3}{2}}} \right) eV + \left( \frac{9 A_0^2}{128 \varphi} \right) (eV)^2$$

Where  $\Delta \varphi$  is the barrier asymmetry,  $\varphi$  is the average barrier height,  $A_0 = 4(2m)^{1/2} \frac{d}{3\hbar}$  where  $m$  is the electron rest mass and  $d$  the barrier thickness. Furthermore, we assume that the barrier has a trapezoid like shape and that the junction's band structure varies slowly compared to the electron wavelength. Figure 6-5b shows the normalized conductance in the HRS state at 100K fitted to the aforementioned model. From this fit we can find the barrier height to be  $\varphi = 0.24eV$  with an asymmetry of 62.5% and the barrier thickness  $d = 5 nm$ . Note that these values are of the same order of magnitude then those obtained on cuprate based junctions presented in Chapter 4). These parameters are also consistent with a tunnelling regime.

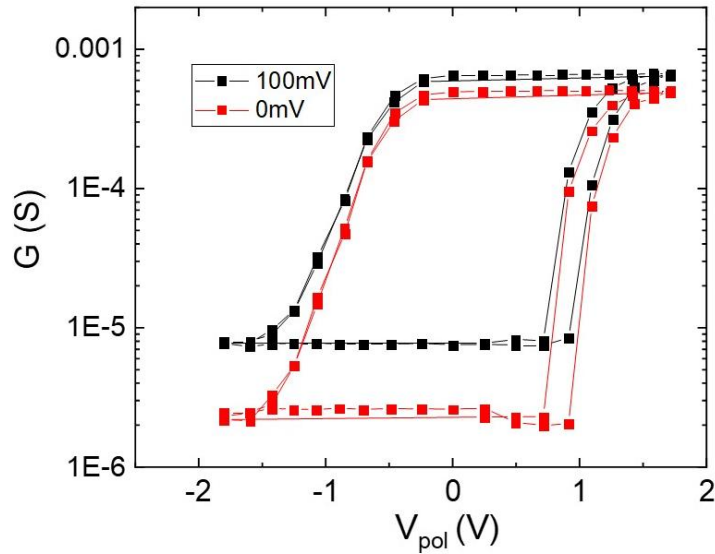


Figure 6-6: Differential conductance calculated at a bias voltage of 100mV (black) and 0 mV (red) as a function of the poling voltage  $V_{pol}$  showing the tunnel electroresistance (TER) effect observed in these junctions. Successive loops were performed to ensure reproducibility.

Figure 6-6 shows the differential conductance calculated at a bias voltage of 0mV (red) and 100mV (black) as a function of the poling voltage at 100K for a NNO/MoSi junction. We note that the resistive change at low bias is close to 3 orders of magnitude but only 2 orders of magnitude at a bias of 100mV.

On the other hand, we note a slight asymmetry in the hysteresis of the obtained loop: i.e. the voltage required to go from the OFF to the ON state is slightly bigger than the one required for the converse. This behaviour is exacerbated in YBCO/MoSi junctions (c.f. Chapter 4) that presented a clear asymmetry in the poling voltage necessary to switch the junctions from one state to the other. This might arise from the differences in reduction potential of the Ni and Cu atoms : 0.3V(Wang *et al.*, 2018) and 2.4V(Milazzo and Carioli, 1978) respectively.

#### 6.4.2) Influence of poling on MIT

We have studied the temperature dependence of the ON and OFF states described in the previous section. The poling voltage  $V_{pol}$  was applied at a temperature of  $T = 100K$  to set either the ON or the OFF state. Conductance measurements in both states were taken at different temperatures, first by decreasing down to 3K and then increasing up to 250K.

Figure 6-7a displays the differential conductance of a NNO/MoSi junction in its LRS and HRS after poling it at 100K. The arrows indicate the direction of the temperature sweep. We first note that the conductance in the ON state is almost constant between 100K and 250K. Note the slight decrease of the conductance as the temperature gets close to 200K. This behaviour is due to a thermal relaxation of the ON state and will be detailed later. We also note a clear temperature hysteresis loop of the conductance in the ON state between 25K and 100K.

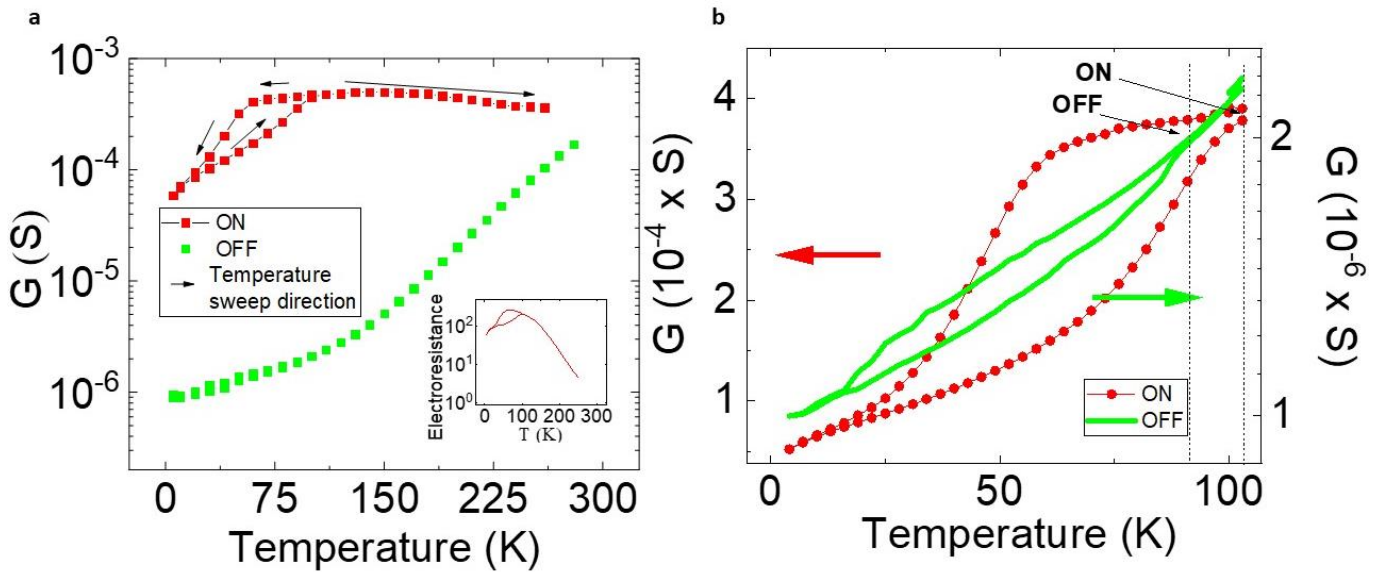


Figure 6-7: (a) Temperature behaviour of the differential conductance calculated at a bias voltage of 0mV after poling the junction at a temperature of  $T = 100\text{K}$  in the ON and OFF states. The sample is cooled down to 5K then warmed up to 250K. The inset shows the temperature dependence of the electroresistance defined as  $ER = G_{ON}/G_{OFF}$ . (b) Zoom of the temperature dependence of the differential conductance calculated at a bias voltage of 0mV in a temperature range close to the NNO MIT in the ON and OFF states.

The conductance in the OFF state however increases with increasing temperature, following a  $\sim$ exponential dependence above  $\sim 100\text{K}$ . This affects the electroresistance, defined as the ratio of the conductance in the ON and OFF states  $ER = G_{ON}/G_{OFF}$ , which as shown in the inset of Figure 6-7a exponentially drops with increase temperature above  $\sim 100\text{K}$ . The exponential behaviour as a function of temperature suggests that the transport across the junction occurs in the direct tunnelling regime. The departure from this behaviour is correlated with the transition of the nickelate into the insulating phase. This can be explained by the fact that below this temperature the charge carriers tunnel from a metal (MoSi) across an insulating barrier and into an insulator.

Upon applying an electric field on the junction, the resistive switching is accompanied by a change of the properties of the nickelate. Figure 6-7b shows a zoom of the temperature dependence of the differential conductance in the OFF and ON states between 5 and 100K. One can see that the temperature at which the hysteresis, characteristic of the metal-to-insulator transition develops, is shifted by about 20K between the OFF and ON states, being higher in the latter. This shows that applying a poling voltage on the junction affects the transition temperature of the nickelate film at the interface.

### 6.5) Poling efficiency as a function of poling temperature

The next section will be dedicated to describing a set of systematic measurements allowing us to investigate the efficiency of the poling at various temperatures. Figure 6-8a shows the differential conductance in the ON (blue) and the OFF (pink) after poling at different temperatures between 4K and 120K. The inset shows the associated ER as a function of the poling temperature. The applied voltage was fixed at +1.71V in order to switch from the OFF to the ON state and -1.8V to switch from the ON to the OFF state. We note that the efficiency of the poling is highest when the temperature is kept at 100K and is more or less constant until approximately 60K. As the temperatures decreases below 60K, the poling efficiency decreases substantially until 30K where it becomes impossible to switch. As the temperature is increased the poling efficiency starts increasing around 50K before

reaching the maximum at 100K. This effect is summarized in the inset of Figure 6-8a where one can see the temperature dependence of the ER.

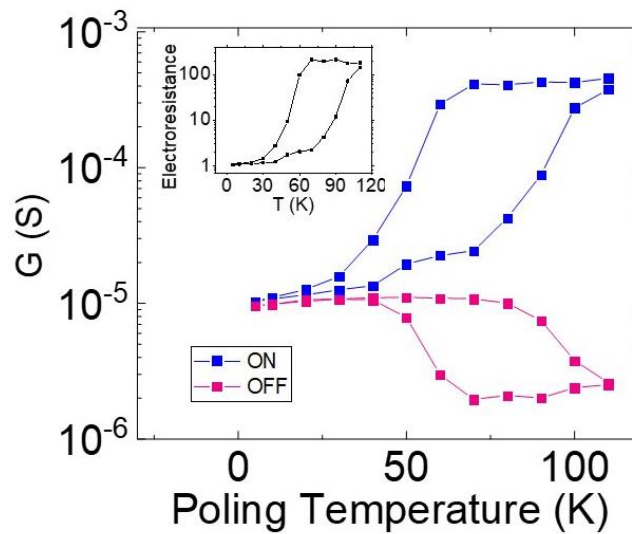


Figure 6-8: Temperature dependence of the differential conductance calculated at a bias of 0mV while poling at temperature ranging from 120K down to 4K. The inset represents the associated temperature behaviour of the electroresistance. It is maximum close to 100K and decreases below 60K when cooling down.

As the temperature decreases below the MIT, the resistivity of the nickelate film increases by order of magnitude (see Figure 6-3). Thus, a priori, a scenario to explain the temperate behaviour of the ER is that much of the applied  $V_{pol}$  drops within the NNO electrode rather than across the junction. However, we have measured the voltage drop across the junction during the poling, in a 4 point configuration, and noted that about 90% of  $V_{pol}$  drops on the junction at 40K.

We also tried performing poling experiments above 100K. However, in that temperature range the junctions degrade upon the poling –their conductance irreversibly decreases independently of the polarity of the applied voltage. Thus, we could not study the poling behaviour in that temperature range.

### 6.6) Relaxation dynamic

As previously stated, this system is stable at low temperature. Both the OFF and ON state are non-volatile as long as the sample is kept at a temperature of around 100K. However, as the temperature increases, we have noted that the conductance in the ON state starts decreasing towards an equilibrium state at a rate that increases with increasing temperature. The OFF state on the other hand is stable and does not change with respect to time at high temperature, which indicates that this is the system's ground state.

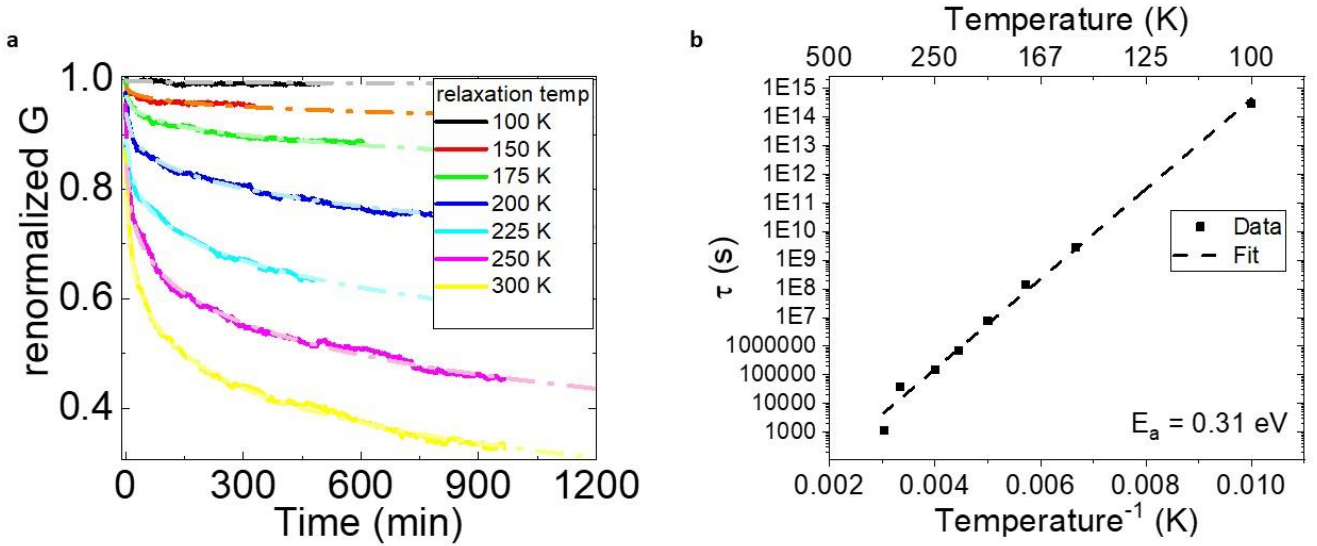


Figure 6-9: (a) Renormalized differential conductance ( $\text{renormalized } G = \frac{G_{\text{measured}} - G_{\text{OFF}}}{G_{\text{ON}}|_{t=0}}$ ) as a function of time during relaxation at different temperatures, after poling the junction in the ON state at a temperature of  $T = 100\text{K}$ . The dashed lines are the stretched exponential fits. (b) Temperature evolution of the characteristic relaxation time constant in log scale. The dotted line is a linear fit.

Figure 6-9a shows the normalized differential conductance as a function time for different temperatures between 100K and 300K for a NNO/MoSi junction. Before each measurement, the junction was first poled in the ON state at 100K for reproducibility purposes then the temperature was quickly changed to the target temperature. The differential conductance was then continuously measured as a function of time for several hours. A normalization was performed on the calculated differential conductance to set the starting point of the apparent ON state to 1 and the OFF state to 0 according to:

$$\text{renormalized } G = \frac{G_{\text{measured}} - G_{\text{OFF}}}{G_{\text{ON}}|_{t=0}}$$

We note that the rate at which the conductance drops increases as a function of increasing temperature.

Furthermore, the relaxation dynamics adopts a stretched exponential behaviour as a function of time. This mathematical function has been extensively used to model disordered and glass systems (Phillips, 1996), where the decay rate  $\kappa = 1/\tau$  decreases over time as  $t^{\beta-1}$ . We have thus fitted our normalized differential conductance to the function:

$$\text{renormalized } \sigma = Ae^{-\left(\frac{t}{\tau}\right)^\beta} + A_0$$

where  $\tau$  is the decay characteristic time,  $0 < \beta < 1$  is a dimensionless parameter that governs the degree of exponential stretch and  $A$  is the amplitude at  $t = 0$  and  $A_0$  is an offset. Due to the normalization of the differential conductance  $A \approx 1$  and  $A_0 \approx 0$ . The fitted curves shown in the figure are calculated after fixing the dimensionless parameter  $\beta = 0.25$ . This allows to vary a single parameter while fitting the various differential conductance measurements.

Figure 6-9b shows the extracted characteristic relaxation time from the previous stretched exponential fits as a function of temperature. The straight dotted line is a linear fit to the data. We can thus model the temperature evolution of  $\tau$  as

$$\tau \propto e^{-E_a/k_B T}$$

Where  $E_a$  is the associated energy barrier and  $k_B T$  is a thermal energy. From this linear fit we can extract the energy barrier that governs the relaxation process  $E_a = 0.31 eV$ .

## 6.7) Model

We propose that the results described in the previous sections are caused by an electrically induced redox reaction at the interface between the nickelate and the metal top electrode. Such a scenario is the same that allows for an understanding of the YBCO/MoSi (Rouco *et al.*, 2020)(Chapter 4) and YBCO/ITO (Chapter 5) junctions.

Once the top electrode is deposited on the nickelate film, an oxidized metallic layer is formed at the interface which depletes the nickelate of its oxygen at the expense of the MoSi. An insulating barrier forms at the interface between the two electrodes which leads to a tunnelling transport behaviour and low conductance. This is the ground state of the system which coincides with the OFF state. The positive reduction potential of nickel ions (Wang *et al.*, 2018) leads to a spontaneous electrochemical reaction at the interface. In this configuration the nickelate layer would be depleted in oxygen (at the expense of the MoSi layer) and as such would present a lower MIT and a higher resistance as is expected from literature (Nikulin *et al.*, 2004). This agrees with the observation of Figure 6-7b.

Once a positive voltage is applied across the junction (the electric field is directed from the nickelate towards the metal electrode) the oxygen ions at the interface between the two layers migrate towards the nickelate restoring its electrical properties and creating a more conductive layer at the interface. This leads to an increase of the conductance across the junction which is labelled ON state. In this state, thermal energy leads to relaxation into the ground (OFF) state, at a rate that depends on the temperature and the number of oxygen vacancies that have already migrated. This allows to understand the relaxation dynamic which shows that the relaxation rate increases as a function of temperature (refer to section 6.6). The observation that the poling efficiency dramatically decreases at low temperature is difficult to explain, but the electrochemical reaction occurring at the interface might be affected by a structural deformation of the NNO layer below the MIT (Freeland, Van Veenendaal and Chakhalian, 2016).

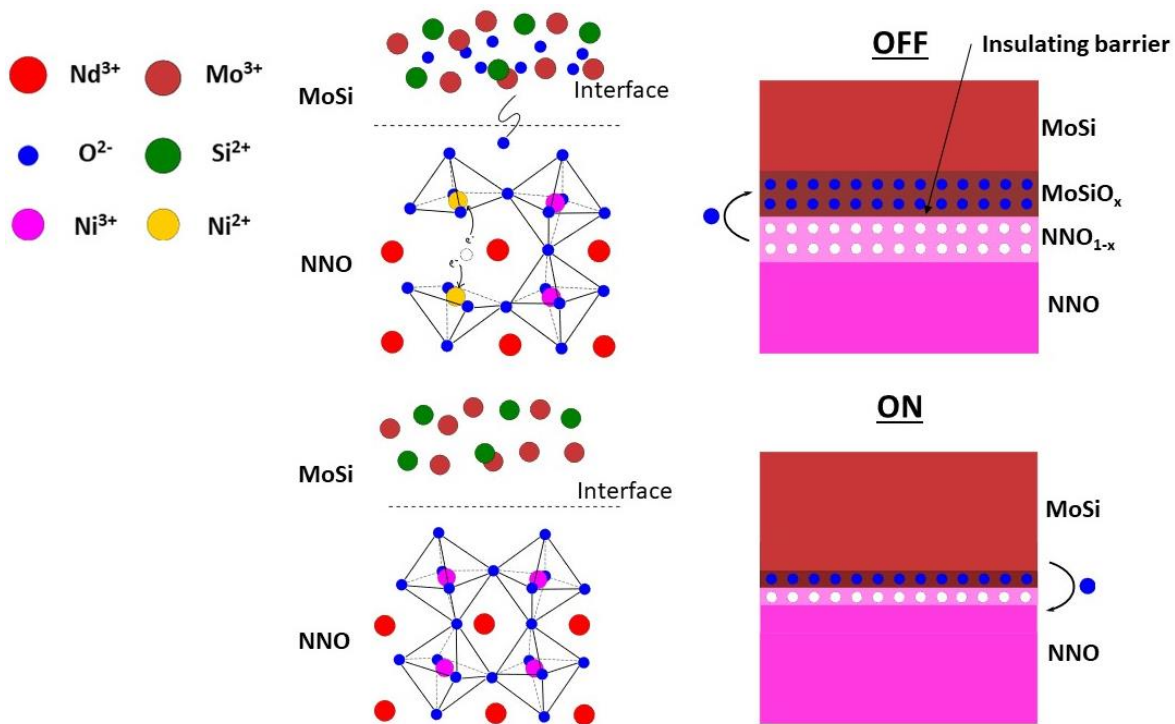


Figure 6-10: Schematic representation of the model proposed to explain the TER effect measured in our junctions in the case of a positive poling voltage (up) and a negative poling voltage (down).

By applying a negative voltage across the junction one can recover the ground state characterized by an oxygen depleted NNO layer and an insulating oxidized barrier at the interface between the two electrodes. A schematic representation of the model is shown in Figure 6-10.

Note that the energy barrier of  $E_a = 0.31\text{eV}$  extracted from 6.6) is remarkably close to the potential required to drive the redox reaction in NdNiO<sub>3</sub> which leads to a  $Ni^{3+}$  to  $Ni^{2+}$  valence change in the nickel atom (Wang *et al.*, 2018).

There are several differences noted between the TER effects observed in cuprate junctions (described in Chapter 4) and Chapter 5), and those observed in nickelates junctions. The TER in nickelate junctions is characterized by a smaller asymmetry in the hysteresis loop. This might be caused by the difference in reduction potential of the Ni and Cu atoms i.e. 0.3V(Wang *et al.*, 2018) vs 2.4V(Milazzo and Carioli, 1978) respectively. A second difference can be noted in the fact that the efficiency of poling drops significantly drops once the temperature decreases below the nickelate MIT solely in nickelate junctions. This might be due to the structural deformation occurring at this temperature as reported by Freeland *et al.* (Freeland, Van Veenendaal and Chakhalian, 2016). This behaviour has not been observed in cuprate based junctions. Finally, differences in the associated barrier for the thermally activated relaxation were noted in nickelate and cuprate based junctions:  $E_a \sim 0.3\text{ eV}$  and  $E_a \sim 0.1\text{ eV}$  section (5.6) respectively. This difference might arise from the differences in the energy associated with oxygen diffusion in these materials.

## 6.8) Conclusion

We have fabricated and investigated the transport properties of tunnel junctions composed of a nickelate thin film NdNiO<sub>3</sub> unto which was deposited the amorphous metallic superconductor MoSi. By applying a voltage ( $\sim\text{V}$ ) across the junction we have observed a fast, non-volatile and reversible change in its differential conductance. This effect, while analogous to what is observed in ferroelectric tunnel junctions, has also been observed in heterostructures lacking a ferroelectric barrier (Rouco *et*

*al.*, 2020) in cuprate based junctions. We have shown that a drastic change in the efficiency of this effect occurs at the nickelate metal-to-insulator transition temperature (MIT). Moreover, we have observed a change in the MIT at the interface between the nickelate and the MoSi when the junction is switched from one state to the other. Finally, while stable in the HRS at all temperatures, the conductance in the ON state relaxes towards the OFF state at a rate that increases with temperature. The energy barrier associated to this relaxation is close to the potential required to drive a redox reaction in NdNiO<sub>3</sub>.

Further measurements are planned in order to deepen our understanding of the TER effect in nickelate heterostructures. As photo-induced resistive switching has been observed in cuprate heterostructures (described in Chapter 4) and Chapter 5), we plan to investigate these effects on nickelate junctions. The interplay between field effect and photo-induced effects on these junctions might lead to novel and exciting phenomena.

## 7) Conclusions and perspectives

The main objective of this thesis has been the investigation of the interplay between field effect and photo-induced effects on oxide thin films and heterostructures based on the high- $T_c$  superconductor  $YBa_2Cu_3O_{7-\delta}$ .

On the one hand, YBCO thin films with different oxygen content and with controlled disorder introduced by ion irradiation have been investigated. In oxygen deficient samples, illumination with UV or visible light one produces persistent photoconductivity (PPC) and persistent photosuperconductivity (PPS), which are accompanied by an increase of the charge carrier density and mobility. Strikingly, and contrary with what has been reported in the literature, the photo-induced increase in  $T_c$  correlates with photo-induced increase the carrier mobility and *not* with the increase of the carrier concentration. This observation is consistent with the behaviour of the samples having induced disorder, for which illumination produces persistent photoconductivity but *not* photosuperconductivity, as well as an increase of the carrier concentration but *not* of the carrier mobility. Furthermore, we show evidence that the illumination-induced enhancement of the carrier mobility and concentration are connected to independent microscopic mechanism, as the mobility/concentration enhancements relax with very different dynamics. Finally, we have performed preliminary Resonant Inelastic X-ray Scattering (RIXS) measurements on oxygen deficient YBCO films which suggest a change in the chemical environment of copper atoms after illumination. All the results strongly supports that changes caused by illumination and leading to a  $T_c$  increase emanate from structural changes. Additional RIXS measurements of the relaxation at high temperature as well as on an ion irradiated film are ongoing to gain additional insight into the nature of the observed phenomena.

On the other hand, we have studied tunnel junctions made of the YBCO(001) and the metallic superconductor MoSi. We have demonstrated a persistent switching in the tunnelling resistance upon application of voltage pulses, with changes of up to four orders of magnitude between a high conductance state (ON state) and a low conductance state (OFF state). This effect is analogous to the Tunnel ElectroResistance (TER) observed in ferroelectric junctions, but here is realized without the need of a ferroelectric barrier. Furthermore, the electroresistance, or ratio between resistance in the ON/OFF states, increases below the superconducting critical temperature, which is due to the opening of the YBCO superconductor gap which reduces density of states at the Fermi level. These switching effects are explained by an electrochemical reaction occurring at the interface between the YBCO and MoSi, by which oxygen is exchanged between YBCO and MoSi. The conductance in the virgin state has been fitted to Blonder-Tinkham-Klapwijk (BTK) model and the tunnelling junction parameters extracted are consistent with this interpretation. Josephson coupling between the two superconductors has not been observed. One way to remedy it is by increasing the YBCO coherence length across the interface. One can do this by changing the c-axis YBCO(001) to a YBCO(103) layer grown on STO(110). The use of a-axis YBCO(100) might further enhance the coupling between the two superconductors.

The interplay between field effect and light induced effects has been studied in tunnel junctions composed of YBCO and the transparent semiconductor ITO. These junctions show the electroresistance effects described above. We have found that, in addition, strong illumination effects can be observed. When the junction is in the ON state, a persistent decrease in the conductance of the junction is produced upon illumination. Contrarily, if the junction is set in the OFF state, illumination leads to a persistent increase in the conductance. In addition to these persistent effects, during illumination a photovoltage appears which scales with the junction

conductance. A standard photovoltaic effect (PVE) is responsible for the appearance of this photovoltage: photons are absorbed in the YBCO layer and a p-n junction at the interface between the YBCO and the ITO provides the necessary electric field to separate the photo-charges. The persistent effects on the other hand are interpreted through the lens of a light-induced electrochemical reaction occurring at the interface. The investigation of these effects is particularly interesting in the field of neuromorphic computing as photo-memristors whose behaviour can be controlled by both electric fields and light. We can pursue the investigation of these effects by changing the top electrode – to Zinc oxide ZnO or Zirconium oxide ZrO – in the junctions thus changing its reduction potential as well as the device band alignment. This would probably affect both the persistent and instantaneous photo-induced effects.

Furthermore, a TER effect can also be observed in vertical junctions composed of a nickelate thin film  $\text{NdNiO}_3$  and a metallic superconductor MoSi. We have found that the efficiency of this effect is correlated to the metal-to-insulator transition of the nickelate film. We also present evidence of a thermal relaxation occurring in the high conductance state at high temperature. The TER effect is qualitatively similar to the one observed in cuprate based tunnel junctions. These effects are thus interpreted through the lens of an electrochemical reaction occurring at the interface between the two materials.

## Bibliography

- Ahn, C. H., Triscone, J. M. and Mannhart, J. (2003) 'Electric field effect in correlated oxide systems', *Nature*, 424(6952), pp. 1015–1018.
- Ament, L. J. P. *et al.* (2011) 'Resonant Inelastic X-ray Scattering Studies of Elementary Excitations', *Reviews of Modern Physics*, 83(2).
- Anderson, P. W. (1959) 'New Approach to the Theory of Superexchange', *Physical Review Journal Archive*, 115(1).
- Anderson, P. W. (1991) 'Hall effect in the two-dimensional Luttinger liquid', *Physical Review Letters*, 67(15), pp. 2092–2094.
- Ando, Y., Komiya, S., *et al.* (2004) 'Electronic phase diagram of high-T<sub>c</sub> cuprate superconductors from a mapping of the In-plane resistivity curvature', *Physical Review Letters*, 93(26 1), pp. 10–13.
- Ando, Y., Kurita, Y., *et al.* (2004) 'Evolution of the hall coefficient and the peculiar electronic structure of the cuprate superconductors', *Physical Review Letters*, 92(19), pp. 13–16.
- Ando, Y. and Murayama, T. (1999) 'Non-Universal Power Law of the "Hall Scattering Rate" in a Single-Layer Cuprate BSLCO', *Phys. Rev. B*, 60(10).
- Arias, D. (2001) *Efectos de la irradiacion con iones de He sobre las propiedades superconductoras de peliculas delgadas de YBCO*.
- Arias, D. *et al.* (2003) 'Pair breaking by chain oxygen disorder in light-ion irradiated YBa<sub>2</sub>Cu<sub>3</sub>O<sub>x</sub> thin films', *Physical Review B - Condensed Matter and Materials Physics*, 68(9), pp. 1–5.
- Armitage, N. P. *et al.* (2002) 'Doping Dependence of an n-Type Cuprate Superconductor Investigated by Angle-Resolved Photoemission Spectroscopy', *Physical Review Letters*, 88(25), p. 4.
- Armitage, N. P., Fournier, P. and Greene, R. L. (2010) 'Progress and perspectives on electron-doped cuprates', *Reviews of Modern Physics*, 82(3), pp. 2421–2487.
- Arnold, D. *et al.* (2019) 'Tuning the superconducting transition of SrTiO<sub>3</sub>-based 2DEGs with light', *Applied Physics Letters*, 115(12).
- Balasubramanian, K. *et al.* (2019) 'Thin-Film-Based Integrated High-Transition-Temperature Superconductor Devices', *Advanced Functional Materials*, 1807379, pp. 1–24.
- Band, T. *et al.* (2020) 'Nanoscale Resistive Switching in Ultrathin PbZr<sub>0.2</sub>Ti<sub>0.8</sub>O<sub>3</sub>-La<sub>0.7</sub>Sr<sub>0.3</sub>MnO<sub>3</sub> Bilayer', *Physica Status Solidi (B) Basic Research*, 257(7), pp. 1–7.
- Bardeen, J., Cooper, L. N. and Schrieffer, J. R. (1957) 'Theory of Superconductivity', *Physical Review*, 108(1175), pp. 1–332.
- Barisic, N. *et al.* (2013) 'Universal sheet resistance and revised phase diagram of the cuprate high-temperature superconductors', *Proceedings of the National Academy of Sciences*, 110(30), pp. 12235–12240.
- Bednorz, J. G. and Müller, K. A. (1986) 'Possible High T<sub>c</sub> superconductivity in the Ba-La-Cu-O system', *Zeitschrift für Physik B Condensed Matter*, 64, pp. 189–193.
- Bégon-Lours, L. (2017) *Ferroelectric Field-Effects in High-T<sub>c</sub> Superconducting Devices*.
- Bégon-Lours, L. *et al.* (2018) 'Factors limiting ferroelectric field-effect doping in complex oxide heterostructures', *Physical Review Materials*, 2(8), pp. 1–9.

- Benzi, P., Bottizzo, E. and Rizzi, N. (2004) 'Oxygen determination from cell dimensions in YBCO superconductors', *Journal of Crystal Growth*, 269(2–4), pp. 625–629.
- Bergeal, N. (2006) *Effet Josephson pour l'étude des supraconducteurs à haute température critique*.
- Bergeal, N. *et al.* (2008) 'Pairing fluctuations in the pseudogap state of copper-oxide superconductors probed by the Josephson effect', *Nature Physics*, 4(8), pp. 608–611.
- Beyreuther, E. *et al.* (2009) 'Large photoconductivity and light-induced recovery of the insulator-metal transition in ultrathin La<sub>0.7</sub> Ce<sub>0.3</sub> MnO<sub>3-δ</sub> films', *Physical Review B - Condensed Matter and Materials Physics*, 80(7), pp. 1–6.
- Beyreuther, E. *et al.* (2010) 'Large photoconductivity of oxygen-deficient La<sub>0.7</sub>Ca<sub>0.3</sub>MnO<sub>3</sub>/SrTiO<sub>3</sub> heterostructures', *Journal of Physics Condensed Matter*, 22(17), pp. 0–7.
- Bibes, M., Villegas, J. E. and Barthélémy, A. (2011) 'Ultrathin oxide films and interfaces for electronics and spintronics', *Advances in Physics*, 60(1), pp. 5–84.
- Blanco-Canosa, S. *et al.* (2014) 'Resonant x-ray scattering study of charge-density wave correlations in YBa<sub>2</sub> Cu<sub>3</sub> O<sub>6+x</sub>', *Physical Review B - Condensed Matter and Materials Physics*, 90(5), pp. 43–45.
- Blonder, G. E., Tinkham, M. and Klapwijk, T. M. (1982) 'Transition from metallic to tunneling regimes in superconducting microconstrictions: Excess current, charge imbalance, and supercurrent conversion', *Physical Review B*, 25(7).
- De Boer, J. H. and Verwey, E. J. W. (1937) 'Semi-conductors with partially and with completely filled 3d-lattice bands', *Proceedings of the Physical Society*, 49(4S), pp. 59–71.
- Bora, L. V. and Mewada, R. K. (2017) 'Visible/solar light active photocatalysts for organic effluent treatment: Fundamentals, mechanisms and parametric review', *Renewable and Sustainable Energy Reviews*, 76(December 2016), pp. 1393–1421.
- Boyn, S. *et al.* (2016) 'Tunnel electroresistance in BiFeO<sub>3</sub> junctions: Size does matter', *Applied Physics Letters*, 109(23), pp. 1–6.
- Brinkman, W. F., Dynes, R. C. and Rowell, J. M. (1970) 'Tunneling conductance of asymmetrical barrier', *Journal of Applied Physics*, 41(5), pp. 1915–1921.
- Bruker.com (no date) *Atomic Force Microscopes*. Available at: <https://www.bruker.com/products/surface-and-dimensional-analysis/atomic-force-microscopes/campaigns/afm-microscopes.html>.
- Bruno, F. Y. *et al.* (2016) 'Millionfold Resistance Change in Ferroelectric Tunnel Junctions Based on Nickelate Electrodes', *Advanced Electronic Materials*, 2(3), p. 1500245.
- Bud'ko, S. L. *et al.* (1993) 'Persistent photoconductivity in insulating and superconducting YBa<sub>2</sub>Cu<sub>3</sub>O<sub>7-x</sub> thin films: Temperature and spectral dependence', *Physical Review B*, 48(22).
- Carrington, A. *et al.* (1992) 'Temperature Dependence of the Hall Angle in Single-Crystal YBa<sub>2</sub>(Cu<sub>1-x</sub>Co<sub>x</sub>)O<sub>7</sub>', *Physical Review Letters*, 69(19), pp. 2855–2858.
- Castellani, C., Di Castro, C. and Grilli, M. (1995) 'Singular quasiparticle scattering in the proximity of charge instabilities', *Physical Review Letters*, 75(25), pp. 4650–4653.
- Catalano, S. *et al.* (2014) 'Electronic transitions in strained SmNiO<sub>3</sub> thin films', *APL Materials*, 2(11).
- Cauro, R. *et al.* (2001) 'Persistent and transient photoconductivity in oxygen-deficient La<sub>2/3</sub>Sr<sub>1/3</sub>MnO<sub>3-δ</sub>', *Physical Review B - Condensed Matter and Materials Physics*, 63(17), pp. 1–6.

- Cava, R. J. *et al.* (1990) 'Structural anomalies, oxygen ordering and superconductivity in oxygen deficient Ba<sub>2</sub>YCu<sub>3</sub>O<sub>x</sub>', *Physica C: Superconductivity and its applications*, 165(5–6), pp. 419–433.
- Ceder, G. *et al.* (1990) 'Phase diagram and low temperature behavior of oxygen ordering in YBCO using ab initio interactions', *Physical Review B*, 41(13).
- Chang, J. *et al.* (2016) 'Magnetic field controlled charge density wave coupling in underdoped YBa<sub>2</sub>Cu<sub>3</sub>O<sub>6+x</sub>', *Nature Communications*, 7(May), pp. 1–7.
- Chen, H. *et al.* (2018) 'Rare-earth nickelates R NiO<sub>3</sub> : thin films and heterostructures'.
- Chew, D. C. *et al.* (1996) 'Infrared quenching of photoinduced persistent conductivity in YBa<sub>2</sub>Cu<sub>3</sub>O<sub>6+x</sub>', *Applied Physics Letters*, 69, p. 3260.
- Chiang, Y., Farrey, G. W. and Soukhovjak, A. N. (1998) 'Lead-free high-strain single-crystal piezoelectrics in the alkaline–bismuth–titanate perovskite family', *Applied Physics Letters*, 73(25), pp. 3683–3685.
- Chien, T. R., Wang, Z. Z. and Ong, N. P. (1991) 'Effect of Zn Impurities on the Normal-State Hall angle in single crystal YBCO', *Physical Review Letters*, 67(15), pp. 2088–2091.
- Chu, Z. *et al.* (2017) 'Origin of photovoltaic effect in (Bi, Pb)<sub>2</sub>Sr<sub>2</sub>Ca<sub>2</sub>Cu<sub>3</sub>O<sub>10+δ</sub> /Ag heterostructure', *Journal of Alloys and Compounds*, 724, pp. 413–420.
- Crassous, A. *et al.* (2010) 'Giant tunnel electroresistance with PbTiO<sub>3</sub> ferroelectric tunnel barriers', *Applied Physics Letters*, 96(4), pp. 10–13.
- Crassous, A. *et al.* (2011) 'Nanoscale electrostatic manipulation of magnetic flux quanta in ferroelectric/superconductor BiFeO<sub>3</sub>/YBa<sub>2</sub>Cu<sub>3</sub>O<sub>7-δ</sub> heterostructures', *Physical Review Letters*, 107(24), pp. 1–5.
- Dadras, S. and Ghavamipour, M. (2016) 'Investigation of the properties of carbon-base nanostructures doped YBa<sub>2</sub>Cu<sub>3</sub>O<sub>7-δ</sub> high temperature superconductor', *Physica B: Condensed Matter*, 484, pp. 13–17.
- Dedyk, A. I., Plotkina, N. W. and Ter-Martirosyan, L. T. (1993) 'The dielectric hysteresis of YBCO-SrTiO<sub>3</sub>-YBCO structures at 4.2 K', *Ferroelectrics*, 144.
- Dynes, R. C., Narayanamurti, V. and Garno, J. P. (1978) 'Direct measurement of quasiparticle-lifetime broadening in a strong-coupled superconductor', *Physical Review Letters*, 41(21), pp. 1509–1512.
- Eason, R. (2007) *Pulsed Laser Deposition of thin films*.
- Endo, T. *et al.* (1996) 'Enhancement of persistent photoconductivity by uv excitation', *Physical Review B - Condensed Matter and Materials Physics*, 54(6), pp. R3750–R3752.
- Esaki, L., Laibowitz, R. and Stiles, P. (1971) 'Polar switch'.
- Feigel'Man, M. V. and Skvortsov, M. A. (2012) 'Universal broadening of the Bardeen-cooper-schrieffer coherence peak of disordered superconducting films', *Physical Review Letters*, 109(14).
- Freeland, J. W., Van Veenendaal, M. and Chakhalian, J. (2016) 'Evolution of electronic structure across the rare-earth RNiO<sub>3</sub> series', *Journal of Electron Spectroscopy and Related Phenomena*, 208, pp. 56–62.
- Fujii, T. *et al.* (2005) 'Hysteretic current-voltage characteristics and resistance switching at an epitaxial oxide Schottky junction SrRuO<sub>3</sub>/SrTi<sub>0.99</sub>Nb<sub>0.01</sub>O<sub>3</sub>', *Applied Physics Letters*, 86(1).
- Garcia, V. *et al.* (2009) 'Giant tunnel electroresistance for non-destructive readout of ferroelectric

states', *Nature*, 460(7251), pp. 81–84.

Garcia, V. and Bibes, M. (2014) 'Ferroelectric tunnel junctions for information storage and processing', *Nature Communications*, 5, pp. 1–12.

Gauquelin, N. *et al.* (2014) 'Atomic scale real-space mapping of holes in YBa<sub>2</sub>Cu<sub>3</sub>O<sub>6+δ</sub>', *Nature Communications*, 5, pp. 1–7.

Di Gennaro, E. *et al.* (2013) 'Persistent photoconductivity in 2D electron gases at different oxide interfaces', *Advanced Optical Materials*, 1(11), pp. 834–843.

Di Gennaro, E. *et al.* (2015) 'Photoresponse dynamics in amorphous-LaAlO<sub>3</sub>/SrTiO<sub>3</sub> interfaces', *Scientific Reports*, 5, pp. 1–6.

Gilabert, A. *et al.* (2000) 'Photodoping effects in high critical temperature superconducting films and josephson junctions', *Journal of Superconductivity and Novel Magnetism*, 13(1), pp. 1–20.

Gonzalez-Rosillo, J. C. *et al.* (2019) 'Engineering Oxygen Migration for Homogeneous Volume Resistive Switching in 3-Terminal Devices', *Advanced Electronic Materials*, 5(9), pp. 1–8.

Goodenough, J. B. (1955) 'Theory of the role of covalence in the perovskite-type manganites [La,M(II)]MnO<sub>3</sub>', *Physical Review*, 100(2), pp. 564–573.

Gor'kov, L. P. (1959) 'Microscopic derivation of the Ginzburg-Landau equations in the theory of superconductivity', *Soviet Physics JTEP-USSR*, 36(6), pp. 1364–1367.

Gough, C. E. *et al.* (1987) 'Flux quantization in a high-T<sub>c</sub> superconductor', *Nature*, p. 855.

Granados, X. *et al.* (1992) 'Metastable metallic state and hysteresis below the metal-insulator transition in PrNiO<sub>3</sub>', *Physical Review B*, 46(24), pp. 15683–15688.

Gruverman, A. *et al.* (2009) 'Tunneling electroresistance effect in ferroelectric tunnel junctions at the nanoscale', *Nano Letters*, 9(10), pp. 3539–3543.

Gull, E. *et al.* (2010) 'Momentum-space anisotropy and pseudogaps: A comparative cluster dynamical mean-field analysis of the doping-driven metal-insulator transition in the two-dimensional Hubbard model', *Physical Review B - Condensed Matter and Materials Physics*, 82(15), pp. 1–14.

Guo, Q. *et al.* (2020) 'Tunable resistivity exponents in the metallic phase of epitaxial nickelates', *Nature Communications*, 11(1), pp. 1–13.

Gurvitch, M. *et al.* (1989) 'Reproducible tunneling data on chemically etched single crystals of YBa<sub>2</sub>Cu<sub>3</sub>O<sub>7</sub>', *Physical Review Letters*, 63(9), pp. 1008–1011.

Hao, F. X. *et al.* (2016) 'Photovoltaic effect in YBa<sub>2</sub>Cu<sub>3</sub>O<sub>7-δ</sub>/Nb-doped SrTiO<sub>3</sub> heterojunctions', *Applied Physics Letters*, 109(13), pp. 0–4.

Hardy, W. N. *et al.* (1993) 'Precision Measurements of the Temperature Dependence of A in YBa<sub>2</sub>Cu<sub>3</sub>O<sub>7-δ</sub>. Strong Evidence for Nodes in the Gap Function', *Physical Review Letters*, 70(25).

Van Harlingen, D. J. (1995) 'Phase-sensitive tests of the symmetry of the pairing state in the high-temperature superconductors-Evidence for dx<sub>2</sub>-y<sub>2</sub> symmetry', *Reviews of Modern Physics*, 67(2), pp. 515–535.

Harris, J. M. *et al.* (1995) 'Violation of Kohler's rule in the normal-state magnetoresistance of YBa<sub>2</sub>Cu<sub>3</sub>O<sub>7-δ</sub> and La<sub>2</sub>Sr<sub>x</sub>CuO<sub>4</sub>', *Physical Review Letters*, 75(7), pp. 1391–1394.

Hasen, J. *et al.* (1995) 'Enhancement of persistent photoconductivity in insulating high- T<sub>c</sub> thin films', *Physical Review B*, 51(2), pp. 1342–1345.

- Hashimoto, M. *et al.* (2014) 'Energy gaps in high-temperature cuprate superconductors', *Nature Physics*, 10(7), pp. 483–495.
- Helm, T. *et al.* (2009) 'Evolution of the Fermi Surface of the Electron-Doped High-Temperature Superconductor  $\text{Nd}_{2-x}\text{Ce}_x\text{CuO}_4$  Revealed by Shubnikov-de Haas Oscillations', *Physical Review Letters*, 103(15), pp. 1–4.
- Heo, S. *et al.* (2017) 'Influence of tensile-strain-induced oxygen deficiency on metal-insulator transitions in  $\text{NdNiO}_3$ - $\delta$  epitaxial thin films', *Scientific Reports*, 7(1), pp. 1–9.
- Hoffman, J. E. *et al.* (2002) 'A Four Unit Cell Periodic Pattern of Quasi-Particle States Surrounding Vortex Cores in  $\text{Bi}_2\text{Sr}_2\text{CaCu}_2\text{O}_{8+\delta}$ ', *Science*, 295(5554), pp. 466–469.
- Hoffmann, A. *et al.* (1997) 'Persistent photoconductivity in high  $T_c$  grain boundary Josephson junctions', *Applied Physics Letters*, 70(18), pp. 2461–2463.
- Homes, C. C. *et al.* (1993) 'Optical conductivity of c axis oriented  $\text{YBa}_2\text{Cu}_3\text{O}_{6.70}$ : Evidence for a pseudogap', *Physical Review Letters*, 71(10), pp. 1645–1648.
- Hussey, N. B. (2003) 'The normal state scattering rate in high- $T_c$  cuprates', *European Physical Journal B*, 31(4), pp. 495–507.
- Hussey, N. E. (2007) 'Normal State Transport Properties', in *Handbook of High-Temperature Superconductivity*, pp. 399–425.
- Hussey, N. E. (2008) 'Phenomenology of the normal state in-plane transport properties of high- $T_c$  cuprates', *Journal of Physics Condensed Matter*, 20(12).
- Imada, M., Fujimori, A. and Tokura, Y. (1990) 'Metal-Insulator Transitions', *Review of Modern Physics*, 70(4).
- Iqbal, Z. *et al.* (1994) 'Superconductivity above 130K in the Hg-Pb-Ba-Ca-Cu-O system', *Physical Review B*, 49(17).
- Ito, T., Takenaka, K. and Uchida, S. (1993) 'Systematic deviation from T-linear behavior in the in-plane resistivity of  $\text{YBa}_2\text{Cu}_3\text{O}_{7-y}$ : Evidence for dominant spin scattering', *Physical Review Letters*, 70(25), pp. 3995–3998.
- Jagtap, V. S., Dégardin, A. F. and Kreisler, A. J. (2012) 'Low temperature amorphous growth of semiconducting Y-Ba-Cu-O oxide thin films in view of infrared bolometric detection', *Thin Solid Films*, 520(14), pp. 4754–4757.
- Jahn, H. and Teller, E. (1936) 'Stability of degenerate electronic states in polyatomic molecules', *physical Review A*, 49(874).
- Jones, E. C., Christen, D. K., Thompson, J. R., Feenstra, R., Zu, S., *et al.* (1993) 'Correlations between the Hall coefficient and the superconducting transport properties of oxygen-deficient  $\text{YBa}_2\text{Cu}_3\text{O}_{7-\delta}$  epitaxial thin films', *Physical Review B*, 47(14), p. 8986.
- Jones, E. C., Christen, D. K., Thompson, J. R., Feenstra, R., Zhu, S., *et al.* (1993) 'Correlations between the Hall coefficient and the superconducting transport properties of oxygen-deficient  $\text{YBaCu}_3\text{O}_7$  epitaxial thin films', *Physical Review B*, 47(14).
- Jorgensen, J. D. *et al.* (1990) 'Structural properties of oxygen-deficient YBCO', *Physical Review B*, 41(4).
- Josephson, B. (1962) 'Possible new effects in superconductive tunnelling', *Physics Letters*, 1(7).
- Kashiwaya, S. *et al.* (1995) 'Origin of zero-bias conductance peaks in high- $T_c$  superconductors',

*Physical Review B*, 51(2), pp. 1350–1353.

Kawae, T. *et al.* (2009) 'Improved leakage and ferroelectric properties of Mn and Ti codoped BiFeO<sub>3</sub> thin films', *Applied Physics Letters*, 94(11), pp. 2007–2010.

Keimer, B. *et al.* (2015) 'From quantum matter to high-temperature superconductivity in copper oxides', *Nature*, 518(7538), pp. 179–186.

Kelly, M. K. *et al.* (1988) 'Oxygen deficiency induced localized optical excitations in YBCO', *Physical Review B*, 38(1).

Kim, H. *et al.* (1999) 'Electrical, optical, and structural properties of indium-tin-oxide thin films for organic light-emitting devices', *Journal of Applied Physics*, 86(11), pp. 6451–6461.

Kinoshita, K. *et al.* (2006) 'Bias polarity dependent data retention of resistive random access memory consisting of binary transition metal oxide', *Applied Physics Letters*, 89(10), pp. 1–4.

Kirilyuk, A. I., Kreines, N. M. and Kudinov, V. I. (1990) 'Frozen photoconductivity in YBCO films Kirilyuk', *JETP Letters*, 52(696–700).

Kittorov, S. A. *et al.* (1994) 'Josephson effect in a junction with a ferroelectric', *Ferroelectrics*, 157, p. 387.

Kleiner, R. and Muller, P. (1994) 'Intrinsic Josephson Effects in high T<sub>c</sub> superconductors', *Physical Review B*, 49(2).

Kohlstedt, H. *et al.* (2008) 'Method to distinguish ferroelectric from nonferroelectric origin in case of resistive switching in ferroelectric capacitors', *Applied Physics Letters*, 92(6), pp. 2006–2009.

Kudinov, V. I. *et al.* (1990) 'Photoinduced superconductivity in YBaCuO films', *Physics Letters A*, 151(6–7), pp. 358–364.

Kudinov, V. I. *et al.* (1993) 'Persistent photoconductivity in YBa<sub>2</sub>Cu<sub>3</sub>O<sub>6+x</sub> films as a method of photodoping toward metallic and superconducting phases', *Physical Review B*, 47(14), pp. 9017–9028.

Kudinov, V. I. (1994) 'Mechanisms for the persistent photoconductivity of oxygen deficient YBa<sub>2</sub>Cu<sub>3</sub>O<sub>6+x</sub>', *Physica B: Physics of Condensed Matter*, 194–196(PART 1), pp. 1187–1188.

Kudinov, V. I., Kirilyuk, A. I. and Kreines, N. M. (1992) 'Relaxation of frozen photoconductivity in YBCO films.pdf', *JETP Letters*, (2), pp. 101–106.

Laliberté, F. *et al.* (2018) 'High field charge order across the phase diagram of YBa<sub>2</sub>Cu<sub>3</sub>O<sub>y</sub>', *npj Quantum Materials*, 3(1), pp. 1–7.

Landau, L. D. (1957) 'Oscillations in a Fermi liquid', *Soviet Physics JTEP-USSR*, 920(3).

LeBoeuf, D. *et al.* (2007) 'Electron pockets in the Fermi surface of hole-doped high-T<sub>c</sub> superconductors', *Nature*, 450(7169), pp. 533–536.

Lederman, D. *et al.* (1994) 'Photoinduced superconductivity and structural changes in high temperature superconducting films', *Applied Physics Letters*, 64(5), pp. 652–654.

Lee, P. A., Nagaosa, N. and Wen, X. G. (2006) 'Doping a Mott insulator: Physics of high-temperature superconductivity', *Reviews of Modern Physics*, 78(1).

Lei, Y. *et al.* (2014) 'Visible-light-enhanced gating effect at the LaAlO<sub>3</sub>/SrTiO<sub>3</sub> interface', *Nature Communications*, 5, pp. 1–7.

Lesueur, J. *et al.* (1990) 'Depairing-like variation of T<sub>c</sub> in YBa<sub>2</sub>Cu<sub>3</sub>O<sub>7-δ</sub>', *Physica C: Superconductivity*

and its applications, 167(1–2), pp. 1–5.

Li, D. *et al.* (2019) 'Superconductivity in an infinite-layer nickelate', *Nature*, 572(7771), pp. 624–627.

Liang, H. *et al.* (2013) 'Giant photovoltaic effects driven by residual polar field within unit-cell-scale LaAlO<sub>3</sub> films on SrTiO<sub>3</sub>', *Scientific Reports*, 3, pp. 24–26.

Liao, Z. *et al.* (2018) 'Metal–insulator-transition engineering by modulation tilt-control in perovskite nickelates for room temperature optical switching', *Proceedings of the National Academy of Sciences of the United States of America*, 115(38), pp. 9515–9520.

Liu, G. Z. *et al.* (2019) 'Negative photoconductivity under visible light illumination in LaAlO<sub>3</sub>/SrTiO<sub>3</sub> heterostructures', *Journal of Physics D: Applied Physics*, 52(9).

Lombardi, F. *et al.* (2002) 'Intrinsic d wave Effects in YBCO Grain Boundary Josephson Junctions', *Physical Review Letters*, 89(20), pp. 2–5.

Loram, J. W. *et al.* (1997) 'Superconducting and normal state energy gaps in Y<sub>0.8</sub>Ca<sub>0.2</sub>Ba<sub>2</sub>Cu<sub>3</sub>O<sub>7-δ</sub> from the electronic specific heat', *Physica C: Superconductivity and its Applications*, 282–287(PART 3), pp. 1405–1406.

M. Tinkham (1973) *Introduction to superconductivity*. 2nd edn.

Magnuson, M. *et al.* (2014) 'Self-doping processes between planes and chains in the metal-to-superconductor transition of YBa<sub>2</sub>Cu<sub>3</sub>O<sub>6.9</sub>', *Scientific Reports*, 4, p. 7017.

Magnuson, M., Schmitt, T. and Duda, L. C. (2018) 'Polarization-dependent resonant inelastic X-ray scattering study at the Cu L and O K-edges of YBa<sub>2</sub>Cu<sub>3</sub>O<sub>7-x</sub>', *Journal of Electron Spectroscopy and Related Phenomena*, 224, pp. 38–44.

Maksymovych, P. *et al.* (2009) 'Polarization control of electron tunneling into ferroelectric surfaces', *Science*, 324(5933), pp. 1421–1425.

Markowitsch, W. *et al.* (1997) 'Photoinduced enhancement of the c-axis conductivity in oxygen-deficient YBa<sub>2</sub>Cu<sub>3</sub>O<sub>x</sub> thin films', *Applied Physics Letters*, 71(9), pp. 1246–1248.

Markowitsch, W. *et al.* (2009) 'Persistent photoconductivity in oxygen-deficient and ion-irradiated YBa<sub>2</sub>Cu<sub>3</sub>O<sub>x</sub>', *Superconductor Science and Technology*, 22(3), p. 034011.

Marshall, D. S. *et al.* (1996) 'Unconventional Electronic Structure Evolution with Hole Doping in BSCCO: Angle-Resolved Photoemission Results', *Physical Review Letters*, 76, pp. 4841–4844.

Martin, S. *et al.* (1990) 'Normal-state transport properties of Bi<sub>2+x</sub>Sr<sub>2-y</sub>CuO<sub>6+</sub> crystals', *Physical Review B*, 41(1), pp. 846–849.

Matthiessen, A. (1863) 'The influence of temperature on the electric conducting power of alloys', *Philosophical transactions of the royal society of London*, pp. 167–200.

Medarde, M. L. (1997) 'Structural, magnetic and electronic properties of RNiO<sub>3</sub> perovskites (R = rare earth)', *Journal of Physics Condensed Matter*, 9(8), pp. 1679–1707.

Milazzo, G. and Carioli, S. (1978) *Tables of Standard Electrode Potentials*.

Mills, A. and Le Hunten, S. (1997) 'An overview of semiconductor photocatalysis', *Journal of Photochemistry and Photobiology A: Chemistry*, 108(1), pp. 1–35.

Miyano, K. *et al.* (1997) 'Photoinduced insulator-to-metal transition in a perovskite Manganite', *Physical Review Letters*, 78(22), pp. 4257–4260.

Monthoux, P. and Pines, D. (1994) 'Spin-fluctuation-induced superconductivity and normal-state

- properties of YBa<sub>2</sub>Cu<sub>3</sub>O<sub>7</sub>', *Physical Review B*, 49(6), pp. 4261–4278.
- Moreno, C. *et al.* (2010) 'Reversible resistive switching and multilevel recording in La<sub>0.7</sub>Sr<sub>0.3</sub>MnO<sub>3</sub> thin films for low cost nonvolatile memories', *Nano Letters*, 10(10), pp. 3828–3835.
- Motoyama, E. M. *et al.* (2007) 'Spin correlations in the electron-doped high-transition-temperature superconductor Nd<sub>2-x</sub>Ce<sub>x</sub>CuO<sub>4±δ</sub>', *Nature*, 445(7124), pp. 186–189.
- Mundet, B. *et al.* (2020) 'Local strain-driven migration of oxygen vacancies to apical sites in YBa<sub>2</sub>Cu<sub>3</sub>O<sub>7-x</sub>', *Nanoscale*, 12(10), pp. 5922–5931.
- Navacerrada, M. A. *et al.* (2000) 'Critical temperature depression and persistent photoconductivity in ion irradiated YBa<sub>2</sub>Cu<sub>3</sub>O<sub>7-x</sub> films and YBa<sub>2</sub>Cu<sub>3</sub>O<sub>7-x</sub>/PrBa<sub>2</sub>Cu<sub>3</sub>O<sub>7</sub> superlattices', *Applied Physics Letters*, 76(22), pp. 3289–3291.
- Nian, Y. B. *et al.* (2007) 'Evidence for an oxygen diffusion model for the electric pulse induced resistance change effect in transition-metal oxides', *Physical Review Letters*, 98(14), pp. 3–6.
- Nieva, G. *et al.* (1992) 'Photoinduced changes in the transport properties of oxygen-deficient YBCO', *Physical Review B*, 46(21).
- Nikulin, I. V. *et al.* (2004) 'Oxygen nonstoichiometry of NdNiO<sub>3-δ</sub> and SmNiO<sub>3-δ</sub>', *Materials Research Bulletin*, 39(6), pp. 775–791.
- Obradors, X. *et al.* (1993) 'Pressure dependence of the metal-insulator transition in the charge-transfer oxides RNiO<sub>3</sub> (R=Pr,Nd,Nd<sub>0.7</sub>La<sub>0.3</sub>)', *Physical Review B*, 47(18), pp. 12353–12356.
- Ohtomo, A. and Hwang, H. Y. (2004) 'A high-mobility electron gas at the LaAlO<sub>3</sub>/SrTiO<sub>3</sub> heterointerface', 427(January), pp. 423–427.
- Ong, N. P. (1991) 'Geometric interpretation of the weak-field Hall conductivity in two-dimensional metals with arbitrary Fermi surface', *Physical Review B*, 43(1), pp. 193–201.
- Osquiguil, E. *et al.* (1993) 'Photoinduced changes in high temperature superconducting films', *Physica Scripta*, 1993(T49A), pp. 119–123.
- Osquiguil, E. *et al.* (1994) 'Photoexcitation and oxygen ordering in YBaCuO films', *Physical Review B*, 49(5), pp. 4–7.
- Palau, A. *et al.* (2018) 'Electrochemical Tuning of Metal Insulator Transition and Nonvolatile Resistive Switching in Superconducting Films', *ACS Applied Materials and Interfaces*, 10(36), pp. 30522–30531.
- Pantel, D. and Alexe, M. (2010) 'Electroresistance effects in ferroelectric tunnel barriers', *Physical Review B - Condensed Matter and Materials Physics*, 82(13), pp. 1–8.
- Park, W. K. *et al.* (2005) 'Andreev reflection at the normal-metal/heavy-fermion superconductor CeCoIn<sub>5</sub> interface', *Physical Review B - Condensed Matter and Materials Physics*, 72(5), pp. 6–9.
- Phillips, J. C. (1996) 'Stretched exponential relaxation in molecular and electronic glasses', *Rep. Prog. Phys.*, p. 1133.
- Pierret, R. (1996) *Semiconductor Device Fundamentals*.
- Plečenič, A. *et al.* (1998) 'Influence of bias voltage history on conductance properties of YBaCuO/normal metal junctions', *Physica C: Superconductivity and its Applications*, 301(3–4), pp. 234–242.
- Plečenič, A. *et al.* (1994) 'Finite-quasiparticle-lifetime effects in the differential conductance of Bi<sub>2</sub>Sr<sub>2</sub>CaCu<sub>2</sub>O<sub>y</sub>/Au junctions', *Physical Review B*, 49(14), pp. 10016–10019.

pngwing (no date) *Light Pulsed laser deposition Thin film, light, angle, text, schematic png*. Available at: <https://www.pngwing.com/en/free-png-pcjja>.

Proust, C. and Taillefer, L. (2019) 'The Remarkable Underlying Ground States of Cuprate Superconductors', *Annual Review of Condensed Matter Physics*, 10(1), pp. 409–429.

Puchkov, A. V., Basov, D. N. and Timusk, T. (1996) 'The pseudogap state in high-T<sub>c</sub> superconductors: An infrared study', *Journal of Physics Condensed Matter*, 8(48), pp. 10049–10082.

Reyren, N. *et al.* (2007) 'Superconducting Interfaces Between Insulating Oxides', *Science*, 317(5842), pp. 1196–1199.

Rouco, V. *et al.* (2020) 'Quasiparticle tunnel electroresistance in superconducting junctions', *Nature Communications*, 11(1), pp. 1–9.

Sawa, A. (2008) 'Resistive switching in transition metal oxides', *Materials Today*, 11(6), pp. 28–36.

Schlaf, R., Murata, H. and Kafafi, Z. H. (2001) 'Work function measurements on indium tin oxide films', *Journal of Electron Spectroscopy and Related Phenomena*, 120(1–3), pp. 149–154.

Segawa, K. and Ando, Y. (2004) 'Intrinsic Hall response of the CuO<sub>2</sub> planes in a chain-plane composite system of YBa<sub>2</sub>Cu<sub>3</sub>O<sub>y</sub>', *Physical Review B - Condensed Matter and Materials Physics*, 69(10), pp. 2–9.

Shen, Z. X. *et al.* (1993) 'Anomalously large gap anisotropy in the a-b plane of Bi<sub>2</sub>Sr<sub>2</sub>CaCu<sub>2</sub>O<sub>8+δ</sub>', *Physical Review Letters*, 70(10).

Shifu, C. *et al.* (2009) 'Preparation, characterization and activity evaluation of p-n junction photocatalyst p-CaFe<sub>2</sub>O<sub>4</sub>/n-ZnO', *Chemical Engineering Journal*, 155(1–2), pp. 466–473.

Shockley, W. and Queisser, H. J. (1961) 'Detailed balance limit of efficiency of p-n junction solar cells', *Journal of Applied Physics*, 32(3), pp. 510–519.

Simmons, J. G. (1963) 'Generalized Formula for the Electric Tunnel Effect between Similar Electrodes Separated by a Thin Insulating Film', *Journal of Applied Physics*, 34(6), pp. 1793–1803.

Sirena, M. *et al.* (2007) 'Improving ion irradiated high T<sub>c</sub> Josephson junctions by annealing: The role of vacancy-interstitial annihilation', *Applied Physics Letters*, 91(14), pp. 1–4.

Stockinger, C. *et al.* (1998) 'Mechanisms of photodoping in oxygen-deficient films studied by in situ transport measurements', *Physical Review B - Condensed Matter and Materials Physics*, 57(14), pp. 8702–8708.

Sun, J. R. *et al.* (2004) 'Temperature-dependent photovoltaic effects in the manganite-based heterojunction', *Applied Physics Letters*, 85(16), pp. 3375–3377.

Sun, Z. *et al.* (2015) 'Reduced carrier recombination in PbS-CuInS<sub>2</sub> quantum dot solar cells', *Scientific Reports*, 5, pp. 1–11.

Taha, M. *et al.* (2017) 'Insulator-metal transition in substrate-independent VO<sub>2</sub> thin film for phase-change devices', *Scientific Reports*, 7(1), pp. 1–10.

Tallon, J. L. *et al.* (1995) 'Generic superconducting phase behavior in high-T<sub>c</sub> cuprates: T<sub>c</sub> variation with hole concentration in YBa<sub>2</sub>Cu<sub>3</sub>O<sub>7-δ</sub>', *Physical Review B*, 51(18), pp. 911–914.

Tanaka, H., Zhang, J. and Kawai, T. (2002) 'Giant Electric Field Modulation of Double Exchange Ferromagnetism at Room Temperature in the Perovskite Manganite/Titanate p-n junction', *Physical Review Letters*, 88(2), p. 4.

Tebano, A. *et al.* (2012) 'Room-temperature giant persistent photoconductivity in SrTiO<sub>3</sub>/LaAlO<sub>3</sub>

- heterostructures', *ACS Nano*, 6(2), pp. 1278–1283.
- Tolpygo, S. K. *et al.* (1996) 'Effect of oxygen defects on transport properties and: Displacement energy for plane and chain oxygen and implications for irradiation-induced resistivity and suppression', *Physical Review B - Condensed Matter and Materials Physics*, 53(18), pp. 12462–12474.
- Torrance, J. B. *et al.* (1992) 'Systematic study of insulator-metal transitions in perovskites RNiO<sub>3</sub> (R=Pr,Nd,Sm,Eu) due to closing of charge-transfer gap', *Physical Review B*, 45(14), pp. 8209–8212.
- Tranquada, J. M. *et al.* (1988) 'Neutron-diffraction determination of antiferromagnetic structure of Cu ions in YBa<sub>2</sub>Cu<sub>3</sub>O<sub>6+x</sub> with x=0.0 and 0.15', *Physical Review Letters*, 60(2), pp. 156–159.
- Tranquada, J. M. *et al.* (1995) 'Evidence for stripe correlations of spins and holes in copper oxide superconductors', *Nature*, 375.
- Tsymbal, E. Y. and Kohlstedt, H. (2006) 'Tunneling across a ferroelectric', *Science*, 313(5784), pp. 181–183.
- Uimin, G. (1994) 'Order and disorder in the ensemble of Cu-O chain fragments in oxygen deficient planes of YBCO', *Physical Review B*, 50(13).
- Varma, C. M. *et al.* (1989) 'Phenomenology of the normal state of Cu-O high-temperature superconductors', *Physical Review Letters*, 63(18), pp. 1996–1999.
- Varma, C. M. and Abrahams, E. (2001) 'Effective Lorentz force due to small-angle impurity scattering: Magnetotransport in high-T<sub>c</sub> superconductors', *Physical Review Letters*, 86(20), pp. 4652–4655.
- Vishik, I. M. *et al.* (2009) 'A momentum-dependent perspective on quasiparticle interference in Bi<sub>2</sub>Sr<sub>2</sub>CaCu<sub>2</sub>O<sub>8+δ</sub>', *Nature Physics*, 5(10), pp. 718–721.
- Wang, L. *et al.* (2015) 'Competition between strain and dimensionality effects on the electronic phase transitions in NdNiO<sub>3</sub> films', *Scientific Reports*, 5(December), pp. 3–9.
- Wang, L. *et al.* (2018) 'Tuning Bifunctional Oxygen Electrocatalysts by Changing the A-Site Rare-Earth Element in Perovskite Nickelates', *Advanced Functional Materials*, 28(39), pp. 1–8.
- Warren, W. W. *et al.* (1989) 'Cu spin dynamics and superconducting precursor effects in planes above T<sub>c</sub> in YBa<sub>2</sub>Cu<sub>3</sub>O<sub>6.7</sub>', *Physical Review Letters*, 62(10), pp. 1193–1196.
- Wei, J. Y. T. *et al.* (1998) 'Directional tunneling and andreev reflection on YBa<sub>2</sub>Cu<sub>3</sub>O<sub>7-δ</sub> single crystals: Predominance of d-wave pairing symmetry verified with the generalized blonder, tinkham, and klapwijk theory', *Physical Review Letters*, 81(12), pp. 2542–2545.
- Wuyts, B. *et al.* (1993) 'Influence of the oxygen content on the normal-state Hall angle in YBa<sub>2</sub>Cu<sub>3</sub>O<sub>x</sub> films', *Physical Review B*, 47(9), pp. 5512–5515.
- Xie, R. *et al.* (2019) 'Enhancing the photovoltaic performance of hybrid heterojunction solar cells by passivation of silicon surface via a simple 1-min annealing process', *Scientific Reports*, 9(1), pp. 1–7.
- Yang, F., Han, M. Y. and Chang, F. G. (2015) 'Origin of photovoltaic effect in superconducting YBa<sub>2</sub>Cu<sub>3</sub>O<sub>6.96</sub> ceramics', *Scientific Reports*, 5, pp. 1–8.
- Yang, J. J., Strukov, D. B. and Stewart, D. R. (2013) 'Memristive devices for computing', *Nature Nanotechnology*, 8(1), pp. 13–24.
- Ye, J. and Nakamura, K. (1993) 'Quantitative structure analyses of YBa<sub>2</sub>Cu<sub>3</sub>O<sub>7-δ</sub> thin films: Determination of oxygen content from x-ray-diffraction patterns', *Physical Review B*, 48(10), pp. 7554–7564.

You, T. *et al.* (2015) 'Engineering interface-type resistive switching in BiFeO<sub>3</sub> thin film switches by Ti implantation of bottom electrodes', *Scientific Reports*, 5(October), pp. 1–9.

Yu, G. *et al.* (1992) 'Phase separation of photogenerated carriers and photoinduced superconductivity in high T<sub>c</sub> materials', *Physical Review B*, 45(9), pp. 4964–4977.

Van Zalk, M. *et al.* (2010) 'Interface resistance of YBa<sub>2</sub>Cu<sub>3</sub>O<sub>7-δ</sub>/La<sub>0.67</sub>Sr<sub>0.33</sub>MnO<sub>3</sub> ramp-type contacts', *Physical Review B - Condensed Matter and Materials Physics*, 82(13), pp. 1–9.

Zhang, F. C. and Rice, T. M. (1988) 'Effective Hamiltonian for the superconducting Cu oxides', *Physical Review B*, 37(7), pp. 3759–3761.

Zhuravlev, M. Y. *et al.* (2005) 'Giant electroresistance in ferroelectric tunnel junctions', *Physical Review Letters*, 94(24), pp. 1–4.